

The Pennsylvania State University  
The Graduate School

**INVESTIGATION OF TRANSDUCERS IN SMALL ENCLOSURES**

A Thesis in  
Acoustics  
by  
Joseph Bradel

© 2020 Joseph Bradel

Submitted in Partial Fulfillment  
of the Requirements  
for the Degree of

Master of Science

December 2020

The thesis of Joseph Bradel was reviewed and approved by the following:

Stephen C. Thompson  
Research Professor of Acoustics  
Thesis Advisor

Micah R. Shepherd  
Assistant Research Professor

Robert W. Smith  
Assistant Research Professor

Victor W. Sparrow  
Director, Graduate Program in Acoustics  
United Technologies Corporation Professor of Acoustics

# Abstract

Recent applications of active noise control (ANC) have been aimed at canceling noise passing through a building's window, and while attempts have been made to implement this in a laboratory setting, the choice of driver and its enclosure is imperative to accurate sound reproduction, specifically between 500 Hz and 3000 Hz. While choosing a driver based on characteristics listed on its specification sheet is easy, these specifications often lack vital information. With the requirements of having a flat frequency response, small physical size, and low distortion, four drivers were chosen and subjected to further testing. An impedance test, which when analyzed calculated driver parameters, allowed theoretical models to be made that predicted the drivers' behavior when sealed in their smallest possible cuboid enclosure. Frequency responses measured using a maximum-length sequence excitation signal showed how each driver-enclosure assembly prototype behaved in practical application. Various nonlinear measurements taken by the Klippel Analyzer 3 apparatus showed the low-level distortion produced by each driver along with nonlinear behaviors of driver parameters such as stiffness and force factor. Ultimately, the Tang Band W2-2243S driver-enclosure assembly proved to be best for this ANC application based on its frequency response, low distortion, and acceptable nonlinear parameter behavior.

# Table of Contents

List of Figures	vii
List of Tables	xvii
List of Symbols	xviii
Acknowledgments	xxiii
<b>Chapter 1</b>	
<b>Introduction</b>	<b>1</b>
1.1 Background and Motivation . . . . .	1
1.2 Electromagnetic Transducers and Enclosures . . . . .	3
1.2.1 Components . . . . .	3
1.2.2 Electromechanical Coupling . . . . .	4
1.2.3 The Damped Mass-Spring System . . . . .	5
1.2.4 Mechanoacoustical Coupling . . . . .	5
1.2.5 Enclosures . . . . .	6
1.2.6 Sound Radiation and Acoustic Size . . . . .	6
1.2.6.1 Radiation from a Baffled Piston . . . . .	6
1.2.6.2 Directivity through Acoustic Size . . . . .	8
1.2.6.3 Source Level . . . . .	9
1.2.7 Radiation Impedance . . . . .	10
1.3 Published Literature . . . . .	12
1.4 Objectives . . . . .	13
<b>Chapter 2</b>	
<b>Driver-Enclosure Designs</b>	<b>14</b>
2.1 Finding The Right Drivers . . . . .	14
2.1.1 Frequency Response Curves . . . . .	14
2.1.2 Impedance Curves and Resonant Frequency . . . . .	15
2.1.3 Diaphragm Size and Driver Depth . . . . .	15
2.1.4 Rated Power and Maximum Excursion Distance . . . . .	15
2.1.5 The Chosen Drivers . . . . .	16
2.1.5.1 Tang Band W1-2121S . . . . .	16



2.1.5.2	Tang Band W2-2243S . . . . .	17
2.1.5.3	Visaton FRS 5X-8 . . . . .	17
2.1.5.4	Tectonic TEBM36S12-8/A . . . . .	18
2.2	Constructing Testable Enclosures . . . . .	18
2.2.1	Enclosure Shape and Material Choice . . . . .	19
2.2.2	Enclosure Size Variability . . . . .	20
2.3	Final Assembly . . . . .	22
2.4	Estimating Internal Volume . . . . .	23

## Chapter 3

<b>Modeling Electromagnetic Transducers</b>	<b>26</b>
3.1 Overview . . . . .	26
3.2 Domains . . . . .	26
3.2.1 Lumped Elements . . . . .	27
3.2.2 The Impedance Analogy . . . . .	27
3.2.3 The Electrical Domain . . . . .	28
3.2.4 The Mechanical Domain . . . . .	29
3.2.5 The Acoustical Domain . . . . .	31
3.3 Connecting Domains . . . . .	35
3.3.1 Electrical to Mechanical . . . . .	37
3.3.2 Mechanical to Acoustical . . . . .	37
3.4 Using Simulation Software [LTSpice] . . . . .	38
3.5 The Full Transducer Model . . . . .	39

## Chapter 4

<b>Simulating Impedance and Frequency Response</b>	<b>40</b>
4.1 Measuring Impedance . . . . .	40
4.2 Calculating Characteristics . . . . .	44
4.3 Simulating Frequency Response . . . . .	51

## Chapter 5

<b>Measuring Frequency Response and Nonlinear Behavior</b>	<b>59</b>
5.1 Measuring Frequency Response . . . . .	59
5.1.1 The Maximum-Length Sequence . . . . .	60
5.1.2 The MATLAB Impulse Response Measurement App . . . . .	61
5.1.3 Frequency Response Measurement Method . . . . .	62
5.1.4 Frequency Response Results . . . . .	63
5.2 Measuring Nonlinear Behavior . . . . .	68
5.2.1 Loudspeaker Distortion . . . . .	68
5.2.2 The Klippel Analyzer 3 System . . . . .	70
5.2.3 KA3 Measurement Methods . . . . .	72
5.2.4 Comparing Measured Linear Parameters . . . . .	73
5.2.5 Measured Multi-Tone Distortion . . . . .	76
5.2.6 Measured Parameter Nonlinearities . . . . .	78

<b>Chapter 6</b>	
<b>Conclusion</b>	<b>88</b>
6.1 Choosing The Best Driver-Enclosure Assembly . . . . .	88
6.2 The Use of Acceptable Displacement Percentages . . . . .	90
6.3 Future Work . . . . .	91
<b>Appendix A</b>	
<b>Specification Sheets</b>	<b>93</b>
<b>Appendix B</b>	
<b>Engineering Drawings for Enclosure Components</b>	<b>99</b>
<b>Appendix C</b>	
<b>MATLAB Code</b>	<b>110</b>
C.1 Volume Finder . . . . .	110
C.2 Linear Parameter Characterization . . . . .	117
C.3 Impulse and Frequency Response . . . . .	123
C.4 KA3 Data Plotter . . . . .	126
<b>Appendix D</b>	
<b>Impulse Response Measurement Results</b>	<b>144</b>
<b>Bibliography</b>	<b>153</b>

# List of Figures

1.1	The cross-section of a typical moving coil driver taken from Müller and Möser [1], p. 29. . . . .	4
1.2	The visual setup for the baffled circular piston pressure radiation as described and drawn by Blackstock [2], p. 446. By summing the pressure observed radiating from differential elements of differential rings, the full shape of the piston will be realized as the radiation source. . . . .	7
1.3	The normalized directivity in decibels of the baffled circular piston at various values of $ka$ [2]. As $ka$ increases, side lobes are formed producing nulls in the pressure radiation. . . . .	9
1.4	The normalized real and imaginary specific radiation impedance as well as its magnitude [2]. The magnitude nearly matches the imaginary impedance when $ka < 0.5$ showing that the imaginary impedance is dominant at low frequencies. Similarly, the real impedance is dominant at high frequencies when $ka > 3$ . . . . .	12
2.1	The W1-2121S Driver (left) and its frequency response and impedance curve (right), given in red (left scale) and in blue (right scale) respectively, as reported by Tang Band [3]. The specification sheet did not give any information about the methods used to measure the frequency response, such as the power of the input signal, the distance the measurement was taken, or if the driver was placed in an acoustically infinite baffle. This driver was small in size and fairly inexpensive. Images were taken directly from <a href="http://www.tb-speaker.com/uploads/files/e99c0126812ca22379a2179932b9e840.pdf">http://www.tb-speaker.com/uploads/files/e99c0126812ca22379a2179932b9e840.pdf</a> . . . . .	17

2.2	The Tang Band W2-2243S Driver (left) and its frequency response and impedance curve (right), given in red (left scale) and in blue (right scale) respectively, from Tang Band [4]. Like the W1-2121S, this drivers specification sheet did not specify anything about the measurement method for the frequency response including the physical placement of the driver. This was the most expensive of the drivers chosen. It also had a more robust design, taking up the more volume behind the face plate. Images were taken from <a href="http://www.tb-speaker.com/uploads/files/e4964df0494335751327c45c1160fc73.pdf">http://www.tb-speaker.com/uploads/files/e4964df0494335751327c45c1160fc73.pdf</a> . . . . .	18
2.3	Visaton's FRS 5X-8 Driver (top) and the frequency response and impedance curve (bottom), given in red (left scale) and in green (right scale) respectively, reported by Visaton [5]. As labeled on the frequency response and impedance curve, the frequency response measurement used a 1 Watt input signal being measured 1 meter away from the driver. The specification sheet does not specify if these measurements were taken while holding the driver in a baffle. This driver had a fairly large dust cap in its design. The magnet was nearly the diameter of the cone, but the overall depth was the same as the W2-2243S [5] [4]. Images were taken from <a href="https://www.visaton.de/sites/default/files/dd_product/frs5x_8.pdf">https://www.visaton.de/sites/default/files/dd_product/frs5x_8.pdf</a> . . . . .	19
2.4	The Tectonic TEBM36S12-8/A Driver (top) and its frequency response and impedance curve (bottom), given in red (left scale) and in blue (right scale) respectively, as reported by Tectonic [6]. The specification sheet reported that the frequency response measurement used a 1 Watt input signal and was measured 1 meter away from the driver but did not specify the mounting technique used. The TEBM36S12-8/A was incredibly shallow, allowing for a small enclosure design. The frame behind the membrane required the mount cutout to be a square with filleted corners rather than a circle. Images taken from <a href="https://www.tectonicaudiolabs.com/wp-content/uploads/woocommerce_uploads/2018/10/T-DS-TEBM36S12-8A.pdf">https://www.tectonicaudiolabs.com/wp-content/uploads/woocommerce_uploads/2018/10/T-DS-TEBM36S12-8A.pdf</a> . . . . .	20
2.5	The engineering drawing for the FRS 5X-8 Faceplate. The design used a simple lip design to nest inside of the rest of the enclosure, providing easy alignment. . . . .	21
2.6	The engineering drawing for the enclosure tube assembly. This print allowed for two sizes of tube to be created: a $3\frac{1}{2}$ inch tube and a 3 inch tube. . . . .	22

2.7	The front (left) and back (right) views of the assembled enclosure with the W2-2243S driver. The hex nut glued on the back was used to mount the enclosure onto a stand for frequency response measurements. . . . .	23
3.1	The electrical domain circuit model, which includes the resistance and the inductance of the voice coil. The constant voltage generator will be the input signal for the whole model. [7] . . . . .	29
3.2	The mechanical domain analog circuit model, including the mechanical resistance, compliance, and mass in series according to the impedance analogy [7]. This domain does not include a constant force generator because it will receive its potential from the connection it has between the other domains. . . . .	31
3.3	The exact solution [2] compared to the modeled solution by Beranek [7] [8] of the acoustic specific radiation impedance. The model lacks the rippling that the exact solution shows, but the real part of the impedance roughly follows the exact solution's real impedance when $ka > 3$ and the imaginary part of the impedance roughly follows the exact solution's imaginary impedance when $ka < 0.5$ . These regions are important to match because the imaginary impedance is dominant when $ka < 1$ and the real impedance is dominant when $ka > 2$ . . . . .	34
3.4	The acoustic radiation model as described by Beranek [7]. The terminals labeled $Z_{acs+}$ and $Z_{acs-}$ are connecting terminals that connect this subcircuit to the transducer acoustical terminals. . . . .	34
3.5	The modeled Source Level calculation. The input volume velocity is pushed through a potential generator that adds no additional potential (left-half of the model). The flow is generated and run through the inductor element, which has an inductance of $\rho_0/(2\pi \times 20 \text{ } \mu\text{Pa})$ . This inductance multiplied by the derivative of the flow variable, which in the acoustical domain is volume velocity, creates a potential that is the Source Level (right-half of the model) prior to the decibel calculation. This potential is read and generated as an output, labeled SL. . . . .	36
3.6	The acoustical domain analog circuit model. The acoustic radiation impedance modeled in Fig. 3.4 and the Source Level modeled in Fig. 3.5 have been modeled as subcircuits labeled here as Zrad and SL respectively. The capacitive element represents the acoustical compliance related to the driver being placed in an enclosure. . . . .	36

3.7	The completed simulation model made using LTSpice. The gyrator, transistor, acoustic radiation impedance (labeled Zrad), and sound pressure level (labeled SPL) were all subcircuits created as separate files. . . . .	39
4.1	A LTSpice representation of the setup for the impedance measurement test. The signal generator, labeled Ao0, was set to input as sine sweep at 0.5 Volts starting from 20 Hz to 4000 Hz. The voltage across the 46.7 $\Omega$ resistor, labeled R_known, was measured at Ai0 and the voltage measured across the driver terminals was measured at Ai1. . . . .	41
4.2	The real part of the DC-shifted driver impedance for the W1-2121S (top-left), W2-2243S (top-right), FRS 5X-8 (bottom-left), and TEBM36S12-8/A (bottom-right) drivers. Unweighted and weighted impedance results are included. . . . .	43
4.3	The linear curve fit for the W1-2121S (top-left), W2-2243S (top-right), FRS 5X-8 (bottom-left), and TEBM36S12-8/A (bottom-right) drivers. The slope of each fit line was the mechanical compliance $C_m$ and the y-intercept was equal to the unweighted moving mass multiplied by the mechanical compliance, $C_m m_m$ . . . . .	45
4.4	The imaginary impedance for the W1-2121S (top-left), W2-2243S (top-right), FRS 5X-8 (bottom-left), and TEBM36S12-8/A (bottom-right) drivers. Finding the difference in frequency between the minimum and maximum imaginary impedance was used in finding the mechanical quality factor, $Q_{ms}$ . . . . .	46
4.5	The maximum DC-shifted real impedance for the W1-2121S (top-left), W2-2243S (top-right), FRS 5X-8 (bottom-left), and TEBM36S12-8/A (bottom-right) drivers. The maximum real impedance for each driver is the electrical equivalent of the mechanical resistance, $R_{em}$ . . . . .	48
4.6	The free-air simulation model made using LTSpice. The addition of the acoustic radiation subcircuit (labeled Zrad) modeled the radiation from the back of the driver. The elimination of the acoustic capacitive element (previously C_acs) accounted for the impedance test not using an enclosure. . . . .	49
4.7	The real part of the impedance (top), imaginary part of the impedance (middle), and impedance magnitude (bottom) of the measured and modeled W1-2121S driver. . . . .	52

4.8	The real part of the impedance (top), imaginary part of the impedance (middle), and impedance magnitude (bottom) of the measured and modeled W2-2243S driver. . . . .	53
4.9	The real part of the impedance (top), imaginary part of the impedance (middle), and impedance magnitude (bottom) of the measured and modeled FRS 5X-8 driver. . . . .	54
4.10	The real part of the impedance (top), imaginary part of the impedance (middle), and impedance magnitude (bottom) of the measured and modeled TEBM36S12-8/A driver. . . . .	55
4.11	The modeled frequency response curves for the W1-2121S driver being modeled in free air and being modeled in the enclosure. The frequency response curve stayed relatively flat between 500 Hz and 3000 Hz. There was an increase in response of 1 dB at 500 Hz followed by a steady return to the free-air response. . . . .	57
4.12	The modeled frequency response curves for the W2-2243S driver being modeled in free air and being modeled in the enclosure. This driver responded the best to the driver-enclosure model. The enclosure raised the resonant frequency enough to flatten the response in the operating bandwidth of 500 Hz to 3000 Hz. . . . .	57
4.13	The modeled frequency response curves for the FRS 5X-8 driver being modeled in free air and being modeled in the enclosure. There was a larger spike in frequency response due to the enclosure that prevented a perfectly flat response from being observed in the model. While the increase in response was only 4 dB above the free-air model, it was one of the more extreme reactions out of the chosen drivers. . . . .	58
4.14	The modeled frequency response curves for the TEBM36S12-8/A driver being modeled in free air and being modeled in the enclosure. This driver had a sharp increase in frequency response, departing from an otherwise flat response from the free-air model. This was due to the driver being modeled in the smallest enclosure volume out of the chosen drivers. . . .	58
5.1	An example comparison between the W2-2243S impulse responses for a 12.36 dBV excitation level (top) and a 6.36 dBV excitation level (bottom). . . .	63
5.2	The frequency response for the W2-2243S driver-enclosure assembly. . . .	64
5.3	The frequency response for the FRS 5X-8 driver-enclosure assembly. . . .	65

5.4	The frequency response for the TEBM36S12-8/A driver-enclosure assembly.	66
5.5	The frequency response for the W1-2121S driver-enclosure assembly. . . .	66
5.6	A general example of what causes of distortion affect what ranges of frequency [9]. In this general example, the stiffness as a function of displacement, labeled $K_m(x)$ , affected the region below the resonant frequency. The distortion caused by the force factor, labeled $Bl(x)$ , affected a more broadband range. Nonlinear induction with varying displacement, labeled $L(x)$ , and with varying current, labeled $L(i)$ , began to cause distortions above the resonant frequency and increased higher into the frequency spectrum. The Doppler Effect and cone vibrations showed significant distortions in a much higher portion of the frequency spectrum. Image taken from <a href="https://www.klippel.de/know-how/measurements/nonlinear-distortion/multi-tone-distortion.html">https://www.klippel.de/know-how/measurements/nonlinear-distortion/multi-tone-distortion.html</a> . . . . .	69
5.7	The displacement spectrum for the W1-2121S driver. The signal tones of the multi-tone response (blue) were separated from the generated distortion (red) and the measurement noise floor (yellow). The average distortion (purple) was calculated in third-octave bands. . . . .	77
5.8	The displacement spectrum for the W2-2243S driver. The signal tones of the multi-tone response (blue) were separated from the generated distortion (red) and the measurement noise floor (yellow). The average distortion (purple) was calculated in third-octave bands. . . . .	78
5.9	The displacement spectrum for the FRS 5X-8 driver. The signal tones of the multi-tone response (blue) were separated from the generated distortion (red) and the measurement noise floor (yellow). The average distortion (purple) was calculated in third-octave bands. . . . .	79
5.10	The displacement spectrum for the TEBM36S12-8/A driver. The signal tones of the multi-tone response (blue) were separated from the generated distortion (red) and the measurement noise floor (yellow). The average distortion (purple) was calculated in third-octave bands. . . . .	80
5.11	The driver stiffness, $k_s(x)$ , characteristics for all drivers as a function of displacement. The dashed traces are each solid trace reversed to visually emphasize asymmetry. Positive displacement ( $+x$ ) signifies the voice coil pushing outwards, moving away from the rear pole plate; whereas, negative displacement ( $-x$ ) refers to the voice coil moving inward towards the rear pole plate. . . . .	81



5.12	The percent change from $k_s(0)$ to $k_s(x)$ for all drivers. . . . .	81
5.13	The percent difference between $k_s(- x )$ and $k_s( x )$ for all drivers. This represents the asymmetry of the $k_s(x)$ curve in Fig. 5.11 where a larger percent difference represents more asymmetry for that displacement magnitude. . . . .	82
5.14	The force factor, $Bl$ , characteristics for all drivers as a function of displacement. The dashed traces are each solid trace mirrored to emphasize asymmetry. Positive displacement ( $+x$ ) signifies the voice coil pushing outwards, moving away from the rear pole plate; whereas, negative displacement ( $-x$ ) refers to the voice coil moving inward towards the rear pole plate. . . . .	84
5.15	The percent change from $Bl(0)$ to $Bl(x)$ for all drivers. . . . .	84
5.16	The percent difference between $Bl(- x )$ and $Bl( x )$ for all drivers. This represents the asymmetry of the $Bl(x)$ curve in Fig. 5.14 where a larger percent difference represents more asymmetry for that displacement magnitude. . . . .	85
A.1	The specification sheet for the Tang Band W1-2121S driver [3]. The spec sheet was taken directly from <a href="http://www.tb-speaker.com/uploads/files/e99c0126812ca22379a2179932b9e840.pdf">http://www.tb-speaker.com/uploads/files/e99c0126812ca22379a2179932b9e840.pdf</a> . . . . .	94
A.2	The specification sheet for the Tang Band W2-2243S driver [4]. The spec sheet was taken directly from <a href="http://www.tb-speaker.com/uploads/files/e4964df0494335751327c45c1160fc73.pdf">http://www.tb-speaker.com/uploads/files/e4964df0494335751327c45c1160fc73.pdf</a> . . . . .	95
A.3	The specification sheet for the Tang Band FRS 5X-8 driver [5]. The spec sheet was taken directly from <a href="https://www.visaton.de/sites/default/files/dd_product/frs5x_8.pdf">https://www.visaton.de/sites/default/files/dd_product/frs5x_8.pdf</a> . . . . .	96
A.4	The specification sheet for the Tectonic TEBM36S12-8/A driver [6]. The spec sheet was taken directly from <a href="https://www.tectonicaudiolabs.com/wp-content/uploads/woocommerce_uploads/2018/10/T-DS-TEBM36S12-8A.pdf">https://www.tectonicaudiolabs.com/wp-content/uploads/woocommerce_uploads/2018/10/T-DS-TEBM36S12-8A.pdf</a> . . . . .	97
A.5	The sound absorption coefficient for the Auralex 2 inch Studiofoam® Pyramid™ foam paneling that lined the room in which the frequency response measurements were conducted [10]. This graph was taken directly from <a href="https://auralex.com/content/performance/2pyramid.pdf">https://auralex.com/content/performance/2pyramid.pdf</a> . . . . .	98

B.1	The engineering drawing for Part 001, the base piece for the tube assembly, for 3.5 inch and 3 inch tube sizes. . . . .	100
B.2	The engineering drawing for Part 002, the side piece for the tube assembly, for 3.5 inch and 3 inch tube sizes. . . . .	101
B.3	The engineering drawing for Part A003, the tube assembly, in 3.5 inch and 3 inch sizes. . . . .	102
B.4	The engineering drawing for Part 004, the W1-2121S face plate, in 3.5 inch and 3 inch sizes. . . . .	103
B.5	The engineering drawing for Part 005, the W2-2243S face plate. . . . .	104
B.6	The engineering drawing for Part 006, the FRS 5X-8 face plate. . . . .	105
B.7	The engineering drawing for Part 007, the TEBM36S12-8/A face plate. .	106
B.8	The engineering drawing for Part 008, the back plate of the enclosure, in 3.5 inch and 3 inch sizes. . . . .	107
B.9	The engineering drawing for Part 009, the hole guide, in 3.5 inch and 3 inch sizes. . . . .	108
B.10	The engineering drawing for Part A010, the full kit of enclosure parts made for this project. . . . .	109
D.1	The impulse response for the W1-2121S driver with an excitation signal level of 12.36 dBV. . . . .	145
D.2	The impulse response for the W1-2121S driver with an excitation signal level of 6.36 dBV. . . . .	145
D.3	The impulse response for the W1-2121S driver with an excitation signal level of 0.36 dBV. . . . .	145
D.4	The impulse response for the W1-2121S driver with an excitation signal level of $-11.36$ dBV. . . . .	146
D.5	The impulse response for the W1-2121S driver with an excitation signal level of $-23.64$ dBV. . . . .	146

D.6	The impulse response for the W1-2121S driver with an excitation signal level of $-29.64$ dBV. . . . .	146
D.7	The impulse response for the W2-2243S driver with an excitation signal level of $12.36$ dBV. . . . .	147
D.8	The impulse response for the W2-2243S driver with an excitation signal level of $6.36$ dBV. . . . .	147
D.9	The impulse response for the W2-2243S driver with an excitation signal level of $0.36$ dBV. . . . .	147
D.10	The impulse response for the W2-2243S driver with an excitation signal level of $-11.36$ dBV. . . . .	148
D.11	The impulse response for the W2-2243S driver with an excitation signal level of $-23.64$ dBV. . . . .	148
D.12	The impulse response for the W2-2243S driver with an excitation signal level of $-29.64$ dBV. . . . .	148
D.13	The impulse response for the FRS 5X-8 driver with an excitation signal level of $12.36$ dBV. . . . .	149
D.14	The impulse response for the FRS 5X-8 driver with an excitation signal level of $6.36$ dBV. . . . .	149
D.15	The impulse response for the FRS 5X-8 driver with an excitation signal level of $0.36$ dBV. . . . .	149
D.16	The impulse response for the FRS 5X-8 driver with an excitation signal level of $-11.36$ dBV. . . . .	150
D.17	The impulse response for the FRS 5X-8 driver with an excitation signal level of $-23.64$ dBV. . . . .	150
D.18	The impulse response for the FRS 5X-8 driver with an excitation signal level of $-29.64$ dBV. . . . .	150
D.19	The impulse response for the TEBM36S12-8/A driver with an excitation signal level of $12.36$ dBV. . . . .	151

D.20	The impulse response for the TEBM36S12-8/A driver with an excitation signal level of 6.36 dBV. . . . .	151
D.21	The impulse response for the TEBM36S12-8/A driver with an excitation signal level of 0.36 dBV. . . . .	151
D.22	The impulse response for the TEBM36S12-8/A driver with an excitation signal level of $-11.36$ dBV. . . . .	152
D.23	The impulse response for the TEBM36S12-8/A driver with an excitation signal level of $-23.64$ dBV. . . . .	152
D.24	The impulse response for the TEBM36S12-8/A driver with an excitation signal level of $-29.64$ dBV. . . . .	152

# List of Tables

2.1	Reported Driver Specifications . . . . .	16
2.2	Tube Assembly Cut Dimensions . . . . .	23
2.3	Estimated Enclosure Cavity Volume . . . . .	25
4.1	Used Masses and Resonant Frequencies from the Impedance Test . . . . .	44
4.2	Measured and Given Driver Parameters . . . . .	50
4.3	Measured to Modeled Resonant Frequency Comparison . . . . .	51
4.4	Modeled Driver-Enclosure Assembly Resonant Frequencies . . . . .	56
5.1	Measured Parameters for the W1-2121S Driver . . . . .	73
5.2	Measured Parameters for the W2-2243S Driver . . . . .	74
5.3	Measured Parameters for the FRS 5X-8 Driver . . . . .	75
5.4	Measured Parameters for the TEBM36S12-8/A Driver . . . . .	75
5.5	Acceptable Displacement Percentages . . . . .	85
5.6	Expected Percent Change of Total Driver-Enclosure Compliance . . . . .	87

# List of Symbols

$\vec{F}$	Force vector, p. 4
$l$	Length of voice coil wire inside the magnetic field, p. 4
$\vec{i}$	Electrical current vector, p. 4
$\vec{B}$	Magnetic flux density vector, p. 4
$\vec{e}$	Electrical voltage vector, p. 5
$\vec{u}$	Velocity vector, p. 5
$\tilde{P}_{cone}$	Complex pressure from the cone, p. 5
$\tilde{F}_{cone}$	Complex force from the cone, p. 5
$A_{cone}$	Area of the cone, p. 5
$p_{baff}$	Pressure radiated from a baffled piston, p. 7
$k$	Acoustic wavenumber, p. 7
$\rho_0$	Density of the fluid medium, p. 7
$c_0$	Sound speed of the fluid medium, p. 7
$u_0$	Velocity Amplitude, p. 7
$\omega$	Angular frequency, p. 7
$t$	Time, p. 7
$R$	Distance from a differential area on a baffled piston and an observation point in space, p. 7
$S$	Surface area, p. 7
$f$	Frequency, p. 7

$\lambda$	Wavelength, p. 7
$\theta$	Vertical angle from the center of the piston to an observation point in space, p. 7
$\psi$	Radial angle from the center of the baffled piston to a differential surface area on a baffled piston, p. 7
$\sigma$	Radial distance from the center of the baffled piston to a differential surface area on a baffled piston, p. 7
$a$	Radius of a baffled piston, p. 7
$r$	Distance from the center of the baffled piston to an observation point in space, p. 7
$kr$	Acoustic distance, p. 8
$D$	Directivity of the baffled piston, p. 8
$ka$	Acoustic size, p. 8
SPL	Sound Pressure Level, p. 9
$p_{rms}$	Root mean squared pressure, p. 9
$p_{ref}$	Reference pressure, p. 9
$p_0$	Pressure amplitude, p. 9
$R_0$	Rayleigh distance, p. 9
SL	Source Level, p. 10
$Z_{rad}$	Radiation impedance, p. 10
$\bar{p}_{surf}$	Average surface pressure, p. 10
$F_{surf}$	Surface force, p. 10
$p_{surf}$	Pressure on the surface of a differential piston area, p. 11
$\theta'$	Angle between the horizontal and the line between two differential areas on a piston face, p. 11
$R'$	Distance between two differential areas on a piston face, p. 11
$X_{max}$	Maximum excursion distance, p. 16
$V_{box}$	Estimated internal enclosure volume, p. 25

$e_{elem}$	Element potential, p. 27
$i_{elem}$	Element flow, p. 27
$R_{elem}$	Element resistance, p. 27
$C_{elem}$	Element compliance, p. 28
$L_{elem}$	Element inductance, p. 28
$Z_{R_{elem}}$	Resistor element impedance, p. 28
$Z_{C_{elem}}$	Compliance element impedance, p. 28
$Z_{L_{elem}}$	Inductor element impedance, p. 28
$L_e$	Voice coil electrical inductance, p. 28
$R_e$	Voice coil electrical resistance, p. 28
$Z_e$	Total electrical impedance, p. 28
$V_{in}$	Input electrical voltage, p. 29
$F_m$	Mechanical force, p. 29
$R_m$	Mechanical resistance, p. 29
$v$	Mechanical velocity, p. 29
$Z_{R_m}$	Mechanical resistance impedance, p. 29
$m_m$	Mechanical moving mass, p. 30
$Z_{m_m}$	Mechanical inductance impedance, p. 30
$k_s$	Mechanical spring constant, p. 30
$C_m$	Mechanical compliance, p. 30
$Z_{C_m}$	Mechanical compliance impedance, p. 30
$Z_m$	Total mechanical impedance, p. 31
$P_{acs}$	Acoustic pressure, p. 31
$m_{acs}$	Acoustic mass, p. 31
$U$	Volume velocity, p. 31
$Z_{m_{acs}}$	Acoustic inductance impedance, p. 32



$R_{acs}$	Acoustic resistance, p. 32
$Z_{R_{acs}}$	Acoustic resistance impedance, p. 32
$C_{acs}$	Acoustic compliance, p. 32
$Z_{C_{acs}}$	Acoustic compliance impedance, p. 32
$V_{encl}$	Enclosure volume, p. 32
$M_{A1}$	Modeled acoustic radiation mass element, p. 33
$R_{A1}$	First modeled acoustic radiation resistor element, p. 33
$R_{A2}$	Second modeled acoustic radiation resistor element, p. 33
$C_{A1}$	Modeled acoustic radiation compliance element, p. 33
$Z_{rad_{model}}$	Total modeled acoustic radiation impedance, p. 33
$Z_{M_{A1}}$	Modeled acoustic radiation mass impedance, p. 33
$Z_{R_{A1}}$	First modeled acoustic radiation resistor impedance, p. 33
$Z_{R_{A2}}$	Second modeled acoustic radiation resistor impedance, p. 33
$Z_{C_{A1}}$	Modeled acoustic radiation compliance impedance, p. 33
$g_m$	Mutual conductance, p. 37
$Bl$	Force factor, p. 37
$\tilde{F}$	Complex force, p. 37
$\tilde{e}$	Complex voltage, p. 37
$\tilde{u}$	Complex velocity, p. 37
$\tilde{i}$	Complex current, p. 37
$\phi$	Transformation ratio, p. 38
$H(f)$	Transfer function as a function of frequency, p. 41
$\bar{G}_{xy}$	Averaged cross-spectral density, p. 41
$\bar{G}_{xx}$	Averaged power spectral density, p. 41
$R_{known}$	Known resistance used in impedance measurements, p. 41
$Z_{shifted}$	Measured driver impedance shifted by the driver's DC offset, p. 42

$R_{DC}$	Measured DC resistance of the driver, p. 42
$f_0$	Resonant frequency, p. 44
$m_i$	Added mass for measuring impedance, p. 44
$Q_{ms}$	Mechanical quality factor, p. 46
$f_{min}$	Frequency at the minimum imaginary impedance signifying the upper half-power frequency, p. 46
$f_{max}$	Frequency at the maximum imaginary impedance signifying the upper half-power frequency, p. 46
$F$	Force scalar, p. 47
$u$	Velocity scalar, p. 47
$e$	Voltage scalar, p. 47
$i$	Current scalar, p. 47
$Z_{em}$	Electrical equivalent of mechanical impedance, p. 47
$m$	Order of the primitive polynomial used to create feedback shift registers for an MLS signal, p. 60
$n$	Length of the generated MLS signal, p. 60
$\Delta T$	Change in temperature of the voice coil, p. 73
$x$	Voice coil displacement, p. 68
$PC(x)$	Percent change as a function of displacement, p. 80
$PD( x )$	Percent difference as a function of displacement magnitude, p. 83
$C_{ma}$	Mechanical equivalent of acoustic compliance, p. 86
$\gamma$	Specific heat ratio of an ideal gas, p. 86
$P_{air}$	Pressure of the air within a sealed enclosure, p. 86

# Acknowledgments

I'd like to thank Dr. Stephen Thompson, my advising professor, for aiding and guiding me through this project. Without his guidance, this project would not be as thorough as it is presented here. From background information to measurement methods to analysis techniques, his input helped me move through this project from start to finish. With his assistance, as well as Penn State University's dedication to their students, this project was able to be completed in the face of global complications that presented unique challenges for researchers.

I would also like to thank my family for supporting me as I took this project from the measurement and analysis phase and into the presentation phase. They have helped me tremendously with their support over my academic years to overcome difficult times. Always optimistic about the future, they created a positive mental attitude that was at times greatly needed.

Finally, I would like to thank my friends for providing me with an outlet to breathe while working on the more involved portions of this project. Both at home and at Penn State, they have been great companions and colleagues while I progressed through the graduate program. The evenings spent unwinding with Nick Carder, Gary Rhoades, and Luke Wade were priceless. These closest colleagues, along with the entirety of the Penn state Graduate Program in Acoustics, also served as valuable resources for academic discussion, always willing to advise me when my progress was slowed by an academic query.

With the wonderful support, both personal and academic, from those mentioned above as well as others I am fortunate enough to have in my life, my journey through graduate school has been a rewarding one, capitalized by this presentation of my research.

# Chapter 1 | Introduction

## 1.1 Background and Motivation

Audio speakers are built in a variety of shapes and sizes, each one having a specifically designed use. This makes some speaker drivers more appropriate for some applications than others, requiring anyone from audio engineers to do-it-yourself specialists to choose their drivers carefully based on their project's needs. When a driver has been chosen, there is then the issue of physically implementing it into the project. In the world of acoustics, that physical implementation can come at the cost of changing the driver's behavior. This adds another layer of design consideration onto the scope of any driver-based project. The drivers chosen for active noise canceling must have a specific frequency response over the bandwidth of interest in order to properly produce the signal that will cancel noise without altering the signal being produced. Choosing the right driver-enclosure combination will help ensure the success of the project as a whole.

In this particular active noise control project, noise passing through a building window was to be canceled. The basics of active noise control can be explained simply, but shed important light onto the design requirements. Active noise control is based around the idea of destructive interference, which occurs when two similar waves that are out of phase with each other sum in a way that results in a reduced pressure at the waves' similar frequencies at a desired location [11]. In the ideal case, summing two sine waves with the same frequency that are opposite in phase would result in a zero-sum, perfectly canceled signal. Assuming that the signal used to create destructive interference is accurate, a driver used in this application should produce the synthesized signal as accurately as possible, meaning that the driver should be linear and have a flat frequency response. This is not necessarily realisable by a single driver size in practical application; however, it was determined that the driver would be canceling noise between 500 Hz and 3000 Hz

thus providing an operating bandwidth for the driver. This ensured that the signal being used to actively cancel noise will be produced as accurately as possible, restricting the generation any excess noise in the process of canceling the original noise.

Aesthetic considerations were important for this application as the drivers chosen were intended to be mounted onto the window frame, each in individual enclosures. This put a size limit on the drivers used as well as the enclosures they mounted into. If the drivers were too big, the window panes would need to shrink or the frame would need to be bigger. If the enclosures were too deep, the window frame would need to be built further into the wall. The enclosure space also affected the characteristics of the driver mounted within, so the enclosure size would need to be considered when determining the speaker system characteristics. The enclosure size chosen needed to meet an acceptable size for mounting in the window frame and would need to affect the speaker characteristics in a way that does not compromise the frequency response in the operating bandwidth.

Making a small driver-enclosure assembly with a flat frequency response comes at a cost. This project, requiring several driver-enclosure assemblies to be made in the future, would need to be cost effective as well. Finding the cheapest solution when choosing a driver and making the enclosure was an important factor when prototyping the driver-enclosure assemblies in preparation for their potential future use.

With the design criteria laid out, the design process began. While working with a theoretical model helped provide an intuition on the design, real-world testing needed to be done to confirm that the designs meet the required specifications. This was the most important part of the design process on the pathway of turning an idea into reality. Various test methods such as driver parameter testing, frequency response testing via maximum-length sequence measurements, and nonlinear behavior measurements were performed throughout the design process to help create theoretical models and confirm that the real-world designs met the criteria.

While the choice of driver and the design of the enclosures were completed using the window ANC application's design constraints, active noise control has been used in other consumer products. The application of active noise control inside of an automobile cabin has similar design considerations to the window ANC application. From a physical design standpoint, both applications require that the drivers and enclosures do not interfere with the automotive passengers' viewing experience through the windows. The speakers used in the cabin have been designed for an entertainment playback application rather than a noise control application. This is due to the automobile cabin becoming a place where people spend significant amounts of time, causing automotive companies to include high-

quality commercial audio systems in the cabin [12]. The automotive active noise control application must also limit distortions produced by the drivers chosen [13]. This has been done by both the use of algorithmic active nonlinear control [14] [15] and using drivers that produce minimal distortion. Driver distortion has been investigated by several members of the audio community. Speaker nonlinearities have been observed to originate from several sources [16] leading to research being done on reducing nonlinearities [17]. Measuring and characterizing distortion has been done in several ways as well. One way has been the use of the two-tone signal, which can be used to classify specific harmonics produced by the driver [17]. While measuring nonlinear distortion has been explored, predicting distortion has also been explored. This has been done by creating a nonlinear model that uses nonlinear behavior of driver parameters to predict the distortion produced by a driver [18]. While the automotive driver-enclosure designs have been aimed at entertainment audio playback, the previous research regarding distortion production and prediction closely aligned with the scope of this design and research.

## 1.2 Electromagnetic Transducers and Enclosures

The electromagnetic transducer, like most acoustic radiators, has several layers of complexity, from its design to the physics of its radiation. This, combined with its interaction with an enclosed back-volume, creates the commercially available speaker. Understanding these layers was paramount to implementing the correct driver choice and enclosure design into this ANC application.

### 1.2.1 Components

While there are a few types of commercially available driver designs, the drivers used in this project have a common design, which is laid out well by Müller and Möser [1] in the Fig. 1.1. Starting with the magnetic circuit, two pole plates are fixed to the front and back of a permanent magnet, the front pole plate shaped like a flat ring. The magnet, shaped like a hollow cylinder, surrounds a pole piece placed at the center of the assembly with the voice coil in between; an air gap separates the magnet, voice coil, and pole piece. The voice coil, mounted on the voice coil former, is attached to a spider that helps keep the voice coil centered and mechanically aids the movement between the voice coil and the cone membrane, otherwise referred to as the diaphragm. The outer edge of the cone is supported by what is commonly referred to as a surround, labeled here as the

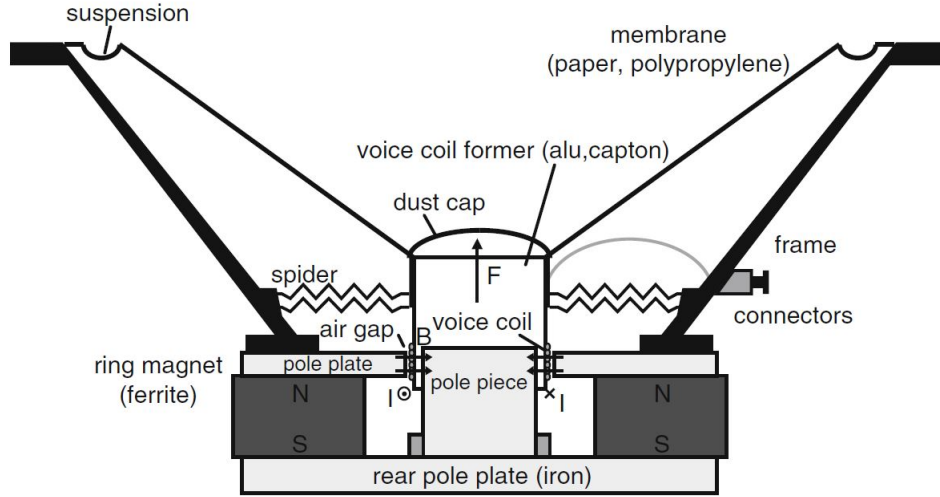


**Figure 1.1.** The cross-section of a typical moving coil driver taken from Müller and Möser [1], p. 29.

suspension, which generally has a roll. While the spider and surround help to keep the components centered, they have another effect as well; as the cone displacement increases the spider corrugations and surround rolls add stiffness to the system. A dust cap at the center of the assembly keeps the coil and air gap of the assembly free from contaminants. While it may not be clear from the cross-sectional view shown in Fig. 1.1, the frame that attaches the edge of the front pole plate to the edge of the surround is not always a closed shape; for drivers like those tested in this project, the frame is usually made with an open framework allowing air to move freely behind the cone.

### 1.2.2 Electromechanical Coupling

The moving coil design generates sound through the interaction between the magnetic field and the solenoid voice coil, radiating sound from the resulting cone movement. The force generated by the voice coil and magnetic field interaction can be seen in Ampère's Law which expresses the force generated  $\vec{F}$  in terms of the magnets properties and current input  $\vec{i}$ ,

$$\vec{F} = l(\vec{i} \times \vec{B}), \quad (1.1)$$

where  $\vec{B}$  is the magnetic flux density of the magnet and  $l$  is the length of the wire within the magnetic field created by the magnet [19]. This law shows that not only will a force be generated but it will be directional. The direction of the generated force is

determined by the direction of the input signal current. With the magnet mechanically fixed to the driver's back plate, the resulting force is seen as the voice coil oscillating. It is important to note that not only is there a force generated in this process, but a voltage is generated as well following Lenz's Law,

$$\vec{e} = l(\vec{u} \times \vec{B}). \quad (1.2)$$

Lenz's Law relates the produced voltage  $\vec{e}$  to mechanical velocity  $\vec{u}$  and the magnetic field. The direction of the generated current and the generated voltage will be opposite. This shows that the field from the magnet is acting as the bridge between the electrical domain and the mechanical domain [19].

### 1.2.3 The Damped Mass-Spring System

The operation of the driver has now become fairly simple. An electrical current is used to create a force that pushes the cone along the axis of the voice coil. The mechanical portion of this system can be modeled as a simple damped mass-spring system, with the mass being the the mass of the cone, voice coil, and dust cap, the spring being analogous to the surround and spider mounting devices [7], and the damper being the various resistances to movement throughout the system that dissipate energy [19]. In this model, the radiation of sound is not included in the damper analogy. This simple models helps to give a little mechanical intuition on how drivers behave by thinking about a larger damped mass-spring system: if the spring is stiffened, the resonant frequency will increase; if more mass is added, inertia is added effectively lowering the resonant frequency; if stronger damping is used, the system will dissipate more energy.

### 1.2.4 Mechanoacoustical Coupling

Just as there is electromechanical coupling used in transducer design, mechanoacoustical coupling is just as important. These particular transducers do this by using the cone vibration to move the fluid medium. This coupling can be seen using the simple definition of pressure and volume velocity. The relationship between pressure and force is

$$\tilde{P}_{cone} = \frac{\tilde{F}_{cone}}{A_{cone}} \quad (1.3)$$

where  $\tilde{P}_{cone}$  is the complex pressure generated by the complex force of the cone  $\tilde{F}_{cone}$  over the area of the cone  $A_{cone}$  [7]. This shows that the directional force of the cone will



induce a directional pressure. This coupling can also be seen in the volume velocity.

$$\tilde{U}_{cone} = \tilde{u}_{cone} A_{cone} \quad (1.4)$$

Here, the complex volume velocity from the cone  $\tilde{U}_{cone}$  is the result of the complex velocity of the cone itself  $\tilde{u}_{cone}$  over the area of the cone [7]. This coupling shows that the pressure and volume velocity radiated from the transducer can be directly linked to the force and velocity of the mechanical cone, using the cone component to implement this transition.

### 1.2.5 Enclosures

Without an enclosure, it is possible for air to move freely behind the cone due to the open framework. Once the driver is mounted into an enclosure, the air behind the cone is constrained and the enclosure behaves as an air spring. Air, a compressible gas, will add stiffness to the system inversely proportional to the volume of air trapped by the enclosure [7]. As the cone pushes inward into the enclosure, the air will compress creating a restoring force to be generated in the outward direction and vise-versa. In the damped mass-spring analogy, the spring will become stiffer, raising the resonant frequency of the system. By reducing the volume of the enclosure, the air will add more stiffness to the system, further increasing the resonant frequency.

### 1.2.6 Sound Radiation and Acoustic Size

#### 1.2.6.1 Radiation from a Baffled Piston

The physics of sound radiation are essential for transducer design. In this particular project, the sound radiation can be modeled using the baffled piston model. Once the assembly is mounted into the window frame, which is subsequently fit into a wall, the wall will act as a baffle, being acoustically larger than the driver.

A brief understanding of the baffled piston model is based off of the pressure radiation of a monopole source radiating into half space. This is especially applicable to drivers in a baffle as the pressure radiated from the front of the driver is decoupled from the pressure radiating from the back of the driver by some rigid baffle. Assuming the piston vibration is time-harmonic, the radiating pressure  $p_{baff}$  at any time  $t$  can be written as the sum of observed pressures radiated from differential surface areas of a vibrating piston of any shape.

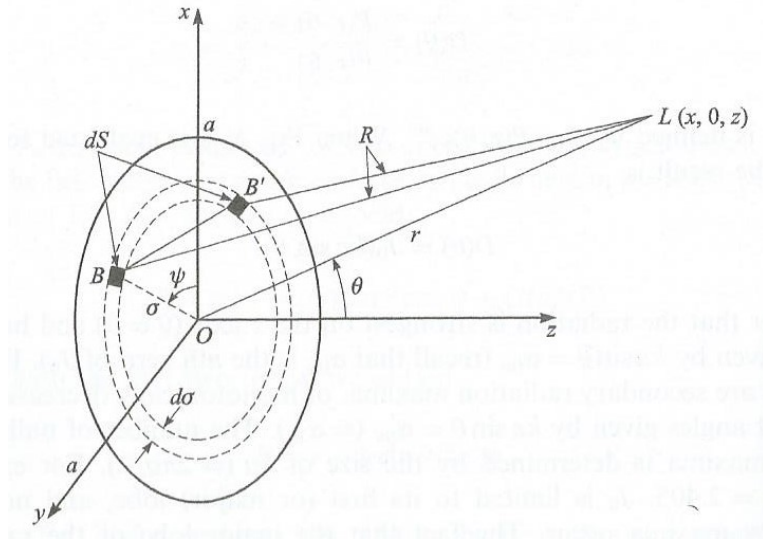


**Figure 1.2.** The visual setup for the baffled circular piston pressure radiation as described and drawn by Blackstock [2], p. 446. By summing the pressure observed radiating from differential elements of differential rings, the full shape of the piston will be realized as the radiation source.

$$p_{baff}(x, y, z; t) = \frac{jk\rho_0 c_0 u_0 e^{j\omega t}}{2\pi} \int_S \frac{e^{-jkR}}{R} dS. \quad (1.5)$$

Here,  $\omega$  is the angular frequency,  $u_0$  is the velocity amplitude, and  $\rho_0 c_0$  is the characteristic impedance of the fluid medium, which is comprised of the sound speed  $c_0$  and the fluid density  $\rho_0$ . The wavenumber  $k$  can be calculated using the frequency (in Hz)  $f$  and the speed of sound in the fluid medium  $c_0$  (in m/s) or by using the wavelength (in meters)  $\lambda$  using the following relationship:

$$k = \frac{2\pi f}{c_0} = \frac{2\pi}{\lambda}. \quad (1.6)$$

The integrand of Eq. (1.5) represents spherical spreading from the source [2]. Eq. (1.5) can be applied to a circular piston by considering the piston shape to be the sum of infinitely small rings of radius  $\sigma$ , as Blackstock has done in Eq. (1.7) and in Fig. 1.2, giving more specificity to the integral boundaries, yielding

$$p_{baff}(r, \theta, \psi; t) = \frac{jk\rho_0 c_0 u_0}{\pi} e^{j\omega t} \int_0^\pi d\psi \int_0^a \sigma \frac{e^{-jkR}}{R} d\sigma, \quad (1.7)$$

with  $R$  being the distance from a differential surface area on a differential ring to an observation point,

$$R = \sqrt{r^2 + \sigma^2 - 2r\sigma \sin \theta \cos \psi}. \quad (1.8)$$

In the farfield, where  $kr \gg 1$ , the distance to the observation point has become far enough where  $R$  can be substituted for  $r$ , the distance from the center of the piston to the observation point. This substitution is only valid for the  $\frac{1}{R}$  portion of the second integral; the distance  $R$  in the exponential can be expanded, which allows a zero-order Bessel function to be used such that

$$p_{baff}(r, \theta; t) = \frac{jk\rho_0 c_0 u_0}{r} e^{j(\omega t - kr)} \int_0^a \sigma J_0(k\sigma \sin \theta) d\sigma. \quad (1.9)$$

Using variable substitution, the integral can be evaluated, resulting in the final farfield pressure equation [2],

$$p_{baff}(r, \theta; t) = \frac{ja\rho_0 c_0 u_0}{r} \frac{J_1(ka \sin \theta)}{\sin \theta} e^{j(\omega t - kr)}. \quad (1.10)$$

Eq. (1.10) can be broken up into three pieces: the amplitude  $\frac{ja\rho_0 c_0 u_0}{r}$ , the angular dependency  $\frac{J_1(ka \sin \theta)}{\sin \theta}$ , and the wave propagation  $e^{j(\omega t - kr)}$ . While the wave propagation portion is important to the final equation, it is the angular dependency and amplitude portions that needs to be examined.

### 1.2.6.2 Directivity through Acoustic Size

The directivity of a radiator can be described as the pressure radiation at angle  $\theta$  normalized to the radiated pressure at  $\theta = 0^\circ$  [2]. It is an indicator of how the radiated pressure changes depending on the angle of observation. Using Eq. (1.10), the directivity  $D$  can be written as

$$D(\theta) = \frac{2J_1(ka \sin \theta)}{ka \sin \theta}. \quad (1.11)$$

While this is a function of  $\theta$ , the directivity is greatly affected by the  $ka$  value. This  $ka$  value relates the size of an object relative to the wavelength that object interacts with. If  $ka \ll 1$ , then the interacting object is considered acoustically small. The effect of acoustic size on the directivity can be seen when comparing directivity plots for a baffled piston using different  $ka$  values, shown in Fig 1.3. The directivity forms lobes as  $ka$  increases (the driver becomes acoustically large), creating nulls in the radiation from the piston. The small  $ka$  values have a more omnidirectional radiation pattern.

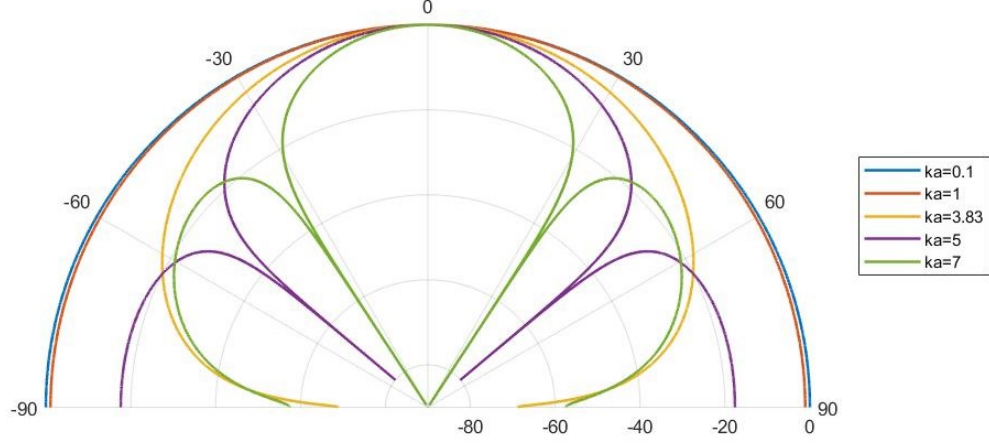


**Figure 1.3.** The normalized directivity in decibels of the baffled circular piston at various values of  $ka$  [2]. As  $ka$  increases, side lobes are formed producing nulls in the pressure radiation.

#### 1.2.6.3 Source Level

The Source Level, referred to as SL, is an on-axis sound pressure level, or SPL, calculation done in the farfield that accounts for the spherical spreading of waves [2]. While this is a useful calculation to determine the radiated SPL from a driver, it is important to note that some levels calculated are not the true SPL because some frequencies may not fit the farfield assumption in the calculation; they are still in the nearfield at the observation distance from the driver cone used in the SL calculation [2]. The Source Level calculation is based on the SPL calculation. While Blackstock uses the root mean square pressure in this calculation, using the peak pressure better represents the results from a lab test as any measured pressure will be a peak pressure rather than a root mean square pressure.

$$\text{SPL} = 20 \log_{10} \frac{p_{peak}}{p_{ref}}. \quad (1.12)$$

where  $p_{ref}$  is the reference pressure. The peak pressure can be calculated using the Rayleigh distance, which roughly represents the distance at which the radiated pressure transitions from the nearfield to the farfield,  $R_0$ ; the pressure amplitude,  $p_0$ ; and the distance from the driver,  $r$ , which will be on-axis in this calculation.

$$p_{peak} = \frac{p_0 R_0}{r} \quad (1.13)$$

This can be rearranged to a more beneficial form for later calculations by substituting in the definitions of the Rayleigh distance and pressure amplitude, which are as follows [2]:

$$R_0 = ka^2/2 \quad (1.14)$$

$$p_0 = \rho_0 u_0 c_0. \quad (1.15)$$

The pressure amplitude here is calculated assuming that the diameter of the piston is infinite and that the pressure calculated is not the pressure on the baffled piston's face.

Using Eqs. (1.13), (1.14), (1.15), and (1.6) yields a  $p_{peak}$  that is more straight-forward when using particle velocity in the calculation.

$$p_{peak} = \frac{\rho_0 u_0 \omega a^2}{2r} \quad (1.16)$$

This peak pressure can be substituted into Eq. (1.12) and rearranged to show the decrease in pressure due to the spherical spreading. This is done by referencing the distance  $r$  to 1 meter away from the source. This presents the final Source Level calculation in terms of the particle velocity,

$$SL = 20 \log_{10} \frac{\rho_0 u_0 \omega a^2}{2p_{ref}} - 20 \log_{10} \frac{r}{1 \text{ meter}}. \quad (1.17)$$

### 1.2.7 Radiation Impedance

The acoustic radiation impedance is another important quality inherent to the baffled piston model. This impedance can be expressed in terms of the average pressure on the circular piston's surface  $\bar{p}_{surf}$  or in terms of the force on the pistons surface  $F_{surf}$  [2],

$$Z_{rad} = \frac{\pi a^2 \bar{p}_{surf}}{u_0} = \frac{F_{surf}}{u_0}. \quad (1.18)$$

The force can be found by integrating the pressure over the surface of the piston. The integration is performed over the surface area between two arbitrary areas on the piston head. This creates an important overlap of pressure when integrating. At any surface area, the pressure created by that area must be accounted for as well as the pressure acting on that surface area being generated by another area on the piston surface. This effectively doubles the result [2]. Arranging the integral to only count every combination of surface areas once, then multiplying by 2 when calculating the force will give the

proper force equation. The pressure on the piston surface can be written as

$$p_{surf} = \frac{jkp_0}{2\pi} \int_{-\pi/2}^{\pi/2} d\theta' \int_0^{2\sigma \cos \theta'} \frac{e^{-jkR'}}{R'} R' dR' \quad (1.19)$$

where  $R'$  is the distance between the two surface areas and  $\theta'$  is the angle between the horizontal and the line between the two surface areas [2]. Integrating  $R'$  to a maximum distance of  $2\sigma \cos \theta'$  when  $\theta' = 0$  results in the maximum value of  $R' = 2\sigma$ , or when the surface areas are on opposite sides of the circle with the diameter of the circle between them. Solving the distance integral leads to the following piston pressure [2],

$$p_{surf} = \frac{p_0}{2} \left[ 1 - \frac{2}{\pi} \int_0^{\pi/2} \cos(2k\sigma \cos \theta') d\theta' + j \frac{2}{\pi} \int_0^{\pi/2} \sin(2k\sigma \cos \theta') d\theta' \right]. \quad (1.20)$$

The first integral can be evaluated as a zero-order Bessel function and the second integral can be evaluated as a zero-order Struve function, prompting the following result [2],

$$p_{surf} = \frac{p_0}{2} [1 - J_0(2ka) + jK_0(2ka)]. \quad (1.21)$$

This allows an easier integration over the surface area to find the force. Multiplying Eq. (1.21) by 2 to compensate for the earlier overlap adjustment and integrating the result over the surface area yields

$$F_{surf} = \pi a^2 p_0 \left[ 1 - \frac{2J_1(2ka)}{2ka} + j \frac{2K_1(2ka)}{2ka} \right]. \quad (1.22)$$

The radiation impedance can now be solved for by using Eqs. (1.18) and (1.22), giving a real and imaginary impedance [2]. The resulting radiation impedance can be expressed as a specific radiation impedance,  $z_{rad}$ , which normalizes the radiation impedance  $Z_{rad}$  by the surface area of the radiator.

$$z_{rad} = \rho_0 c_0 \left[ 1 - \frac{2J_1(2ka)}{2ka} + j \frac{2K_1(2ka)}{2ka} \right]. \quad (1.23)$$

Plotting the specific radiation impedance as a function of  $ka$  shows how the impedance changes with frequency. At low frequencies, where  $ka < 0.5$ , the imaginary part of the impedance is dominant – showing an almost constant power-law increase – where at higher frequencies, regions of  $ka > 3$ , the real part of the impedance is dominant, stabilizing to a constant value. Between these regions, when  $0.5 < ka < 3$ , the impedance magnitude

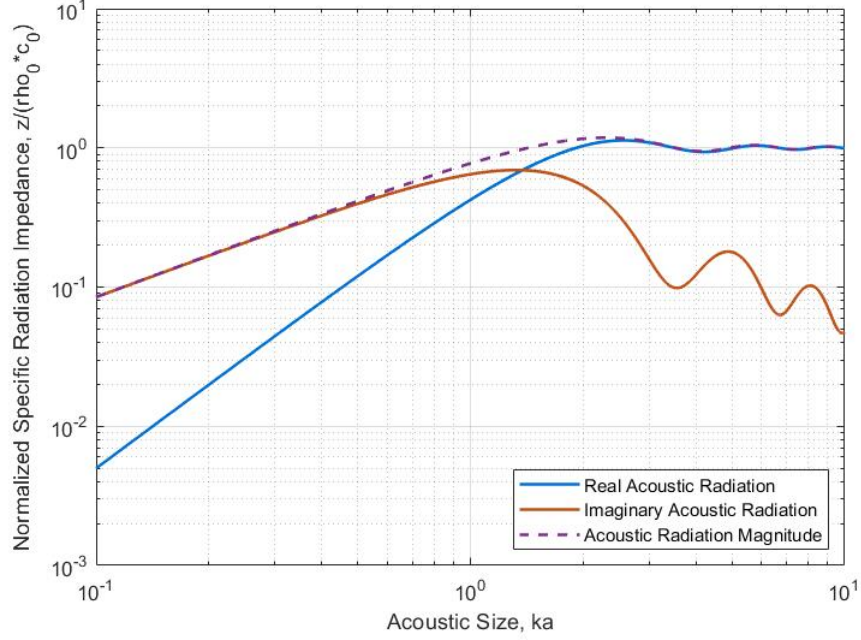


**Figure 1.4.** The normalized real and imaginary specific radiation impedance as well as its magnitude [2]. The magnitude nearly matches the imaginary impedance when  $ka < 0.5$  showing that the imaginary impedance is dominant at low frequencies. Similarly, the real impedance is dominant at high frequencies when  $ka > 3$ .

undergoes a transition from being imaginary-dominant to being real-dominant. If a low-frequency assumption can be made, treating the impedance as just the imaginary part of Eq. 1.23 that has a power-law increase is justified. If a high-frequency assumption is used, treating the radiation impedance as a frequency-independent constant impedance can be justified. If the frequency crosses into the transition region, a different approach should be used that attempts to compensate for the region's behavior.

### 1.3 Published Literature

While the driver-enclosure designs were unique to this project, there are several reference materials that were referred to throughout the design, modeling, and test process. Classic textbooks authored by Hunt [19] and Beranek [8] and more recent textbooks by Beranek and Mellow [7] and Blackstock [2] provided a technical understanding regarding sound radiation from an electromagnetic transducer. These established the set of design requirements for the project. Beranek, in his original text [8], and Mellow [7], supplying additions to Beranek's original publication, also established a theoretical model for

characterizing transducer behavior, both in impedance and frequency response. Testing methods were in part outlined by Vanderkooy [20] and AES Standard AES2-2012 [21] in order to maintain some similarity to commonly used practices in industry. Distortion measurements and interpretations have been investigated by Klippel [17] [16] [18] among others.

## **1.4 Objectives**

The overall purpose of this project was to design and test driver-enclosure assemblies for the window noise control application. Included in this was choosing drivers that closely matched the design requirements and designing and fabricating the enclosures for each driver. Along with fabrication of the assemblies, theoretical models of the designed assemblies that showed the assemblies' frequency responses were to be made. With the assemblies fabricated, frequency response testing was to be completed in a sound controlled environment. Nonlinear testing was to be performed on the drivers as well as any distortion produced by the drivers can be perceived as an addition of noise in the final application. Analysis of the results allowed for a comparison between the theoretical and measured assembly characteristics as well as show nonlinear behavior not shown in the model. Finally, an assembly was to be selected as the most appropriate to be used in the original noise control application.



# Chapter 2 |

## Driver-Enclosure Designs

### 2.1 Finding The Right Drivers

Choosing the driver was the first step in this design process. As stated before, the drivers needed to have a flat frequency response between 500 Hz and 3000 Hz and needed to be acoustically small in diameter, 2 inches or less. Because the drivers were not custom made for this project, a search for acceptable drivers was done online. The drivers' specification sheets gave some insight into how each driver behaves, but some specifications required confirmation once the drivers were acquired.

#### 2.1.1 Frequency Response Curves

Driver specification sheets are rich with information but there are a few important parameters that needed to be examined. The most obvious was the frequency response curve. This was presented in the form of a graph showing the decibel level the speaker is expected to produce at certain frequencies. While there are standards that provide outlines for measuring and reporting frequency response curves – such as AES2-2012 and IEC 60268-5 – there is some amount of question placed on the manufacturer reported frequency response curves. One of the biggest components of this question in the reported results is the post-processing done to any frequency response curve; some data has been windowed, averaged, or smoothed to present a more appealing curve to potential consumers. The reported curves should be used as guidelines for the drivers' behaviors, which was helpful for choosing drivers with a presumably flat response in the bandwidth of interest.

## 2.1.2 Impedance Curves and Resonant Frequency

The electrical impedance curve reported on a specification sheet shows, among other things, the resonant peak and frequency. Knowing the resonant frequency helped shed light on how the driver would behave when combined with the enclosure. As previously discussed, the resonant frequency increases as a driver's back volume is reduced in an enclosure [7]. Drivers with low resonant frequencies avoided raising their resonant frequencies too far into the operating bandwidth when mounted into the small enclosures. The resonant frequency and impedance curve were important in finding drivers that would keep an acceptable frequency response after being placed in their enclosures.

## 2.1.3 Diaphragm Size and Driver Depth

As previously discussed, the more acoustically small a driver is, the less directional it will be. While having  $ka \ll 1$  was desirable for having an even directivity pattern, it was not as practical as the frequency approached the upper limit of the operating band, 3000 Hz. Setting a maximum diaphragm diameter of 2 inches and using Eq. (1.6) to find the wavenumber gave  $ka = 0.229$  at 500 Hz and  $ka = 1.37$  at 3000 Hz for the maximum diaphragm diameter. While having chosen the maximum 2 inch diaphragm diameter did not meet the ideal case of  $ka \ll 1$ , it did open the opportunity to find drivers that may have better characteristics despite forcing a directional pattern. Along with the size of the diaphragm diameter, the depth of the driver was important as well to ensure a shallow enclosure could be designed to house the driver. There was not a maximum depth assigned; however, a driver depth of less than 50.8 mm (2 inches) was a rough estimate for the maximum depth. Having a diaphragm diameter of no more than 2 inches and an maximum depth of 50.8 mm placed restrictions on how big and how deep the drivers could be to meet the parameters of the project.

## 2.1.4 Rated Power and Maximum Excursion Distance

While the parameters discussed above carried significant weight in driver selection, they are not the only parameters that mattered. These drivers, producing a carefully constructed noise canceling signal, were required to produce as little distortion as possible while in use. This led to the hope that choosing drivers with higher power ratings and maximum voice coil excursion distances would produce less distortion due to the lowered chance that the drivers would not be excited near their rated limits. The rated power

and maximum excursion distance,  $X_{\max}$ , needed to be as high as possible so that the driver cones could move without electrical or mechanical failure and to minimize the produced distortion when implemented into the window frame.

## 2.1.5 The Chosen Drivers

With the design parameters specified, a variety of drivers were examined as candidates. Comparing each drivers' characteristics allowed the most suitable four drivers to be chosen. Each driver had a unique feature in its design, excelling at one or more qualities over the others chosen. Their parameters of interest are shown in Table 2.1.

**Table 2.1.** Reported Driver Specifications

Specification	Driver Model			
	<i>W1-2121S</i>	<i>W2-2243S</i>	<i>FRS 5X-8</i>	<i>TEBM36S12-8/A</i>
Nominal Impedance	4 $\Omega$	4 $\Omega$	8 $\Omega$	8 $\Omega$
Sensitivity at 1 W/1 m	79 dB	87 dB	86 dB	72 dB
Diameter	1 inch	2 inches	2 inches	2 inches
Depth	20.8 mm	32.7 mm	33.5 mm	20.6 mm
Resonant Frequency	120 Hz	160 Hz	190 Hz	148 Hz
Rated Power	6 W	10 W	5 W	12 W
Maximum Excursion	2.3 mm	1 mm	Not Given	4 mm

### 2.1.5.1 Tang Band W1-2121S

The first driver chosen was the smallest driver of the set. This driver was compact, allowing for a very small enclosure to be built for it. The frequency response seemed to smooth out as it approaches 1500 Hz in Fig. 2.1, making it a fantastic candidate for higher frequency operation. The reported resonant frequency was below the 500 Hz operating frequency of the operating bandwidth. Being so small, it had a lower power rating, but did not have the smallest  $X_{\max}$  out of the chosen drivers. There was a notable complication with the terminal placement being on the edges of the driver housing making it difficult to fit into a sealed enclosure without compromising the wire connections to the terminals. [3]

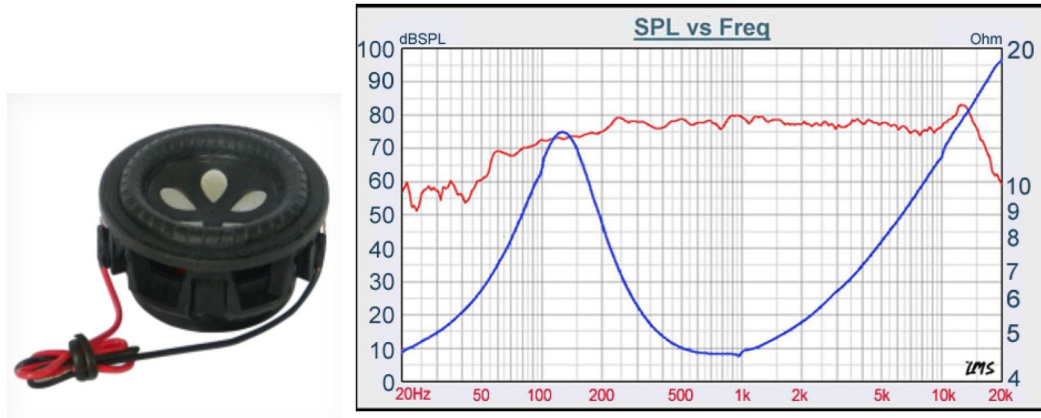


**Figure 2.1.** The W1-2121S Driver (left) and its frequency response and impedance curve (right), given in red (left scale) and in blue (right scale) respectively, as reported by Tang Band [3]. The specification sheet did not give any information about the methods used to measure the frequency response, such as the power of the input signal, the distance the measurement was taken, or if the driver was placed in an acoustically infinite baffle. This driver was small in size and fairly inexpensive. Images were taken directly from <http://www.tb-speaker.com/uploads/files/e99c0126812ca22379a2179932b9e840.pdf>.

#### 2.1.5.2 Tang Band W2-2243S

This driver had the second-highest rated power, but had the smallest reported maximum excursion distance. The design was rather bulky compared to the other drivers and was at the maximum diaphragm diameter. The resonant frequency was well below the minimum operating frequency of 500 Hz, but the frequency response curve showed a gradual increase in response from 500 Hz to about 1000 Hz. Even with this gradual increase, the frequency response curve remained relatively flat without having a change of more than about  $\pm 3$  dB, the largest jump happening at around 2250 Hz. [4]

#### 2.1.5.3 Visaton FRS 5X-8

While similar in size to the W2-2243S, this driver had the lowest power rating. There was a slow, steady rise in response as the frequency increased and the resonant frequency was higher than the other drivers. This driver had a unique bullet-shaped dust cap, something that the other drivers did not have. The specification sheet for this driver did not include a  $X_{\max}$  value, putting the true limitations of the speaker into question. [5]

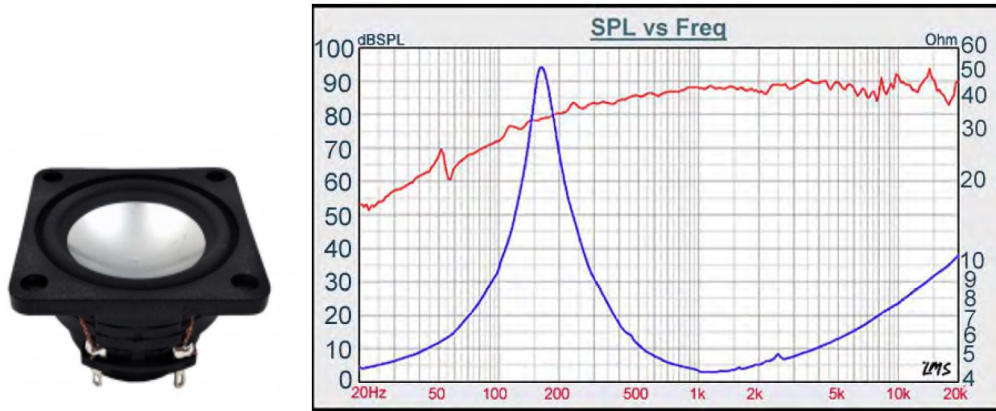


**Figure 2.2.** The Tang Band W2-2243S Driver (left) and its frequency response and impedance curve (right), given in red (left scale) and in blue (right scale) respectively, from Tang Band [4]. Like the W1-2121S, this drivers specification sheet did not specify anything about the measurement method for the frequency response including the physical placement of the driver. This was the most expensive of the drivers chosen. It also had a more robust design, taking up the more volume behind the face plate. Images were taken from <http://www.tb-speaker.com/uploads/files/e4964df0494335751327c45c1160fc73.pdf>.

#### 2.1.5.4 Tectonic TEBM36S12-8/A

This driver had the most unique physical qualities of the drivers chosen. Obvious differences included its square diaphragm and its shallow design. The specification sheet's frequency response curve flattened out well before 500 Hz and maintained an acceptably flat response through 3000 Hz. This driver also had the highest reported power rating and excursion distance [6]. Because of this driver's square diaphragm, for modeling and calculation purposes an equivalent circular radius was used by calculating what the radius of a circle with the same area as that of the driver's square diaphragm would be.

## 2.2 Constructing Testable Enclosures

The enclosure design constituted the other half of this design process for this project, but depended on the size of the chosen drivers. The enclosures needed to be small to satisfy the space constraints, but needed to provide each driver with the ability to mount easily into the window frame. It was decided that having an enclosure design with interchangeable driver-mounted front faces was the most efficient construction and test design.

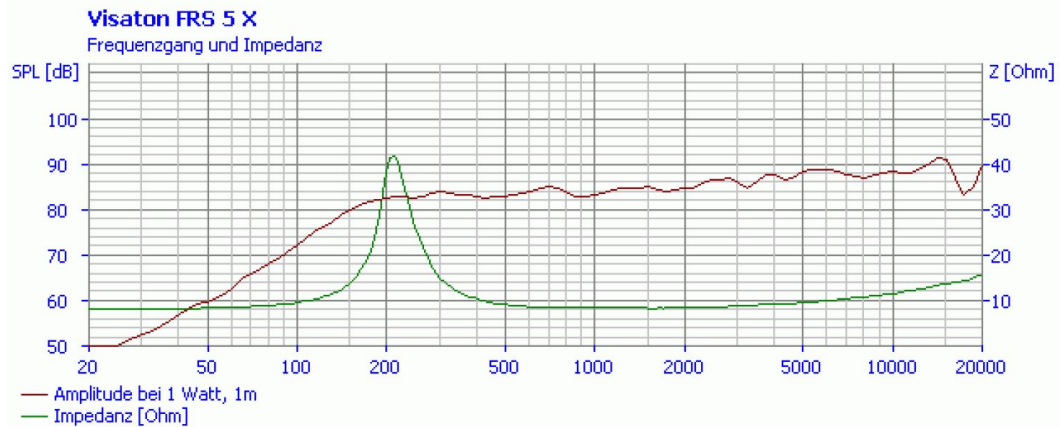


**Figure 2.3.** Visaton’s FRS 5X-8 Driver (top) and the frequency response and impedance curve (bottom), given in red (left scale) and in green (right scale) respectively, reported by Visaton [5]. As labeled on the frequency response and impedance curve, the frequency response measurement used a 1 Watt input signal being measured 1 meter away from the driver. The specification sheet does not specify if these measurements were taken while holding the driver in a baffle. This driver had a fairly large dust cap in its design. The magnet was nearly the diameter of the cone, but the overall depth was the same as the W2-2243S [5] [4]. Images were taken from [https://www.visaton.de/sites/default/files/dd\\_product/frs5x\\_8.pdf](https://www.visaton.de/sites/default/files/dd_product/frs5x_8.pdf).

### 2.2.1 Enclosure Shape and Material Choice

The enclosure design began by deciding shape of the enclosure. There were two shapes considered: a cuboid and a cylinder and ultimately, the cuboid shape was chosen. The cuboid was easy to construct and could be made out of a variety of materials that could be customized to specific sizes. In contrast, constructing a cylinder enclosure would require either having a cylinder of the exact diameter needed or creating one from scratch. This was decidedly inefficient for prototype construction and potentially expensive due to prototyping methods. The TEBM36S12-8/A driver, with its square diaphragm, most certainly benefited from being in a cuboid enclosure.

With the choice of enclosure shape set, the choice of material was decided next. For ease of use and with a low material cost, medium-density fiberboard, or MDF, was chosen. This is a common prototype material made from wood dust that comes in the form of

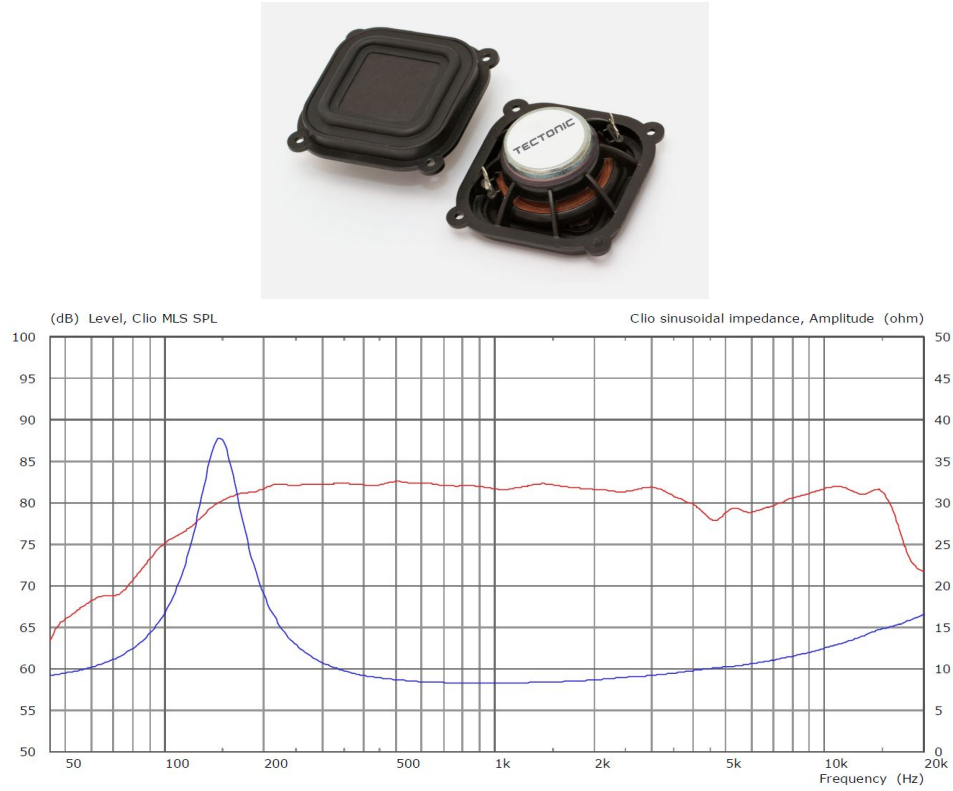


**Figure 2.4.** The Tectonic TEBM36S12-8/A Driver (top) and its frequency response and impedance curve (bottom), given in red (left scale) and in blue (right scale) respectively, as reported by Tectonic [6]. The specification sheet reported that the frequency response measurement used a 1 Watt input signal and was measured 1 meter away from the driver but did not specify the mounting technique used. The TEBM36S12-8/A was incredibly shallow, allowing for a small enclosure design. The frame behind the membrane required the mount cutout to be a square with filleted corners rather than a circle. Images taken from [https://www.tectonicaudiolabs.com/wp-content/uploads/woocommerce\\_uploads/2018/10/T-DS-TEBM36S12-8A.pdf](https://www.tectonicaudiolabs.com/wp-content/uploads/woocommerce_uploads/2018/10/T-DS-TEBM36S12-8A.pdf).

a board. It is dense, providing stability for the enclosure and is readily available. The front faces required a thickness of at least  $\frac{1}{4}$  inch in order to mount the drivers onto the face using screws – with the exception of the W1-2121S – so  $\frac{1}{2}$  inch MDF was used to construct the front face. To keep the material the same, allowing several parts to be cut out of a single board, the same MDF thickness was used for the rest of the enclosure.

### 2.2.2 Enclosure Size Variability

As mentioned before, the driver size dictated the enclosure size, starting with the front face. The drivers chosen grouped together relatively conveniently, falling into one of two sizes: a  $3\frac{1}{2}$  inch size that mounted the W2-2243S, FRS 5X-8, and the TEBM32S12-8/A;

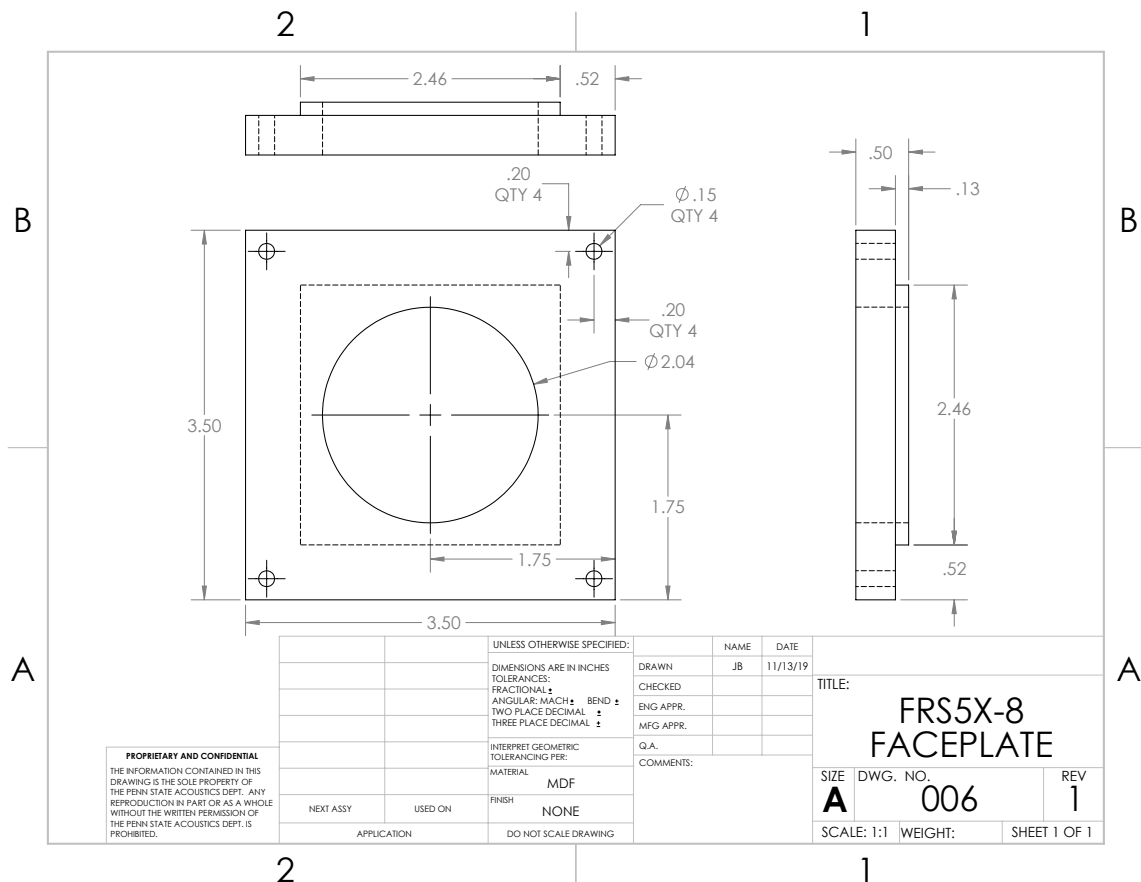


**Figure 2.5.** The engineering drawing for the FRS 5X-8 Faceplate. The design used a simple lip design to nest inside of the rest of the enclosure, providing easy alignment.

and a 3inch size that mounted the W1-2121S. These sizes were just large enough to fit their respective drivers as well as cap the end of the enclosure. The driver mount cutout for each face was designed to fit each driver with little movement to ensure the openings were not bigger than driver frame, which would cause air to leak out of the enclosure during use. The back face was designed in similar sizes but without the driver cutouts. To cap the enclosure, a small lip was cut out of each face to properly center it on the ends of the enclosure. As an example, the front face design for the FRS 5X-8 driver can be seen in Fig. 2.5.

After the front and back face sizes were determined, the rest of the enclosure was designed. With the possibility of making several volume sizes, the remainder of the enclosure was designed to be a tube with a square cross-section. When a new enclosure depth was needed, a new section of the tube would be cut. Utilizing a simple groove joint, panels were designed so that they could be easily aligned and glued together to



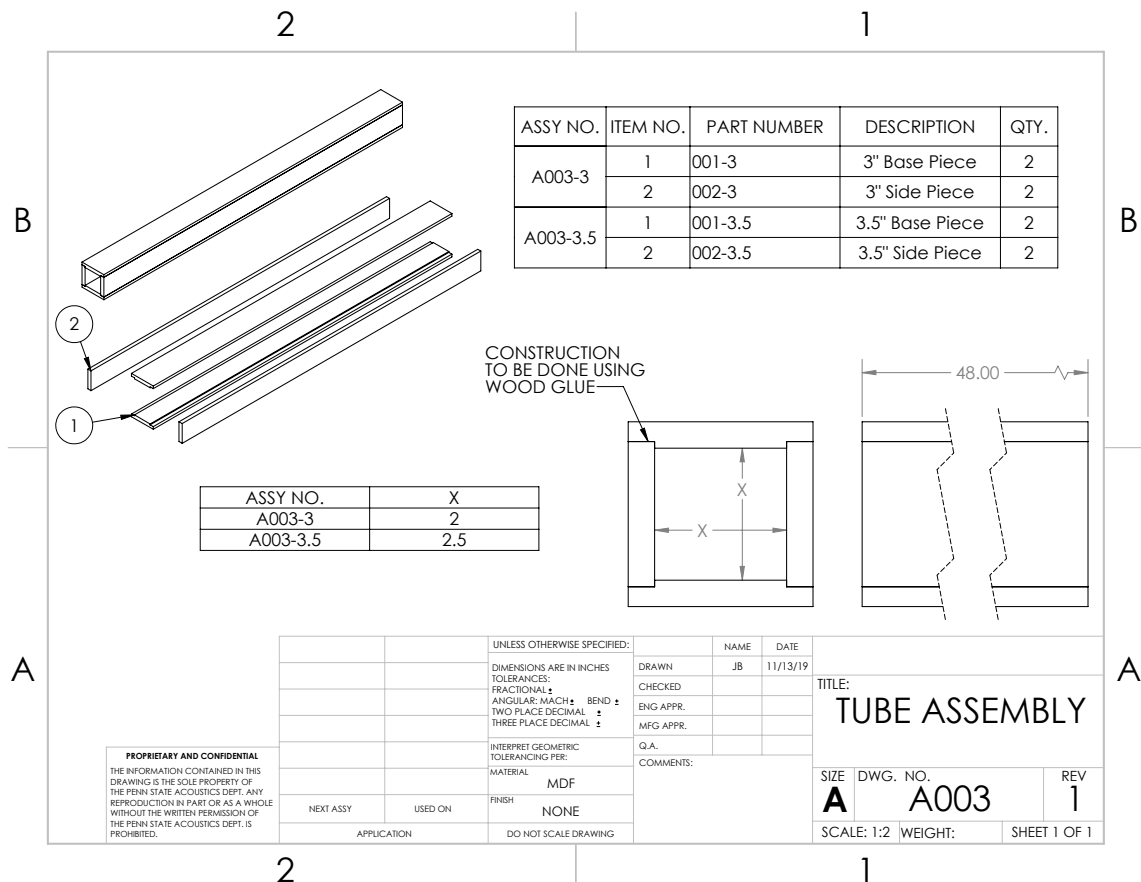


**Figure 2.6.** The engineering drawing for the enclosure tube assembly. This print allowed for two sizes of tube to be created: a  $3\frac{1}{2}$  inch tube and a 3 inch tube.

form the long tube, as seen in Fig. 2.6.

## 2.3 Final Assembly

Once the tube was constructed, a section of the tube was cut as close to the protruding drivers as possible, giving the smallest possible enclosure depth. The measurements of the final tube sections are displayed in Table 2.2. The enclosures were held together using through bolts in each corner of the faces. This allowed for easy switching between front faces between tests. Binding posts were placed through the back face in a diagonal orientation so as to not contact the enclosed portion of the driver, which would have prevented a tight seal from being made as the enclosure was bolted together. With a tight seal made by the through bolts, the enclosures were complete. The W2-2243S assembly can be seen in Fig. 2.7.

**Table 2.2.** Tube Assembly Cut Dimensions

Internal Dimension	Driver Model			
	<i>W1-2121S</i>	<i>W2-2243S</i>	<i>FRS 5X-8</i>	<i>TEBM36S12-8/A</i>
Cavity Width	51.18 mm	64.65 mm	64.65 mm	64.65 mm
Cavity Height	52.03 mm	64.05 mm	64.05 mm	64.05 mm
Cavity Depth	18.54 mm	28.08 mm	28.08 mm	14.01 mm

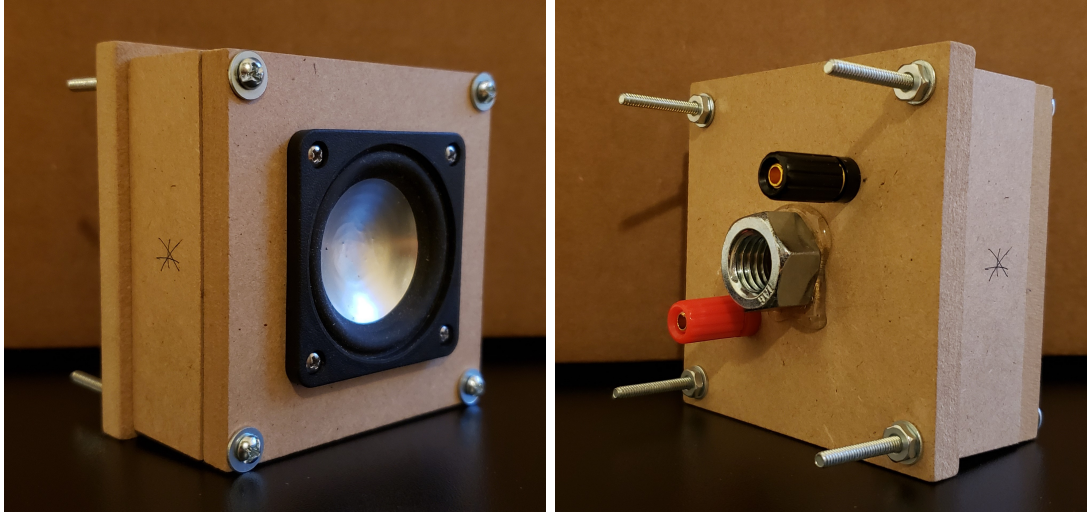


**Figure 2.7.** The front (left) and back (right) views of the assembled enclosure with the W2-2243S driver. The hex nut glued on the back was used to mount the enclosure onto a stand for frequency response measurements.

## 2.4 Estimating Internal Volume

While the internal volume of the enclosure could have been simply calculated using the dimensions of each enclosure, a more accurate estimate was calculated that accounted for the enclosure volume that was taken up by the driver components. This estimate helped more accurately determine the changes in frequency response due to the implementation of the enclosures. The internal volume was estimated by calculating the internal volume of the enclosure and subtracting the estimated volume of the driver components and binding posts that were housed within the enclosure.

The internal volume of the enclosure consisted of three sections: the volume created by the tube assembly lengths, the volume removed by the lips, and the volume taken up by the binding posts. The volume created by the tube assembly lengths was found by using the values in Table 2.2 to find the volume of the cuboid created by the cut tube

lengths. The volume removed by the lip on the back plate was calculated by finding the volume of the lip that protrudes from the mating surface of the plate into the cuboid volume. With the height, width, and depth, this volume was also calculated as a cuboid, albeit a thin one. The binding posts included a hole drilled partly into the lip as well as the binding posts themselves. These were simply calculated using the diameter of the drilled hole and its depth as well as the diameter and length of the binding posts. This did not account for changes in the binding posts' cylinder radius; however, these changes were small compared to the overall volume and were neglected. Subtracting the lip volume, adding the binding post hole volumes, and subtracting the binding post volumes from the cuboid volume created by the tube assembly length gave the volume of the enclosure before mounting the front face and is referred to as the back volume assembly in Table 2.3.

To determine the volume contribution by a driver-mounted front face, the contribution of the lip, driver mounting cutout, and driver components in the enclosure volume were considered. The cutout for the driver added to the overall volume, but the driver itself subtracted from the volume inside the back volume assembly. The drivers were assumed to be a series of cylinders and small cuboids, compensating for the magnet and any structural support incorporated into the driver's design. This was where most of the estimating was done as the assumptions made do not truly represent the volume taken up by the driver's components. In all cases except for the TEBM36S12-8/A front face assembly, these estimated volumes reduced the overall volume of the enclosure, being considered as negative volume as seen in Table 2.3. The TEBM36S12-8/A design, unlike the other drivers, protruded from the face plate outside the enclosure in a way that added more volume than just what had been cut to mount the driver. This resulted in this front face assembly adding volume to the back volume assembly rather than taking it away.

The summation of the volume created by the back volume assembly and the volume contribution of the front face assembly gave an estimate for the final volume of air inside each enclosure. These results can be seen in Table 2.3. These volumes were used later to estimate the effects of mounting the drivers in a small enclosure in section 4.3, but because of the assumptions made, those estimates would not be absolutely perfect representations.

**Table 2.3.** Estimated Enclosure Cavity Volume

<b>Driver Model</b>	<b>Volume</b>		
	<i>Back Volume</i>	<i>Front Face Assembly</i>	<i>Cavity Volume, <math>V_{box}</math></i>
W1-2121S	$4.32 \times 10^{-5} \text{ m}^3$	$-1.01 \times 10^{-5} \text{ m}^3$	$3.31 \times 10^{-5} \text{ m}^3$
W2-2243S	$10.57 \times 10^{-5} \text{ m}^3$	$-1.82 \times 10^{-5} \text{ m}^3$	$8.75 \times 10^{-5} \text{ m}^3$
FRS 5X-8	$10.57 \times 10^{-5} \text{ m}^3$	$-1.77 \times 10^{-5} \text{ m}^3$	$8.80 \times 10^{-5} \text{ m}^3$
TEBM36S12-8/A	$4.75 \times 10^{-5} \text{ m}^3$	$0.77 \times 10^{-5} \text{ m}^3$	$5.52 \times 10^{-5} \text{ m}^3$

# Chapter 3 | Modeling Electromagnetic Transducers

## 3.1 Overview

Creating theoretical models of drivers is a reliable way to predict driver behavior. In this instance, theoretical models were used to predict the frequency response of the driver-enclosure assemblies. This was done using analogous circuits to represent the electrical, mechanical, and acoustical domains associated with the transducer. Each domain used its own circuit analogies for different components native to that domain. Once a theoretical model of the transducer was created, the parameters could be altered to place the theoretical transducer into a theoretical box, predicting the transducer's behavior when it is physically placed into an enclosure.

## 3.2 Domains

The main goal of the transducer is to convert energy from one domain to another. In the case of electromagnetic speakers, the energy starts in the electrical domain, is coupled to the mechanical domain, and is finally radiated into the acoustical domain. Each domain can be modeled separately and connected to form a full model. Domains contain a flow variable and a potential variable. Defining these variables is important to creating the analogy for each domain, allowing for an analog circuit to be used to model the system as a whole.

### 3.2.1 Lumped Elements

Modeling the components that affect the oscillation of a system can be done using the lumped-elements model. This is a useful method for breaking up the components of a system into easy-to-use analogy blocks. This can be seen by using mass, spring, and damper analogies in the mechanical domain, similar to the analogy created in section 1.2.3. It is also observed as using resistor, capacitor, and inductor elements in the electrical domain. The lumped-element model works best when the object and waves being modeled are acoustically small,  $ka \ll 1$ , meaning that the lumped-elements model is valid when the wavelengths being produced by the driver are much larger than the driver size. Using this modeling method, modeling the full driver-enclosure assembly can be simplified. [7]

### 3.2.2 The Impedance Analogy

The analog circuit usually follows one of two analogies: the impedance analogy and the admittance analogy. These analogies both relate a flow variable and a potential variable related to the specific domain to the analog circuit flow and potential variables. The flow variable acts through the analogous component, acting as the current in the analog circuit. The potential variable acts across the component, acting as the voltage in the analog circuit [7]. Depending on the choice of analogy, impedance or admittance, the assignment of these variables changes. Each analogy produces impedance elements or admittance elements in the analog circuit. This theoretical model was made using the impedance analogy.

The main elements of the analog circuit are the resistor, capacitor, and inductor. Defining the flow variable of the element  $i_{elem}$  and the potential variable of the element as  $e_{elem}$  for the following examples, the relationships for the analog circuit resistor, capacitor, and inductor elements can be defined thusly [7]:

$$e_{elem} = i_{elem} R_{elem} \quad (3.1)$$

$$e_{elem} = \frac{1}{C_{elem}} \int i_{elem} dt \quad (3.2)$$

$$e_{elem} = L_{elem} \frac{di_{elem}}{dt} \quad (3.3)$$

Considering that the time-harmonic derivative can be evaluated as multiplying by  $j\omega$  and the time-harmonic integral as multiplying by  $\frac{1}{j\omega}$ , Eqs. (3.2) and (3.3) can be

rewritten as the following equations:

$$e_{elem} = \frac{i_{elem}}{j\omega C_{elem}} \quad (3.4)$$

$$e_{elem} = L_{elem}j\omega i_{elem} \quad (3.5)$$

Using Eqs. (3.1), (3.4), and (3.5) will define the impedance elements for each domain as well. Impedance, being defined as the potential variable divided by the flow variable, can be represented as the following set of equations [7]:

$$Z_{R_{elem}} = R_{elem} \quad (3.6)$$

$$Z_{C_{elem}} = \frac{1}{j\omega C_{elem}} \quad (3.7)$$

$$Z_{L_{elem}} = j\omega L_{elem} \quad (3.8)$$

The impedance equations create a way to model the electromagnetic transducer components as impedance elements in the analog circuit for each domain that contains energy.

### 3.2.3 The Electrical Domain

The electrical domain is used while energy is in the form of voltage and current. Because the voltage and current variables are the defining variables in the electrical domain, the analog circuit representation of the electrical domain is equivalent to the circuit diagram of the electrical components involved. That assigns the flow variable to be the electrical current and the potential variable to be the voltage. In the case of the transducer, the electrical components are the voice coil and an input signal. The input signal is modeled as a constant voltage generator  $V_{in}$ . The voice coil, being a solenoid, is essentially an inductor,  $L_e$  in series with some resistance through the voice coil  $R_e$  [7]. This circuit model can be seen in Fig. 3.1. The total electrical impedance can be written as the series sum of the impedance of the circuit components.

$$Z_e = j\omega L_e + R_e \quad (3.9)$$

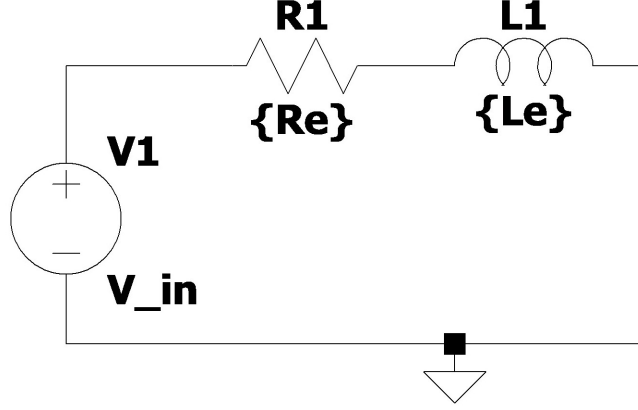


**Figure 3.1.** The electrical domain circuit model, which includes the resistance and the inductance of the voice coil. The constant voltage generator will be the input signal for the whole model. [7]

### 3.2.4 The Mechanical Domain

The mechanical domain is the bulk of the physical transducer design. Once the energy has been converted from voltage and current in the electrical domain to force and velocity in the mechanical domain, the impedance analogy can be defined, assigning the flow variable to be the mechanical velocity  $v$  m/s and the potential variable to be the mechanical force  $F_m$  N [7]. These flow and potential variables can be observed in the basic damped mass-spring system established in section 1.2.3. The force driving the system would be modeled as the constant voltage generator in the analog circuit, but is not included here with the understanding that the energy in the mechanical domain will be coming from the electrical domain once the two are connected. The damper in the damped mass-spring system, representing the physical elements throughout the transducer design that dissipate energy, interacts with the velocity to create a resisting force so that

$$F_m = vR_m \quad (3.10)$$

where  $R_m$  is reported in kg/s [7]. This is similar to the definition of the general resistive element, given in Eq. (3.1). Following the impedance definition gives the impedance for the mechanical resistive element to be

$$Z_{R_m} = R_m \quad (3.11)$$

As expected, this is easily comparable to Eq. (3.6), completing the analogy. Making these comparisons allows the mechanical resistance to be modeled as a resistor in the



analog circuit [7]. Following this logic process, the capacitive and inductive elements can be determined. Following Newton's Law of Motion, the interaction of the moving mass in the transducer  $m_m$  kg – being the combined weight of the cone, voice coil, voice coil former, and dust cap – and force can be expressed as

$$F_m = m_m \frac{dv}{dt} \quad (3.12)$$

This is analogous to Eq. (3.3), allowing the mechanical moving mass to be represented by an inductor element in the analog circuit [7] with an impedance of

$$Z_{m_m} = j\omega m_m. \quad (3.13)$$

The final element in the mechanical domain is the spring element in the damped mass-spring system. The spring creates a restoring force dependent on the displacement of the system. Going back to Newton's Second Law of Motion, the restoring force generated by a spring can be written as

$$F_m = k_s \int v dv \quad (3.14)$$

where  $k_s$  is the spring constant in N/m. Eq. (3.14) is analogous to Eq. (3.2) so long as the mechanical compliance  $C_m$  is equal to the inverse of the spring constant, giving the mechanical compliance units of m/N. This completes the capacitive element analogy where the mechanical spring element can be represented as a capacitor component in the analog circuit with capacitance of  $C_m$  [7], giving the expression

$$F_m = \frac{1}{C_m} \int v dv \quad (3.15)$$

with the impedance represented as

$$Z_{C_m} = \frac{1}{j\omega C_m}. \quad (3.16)$$

With each element of the mechanical domain related to a circuit component, the mechanical domain can be represented as a full analog circuit. Because the velocity is equally applied to each element before leading to ground in the damped mass-spring system, each mechanical component can be placed in series in the analog circuit, thus using the same analog current through each analog component [7], shown in Fig. 3.2 (this would be different for the admittance analogy). The mechanical impedance can be calculated the same way as the impedance for the analog circuit, summing each

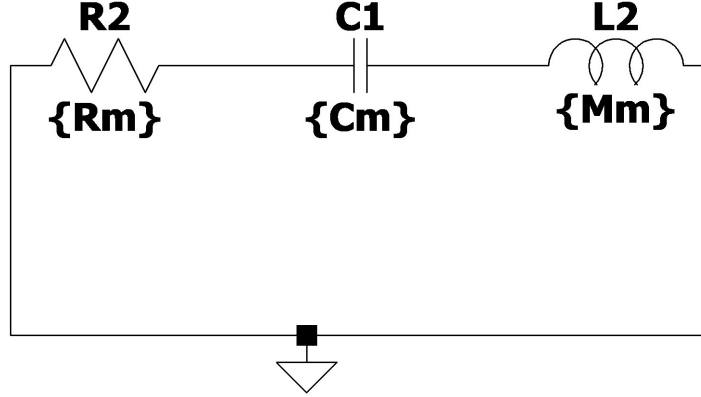


**Figure 3.2.** The mechanical domain analog circuit model, including the mechanical resistance, compliance, and mass in series according to the impedance analogy [7]. This domain does not include a constant force generator because it will receive its potential from the connection it has between the other domains.

impedance element in series such that

$$Z_m = Z_{R_m} + Z_{m_m} + Z_{C_m}. \quad (3.17)$$

### 3.2.5 The Acoustical Domain

The final domain of the transducer is the acoustical domain. This domain relies on the physical properties of pressure and volume velocity which are assigned as the potential variable and the flow variable respectively in the impedance analogy. Any existing pressure would be represented in the analog circuit as the constant voltage generator. The air in front of the cone, containing mass of its own, can be modeled as acoustical mass  $m_{acs}$  with units of  $\text{kg}/\text{m}^4$  [7]. Applying Newton's Second Law of Motion to the acoustical domain gives the relationship between acoustic pressure  $P_{acs}$  and acoustic mass through the volume velocity  $U$ , such that

$$P_{acs} = m_{acs} \frac{dU}{dt} \quad (3.18)$$

which follows Eq. (3.3). This analogy allows the acoustic mass to be modeled as an inductor element in the analog circuit. Following the logic to find the impedance of the inductive element, shown in Eq. (3.8), the impedance for the acoustic mass can be written as

$$Z_{m_{acs}} = j\omega m_{acs}. \quad (3.19)$$

Acoustic resistance  $R_{acs}$  is due to the dissipation of energy through the fluid medium or any energy-absorbing object. This can be expressed in units of  $\text{N} \cdot \text{s}/\text{m}^5$ . Justified with a simple unit check, acoustic resistance is related to pressure and volume velocity using the following interpretation of Newton's Second Law:

$$P_{acs} = R_{acs}U. \quad (3.20)$$

This will be modeled in the analog circuit as a resistor element [7] with impedance of

$$Z_{R_{acs}} = R_{acs}. \quad (3.21)$$

Acoustic compliance is, in most cases, due to the compression of a fluid medium due to a small change in the volume that occurs with negligible motion of the volume. In the case of this transducer design, this is seen in some cavity where the air stiffness produces a restoring force in reaction to the movement of the transducer cone. Acoustic compliance  $C_{acs}$ , with units of  $\text{m}^5/\text{N}$ , creates pressure through volume, as seen in the following equation,

$$P_{acs} = \frac{1}{C_{acs}} \int U dt. \quad (3.22)$$

This follows the general form of Eq. (3.2). The acoustic compliance can be modeled as a capacitor element in the acoustical domain [7]. This is how the enclosure volume will be modeled in the analog circuit. The impedance from acoustic compliance will be equal to

$$Z_{C_{acs}} = \frac{1}{j\omega C_{acs}}. \quad (3.23)$$

The model of the driver-enclosure assembly's acoustical domain will include three acoustic elements: the enclosure, the acoustic radiation impedance discussed in section 1.2.7, and the farfield pressure radiated by the driver. The enclosure has been shown to be acoustic compliance, which is analogous to a capacitor element in the analog circuit. The compliance is represented as a function of the enclosure volume  $V_{encl}$  [7], such that

$$C_{acs} = \frac{V_{encl}}{\rho_0 c_0^2}. \quad (3.24)$$

where  $c_0$  and  $\rho_0$  are the sound speed and density of the fluid medium, respectively.

The acoustic radiation impedance can be modeled as a combination of impedance elements that best fit the real and imaginary components of the radiation impedance in Eq. (1.23) and represented in Fig. 1.4. Beranek [7] [8] has done this to create a simplified analog circuit model for the acoustic radiation impedance as shown in Fig. 3.4; the outcome is plotted in Fig. 3.3 and the circuit model is shown in Fig. 3.4. The acoustic elements employed by Beranek are as follows:

$$M_{A1} = \frac{8\rho_0}{3\pi^2 a} \text{ kg/m}^4 \quad (3.25)$$

$$R_{A1} = \frac{0.1404\rho_0 c_0}{a^2} \text{ N} \cdot \text{s/m}^5 \quad (3.26)$$

$$R_{A2} = \frac{\rho_0 c_0}{\pi a^2} \text{ N} \cdot \text{s/m}^5 \quad (3.27)$$

$$C_{A1} = \frac{1.89\pi a^3}{\rho_0 c_0^2} \text{ m}^5/\text{N} \quad (3.28)$$

This radiation impedance can be implemented as its own combination of impedance elements in the acoustical domain's analog circuit. This creates a much more complete model than assuming  $ka \ll 1$ , which uses an acoustic mass and an acoustic resistance element in series to model the radiation [7]. As seen in section 2.1.3, using the acoustically small ( $ka \ll 1$ ) assumption to model the acoustic radiation is not a fair assumption to use, as the driver size may force  $ka$  to be slightly greater than 1 as the frequency approaches 3000Hz. The combination of these elements in the analog circuit, seen in Fig. 3.4, and are arranged such that the radiation impedance  $Z_{rad_{model}}$  can be expressed as

$$Z_{rad_{model}} = \left[ Z_{M_{A1}}^{-1} + \left( (Z_{C_{A1}}^{-1} + Z_{R_{A1}}^{-1})^{-1} + Z_{R_{A2}} \right)^{-1} \right]^{-1}. \quad (3.29)$$

The final portion of the model is the calculation of the farfield pressure radiated from the driver. This can be estimated by calculating the Source Level, discussed in subsection 1.2.6.3, of the driver at 1meter away from the cone's surface. Referring back to Eq. (1.17) and using an observation distance of 1 meter, the Source Level calculation can be rewritten as

$$\text{SL} = 20 \log_{10} \frac{\rho_0 u_0 \omega a^2}{2p_{ref}}. \quad (3.30)$$

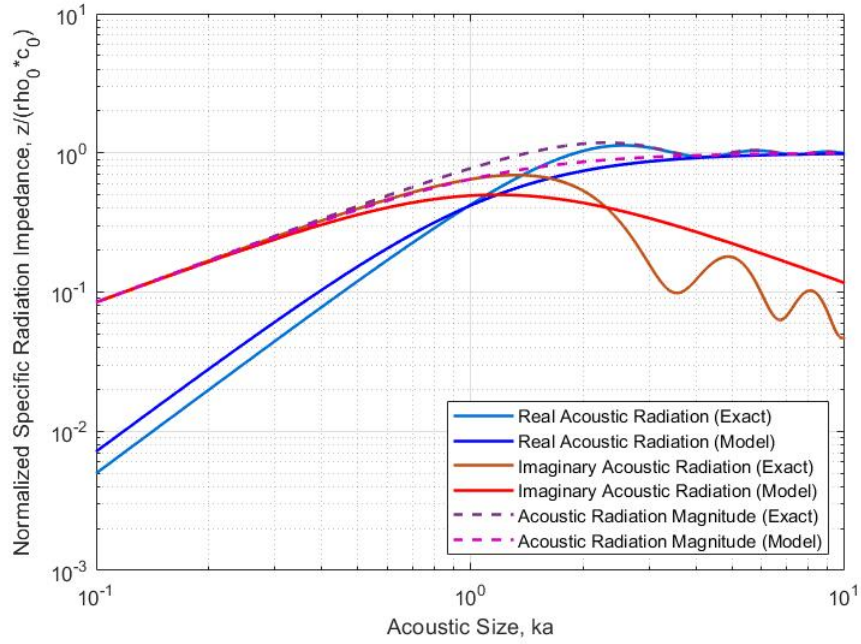


**Figure 3.3.** The exact solution [2] compared to the modeled solution by Beranek [7] [8] of the acoustic specific radiation impedance. The model lacks the rippling that the exact solution shows, but the real part of the impedance roughly follows the exact solution's real impedance when  $ka > 3$  and the imaginary part of the impedance roughly follows the exact solution's imaginary impedance when  $ka < 0.5$ . These regions are important to match because the imaginary impedance is dominant when  $ka < 1$  and the real impedance is dominant when  $ka > 2$ .

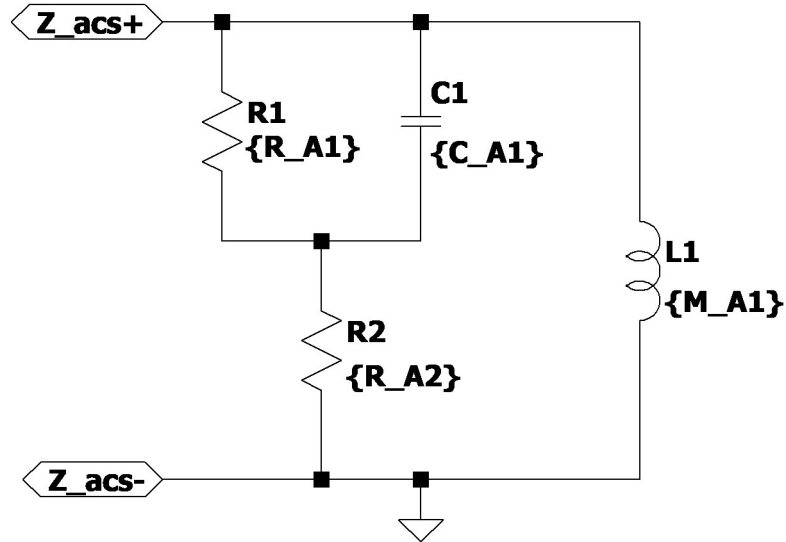


**Figure 3.4.** The acoustic radiation model as described by Beranek [7]. The terminals labeled  $Z_{acs+}$  and  $Z_{acs-}$  are connecting terminals that connect this subcircuit to the transducer acoustical terminals.

Due to the nature of the model, rewriting Eq. (3.30) in terms of the surface area of the driver,  $A_{cone}$ , is beneficial to integrating the Source Level into the model. Knowing that the drivers can be modeled as circles (using the equivalent circular radius for the TEBM36S12-8/A) and using a reference pressure of 20  $\mu\text{Pa}$  for air, Eq. (3.30) can be expressed as

$$\text{SL} = 20 \log_{10} \frac{\rho_0 u_0 \omega A_{cone}}{2\pi \times 20 \mu\text{Pa}}. \quad (3.31)$$

The modeling software will calculate the decibel level, meaning that the only calculation needing to be modeled is the logarithm's argument. This can be modeled in the analog circuit by taking advantage of the fact that the inductor element calculates the derivative of the flow variable as seen in Eq. (3.3), which is rewritten in the form of Eq. (3.5), providing an angular frequency,  $\omega$ , and a flow variable for calculations. Calculating the Source Level from the acoustical domain, the flow variable is volume velocity which accounts for the particle velocity and the cone area,  $A_{cone}$ , needed in Eq. (3.31). This division will cancel out the  $A_{cone}$  in the numerator in the logarithm's argument. Setting the inductance equal to  $\rho_0/(2\pi \times 20 \mu\text{Pa})$  will complete the modeling of the logarithm's argument. The full implementation of this can be seen in Fig. 3.5. While using the Source Level model can be useful, it does not account for any edge effects and assumes that the driver is omnidirectional at all frequencies, which is not true as the driver becomes acoustically large compared to the increasing radiated frequency as discussed in subsection 1.2.6.2.

The acoustical radiation impedance, the acoustical compliance of the enclosure, and the Source Level make up the acoustical domain for this particular model as seen in Fig. 3.6. They have been placed in series because they share the same flow through analog circuit.

### 3.3 Connecting Domains

With each domain defined, the domains need to be connected to allow energy to move between them. Connecting domains can be seen in the electromechanical coupling via the magnetic flux to voice coil interaction and in the mechanoacoustical coupling via the speaker cone's interaction with the fluid medium. Using the coupling properties in each domain will allow a modeled equivalent to be used in the analog circuit.

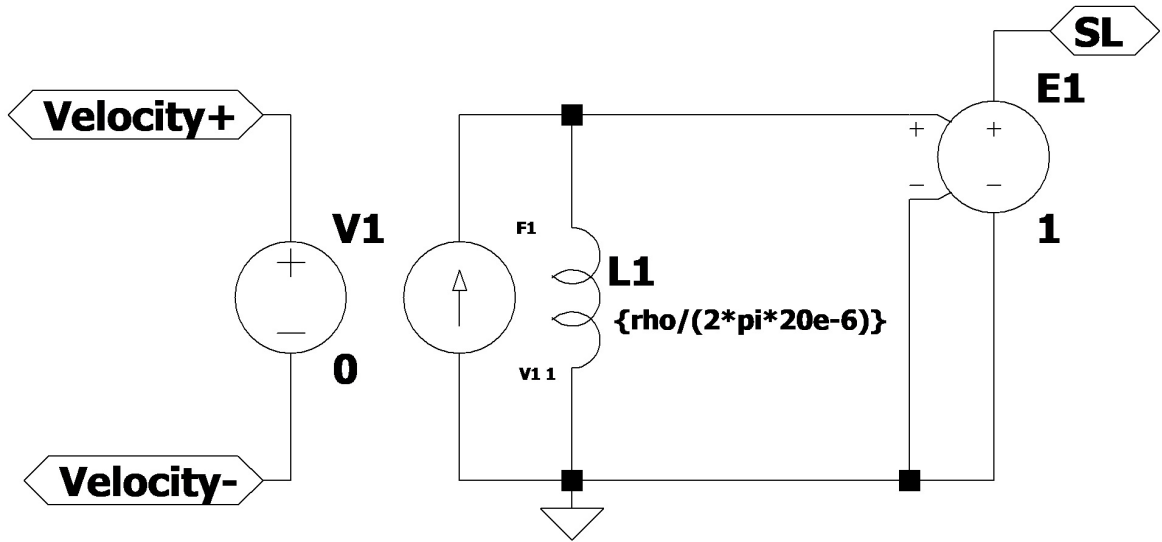


**Figure 3.5.** The modeled Source Level calculation. The input volume velocity is pushed through a potential generator that adds no additional potential (left-half of the model). The flow is generated and run through the inductor element, which has an inductance of  $\rho_0/(2\pi \times 20 \text{ } \mu\text{Pa})$ . This inductance multiplied by the derivative of the flow variable, which in the acoustical domain is volume velocity, creates a potential that is the Source Level (right-half of the model) prior to the decibel calculation. This potential is read and generated as an output, labeled SL.

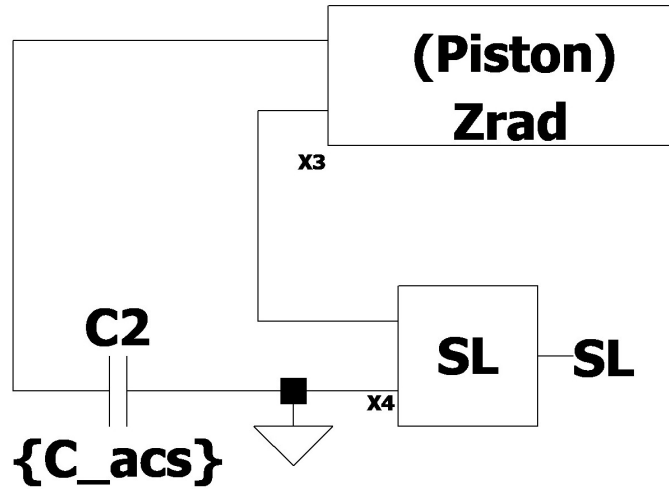


**Figure 3.6.** The acoustical domain analog circuit model. The acoustic radiation impedance modeled in Fig. 3.4 and the Source Level modeled in Fig. 3.5 have been modeled as subcircuits labeled here as Zrad and SL respectively. The capacitive element represents the acoustical compliance related to the driver being placed in an enclosure.

### 3.3.1 Electrical to Mechanical

The electromechanical coupling is the result of the magnetic field and current flow interaction, as seen in subsection 1.2.2 [19]. Using Eqs. (1.1) and (1.2), the following matrix relationship can be formed [7],

$$\begin{bmatrix} \vec{F} \\ \vec{e} \end{bmatrix} = \begin{bmatrix} 0 & \vec{B}l \\ \vec{B}l & 0 \end{bmatrix} \begin{bmatrix} \vec{u} \\ \vec{i} \end{bmatrix} \quad (3.32)$$

The coupling here is dependent on the voice coil and magnet property  $\vec{B}l$ , which is sometimes called the force factor, with units of Tm. Because the analog circuit will include direction in the potential and flow variables, the coupling can be expressed simply as  $Bl$ . Eq. (3.32) is similar to that of an ideal gyrator, which relates the potential and flow variables using a mutual conductance  $g_m$  [7]. This can be used to model the movement of energy between the electrical and mechanical domains, again using the impedance analogy to define the potential variables as voltage  $\vec{e}$  and force  $\vec{F}$  and to define the flow variables as current  $\vec{i}$  and velocity  $\vec{u}$ . The flow of energy into and out of the ideal gyrator requires that the flow of one domain be reversed, prompting a negative sign to be added. Because this is a circuit model, the variables will be written as the complex values  $\tilde{F}$ ,  $\tilde{u}$ ,  $\tilde{e}$ , and  $\tilde{i}$ . Using the mutual conductance of the ideal gyrator, Eq. (3.32) can be rewritten as

$$\begin{bmatrix} \tilde{F} \\ \tilde{e} \end{bmatrix} = \begin{bmatrix} 0 & \frac{1}{g_m} \\ \frac{1}{g_m} & 0 \end{bmatrix} \begin{bmatrix} -\tilde{u} \\ \tilde{i} \end{bmatrix} \quad (3.33)$$

where

$$g_m = \frac{1}{Bl} \quad (3.34)$$

The electrical and mechanical domains can now be coupled in the analog circuit model using the ideal gyrator with the mutual conductance of  $\frac{1}{Bl}$  [7].

### 3.3.2 Mechanical to Acoustical

As discussed in section 1.2.4, the interaction between the speaker cone and the fluid medium is what brings energy from the mechanical domain into the acoustical domain. Establishing the relationships between the potential and flow variables of these domains can be done using Eqs. (1.3) and (1.4).



$$\begin{bmatrix} \tilde{P}_{cone} \\ \tilde{U}_{cone} \end{bmatrix} = \begin{bmatrix} \frac{1}{A_{cone}} & 0 \\ 0 & A_{cone} \end{bmatrix} \begin{bmatrix} \tilde{F}_{cone} \\ \tilde{u}_{cone} \end{bmatrix} \quad (3.35)$$

Here, it is clearly seen that the coupling is done using the area of the cone  $A_{cone}$ . This relationship, as opposed to the electromechanical matrix in Eq. (3.32), relates one potential variable to the other potential variable and one flow variable to the other flow variable. This is similar to the ideal transformer, which uses a transformation ratio to relate the potentials on either side and the flows on either side [7]. The transformation ratio  $\phi$  can be introduced into Eq. (3.35) to create the resulting matrix,

$$\begin{bmatrix} \tilde{P}_{cone} \\ \tilde{U}_{cone} \end{bmatrix} = \begin{bmatrix} \frac{1}{\phi} & 0 \\ 0 & \phi \end{bmatrix} \begin{bmatrix} \tilde{F}_{cone} \\ \tilde{u}_{cone} \end{bmatrix} \quad (3.36)$$

where

$$\phi = A_{cone} \quad (3.37)$$

which in turn gives the transformation ratio of  $A_{cone}:1$  [7]. This ideal transformer can now be used to bring energy from the mechanical domain into the acoustical domain in the analog circuit.

### 3.4 Using Simulation Software [LTSpice]

An advantage to modeling the driver-enclosure assembly as an analog circuit is that any analysis can be done using circuit simulation software rather than calculating each component's impedance by hand. While several versions of simulation software exist, the models created here used LTSpice XVII, Simulation Program with Integrated Circuit Emphasis by Linear Technologies Corporation, a free simulation software suited for circuit analysis [22].

The model in LTSpice was made up of individual circuitry components or of subcircuits, which helped simplify the look of the model in the software. The ideal transformer, ideal gyrator, and acoustic radiation impedance were all modeled using subcircuits to keep the model as basic-looking as possible. The transformation ratio was defined as  $1/A_{cone}$  or  $1:\frac{1}{A_{cone}}$  and the mutual conductance was modeled to be  $Bl$ . These are mathematically handled correctly within the ideal transformer and ideal gyrator subcircuits.

LTSpice can be used, among other things, to measure voltage across a component or the current through the component. This was particularly useful to model impedance by

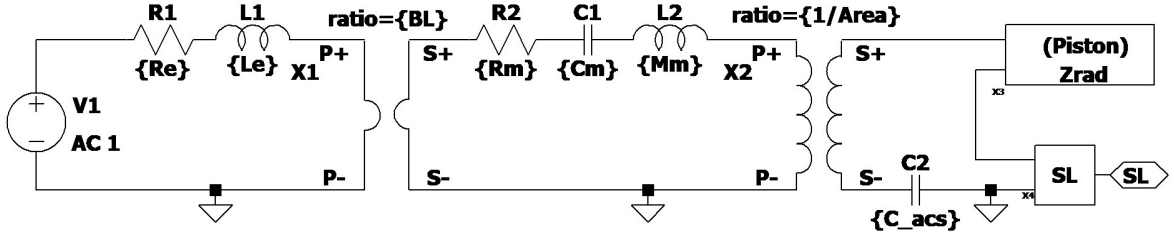


**Figure 3.7.** The completed simulation model made using LTSpice. The gyrator, transistor, acoustic radiation impedance (labeled Zrad), and sound pressure level (labeled SPL) were all subcircuits created as separate files.

setting the voltage input to be 1 volt. By measuring the current at the voltage generator and calculating its inverse, the impedance, defined as voltage divided by current, was displayed.

Measuring the Source Level was done by measuring the output voltage at the SL tag. The decibels were calculated by LTSpice by taking the base-10 logarithm of the measurement and multiplying it by 20. This completed the modeling of Eq. (3.31).

### 3.5 The Full Transducer Model

Putting each domain together and connecting them with the ideal gyrator and ideal transformer finalized the driver-enclosure assembly model. The model used a constant voltage generator, which passed voltage through the electrical domain components before passing the voltage into the ideal gyrator, converting the electrical energy into mechanical energy. The energy passed through the lumped element representations of the mechanical domain components and was passed into the ideal transformer, where the energy was converted into acoustical energy. In the acoustical domain, the energy was subjected to the radiation impedance from the driver as well as the stiffness from the enclosure volume. The model was now complete and could be used to model the driver-enclosure assemblies. This model used a few assumptions and simplifications, such as the acoustically small driver assumption and the acoustic radiation simplified model. It is important to note that the actual drivers had imperfections and nonlinear properties that were not modeled here, so the model represented an approximate solution, rather than an exact solution.

# Chapter 4 |

## Simulating Impedance and Frequency Response

The theoretical model shown in Fig. 3.7 is complete but it needs values for each analog component. While most of these values were reported on the specification sheets for each driver, measurements were done in a laboratory setting to determine the values of each driver, accounting for any discrepancies that each driver had compared to their reported values. Once measurements were taken and the necessary values were found, the models were able to simulate the frequency response of each driver mounted in their respective enclosures. This helped predict the changes in frequency response between 500 Hz and 3000 Hz due to each driver being placed within a small enclosure.

### 4.1 Measuring Impedance

The values needed to model the impedance and frequency response of a driver were found by implementing a simple measurement method and calculating the necessary values based on the data taken. These parameters were some of the Thiele-Small parameters, parameters used to characterize various mechanical and electrical qualities of a transducer. The procedure used followed one similar to that outlined in Beranek [7].

Beginning with a signal generator, a resistor of known value,  $R_{known}$ , was placed in series with the driver which was suspended in air. Suspending the driver in air rather than resting it face-up on a table ensured that any holes created in the driver design were not covered up, as this would change the response of the driver by creating a small closed cavity. A frequency sweep was supplied by the signal generator and voltage measurements were taken across the known resistor and across the terminals of the driver, labeled Ai0 and Ai1 in Fig. 4.1. This particular data was taken with a sample frequency of 20 kHz.

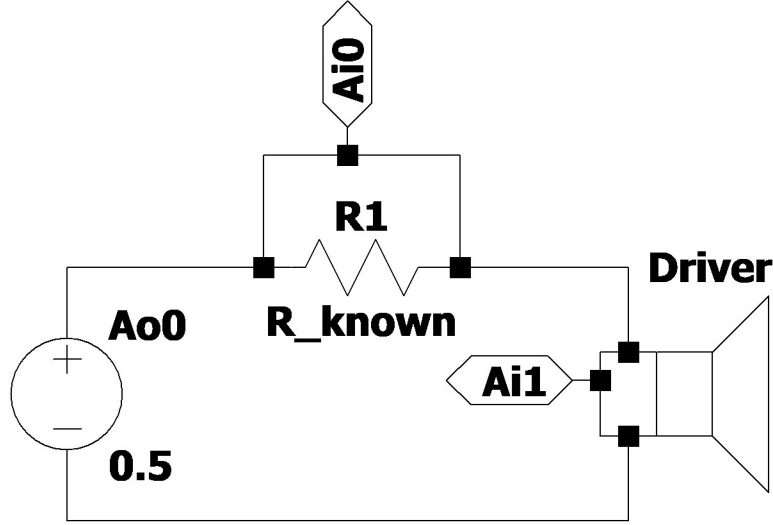


**Figure 4.1.** A LTSpice representation of the setup for the impedance measurement test. The signal generator, labeled Ao0, was set to input as sine sweep at 0.5 Volts starting from 20 Hz to 4000 Hz. The voltage across the 46.7  $\Omega$  resistor, labeled R\_known, was measured at Ai0 and the voltage measured across the driver terminals was measured at Ai1.

The signal generator swept with an amplitude of 0.5 Volts from 20 Hz to 4000 Hz with each sweep taking a total of 10 seconds. Once data had been collected for the unmodified driver, a known amount of a nonferrous mass was added to the driver cone, secured with a small amount of wax, and the voltage measurements were taken again. This was repeated three more times with increasing mass, giving one unweighted data set and four weighted data sets.

The data acquired was transformed into an averaged power spectral density of Ai0,  $\bar{G}_{xx}$ , and an averaged cross-spectral density of Ai0 and Ai1,  $\bar{G}_{xy}$ . The data collected was windowed using a Hann window and averaged with a 50% window overlap. These were divided to give the transfer function as a function of frequency,  $H(f)$ ,

$$H(f) = \frac{\bar{G}_{xy}}{\bar{G}_{xx}}. \quad (4.1)$$

This transfer function, multiplied by  $R_{known}$ , gave the impedance of the driver across the swept frequencies. This impedance included the DC resistance of the driver,  $R_{DC}$ , which was measured using a multimeter. The multimeter itself had some DC resistance across its terminals which was subtracted from the drivers' measured DC resistance values and the measured  $R_{known}$ . The known resistance used in these tests had a measured resistance of 46.7  $\Omega$ . This resistance was chosen to properly load the data acquisition

instrumentation used when connected to the lower impedance of the drivers. By directly measuring the voltage at the driver terminals and finding a transfer function, the voltage drop across the known resistor was accounted for. Subtracting  $R_{DC}$  from the measured driver impedance shifted the impedance curves removing the DC offset at 0 Hz. This gave the DC-shifted driver impedance,  $Z_{shifted}$ ,

$$Z_{shifted} = H(f) * R_{known} - R_{DC}. \quad (4.2)$$

The real part of the shifted impedance measurement can be seen in Fig. 4.2. It was important to note that any impedance values taken directly from Fig. 4.2 are electrical equivalents of any inferred mechanical impedance in combination with any electrical inductance. This was remedied by using the drivers'  $Bl$  value to transform from an electrical equivalent to a mechanical equivalent, similar to how the gyrator was used in the theoretical model.

The shifted impedance measurement for the unweighted and weighted drivers showed how the resonance frequencies shifted lower as mass was added to the system. This tendency agreed with the intuition used in the damped mass-spring system analogy established in subsection 1.2.3. The resonant frequencies and masses were recorded based off of the peaks of each trace. With small masses being added, the resonant frequencies should decrease relatively linearly; however, this may not be the case if the added mass becomes too heavy. Because of this, the fourth and fifth added mass trials for the W2-2243S driver were discarded, and the third, fourth, and fifth added mass trials for the W1-2121S, FRS 5X-8, and TEBM36S12-8/A drivers were discarded. The discarded traces also showed unexpected trends, showing a separation of the resonant frequency peak into two peaks; often times the higher frequency impedance peak had a larger impedance. This inconsistency suggested a system was created with two degrees of freedom, potentially from the added mass moving relative to the cone while trials were taking place. This potential for error was particularly relevant for the W1-2121S driver due to the black rubber coating on the driver cone. The added peaks in impedance higher on the frequency spectrum (above 1000 Hz) suggested a similar movement. The peaks in the W1-2121S were particularly noticeable and while better results were sought out by placing the added mass in different locations on the cone, these humps were still prominent. These humps did not occur for the FRS 5X-8 driver, most likely due to the unique placement of the added mass on the cone. The FRS 5X-8 cone, sporting a protruding dust cap, made it difficult to add mass to the exact center of the cone. To remedy this, mass was added around the dust cap in an equally spaced circular

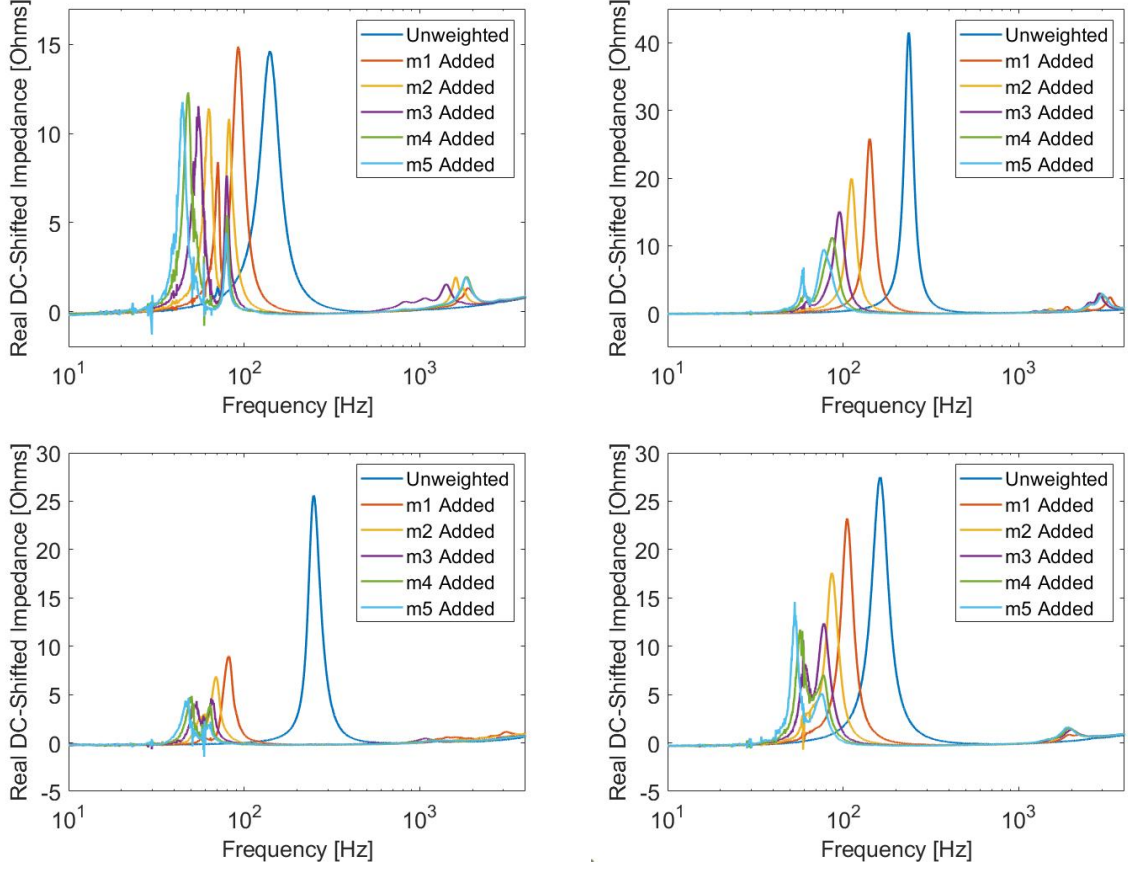


**Figure 4.2.** The real part of the DC-shifted driver impedance for the W1-2121S (top-left), W2-2243S (top-right), FRS 5X-8 (bottom-left), and TEBM36S12-8/A (bottom-right) drivers. Unweighted and weighted impedance results are included.

patterns. It is important to notice that these oddities did not occur in the unweighted cases, showing that adding mass must have provoked the resonant peak separation and the addition of an impedance hump further in the sweep. One way to ensure the quality of the trials would be to listen for any buzzing while the sweep is happening, which would imply that the added mass was shaking on the driver cone. The used resonant frequencies and masses can be seen in Table 4.1.

The final measurement to be made was the area of the cone,  $A_{cone}$ , for each driver. This was done with a pair of calipers, measuring the diameter of each driver cone – or side length in the case of the TEBM36S12-8/A driver – as being half-way across the surround, accounting for the extra area provided by the surround’s movement with the cone. The cone areas, which were used to couple the mechanical and acoustical domains, are displayed in Table 4.2.

**Table 4.1.** Used Masses and Resonant Frequencies from the Impedance Test

Driver	Total Added Mass, $m_i$	Resonant Frequency, $f_0$
W1-2121S	0 g	140.0 Hz
	2.62 g	92.4 Hz
	5.25 g	82.0 Hz
W2-2243S	0 g	236.4 Hz
	2.62 g	142.0 Hz
	5.29 g	111.6 Hz
	7.90 g	95.4 Hz
FRS 5X-8	0 g	249.4 Hz
	5.31 g	81.8 Hz
	7.94 g	69 Hz
TEBM36S12-8/A	0 g	162.6 Hz
	2.62 g	105.2 Hz
	5.24 g	86.2 Hz

## 4.2 Calculating Characteristics

The data taken was used in several ways to calculate each driver's characteristics. Already calculated by virtue of the measurement process was each drivers' DC resistance. The rest of the characteristics required further data analysis and calculation.

The observed resonant frequencies and moving mass – the unweighted moving mass in addition to any added mass – were related through the modified equation for natural frequency below which separates total moving mass into added mass and unweighted mass [7],

$$f_0 = \frac{1}{2\pi\sqrt{(m_m + m_i) * C_m}} \quad (4.3)$$

where  $f_0$  is the resonant frequency and  $m_i$  is the added mass. This was rearranged to form a linear equation that could be used to find the unweighted moving mass,  $m_m$ , and the mechanical compliance,  $C_m$ ,

$$\left(\frac{1}{2\pi f_0}\right)^2 = C_m m_i + C_m m_m. \quad (4.4)$$

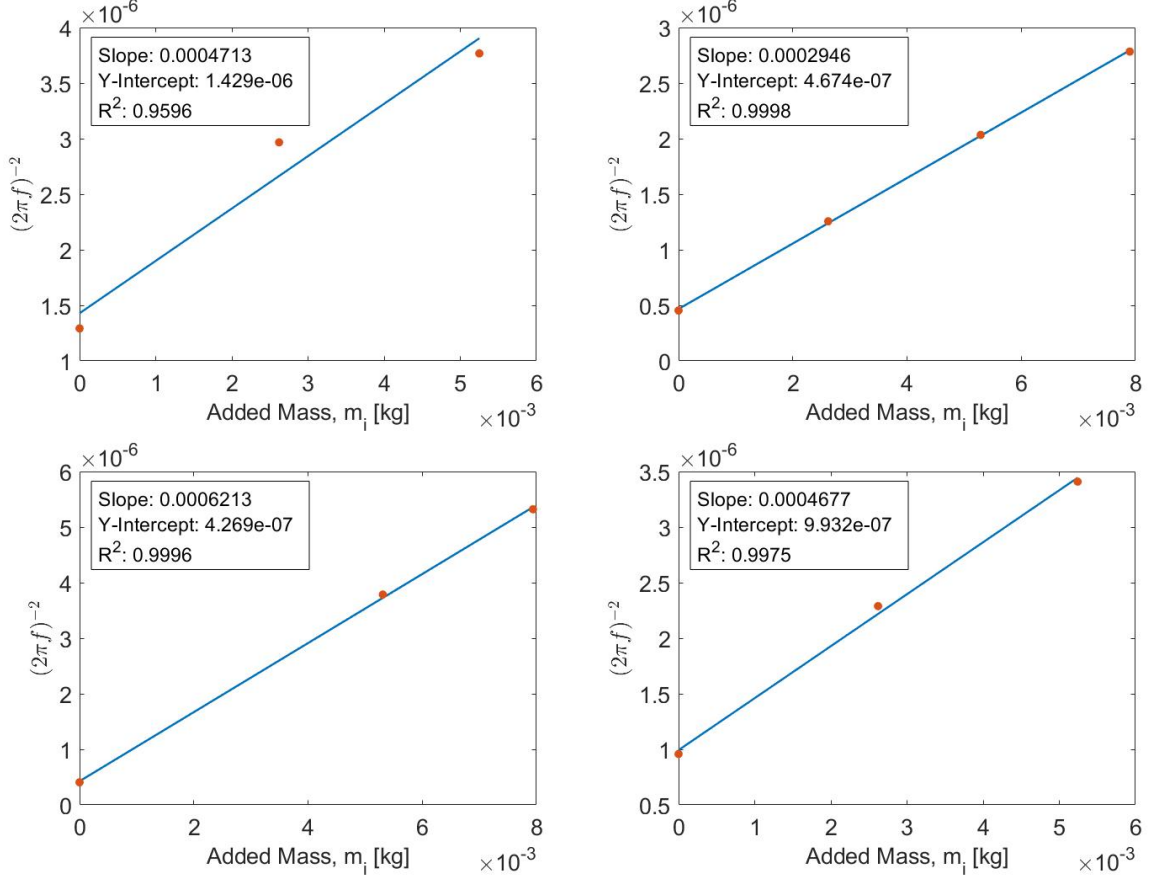


**Figure 4.3.** The linear curve fit for the W1-2121S (top-left), W2-2243S (top-right), FRS 5X-8 (bottom-left), and TEBM36S12-8/A (bottom-right) drivers. The slope of each fit line was the mechanical compliance  $C_m$  and the y-intercept was equal to the unweighted moving mass multiplied by the mechanical compliance,  $C_m m_m$ .

Considering the left-hand side of Eq. 4.4 to be the dependent variable of a linear equation and  $m_i$  to be the independent variable, a line was fit to the variables whose slope was the mechanical compliance and whose y-intercept could be used to solve for  $m_m$  after solving for  $C_m$ . The linear curve fits for each driver can be seen in Fig. 4.3 and the resulting mechanical compliance and unweighted moving mass can be seen in Table 4.2. This was a significant source of error in these calculations. While most of the drivers had high R-squared values from their linear curve fits, the W1-2121S driver linear curve fit had a significant departure in its R-squared value.

The mechanical quality factor, often denoted as  $Q_{ms}$ , describes the sharpness of the resonant frequency peak and was found by dividing the resonant frequency by the difference between the frequencies of the half-power points of the impedance magnitude [7],



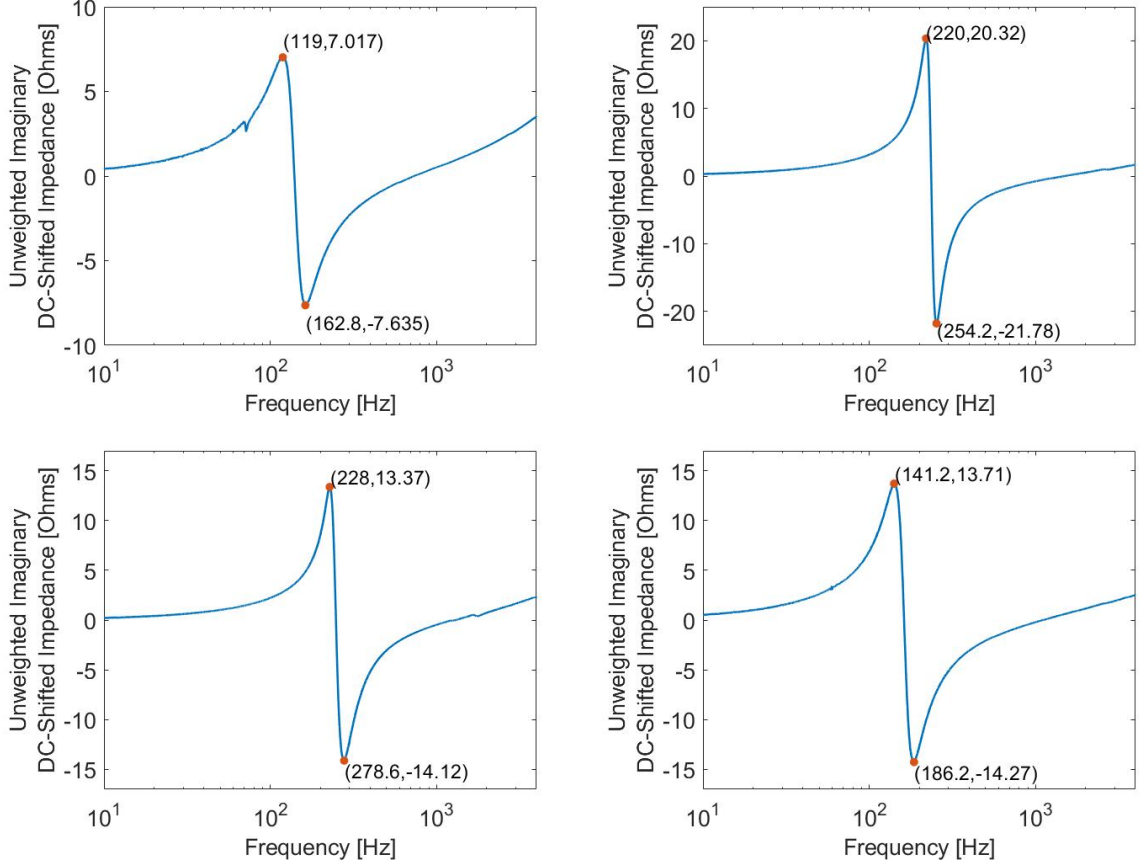


**Figure 4.4.** The imaginary impedance for the W1-2121S (top-left), W2-2243S (top-right), FRS 5X-8 (bottom-left), and TEBM36S12-8/A (bottom-right) drivers. Finding the difference in frequency between the minimum and maximum imaginary impedance was used in finding the mechanical quality factor,  $Q_{ms}$ .

$$Q_{ms} = \frac{f_0}{|f_{max} - f_{min}|} \quad (4.5)$$

where  $f_{max}$  and  $f_{min}$  are the frequencies at half-power. One way to find the half-power points would be to find the frequency at which the impedance magnitude is approximately 0.707 times the resonant frequency impedance magnitude. Another way to find the half-power points, and the method that was implemented here, would be to observe the local maximum and minimum surrounding the resonant frequency, which ideally should have 0  $\Omega$  of imaginary impedance, as the frequencies of these local maximum and minimum are the frequencies at which the impedance magnitude is at half-power. The mechanical quality factor was related to the moving mass and the mechanical damping by the following equation [7],

$$R_m = \frac{2\pi f_0 m_m}{Q_{ms}}. \quad (4.6)$$

Just as with the calculated moving mass  $m_m$  and the mechanical compliance  $C_m$ , the mechanical damping  $R_m$  results can be seen in Table 4.2.

Using the DC-shifted impedance curve and the calculated mechanical resistance  $R_m$ , the force factor  $Bl$  was calculated based on the relationship established by the electromechanical coupling created by the magnetic field and the voice coil current flow. By separating the matrix in Eq. 3.33 into two equations, assuming a time-harmonic system to use magnitudes in further calculations, and rearranging to combine the two equations into a single equation, the following equation could be created,

$$\frac{1}{g_m} = \sqrt{\frac{F}{-u} * \frac{e}{i}}. \quad (4.7)$$

Impedance, being the potential divided by the flow variables in a domain, can be seen in Eq. 4.7 for both the mechanical and electrical domains. The mechanical impedance equals the force divided by the negative velocity in order to preserve flow conventions. Eq. 4.7 shows that any mechanical impedance and the electrical equivalent of that mechanical impedance,  $Z_{em}$ , are related in the following way as they interact with an ideal gyrator with a mutual conductance of  $g_m = \frac{1}{Bl}$ ,

$$Bl = \sqrt{Z_m * Z_{em}}. \quad (4.8)$$

With the understanding that the impedance created by the mechanical resistance is equal to the mechanical resistance, as seen in Eq. 3.11, Eq. 4.8 can be rewritten for the case of mechanical resistance as,

$$Bl = \sqrt{R_m * R_{em}} \quad (4.9)$$

where  $R_{em}$  is the electrical equivalent of the mechanical resistance [7]. This was observed in the unweighted DC-shifted impedance measurement, being the DC-shifted real impedance at the measured resonant frequency. These can be seen on the traces in Fig. 4.5, which contains closer looks at the resonant peaks of the unweighted impedance tests.

The final value that was determined was the voice coil electrical inductance,  $L_e$ . With all other parameters measured or solved for,  $L_e$  was solved for using a crude guess-and-check method comparing the imaginary impedance of the theoretical model using a guessed  $L_e$  value to the measured imaginary unweighted impedance with adjustments to

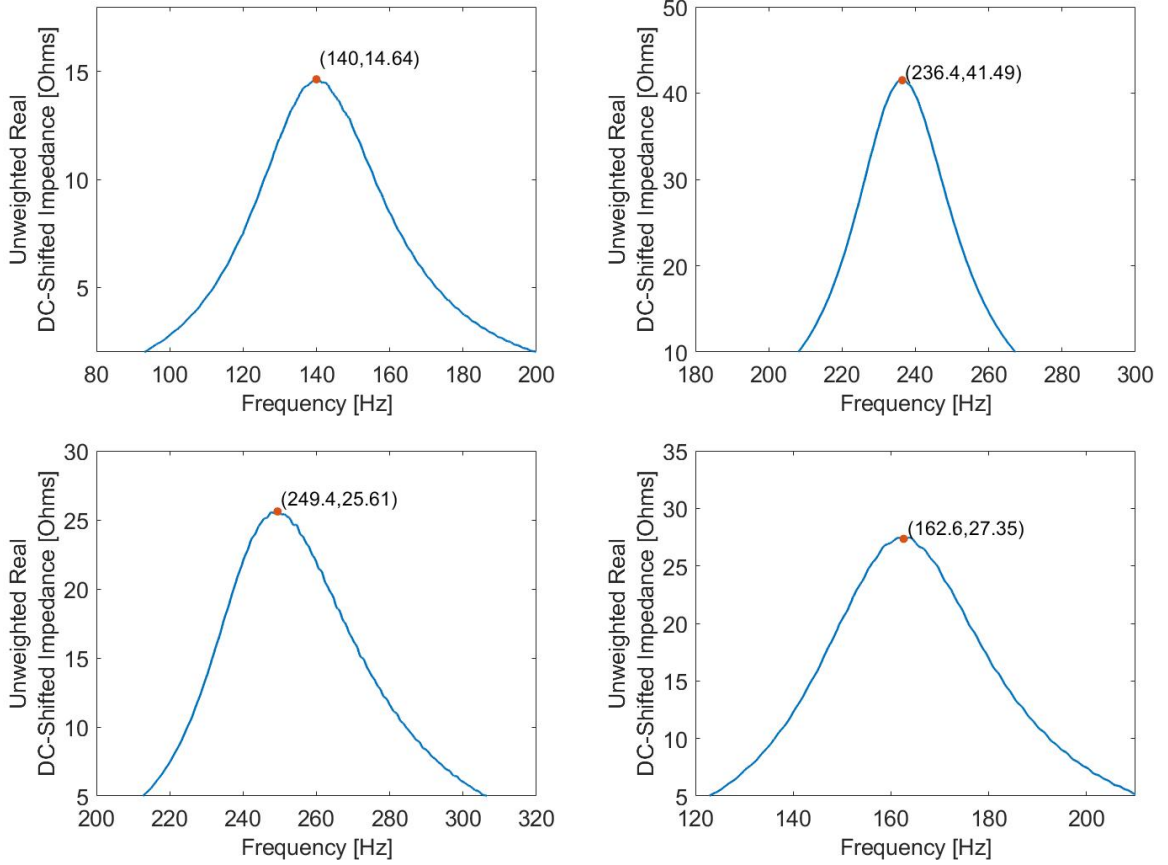


**Figure 4.5.** The maximum DC-shifted real impedance for the W1-2121S (top-left), W2-2243S (top-right), FRS 5X-8 (bottom-left), and TEBM36S12-8/A (bottom-right) drivers. The maximum real impedance for each driver is the electrical equivalent of the mechanical resistance,  $R_{em}$ .

the  $L_e$  value being made to better match the model to the measured impedance. Using the previously established model from section 3.5 would be inaccurate for this guess-and-check method because the model included the enclosure whereas the measurements were made in free-air without the enclosure. Including the enclosure stiffness would have two consequences: the added acoustical compliance from the trapped air in the enclosure would shift the resonant frequency higher and the radiation from the back of the driver would be neglected causing the acoustical impedance from the back of the driver to not be accounted for. Because of these differences, the model was modified to the model shown in Fig. 4.6 where the acoustic compliance representing the enclosure volume was removed and a second acoustic radiation subcircuit was added, accounting for the radiation from the back of the driver. The inclusion of another acoustic radiation subcircuit identical to the originally included subcircuit was not completely accurate as the radiation from

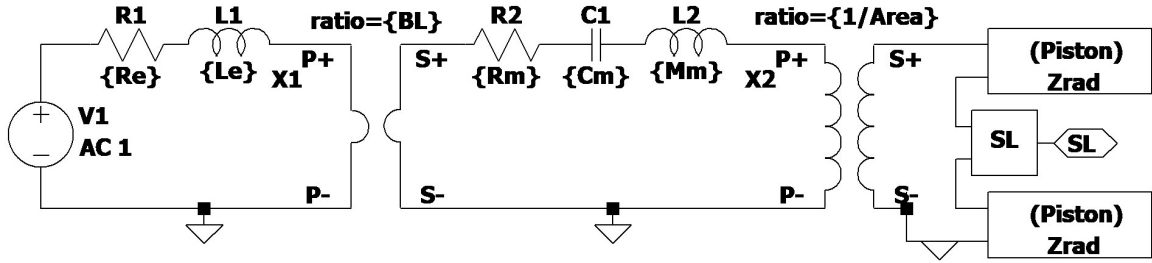


**Figure 4.6.** The free-air simulation model made using LTSpice. The addition of the acoustic radiation subcircuit (labeled Zrad) modeled the radiation from the back of the driver. The elimination of the acoustic capacitive element (previously C\_acs) accounted for the impedance test not using an enclosure.

the rear of the driver is additionally impeded by the driver components directly behind the back of the driver cone. This error mattered very little in the scope of this model as adding an additional radiation impedance subcircuit produced a frequency-dependent total acoustic radiation impedance that was only 4% different than using just one radiation subcircuit. This was observed by modeling the total acoustic radiation impedance of the model with and without the addition of the second impedance subcircuit. While the radiation impedance varied with frequency, the percent difference only decreased as higher frequencies were modeled. Furthermore, the electrical representation of the full driver impedance was minimally affected by the addition of the radiation impedance subcircuit, as there was at most a 0.25% difference in the total modeled electrical impedance with and without the second radiation impedance subcircuit.

As seen in Table 4.2, the measured characteristics often differed from those given by the specification sheets for each driver. The measured mechanical compliance was much lower than those reported on the specification sheets. The moving masses also differed significantly with the W2-2243S measured moving mass being the closest to the reported moving mass. These discrepancies between the measured and given values could be due to manufacturing tolerances of the materials and construction methods used to make each driver. Another possible reason for the difference in parameters was a likely difference in testing procedure as minimal information about the testing conditions was provided by the manufacturers. If the model parameters were populated with the specifications given by the parameters given by the manufacturers, the models would give a false representation of the drivers moving forward.

With all parameters measured and calculated, the model was checked against the unweighted impedance measurement. The model, using an AC voltage of 1 Volt could model the impedance by measuring the current at the voltage supply V1 in Fig. 4.6.

**Table 4.2.** Measured and Given Driver Parameters

Parameter	Driver Model			
	<i>W1-2121S</i>	<i>W2-2243S</i>	<i>FRS 5X-8</i>	<i>TEBM36S12-8/A</i>
$f_0$ , Measured	140.0 Hz	236.4 Hz	249.4 Hz	162.6 Hz
$f_0$ , Given	120.0 Hz	160 Hz	190 Hz	148 Hz
$R_e$ , Measured	3.6 $\Omega$	3.7 $\Omega$	7.6 $\Omega$	7.6 $\Omega$
$R_e$ , Given	3.5 $\Omega$	3.4 $\Omega$	7.7 $\Omega$	7.9 $\Omega$
$L_e$ , Measured	0.150 mH	0.080 mH	0.100 mH	0.127 mH
$L_e$ , Given	0.070 mH	0.036 mH	Not Given	0.137 mH
$Bl$ , Measured	3.4947 Tm	3.7619 Tm	2.3655 Tm	4.0627 Tm
$Bl$ , Given	3.14 Tm	3.80 Tm	2.67 Tm	3.87 Tm
$R_m$ , Measured	0.8344 kg/s	0.3409 kg/s	0.2185 kg/s	0.6004 kg/s
$R_m$ , Given	1.00 kg/s	0.302 kg/s	0.334 kg/s	0.49 kg/s
$C_m$ , Measured	0.4713 mm/N	0.2946 mm/N	0.6213 mm/N	0.4677 mm/N
$C_m$ , Given	0.9494 mm/N	0.7300 mm/N	0.7181 mm/N	0.70 mm/N
$m_m$ , Measured	3.0320 g	1.5866 g	0.6871 g	2.1236 g
$m_m$ , Given	1.68 g	1.35 g	0.977	1.68 g
$A_{cone}$ , Measured	8.86 cm <sup>2</sup>	15.21 cm <sup>2</sup>	12.64 cm <sup>2</sup>	16.69 cm <sup>2</sup>
$A_{cone}$ , Given	9 cm <sup>2</sup>	15 cm <sup>2</sup>	12.5 cm <sup>2</sup>	17.2 cm <sup>2</sup>

Dividing the supplied voltage by the current at the voltage supply V1 produced the impedance of the system. One metric of having a successful model was that the impedance modeled visually matched the measured impedance without much divergence when plotted together. Each model did this well; however, there was a frequency-dependent real impedance that was not modeled, most likely due to the unmodeled Eddy currents in the electrical domain [23]. This divergence in real impedance was deemed insignificant for the purpose of this model as the main purpose of this model was to predict the frequency response change due to a shift in resonant frequency from the enclosure stiffness. While this metric may show any obvious issues with the model, it was a rather subjective metric. As an objective metric, the resonant frequency of the model was to be within 10% difference of the measured resonant frequency. This ensured that when the resonant frequency shifts from modeling the enclosure as part of the system, the shift

in the resonant frequency would be closer to what could be expected in the practical application. As seen in the resonant frequency comparisons in Table 4.3, all models produced a resonant frequency within 10% of the measured resonant frequency but they were not perfect. All modeled resonant frequencies were lower than the measured resonant frequencies, signifying that there may have been some inaccuracy to the measurement and calculation for the moving mass and mechanical compliance due to having a small sample size of acceptable weighted measurements to create the linear curve fits seen in Fig. 4.3. This was the most concerning with the W1-2121S driver. While the modeled resonant frequency was within 10% of the measured unweighted resonant frequency, the lower R-squared value of the linear curve fit was notable when considering the reliability of some of the calculated parameters.

**Table 4.3.** Measured to Modeled Resonant Frequency Comparison

Parameter	Driver Model			
	<i>W1-2121S</i>	<i>W2-2243S</i>	<i>FRS 5X-8</i>	<i>TEBM36S12-8/A</i>
Modeled $f_0$	132.4 Hz	228.0 Hz	235.0 Hz	156.7 Hz
Measured $f_0$	140.0 Hz	236.4 Hz	249.4 Hz	162.6 Hz
Percent Difference	5.58 %	3.62 %	5.95 %	3.70 %

### 4.3 Simulating Frequency Response

Reverting back to the model in Fig. 3.7 and using the values from Table 4.2 and the estimated volume of trapped air for each enclosure,  $V_{box}$  in Table 2.3, the frequency response for each driver-enclosure assembly was simulated. Measuring the voltage at the Source Level subcircuit showed the radiated on-axis pressure 1 meter away from the cone surface. To match the test conditions given on each specification sheet, the voltage supply was modified so that 1 Watt of power was supplied to each model: 2.00 Volts for the W1-2121S and W2-2243S drivers (which had a nominal impedance of 4  $\Omega$ ) and 2.83 Volts for the FRS 5X-8 and TEBM36S12-8/A drivers (which had a nominal impedance of 8  $\Omega$ ).

Comparing the frequency responses modeled by Fig. 3.7 to the frequency responses modeled by Fig. 4.6 using the appropriate input voltages showed how the enclosure changed the frequency response of each driver. As seen in Fig. 4.11 and Fig. 4.12, the responses for the W1-2121S and W2-2243S drivers respectively, the effect of the enclosure was relatively minimal above 500 Hz, only raising the response by about 1 dB. In the

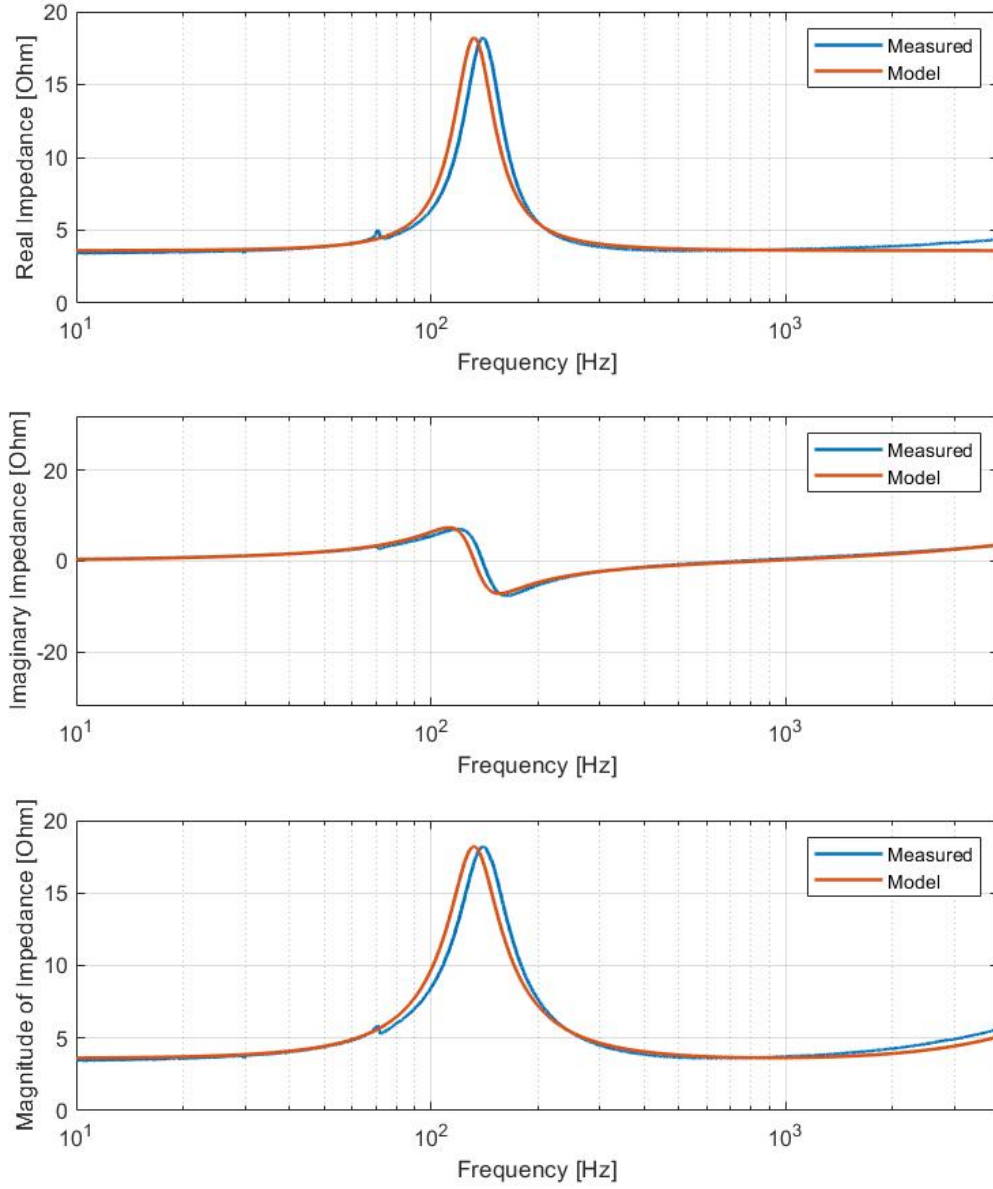


**Figure 4.7.** The real part of the impedance (top), imaginary part of the impedance (middle), and impedance magnitude (bottom) of the measured and modeled W1-2121S driver.

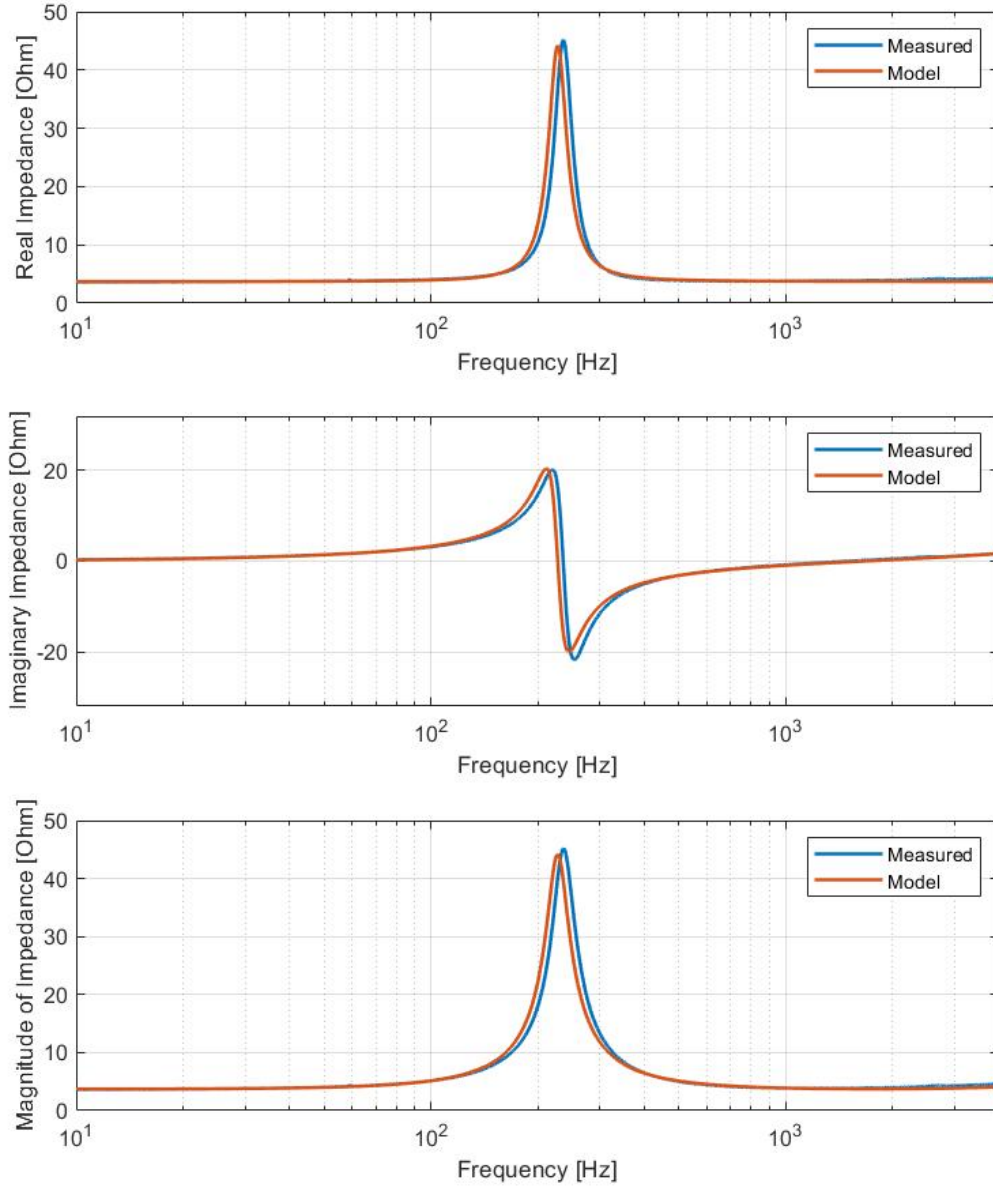


**Figure 4.8.** The real part of the impedance (top), imaginary part of the impedance (middle), and impedance magnitude (bottom) of the measured and modeled W2-2243S driver.



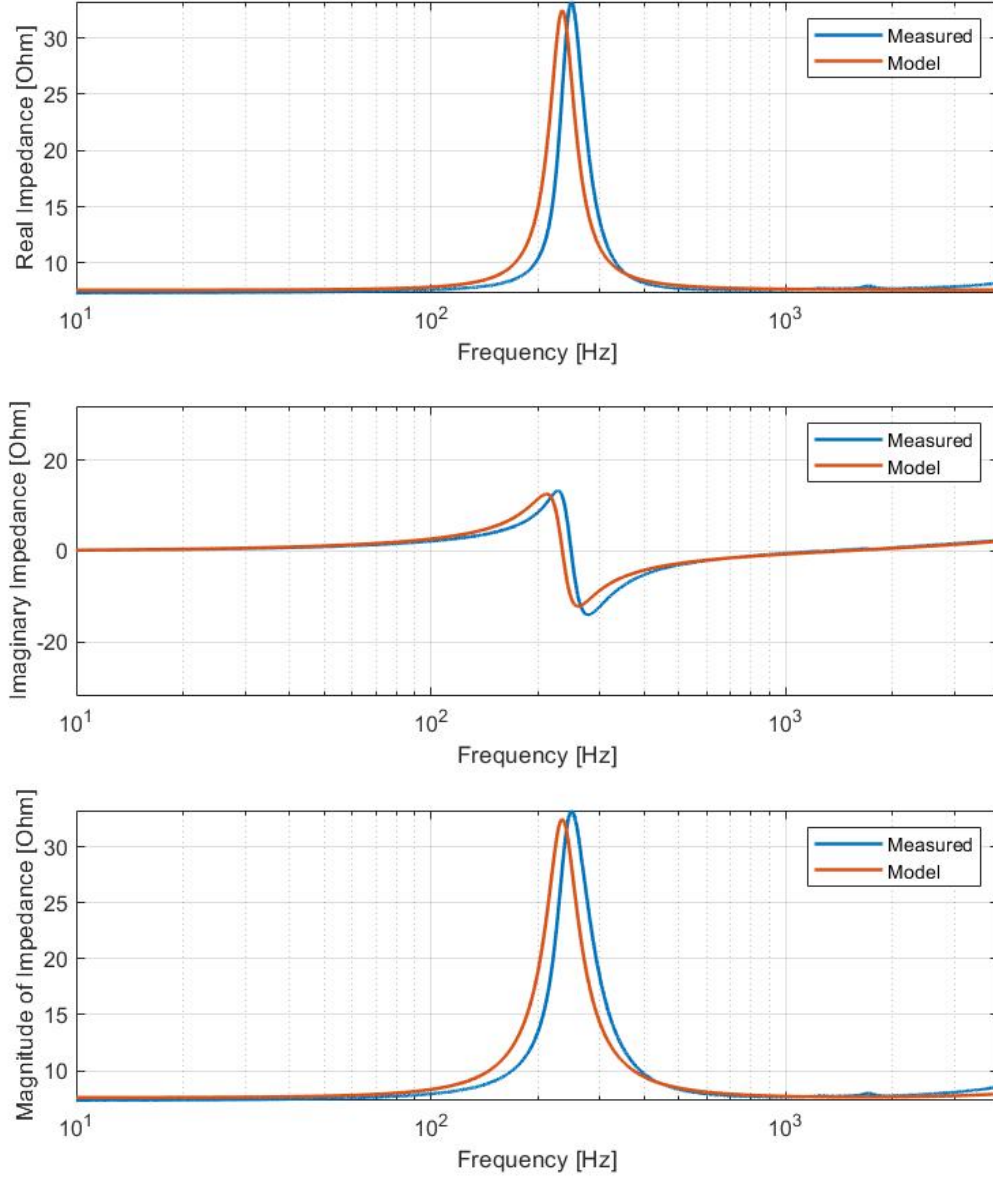


**Figure 4.9.** The real part of the impedance (top), imaginary part of the impedance (middle), and impedance magnitude (bottom) of the measured and modeled FRS 5X-8 driver.

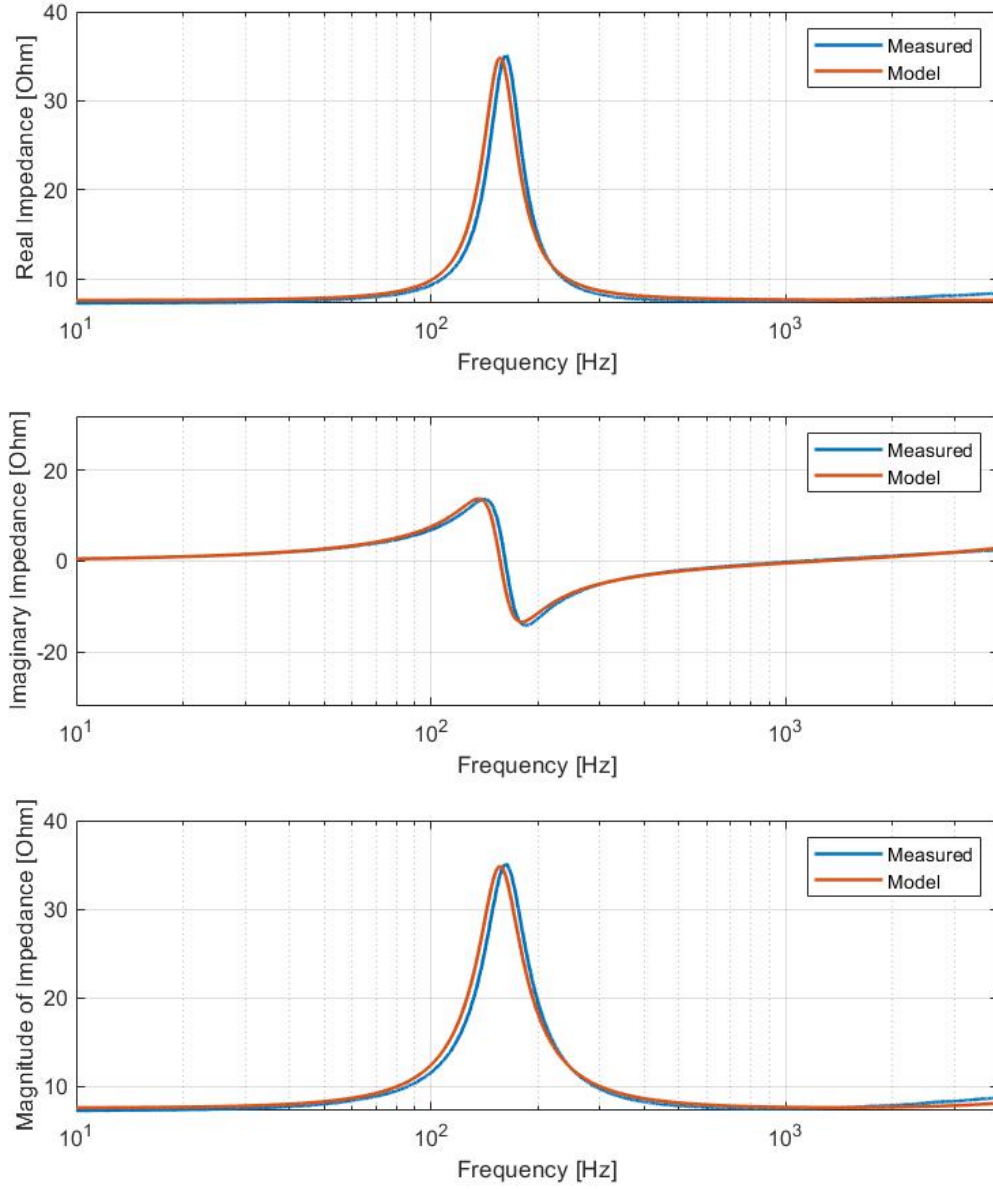


**Figure 4.10.** The real part of the impedance (top), imaginary part of the impedance (middle), and impedance magnitude (bottom) of the measured and modeled TE6M36S12-8/A driver.

case of the W2-2243S driver, the enclosure increased the response at 500 Hz in a way that somewhat flattened its frequency response curve more than what the free-air model response was. As for the FRS 5X-8 and TEBM36S12-8/A drivers' responses, shown in Fig. 4.13 and Fig. 4.14, the enclosure produced an increase of about 3 dB and 4 dB respectively at 500 Hz due to sharper increases at lower frequencies, creating a sloped return to the response produced by the free-air model. These peaks, along with the peak found in the W1-2121S assembly model, suggested that the designed enclosure volumes may be a too small for these drivers to operate with a flat response. While the residual effects of the peaks can be seen affecting the lower end of the operating bandwidth, the resonant frequencies remained below 500 Hz which met the original requirement of keeping the resonant frequency of each driver-enclosure assembly below the operating bandwidth. The resonant frequencies of each driver-enclosure assembly can be seen in Table 4.4. Keeping the driver-enclosure resonant frequencies bellow 500 Hz suggested that in application these peaks should interfere very little with achieving a flat response within the operating bandwidth of 500 Hz to 3000 Hz; however, the modeled frequency response suggested that some of the drivers, particularly the FRS 5X-8 and TEBM36S12-8/A drivers, may have responses that are impacted by the enclosure stiffness withing the operating bandwidth. Of the chosen drivers, the W1-2121S and W2-2243S drivers showed the best modeled response to being mounted in their respective enclosures.

**Table 4.4.** Modeled Driver-Enclosure Assembly Resonant Frequencies

<b>Model</b>	<b>Driver Model</b>			
	<i>W1-2121S</i>	<i>W2-2243S</i>	<i>FRS 5X-8</i>	<i>TEBM36S12-8/A</i>
Full Assembly $f_0$	213.8 Hz	334.2 Hz	385.4 Hz	330.4 Hz
Free-Air $f_0$	132.4 Hz	228.0 Hz	235.0 Hz	156.7 Hz

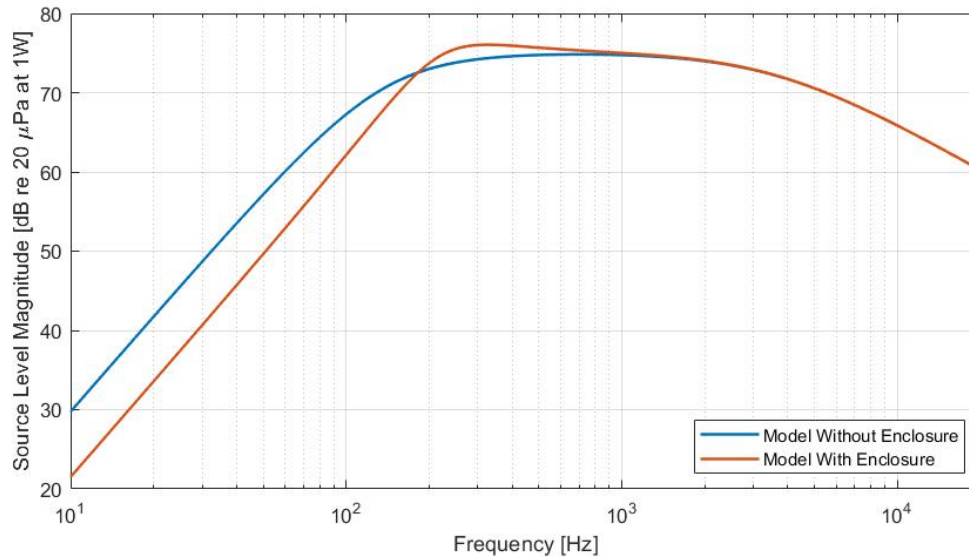


**Figure 4.11.** The modeled frequency response curves for the W1-2121S driver being modeled in free air and being modeled in the enclosure. The frequency response curve stayed relatively flat between 500 Hz and 3000 Hz. There was an increase in response of 1 dB at 500 Hz followed by a steady return to the free-air response.

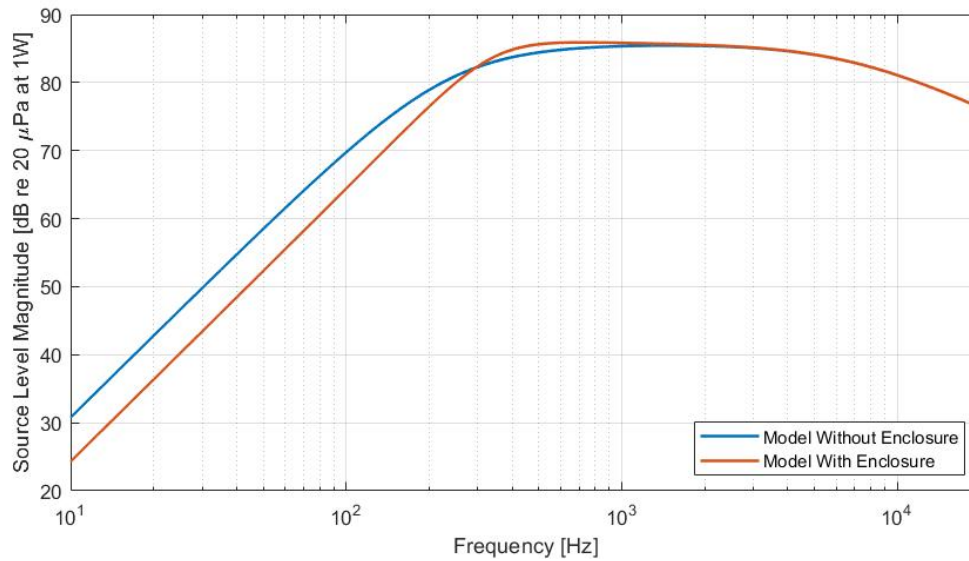


**Figure 4.12.** The modeled frequency response curves for the W2-2243S driver being modeled in free air and being modeled in the enclosure. This driver responded the best to the driver-enclosure model. The enclosure raised the resonant frequency enough to flatten the response in the operating bandwidth of 500 Hz to 3000 Hz.

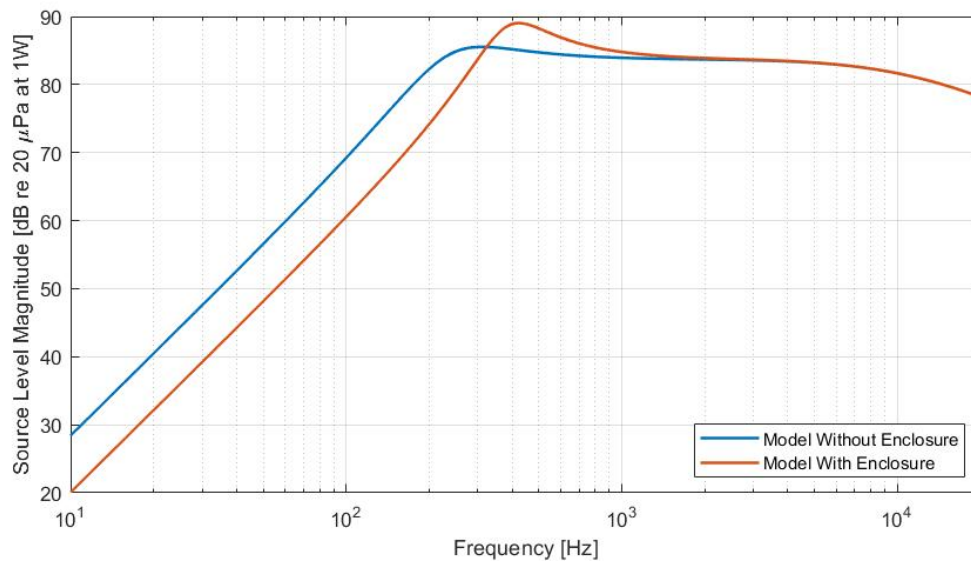


**Figure 4.13.** The modeled frequency response curves for the FRS 5X-8 driver being modeled in free air and being modeled in the enclosure. There was a larger spike in frequency response due to the enclosure that prevented a perfectly flat response from being observed in the model. While the increase in response was only 4 dB above the free-air model, it was one of the more extreme reactions out of the chosen drivers.

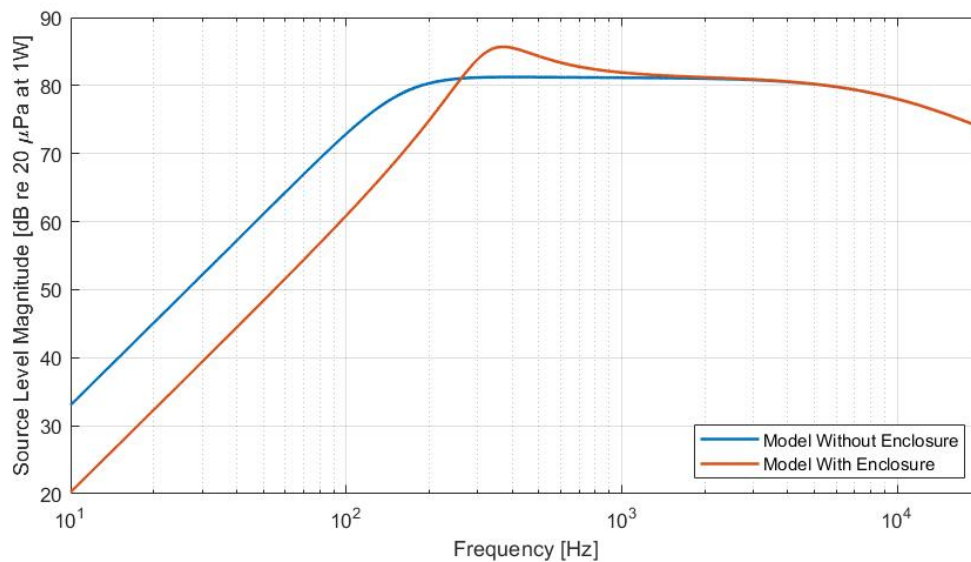


**Figure 4.14.** The modeled frequency response curves for the TEBM36S12-8/A driver being modeled in free air and being modeled in the enclosure. This driver had a sharp increase in frequency response, departing from an otherwise flat response from the free-air model. This was due to the driver being modeled in the smallest enclosure volume out of the chosen drivers.

# Chapter 5 |

## Measuring Frequency Response and Nonlinear Behavior

Simulating the frequency response of each driver-enclosure assembly was a plausible way to determine the behavior of each assembly but measuring the assemblies in a controlled environment showed the assemblies' true behavior. This was done by supplying a maximum-length sequence, or MLS, to the assemblies and measuring the corresponding output. After post-processing, the frequency responses of each enclosed driver was made apparent. The measurements of the actual driver-enclosure assembly responses were also accompanied by measurements of linear and nonlinear parameters done by the Klippel Analyzer 3 system, abbreviated as the KA3 system. This series of measurements served to check against the previously measured and calculated values using the process described in 4.1 and 4.2 and as a way of measuring the produced distortion and nonlinear behaviors of the free-air drivers.

### 5.1 Measuring Frequency Response

Measuring the frequency response involved some consideration before and after the measurement had taken place and before any results could be evaluated. The method for measuring the frequency response began with a decision on what excitation signal should be used. The excitation signal can have adverse effects on the measurement results, so choosing the best excitation signal was important. Once the signal was chosen, recording and post-processing software that complimented the excitation signal choice was needed. MATLAB R2019b had a package that included impulse response measurement software that fit the needs of this test. This was convenient, but required investigation as to what the software did to create the excitation signal as well as its post-processing calculations.

Once the measurements were made and the post-processing was understood accompanied by the user adjustments deemed necessary, the results could be interpreted properly.

### 5.1.1 The Maximum-Length Sequence

The maximum-length sequence, or MLS, is a pseudo-random binary signal with a list of advantages for being used as an excitation signal. The MLS is created by using a polynomial of degree  $m$  to specify a feedback shift register of length  $n = 2^m - 1$  that uses exclusive-or gates. By using a primitive polynomial (a polynomial that cannot be reduced) to create the feedback shift register, the sequence becomes periodic [24], which is both mathematically and practically useful. For measurements where the generated MLS signal is used as an excitation source, the binary 1's and 0's are converted into a positive and negative voltage of equal amplitude (e.g.  $\pm 1$  Volt or  $\pm 0.5$  Volts) [20]. The measured signal and the known MLS input can be used to calculate an impulse response by using circular cross-correlation [25].

One advantage that the MLS excitation signal holds over methods like the sine-sweep and the periodic impulse excitation measurement methods is that the MLS excitation reduces nonlinearities in the system. This advantage can be negated by either adding nonlinearities into the system [26] or by driving the system to produce nonlinear behavior. The later presents an interesting trade-off between providing a strong excitation signal to ensure that the measurement's noise floor does not interfere with the measured response and keeping the excitation signal amplitude low enough to not generate distortions from the system [27]. Any nonlinearities can be seen in the calculated impulse response, the obvious signs being described as 'spikes' or 'lumps' in the tail of the impulse response [26]. This can help determine if the amplitude of the excitation signal was too large, causing distortion.

One known disadvantage to the MLS measurement method is a time-aliasing error. The error occurs when the generated signal length of a period of the MLS signal is shorter than the impulse response being measured. Similar to aliasing in the frequency domain, aliasing in the time domain would show impulses somewhere further in time in the calculated impulse response where there should not be an impulse. The potential for this error can be reduced by using a higher order primitive polynomial, i.e. increasing  $m$ . [27]

Ultimately, the MLS signal was chosen as the excitation signal due to its limited distortion characteristics assuming the signal amplitude was low enough to minimize distortion but high enough to be above the noise floor. This provided a better chance to

observe the enclosed drivers' true frequency response.

### 5.1.2 The MATLAB Impulse Response Measurement App

Mathworks, the creators of MATLAB, created and implemented an Impulse Response Measurement application *ImpulseResponseAppModel.m* that conveniently performs the excitation signal generation, data acquisition, and post-processing for measuring the impulse and frequency response of a system [28]. While using a packaged application was favorable, it was also important to understand the inner workings of the application in order to properly interpret any results.

When set to use the MLS excitation signal, the application would run *MLSMMethod.m* which contained the function *getExcitationSignal* which referenced *Pseudo-Random Sequences and Arrays* by F.J. McWilliams and N.J.A Sloane [24] to create the MLS signal. The signal was created with the user-set signal duration time and sample frequency. Beginning with a randomly generated sequence, *getExcitationSignal* employed the primitive polynomial shift register method. The order of the primitive polynomial was dependent on the length of the of the MLS signal by the following equation,

$$m = \text{ceil}\left(\log_2(n + 1)\right) \quad (5.1)$$

where  $\text{ceil}()$  represented the solution of the enclosed mathematics rounded up to the nearest whole number, ensuring a whole-numbered order while being as high as possible to create the desired MLS signal. The pseudo-random signal was then adjusted according to the specified excitation level, which was an input by the user in terms of dBV, the decibel level of voltage referencing 1 Volt. For this application, 0 dBV was equivalent to the signal being at  $\pm 1$  Volt peak-to-peak. The excitation signal was now fed into the system being measured, which in this case was a driver-enclosure assembly.

The application gave the option to perform a certain number of warm-up runs, delaying the measurement of the system by that many runs through the excitation signal. All runs in the system were conducted consecutively without pausing in between each run. Using warm-up runs helped reduce the effects of a transient response due to the system initializing. Once the system to be measured had completed the number of runs and the results were recorded, they were fed back into *MLSMMethod.m*. [28]

From here, the excitation signal and the recorded signal were passed into the function *estimateImpulseResponse*, which is also contained in *MLSMMethod.m*, and were used to solve for the impulse response using circular convolution to find the cross-correlation [28].



The impulse response was then normalized by the mean-squared of the excitation signal magnitude. Finally, the normalized impulse response was passed into *freqz.m* where the impulse response was treated like a FIR filter and the frequency response was found [29].

Data could be extracted from several points in this measurement and calculation process allowing the user to do their own post-processing. This was convenient for averaging, filtering, and applying factors like microphone sensitivity and amplifier gain in post-processing.

### 5.1.3 Frequency Response Measurement Method

Starting at the computer workstation, the excitation signal generated by *ImpulseResponseAppModel.m* was passed into a MOTU 24Ao digital-to-analog converter and then into a Dayton Audio MA1240a amplifier. The amplifier added a gain known to within 0.5 dB, changing the voltage at the terminals of the driver-enclosure assembly. The assembly to be tested was mounted onto a stand and placed in a sealed, acoustically dead room. The room was lined with Auralex 2 inch Studiofoam® Pyramid™ foam paneling, which has a noise reduction coefficient of 0.7 [30]. The specification sheet for this foam paneling shows that the sound absorption coefficient is greater than 0.95 above 1000 Hz, allowing reflections below 1000 Hz to be observed [10]. A Dayton Audio EMM-6 measurement microphone was placed on-axis 1 meter away from the driver diaphragm. The recorded signal went into an interface and back into the computer. Several tests were run using various excitation signal levels in an attempt to find the equilibrium between being quiet enough to not cause distortions but loud enough to be above the measurement noise floor.

The impulse response calculated by *ImpulseResponseAppModel.m* was used to find the proper excitation level. The frequency response was calculated separate from the application using the known excitation signal at the speaker terminals (after gain was applied by the amplifier) and the recorded signal (after the microphone sensitivity was applied). The response was found using the same method in Eq. (4.1), using the microphone sensitivity to convert the recorded signal into Pascals and the excitation signal voltage at the speaker terminals (resulting in a transfer function with units of Pa/V). The spectral densities were calculated using a rectangle window and averaged using a 50% window overlap. A third-octave average was applied separately for a simpler interpretation of the assembly responses to reflect a more perceivable driver-enclosure assembly response by averaging through various room acoustic characteristics. The frequency response in decibels was calculated using the following equation,

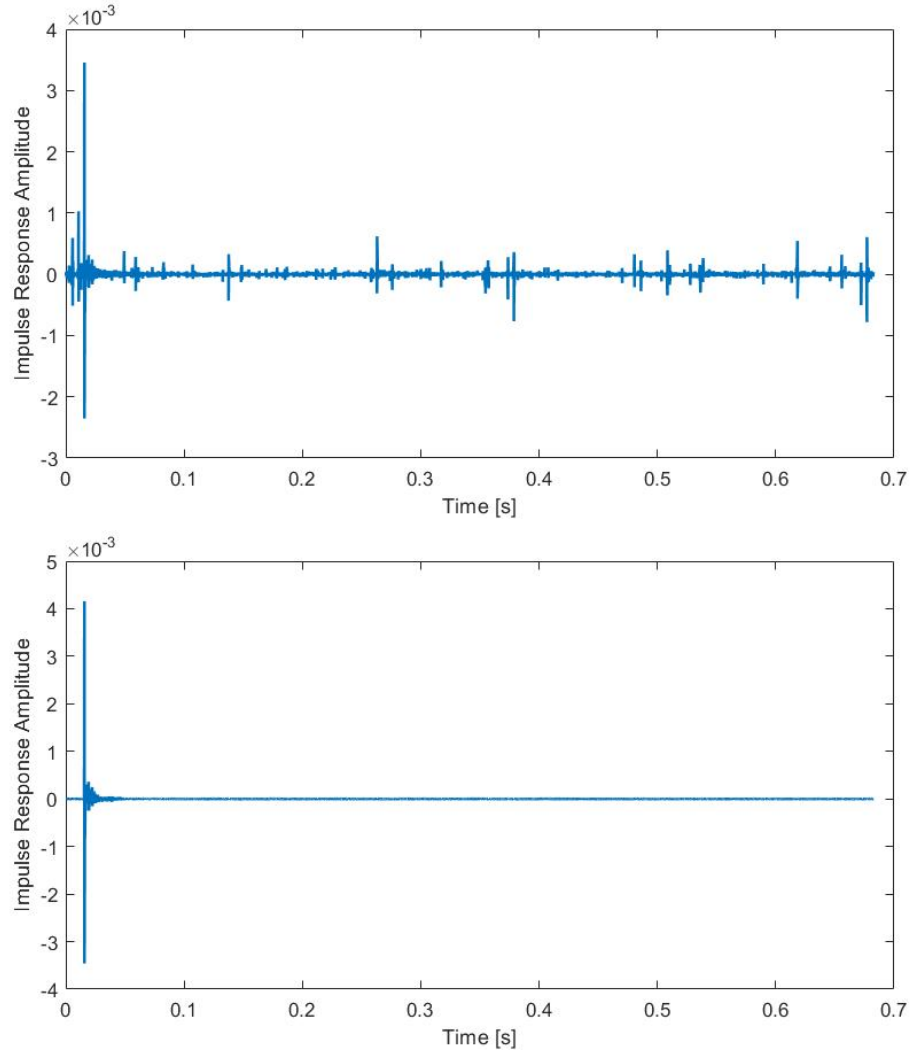


**Figure 5.1.** An example comparison between the W2-2243S impulse responses for a 12.36 dBV excitation level (top) and a 6.36 dBV excitation level (bottom).

$$\text{dB} = 20 \log_{10} \left( \frac{H(f)}{20 \text{ } \mu\text{Pa/Voltage at 1 W}} \right). \quad (5.2)$$

By referencing 20  $\mu\text{Pa}$ /Voltage at 1 W, the transfer function was now observable as a Sound Pressure Level at the voltage required to create 1 Watt of electrical power at the driver terminals based on each driver's nominal impedance.

#### 5.1.4 Frequency Response Results

The impulse responses for each driver at a generated excitation level of 12.36 dBV at the driver's terminals showed significant 'spikes' whereas the impulse responses for a

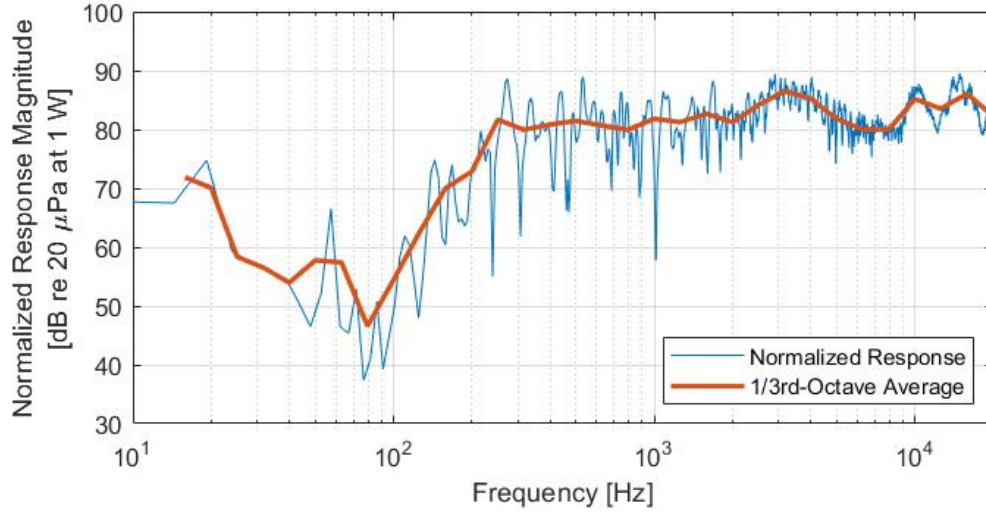


**Figure 5.2.** The frequency response for the W2-2243S driver-enclosure assembly.

6.36 dBV excitation level showed a much smoother tail. An example of this can be seen in Fig. 5.1. As stated earlier, the display of 'lumps' or 'spikes' can signify distortion in the measurement [26], so using an excitation level of 6.36 dBV was determined to be the optimal level of the recorded tests to show the best results. The sharp peaks and dips in the measured frequency responses were most likely due to the acoustical environment of the measurements.

The measured responses displayed similar sharp peaks and dips at similar frequencies, some to varying degrees of magnitude. For example, nearly all measurements showed sharp resonances at around 274 Hz, 525 Hz, and 1690 Hz as well as anti-resonances at 300 Hz, 463 Hz, and 1000 Hz. This was evidence that the room's acoustical characteristics were being captured in the measurement as well. The driver-enclosure assemblies' frequency responses were better represented as the third-octave average, which averaged out these sharp resonances and anti-resonances from the room's acoustic properties.

The W2-2243S assembly response, seen in Fig. 5.2, was flat within  $\pm 1.5$  dB of 81.28 dB between 500 Hz and 2000 Hz. This was considered to be a significantly flat response. This measured response reflected the flatter nature of the model seen in Fig. 4.12 which showed an increased response around 400 Hz. There was a response increase of about 5 dB at 3000 Hz. This did not match the modeled frequency response in Fig. 4.12, but did nearly match the reported frequency response in Fig. 2.2, which also had an increase in response starting at just over 3000 Hz. There appeared to be the beginnings of a decrease in response at around 4000 Hz, but it was not fulfilled as predicted by the model as peaks in response at 10 kHz and 16 kHz raised the response. The overall level

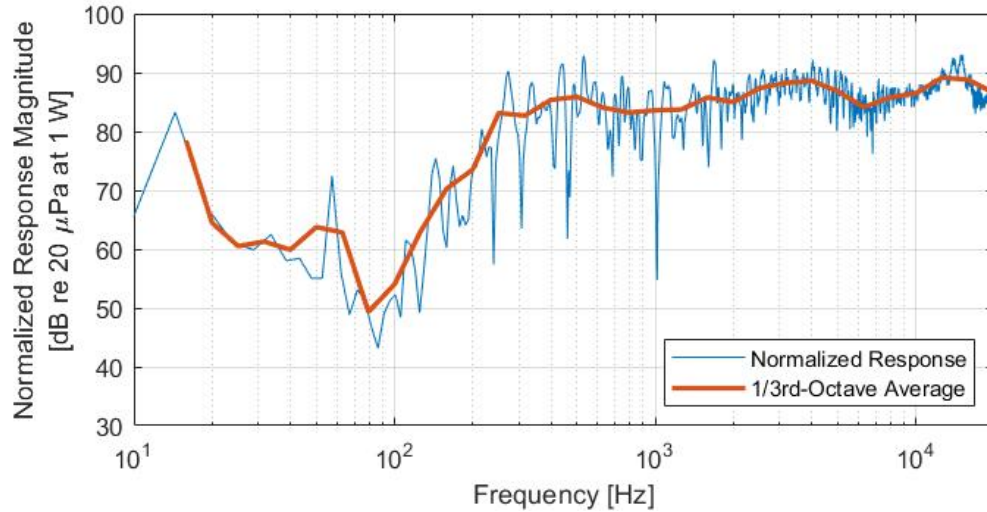


**Figure 5.3.** The frequency response for the FRS 5X-8 driver-enclosure assembly.

of the measured response was about 5 dB lower than the driver sensitivity reported on the specification sheet, once again showing that the specification sheet does not always reflect the actual product. Overall, within the operating bandwidth, this assembly was mostly flat other than the increase at 3000 Hz.

The FRS 5X-8 assembly showed a steady increase in response starting at around 1000 Hz. There was a 3 dB peak in response between 400 Hz and 500 Hz, which was above the modeled resonant frequency in Table 4.4. The assembly model in Fig. 4.13 showed a peak between similar frequencies, but with a more drastic response increase. Just like the W2-2243S assembly response, there was a decrease in response above the operating bandwidth as shown in Fig. 4.13, but this decrease was also truncated by a response peak at around 16 kHz. Within the operating bandwidth, there was slight bump in response at 500 Hz and an increase of about 2.5 dB/octave starting at 1000 Hz, creating a "scooped" response between 700 Hz and 2000 Hz.

The TEBM36S12-8/A assembly showed a 4 dB peak starting around 250 Hz and lasting through 500 Hz, leveling out at about 650 Hz. This peak encompassed the modeled resonant frequency from Table 4.4 and was similar to the trend seen in the assembly model frequency response in Fig. 4.14. The remainder of the response appeared to remain relatively flat through 3000 Hz, above which there were various peaks and valleys rather than the decrease seen in the assembly model. Again, these peaks and valleys hinted at the beginnings of a response decrease at around 3000 Hz but then displayed peaks at around 8 kHz and 12.6 kHz. While these peak values were below the previously discussed drivers' response peaks, similar parallels could be seen. While

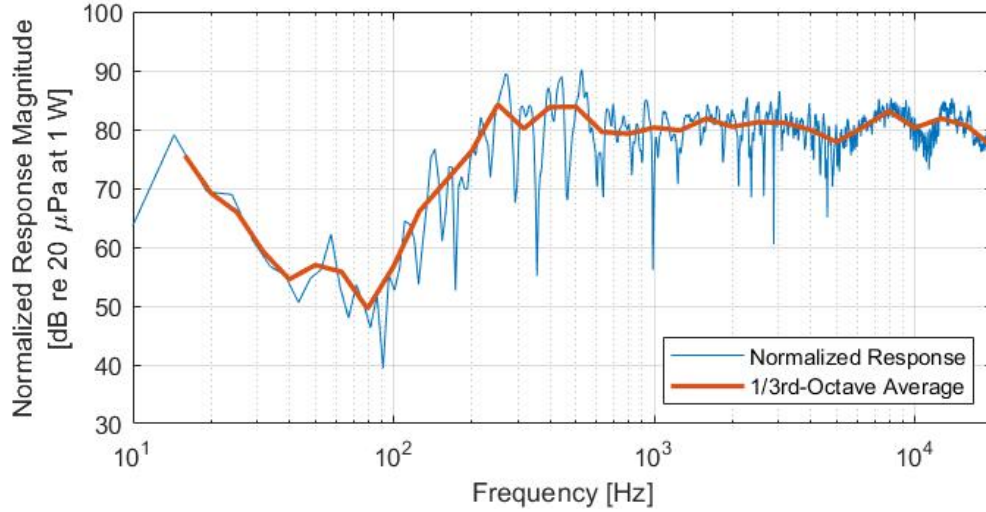


**Figure 5.4.** The frequency response for the TEBM36S12-8/A driver-enclosure assembly.

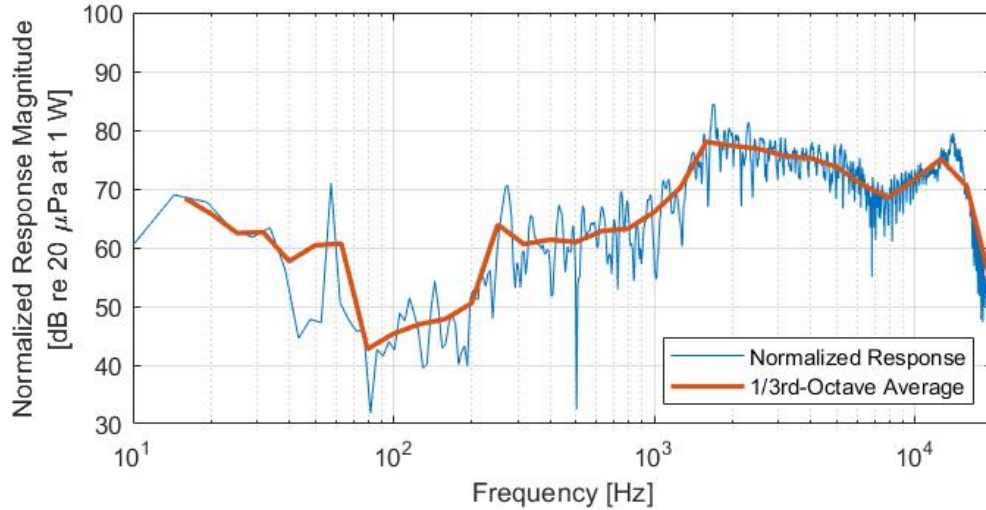


**Figure 5.5.** The frequency response for the W1-2121S driver-enclosure assembly.

containing an increase in response centered at 500 Hz, the measured response remained fairly flat within the operating bandwidth.

The W1-2121S assembly showed a 15 dB increase in response from 500 Hz to about 1500 Hz, which does not match the assembly model in Fig. 4.11. Thinking that this change was due to an error in stiffness led to the consideration of the legitimacy of the estimated enclosed air volume for the W1-2121S enclosure,  $V_{box}$  in Table 2.3. There was the possibility that this estimated air volume was wrong and that the W1-2121S driver filled more volume inside the enclosure than what was initially estimated. Returning to

the model in Fig. 3.7 and adjusting the volume of air trapped within the cavity,  $V_{encl}$  in Eq. (3.24) which in turn adjusted  $C_{acs}$  in Fig. 3.7, showed that in order to match the measured response changing only the acoustic compliance of the enclosure, the enclosed air volume had to be set to  $5 \times 10^{-7} \text{ m}^3$  rather than  $3.3054 \times 10^{-5} \text{ m}^3$  as estimated in Table 2.3. This would be roughly 1% of the available volume, which by the nature of fitting a cylinder – being the generalized shape for the driver components that were housed by the enclosure – inside of the smallest allowable cuboid is not possible. If a cylinder’s diameter is equal to a cuboid’s side length and both the cylinder and cuboid are equal in depth, creating the smallest possible cuboid to fit the cylinder, the cylinder would only take up 78.5% of the cuboid volume. In the application of the cylindrical driver components and cuboid enclosure assembly, at least 21.5% of the enclosed volume must be air. This quick investigation into what is and what is not geometrically possible ruled out the possibility that an inaccurate estimate of the enclosed air volume was the dominant reason for the drastic discrepancy observed between the modeled response in Fig. 4.11 and the measured response. This discrepancy was evident across measurements for this assembly taken at all excitation levels. This suggested that there must be some extra added stiffness in the driver-enclosure assembly that was not amplitude dependent. This added stiffness could have come from the driver in the form of a manufacturing or quality control error or possibly an error in the construction of the enclosure. Due to this large dip in response, the modeled response peak between about 250 Hz and 600 Hz was not observed; however, there was an increase in measured response at 250 Hz, near the predicted resonant frequency for the assembly, as seen in Table 4.4, and where the modeled response peak occurred, as seen in Fig. 4.11. A feature that did match the modeled response was the decrease in response starting at 1500 Hz. Similar to the previously discussed drivers, this decrease did not follow through the entire bandwidth above 3000 Hz as yet again there was a peak in response at 14 kHz. Of all driver-enclosure assemblies measured, this assembly produced a response that was the least flat in the operating bandwidth of 500 Hz to 3000 Hz, bringing into question the quality of the driver and the reliability of the enclosure assembly. Additional impedance testing could have been done to determine the actual acoustic stiffness applied to the system by using the methods outlined in section 4.2 to determine the total stiffness of the system and then using the previously calculated free-air stiffness to separate the driver stiffness from the acoustical stiffness. The measured acoustical stiffness could then be used to find the actual volume of the enclosure, which would either agree or disagree with the estimated volume in Table 2.3.

All measurements showed an increase in response below 80 Hz which was most likely due to noise and a lack of absorption in the measurement space. There was a noticeable tone seen in all responses at around 60 Hz which may have been electrical noise. The W1-2121S assembly matched the modeled response the least. Each of the other assemblies, which had flatter responses, had one peak within the operating bandwidth; the FRS 5X-8 and TEBM36S12-8/A assemblies had peaks closer to 500 Hz and the W2-2243S assembly had a peak at 3000 Hz. These peaks did not exceed 5 dB. Of these three drivers, the W2-2243S and the TEBM36S12-8/A assemblies maintained the flattest response within the operating bandwidth aside from their respective peaks, which suggested that they would be able to reproduce a low-level signal without drastically changing the levels of frequency production.

## 5.2 Measuring Nonlinear Behavior

Up to this point, the parameters measured and discussed in Chapters 3 and 4 have been assumed to be linear. This is unfortunately not true but allowed the drivers to be modeled easily. Viewing the nonlinear behavior of these parameters and the measured distortions was valuable for understanding how accurately the driver could produce whatever signal is given to it.

### 5.2.1 Loudspeaker Distortion

The consideration of the distortion a given driver adds to the excitation signal is an important metric for finding or designing drivers for a given application. Distortion can come from several nonlinear sources. Diagnosing the causes of these distortions can determine which nonlinear characteristics to focus on when choosing or designing a driver for a particular application.

The three main parameters that have a large impact on distortion are the force factor  $Bl$ , the suspension stiffness  $k_s$  which is the inverse of the mechanical compliance  $C_m$ , and the voice coil inductance  $L_e$ . The behavior of  $Bl$  and  $k_s$  depend on the displacement of the voice coil,  $x$ , and by extension the cone, whereas the nonlinearities in  $L_e$  depend on both the voice coil displacement  $x$  and the current  $i$  [17]. Their nonlinear behavior can make up a significant amount of observable distortion at large amplitude signals [16]. The  $Bl(x)$  and  $k_s(x)$  values can also show asymmetry in their nonlinear behavior, producing different parameter values at the same positive and negative displacements, which can

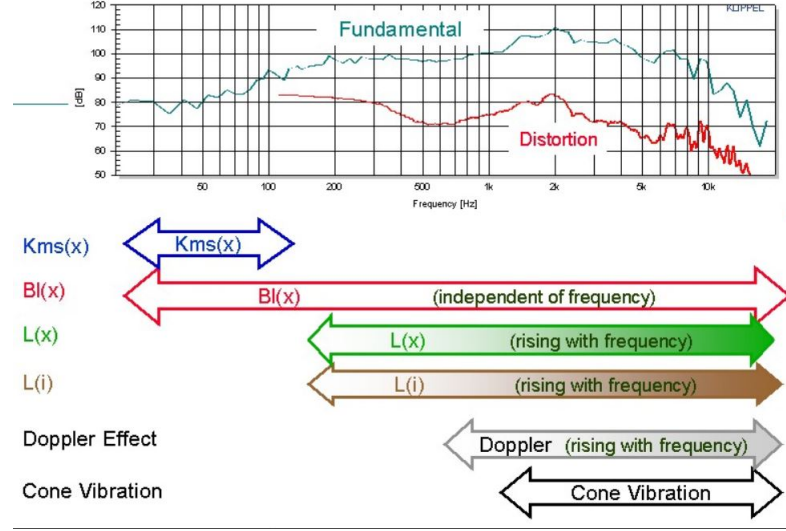


**Figure 5.6.** A general example of what causes of distortion affect what ranges of frequency [9]. In this general example, the stiffness as a function of displacement, labeled  $K_{ms}(x)$ , affected the region below the resonant frequency. The distortion caused by the force factor, labeled  $Bl(x)$ , affected a more broadband range. Nonlinear induction with varying displacement, labeled  $L(x)$ , and with varying current, labeled  $L(i)$ , began to cause distortions above the resonant frequency and increased higher into the frequency spectrum. The Doppler Effect and cone vibrations showed significant distortions in a much higher portion of the frequency spectrum. Image taken from <https://www.klippel.de/know-how/measurements/nonlinear-distortion/multi-tone-distortion.html>

cause distortion as well; however, if the asymmetry for a given voice coil displacement is less than 5%, distortions due to asymmetry can be neglected [17]. Other causes of distortion include the Doppler Effect, causing phase modulation as the diaphragm moves closer or further away from an observation point, and cone vibrations due to nonlinear material properties of the cone [17]. Keeping these nonlinear characteristics at a minimum by only using small amplitude signals would be one solution to this problem; however, the signals that would be passed through these drivers in application could exceed what is to be considered small amplitude.

The distortions produced by nonlinearities in  $Bl(x)$ ,  $k_s(x)$ ,  $L_e(x)$ , and  $L_e(i)$  contribute differently to overall distortion. In general, the surround and spider stiffness nonlinearities cause distortions closer to the driver's resonant frequency as  $k_s(x)$  nonlinearities require large displacements to generate distortion [17]. The force factor generates distortions across a large frequency band, producing displacement-dependent harmonic distortion at low frequencies and frequency-independent distortion well above the resonant frequency [17]. The voice coil inductance displacement-dependent distortions are minimal compared



to other distortion produced by the driver and the current-dependent distortion is more apparent at frequencies well above resonance [17]. The distortion created by the Doppler Effect and cone vibrations also affect a higher frequency range, with the Doppler Effect generating more distortions with increasing frequency [17]. This can be seen as a general example in Fig. 5.6, found on the Klippel audio system diagnostics product web page that briefly explains multi-tone distortion [9]. Because of the operating range for this application, 500 Hz to 3000 Hz, the frequency range affected by distortions due to the Doppler Effect and cone vibration, and the lower distortion level contributions by both  $L_e(x)$  and  $L_e(i)$  nonlinearities, only the  $Bl(x)$  and  $k_s(x)$  nonlinearities were considered in the nonlinear parameter results.

### 5.2.2 The Klippel Analyzer 3 System

One of the prominent investigators, modelers, and designers of speakers and audio systems, Wolfgang Klippel [17] [16] [18], has designed the Klippel Analyzer 3 system, a measurement and analysis system aimed at defining nonlinear behaviors of a driver. This apparatus includes, among other things, an amplifier, an interface, and a Keyence LK-H052 laser displacement sensor [31] that measures the displacement of the driver cone. The voltage and current at the driver terminals can be measured as well. This system can also be outfitted with a microphone, but this feature was not used in these measurements. [32]

The driver was mounted in free-air in the supplied driver grip to face the laser head so that the laser was set in the center of the driver cone. The distance from the laser head to the driver head was calibrated; it was recommended that this distance be around 2 cm. The driver and laser head were connected to the amplifier and interface, which passed information to and from a computer. This hardware was coupled with computer software developed by Klippel called dB-Lab [33] that completed the measurement analysis. There were two tests performed for each driver: a Linear Parameter Measurement, or LPM [34], and a Large Signal Identification, referred to as LSI3 [35].

The LPM test produced parameters similar to those seen in Chapter 4, calculating the characteristics of the measured driver and considering them to be linear. The LPM test software derived these values as if they modeled the electrical and mechanical domains of the driver; however, there were three options for modeling the electrical inductance of the voice coil built into the software. Each option attempted to model Eddy current and magnetic losses in the electrical inductance. The option used for these tests was the LR-2 Model. The most similar to the electrical domain presented in Fig. 3.7, this model

used the already-established inductance  $L_e$  but placed in series with  $L_e$  was an additional resistance and inductance that were parallel with each other. This model proved to satisfactorily match the measured impedance of the LPM test as the bandwidth for these tests did not extend high enough into the frequency domain for misrepresentation to occur. Other models offered for modeling the inductance impedance were the Leach Model [36] and the Wright Model [37].

The LPM test also measured diaphragm displacement, impedance, current, and voltage. The excitation signal used was a summation of several specific frequencies, forming a multi-tone excitation signal [9], rather than a sine sweep or a random noise-like signal. When the LPM test was initiated, the KA3 system first measured the noise floor before applying the multi-tone excitation signal. This would go on to ensure that the user-specified excitation amplitude was large enough to produce data above the noise floor by allowing the user to compare the measured noise floor to the produced data rather than trying to decouple them in post-processing. Separating the produced tones, generated distortion, and noise floor gave the user the opportunity to optimize the excitation level so that a small signal linear measurement could be made without being so small that the data would be covered up by the noise floor. By using specific frequencies rather than a harmonically saturated signal the distortion generated could be observed as harmonics that were not apart of the test signal or the noise floor [17]. Using the multi-tone excitation signal to observe distortion also had the benefit of being more like the expected broadband signal that would be used in the noise canceling application. By contrast, using a two tone signal to view distortions, which is another method of observing generated distortions [18] [17], may not have represented the distortion fully produced by the tested driver due to its lack of broadband content. This multi-tone distortion test result within the LPM test was important when investigating distortions; however, this test used a user-specified excitation level, so this distortion could change as the excitation level increased or decreased.

The LSI3 test used a carefully constructed noise-like excitation signal at varying amplitudes to measure the nonlinear behavior of a driver. The test began with a small signal to determine linear parameters. The signal was then increased until one of the internally set protection criteria was met. The protection criteria ensured that the driver would not be damaged during the test. These criteria included the estimated temperature change of the voice coil, the ratio between the  $Bl$  at a displacement of 0 mm and the  $Bl$  at maximum displacement (expressed as a percent), the ratio between the  $C_m$  at a displacement of 0 mm and the  $C_m$  at maximum displacement (expressed as a percent),

and the maximum electrical power provided to the driver. The default parameters, and the parameters used for these tests, were set to be a 60 K change in estimated voice coil temperature, a 50%  $Bl$  ratio, a 50%  $k_s$  ratio, and 50 W of power provided to the driver terminals. If any of the protection criteria were met, the signal would stop increasing and the large signal measurements would be taken. The LSI3 test depicted the relationship between the cone displacement and  $Bl$ ,  $k_s$ , as well as the displacement and current dependency of  $L_e$ . The  $Bl(x)$ ,  $k_s(x)$  as well as  $C_m(x)$ , and  $L_e(x)$  nonlinear curves were also represented as a fourth-order power series expansion; the  $L_e(i)$  nonlinearity was represented as a second-order power series expansion.

### 5.2.3 KA3 Measurement Methods

While the KA3 system standardized most of the measurements for the user, there were some measurement parameters that were set for each measurement. These measurements were not conducted in a sound controlled space. Because the drive cone displacement was being measured and not the pressure produced by the driver, the resulting measured displacement was negligibly affected by the reverberated pressure from the space's room acoustic properties. If the microphone option was utilized for these tests, they most certainly would have needed to be conducted in a sound controlled space due to potential reverberations and environmental noise being recorded by the microphone. Testing one driver at a time, drivers were mounted in free-air in the vice included with the system. The drivers were oriented to project horizontally as if mounted in a wall. The vice was attached to a heavy metal base which also mounted the laser displacement sensor. The laser head was positioned to point perpendicular to the driver cone's surface with the laser pointed in the best approximated center of the driver cone. This proved difficult for the FRS 5X-8 driver due to its pronounced dust cap. The laser head was set at the recommended distance away from the center of each driver.

Both the LPM and LSI3 tests required the cone area, so the same cone areas,  $A_{cone}$ , listed in Table 4.2 were used. The multi-tone excitation signal in the LPM test was set to have 30 tones per octave above 20 Hz. The LPM test also requested that the user specified the excitation voltage, which was varied over several tests to find an appropriate signal-to-noise ratio. It was found that an excitation voltage of 0.07 Volts was sufficient to minimize distortions but stay above the measurement noise floor which produced small signal parameter results. Another LPM test was conducted that used an excitation voltage of 0.5 Volts but the drivers were connected to the system with a 50.0  $\Omega$  resistor in series to mirror the impedance measurements done in section 4.1 that used a 46.7  $\Omega$

resistor. The LSI3 test provided its own excitation level and signal.

#### 5.2.4 Comparing Measured Linear Parameters

The LPM test produced linear parameters comparable to the test conducted and discussed in section 4.1. The LPM test using an excitation level of 0.07 V served as the known small signal amplitude test while the LPM test using an excitation signal of 0.5 V with a 50.0  $\Omega$  resistor in series with the driver served as a comparison between the LPM multi-tone measurement method and the previously conducted impedance test method. The results of the impedance test were predicted to be similar to both the 0.5 V with 50  $\Omega$  resistor test and the 0.07 V test due to the expectation that the impedance test was conducted using a small signal and that the LPM measurement method would produce results similar to those using the impedance method.

**Table 5.1.** Measured Parameters for the W1-2121S Driver

Parameter	Test		
	<i>Impedance</i>	<i>LPM - 0.5 V with 50 <math>\Omega</math> Resistor</i>	<i>LPM - 0.07 V</i>
$f_0$	140.0 Hz	153.0 Hz	135.0 Hz
$R_e$	3.6 $\Omega$	3.32 $\Omega$	3.71 $\Omega$
$L_e$	0.150 mH	0.127 mH	0.136 mH
$Bl$	3.4947 Tm	2.823 Tm	2.862 Tm
$R_m$	0.8344 kg/s	1.624 kg/s	1.114 kg/s
$C_m$	0.4713 mm/N	0.549 mm/N	0.764 mm/N
$m_m$	3.0320 g	1.970 g	1.819 g

The W1-2121S driver had 9 of the 14 measured LPM parameters above 10% different than the impedance test parameters, the most inconsistent results, while still maintaining resonant frequencies that were less than 10% different between the two test methods. This difference could have been due to the lack of data points used in the line fit applied in Eq. (4.4). It was worth remembering that the W1-2121S linear curve fit in Fig. 4.3 had the lowest R-squared value out of all the drivers. With the similarities in resonant frequency, it was confirmed that the impedance test was conducted as a small signal test, satisfying that requirement for assuming linear parameters. The difference between measured parameters suggested that there was a significant difference between measurement methods; however, the conclusion of similar resonant frequencies showed

that the measurement methods achieved similar ending results using their respective measurement and analysis processes. Again, with the potential for error from the impedance test, these differences could not confirm the validity of the impedance test or the LPM mulit-tone test.

**Table 5.2.** Measured Parameters for the W2-2243S Driver

Parameter	Test		
	<i>Impedance</i>	<i>LPM - 0.5 V with 50 <math>\Omega</math> Resistor</i>	<i>LPM - 0.07 V</i>
$f_0$	236.4 Hz	220.6 Hz	222.3 Hz
$R_e$	3.7 $\Omega$	3.12 $\Omega$	3.86 $\Omega$
$L_e$	0.080 mH	0.060 mH	0.070 mH
$Bl$	3.7619 Tm	3.932 Tm	4.100 Tm
$R_m$	0.3409 kg/s	0.324 kg/s	0.359 kg/s
$C_m$	0.2946 mm/N	0.310 mm/N	0.283 mm/N
$m_m$	1.5866 g	1.678 g	1.808 g

The measured parameters for the W2-2243S driver closely matched those calculated in the impedance measurement. Quite opposite to the findings of the W1-2121S driver measurements, 10 out of the 14 parameters measured by the LPM tests were within 10% of the parameters measured in the impedance test; only  $R_e$  and  $L_e$  from the 0.5 V test and  $L_e$  and  $m_m$  from the 0.07 V test were more than 10% different than their impedance test counterparts. An interesting point can be made that the W2-2243S impedance test used the most added mass measurements of all the drivers tested and had the largest R-squared value for its line fit as seen in Fig. 4.3, suggesting that the impedance test and the LPM multi-tone method could produce similar results given an impedance test with higher certainties.

The FRS 5X-8 linear parameter results supported the suggestion made by the W2-2243S parameter measurements that the LPM and impedance test results could be similar with a high accuracy impedance test analysis. Showing the second-highest R-squared value, the FRS 5X-8 LPM test results were less than 10% different of the impedance test results for 9 out of the 14 parameters, including both of the LPM test's  $L_e$  parameter. Along with the  $L_e$  parameters being significantly different, the  $R_m$  parameters were also significantly different. This would most likely reflect a difference in the mechanical quality factor,  $Q_{ms}$ , forcing the resonant frequency peak to be wider rather than sharper.

The linear parameters for the TEBM36S12-8/A driver were also very close to those

**Table 5.3.** Measured Parameters for the FRS 5X-8 Driver

Parameter	Test		
	<i>Impedance</i>	<i>LPM - 0.5 V with 50 <math>\Omega</math> Resistor</i>	<i>LPM - 0.07 V</i>
$f_0$	249.4 Hz	249.5 Hz	255.9 Hz
$R_e$	7.6 $\Omega$	6.55 $\Omega$	7.56 $\Omega$
$L_e$	0.100 mH	0.073 mH	0.081 mH
$Bl$	2.3655 Tm	2.339 Tm	2.301 Tm
$R_m$	0.2185 kg/s	0.159 kg/s	0.152 kg/s
$C_m$	0.6213 mm/N	0.629 mm/N	0.599 mm/N
$m_m$	0.6871 g	0.646 g	0.646 g

**Table 5.4.** Measured Parameters for the TEBM36S12-8/A Driver

Parameter	Test		
	<i>Impedance</i>	<i>LPM - 0.5 V with 50 <math>\Omega</math> Resistor</i>	<i>LPM - 0.07 V</i>
$f_0$	162.6 Hz	164.9 Hz	165.8 Hz
$R_e$	7.6 $\Omega$	7.12 $\Omega$	7.79 $\Omega$
$L_e$	0.127 mH	0.084 mH	0.095 mH
$Bl$	4.0627 Tm	3.781 Tm	3.888 Tm
$R_m$	0.6004 kg/s	0.465 kg/s	0.477 kg/s
$C_m$	0.4677 mm/N	0.503 mm/N	0.469 mm/N
$m_m$	2.1236 g	1.854 g	1.965 g

measured in the impedance test. Just as with the FRS 5X-8 driver, 9 out of the 14 LPM-derived parameters were less than 10% different than the impedance test parameters. Again, both  $L_e$  and  $R_m$  parameters were among the parameters that were more than 10% different. With an linear curve fit R-squared value closer to the R-squared values of the W2-2243S and FRS 5X-8 linear curve fits, this driver continued the trend that suggested that the LPM multi-tone results were more likely to match the results from a more certain impedance test. This driver, like the others, confirmed that the impedance test was done as a small signal test and that the multi-tone method could produce results that were similar to the previously conducted linear measurements.

There were a few trends that were consistent throughout the LPM tests. The  $R_e$  values

derived from the 0.5 V was always lower than the  $R_e$  values measured by the impedance test and the 0.07 V LPM tests; however, this difference was not always more than 10% from the impedance test. This could suggest that the added resistance used in the 0.5 V measurements was not as well defined as it should have been. While the resistance was measured using a digital multimeter similar to the one used in section 4.1, the multimeter measurement could have been inaccurate. Another trend that was observed was that the  $L_e$  parameters derived from the LPM tests were almost always more than 10% different than those determined during the impedance test. This was most likely due to using a rough guess-and-check method to determine the  $L_e$  values during the impedance test analysis rather than fully modeling the inductance of the voice coil using the LR-2 Method. With the exception of the W1-2121S LPM results, cohesiveness was shown between the measurement method outlined in sections 4.1 and 4.2 and the LPM multi-tone signal method. Every driver except for the W1-2121S had a high R-squared value when creating the linear curve fits which was a strong candidate for the cause of the W1-2121S linear parameter discrepancies. For the other drivers, the similar results confirmed the validity of both the test method from section 4.1 and the LPM multi-tone method and confirmed that the impedance test was indeed run using a small signal.

### 5.2.5 Measured Multi-Tone Distortion

While the LPM tests used a small signal, distortion was still generated by each driver. The distortions measured by the LPM multi-tone signal showed the displacement distortions produced by the drivers using the low-amplitude signal of 0.07 Volts. Included in these results was the noise floor. It was important to note that while the distortions of some drivers may appeared to be nonexistent at higher frequencies, produced distortion could have been hidden in the noise floor and would more likely appear using a larger amplitude test signal. The average distortion was calculated as the average distortion within the relevant third-octave band.

Looking at the multi-tone displacement spectra in Figs. 5.7–5.10, the distortion relative to the produced signal-tones can be seen. The TEBM36S12-8/A driver had the smallest signal-tone response but had the lowest distortion response as well. As seen in Fig. 5.10, the average distortion seemed to slow its decrease rate at around 1200 Hz, but this was close to the noise floor. Ultimately, the average distortion met the peaks of the noise floor at 2000 Hz. The W1-2121S driver had the second-largest diaphragm displacement response. This was coupled with a distortion response that started slightly higher than the TEBM36S12-8/A, but decreased steadily with increasing frequency. The

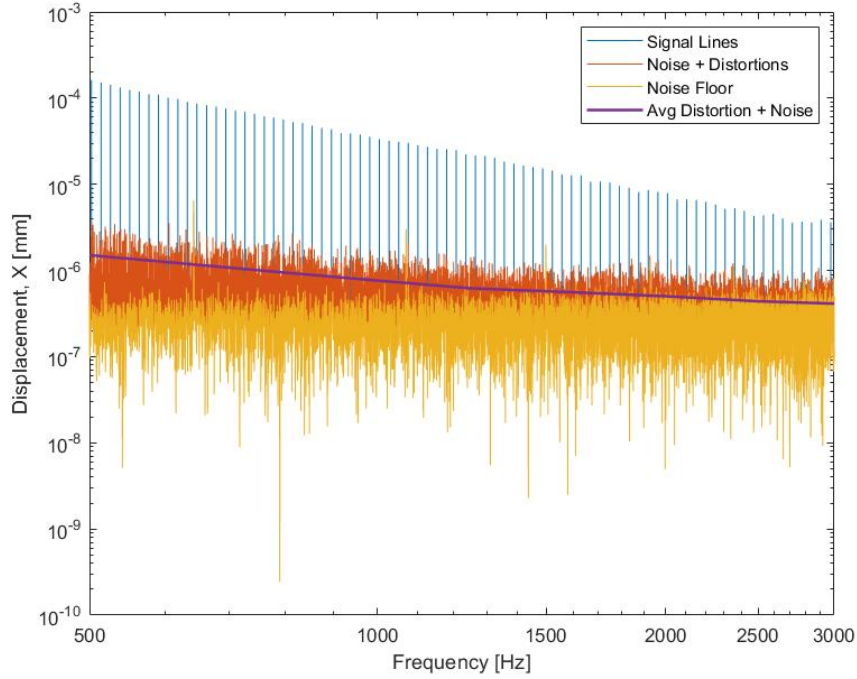


**Figure 5.7.** The displacement spectrum for the W1-2121S driver. The signal tones of the multi-tone response (blue) were separated from the generated distortion (red) and the measurement noise floor (yellow). The average distortion (purple) was calculated in third-octave bands.

average distortion for this driver met the noise floor at around 2250 Hz. The FRS 5X-8 and the W2-2243S drivers, whose responses are shown in Figs. 5.9 and 5.8 respectively, had more signal-tone displacement near 500 Hz than the other two drivers, but the FRS 5X-8 driver showed more distortion in that area of the spectrum. Moving higher in the spectrum, the FRS 5X-8 driver distortion decreased but not nearly as fast as the signal-tone displacement. By contrast, the W2-2243S driver had a stronger signal-tone displacement at higher frequencies while decreasing the amount of distortion at a similar rate. Consequentially, the W2-2243S average distortion met the noise floor at around 2000 Hz, whereas the FRS 5X-8 average distortion met the noise floor at around 3000 Hz. Comparing all drivers, the W2-2243S driver produced the least amount of distortion relative to the signal-tone displacement with the FRS 5X-8 driver producing the most, especially at higher frequencies. The TEBM36S12-8/A and W1-2121S drivers produced similar distortion compared to their signal-tone displacements. These results reflected the small signal distortions produced by each driver, but attempting to predict the large signal distortions based on these results may not fully reflect nonlinear behavior.



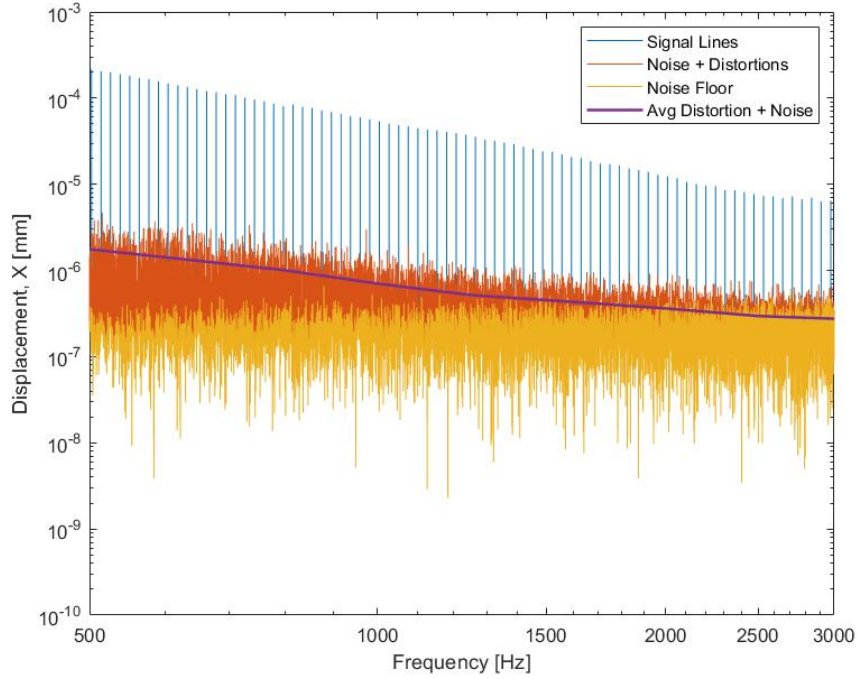


**Figure 5.8.** The displacement spectrum for the W2-2243S driver. The signal tones of the multi-tone response (blue) were separated from the generated distortion (red) and the measurement noise floor (yellow). The average distortion (purple) was calculated in third-octave bands.

### 5.2.6 Measured Parameter Nonlinearities

Because the multi-tone test signal was small in amplitude, the distortion behaviors were not necessarily the same at higher-amplitude displacements. These behaviors were inferred by the  $k_s(x)$  and  $Bl(x)$  trends. As stated earlier, distortions can be caused by the nonlinear behavior of these parameters as well as any asymmetry they have as the voice coil moves in and out.

There were two metrics used to determine the extent of parameter nonlinearities. The first metric was the percentage of the measured excursion distance that a nonlinear parameter stayed within 5% of the parameter value at 0 mm of displacement. While 5% was chosen as the metric's acceptable displacement percentage, this metric would be able to compare the capabilities of each driver no matter what the choice in percent was as long as each driver's parameter in question eventually changed more than the chosen percentage. The second metric was the percentage of measured excursion distance that the driver parameters showed less than 5% asymmetry in their nonlinear parameters. This was done by calculating the percent difference between the parameter value at a

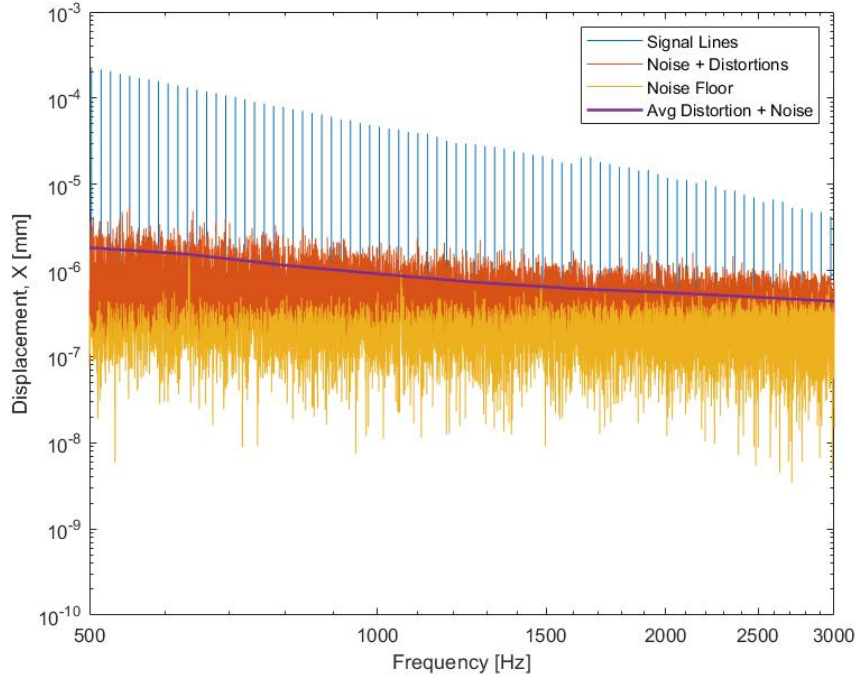


**Figure 5.9.** The displacement spectrum for the FRS 5X-8 driver. The signal tones of the multi-tone response (blue) were separated from the generated distortion (red) and the measurement noise floor (yellow). The average distortion (purple) was calculated in third-octave bands.

positive and negative excursion distance of the same magnitude. This followed suit with Klippel’s assessment of asymmetry, claiming that asymmetry of low-percent difference can be neglected as a major source of total nonlinearities [17]. With both metrics, the higher the percentage of measured excursion distance that the parameter met the metric requirements, the less distortion that driver would be expected to produce at higher amplitudes.

The  $k_s(x)$  nonlinearities can be seen in Fig. 5.11 showing the stiffness as a function of displacement. This plot clearly showed that each driver had nonlinear  $k_s(x)$  values in two ways. First, the stiffness changed as a function of displacement producing a non-constant value, represented as a more cupped  $k_s(x)$  trace rather than a flatter line shape. These changes were seen in varying degrees where the TEBM36S12-8/A driver showed rapid change over a shorter displacement than the FRS 5X-8 driver. Second, the changes in stiffness were not always symmetric about the resting position of the voice coils at  $x = 0$  mm. This was emphasized by the dashed lines in Fig. 5.11, which are a mirror image of their solid-traced counterparts to depict asymmetry as a qualitative observation. As discussed before, this asymmetry can cause distortions at higher amplitudes [18]. Using

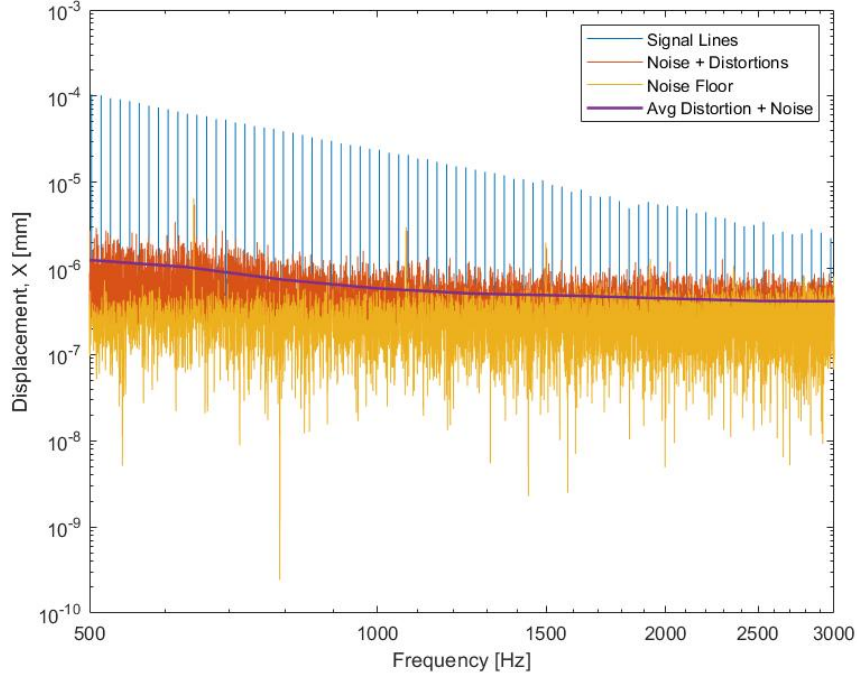


**Figure 5.10.** The displacement spectrum for the TEBM36S12-8/A driver. The signal tones of the multi-tone response (blue) were separated from the generated distortion (red) and the measurement noise floor (yellow). The average distortion (purple) was calculated in third-octave bands.

the data presented in Fig. 5.11, the Acceptable Displacement Percentage, abbreviated henceforth as ADP, was found for both the change in  $k_s$  relative to the  $k_s(0)$  value and the asymmetry of  $k_s$ . This two-part metric quantified both the change in stiffness compared to the zero-displacement value and the asymmetry of the changing stiffness.

Starting with the ADP of the change in  $k_s$ , the percent change was found for each driver's  $k_s(x)$  value using the following equation where  $PC(x)$  is the percent change at displacement  $x$ ,

$$PC(x) = \frac{k_s(x) - k_s(0)}{k_s(0)} \times 100\%. \quad (5.3)$$

The percent change as a function of displacement for each driver was compiled in Fig. 5.12, where the excursion distance that the change in  $k_s(x)$  was less than  $\pm 5\%$  of the zero-displacement value could be more easily observed. For all drivers, it can be seen that the percent change goes above  $5\%$  in at least two points during the displacement of the voice coil. Using the lesser of the  $5\%$  change displacement magnitudes ensured that the displacement value considered would produce a  $k_s(x)$  value that experienced less than

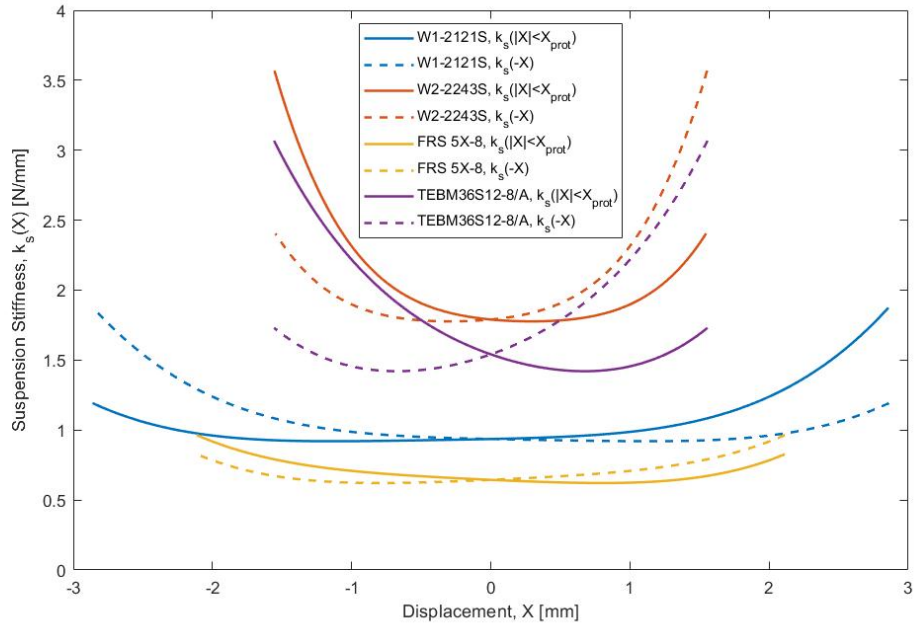


**Figure 5.11.** The driver stiffness,  $k_s(x)$ , characteristics for all drivers as a function of displacement. The dashed traces are each solid trace reversed to visually emphasize asymmetry. Positive displacement ( $+x$ ) signifies the voice coil pushing outwards, moving away from the rear pole plate; whereas, negative displacement ( $-x$ ) refers to the voice coil moving inward towards the rear pole plate.

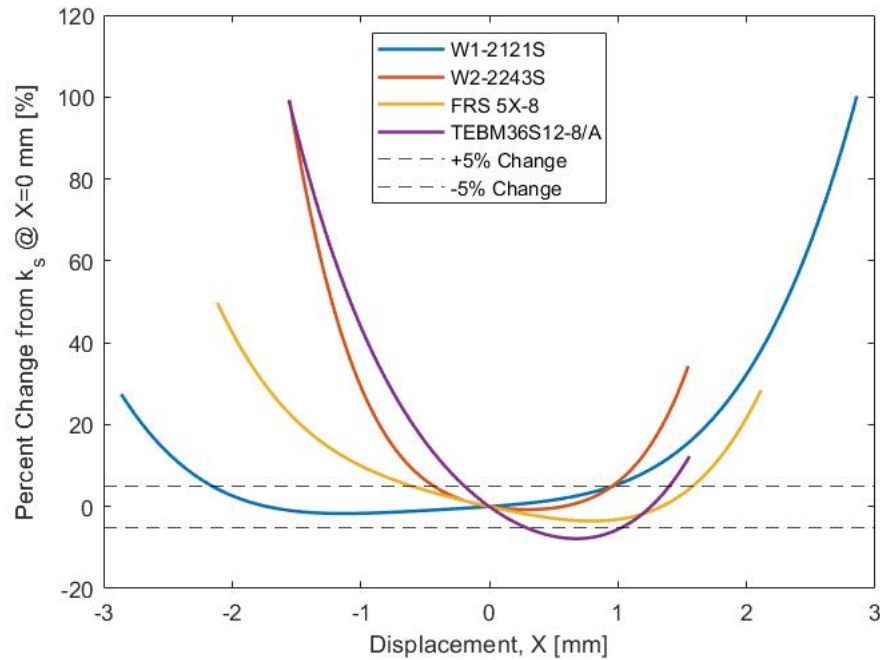


**Figure 5.12.** The percent change from  $k_s(0)$  to  $k_s(x)$  for all drivers.

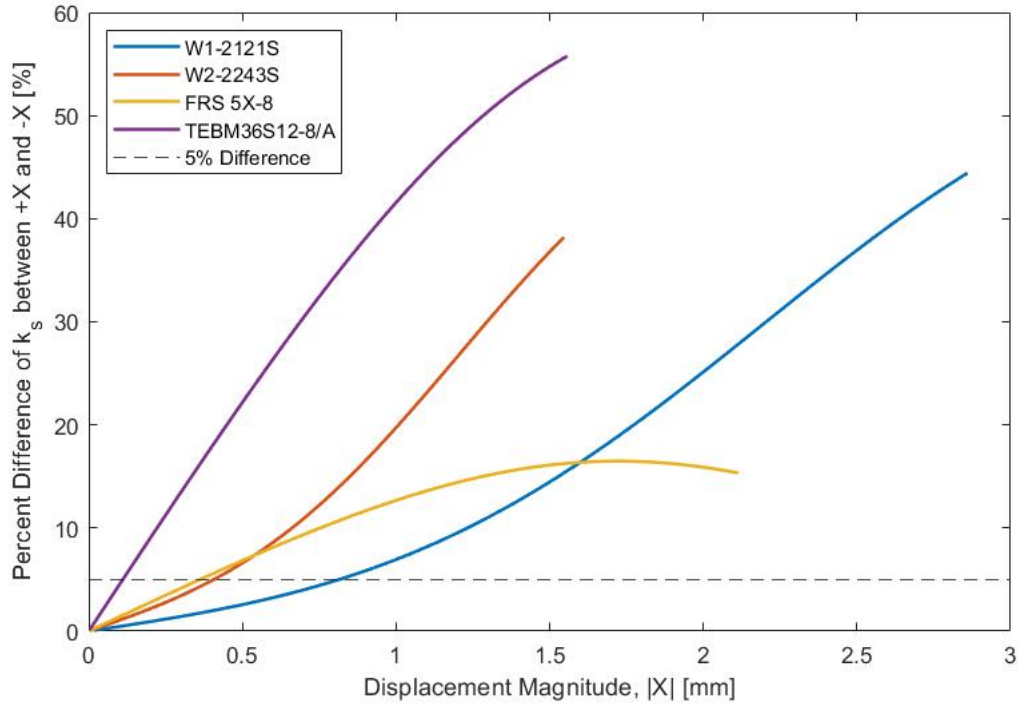


**Figure 5.13.** The percent difference between  $k_s(-|x|)$  and  $k_s(|x|)$  for all drivers. This represents the asymmetry of the  $k_s(x)$  curve in Fig. 5.11 where a larger percent difference represents more asymmetry for that displacement magnitude.

$\pm 5\%$  change from the resting value in both positive and negative displacement directions. For example, using Fig. 5.12 to determine displacement values of interest, the W1-2121S driver crossed above the 5% change boundary at  $x = -2.155$  mm and at  $x = 0.960$  mm; however, using the larger displacement magnitude of  $|x| = 2.155$  mm produced a 5% change in  $k_s$  as the voice coil reached  $x = -2.155$  mm but produced a 38.3% change in  $k_s$  as the voice coil reached  $x = 2.155$  mm, no longer satisfying the metric. Using the  $|x| = 0.960$  mm displacement magnitude produced a 5% change in  $k_s$  at  $x = 0.960$  mm and a  $-1.6\%$  change at  $x = -0.960$  mm, which was still within the  $\pm 5\%$  change metric. After the acceptable displacement magnitude was determined, it was calculated as a percent of the maximum displacement, solving for the ADP. These results can be seen in Table 5.5 where they are referred to as the Linear ADP of  $k_s(x)$ . The higher the reported percent value, the more of the driver's displacement kept the  $k_s(x)$  value change within 5%, producing a flatter curve relative to the maximum displacement.

The asymmetry was found using the percent difference between values of  $k_s(|x|)$  and  $k_s(-|x|)$ . This was represented by the following equation,

$$\text{PD}(|x|) = 2 \times \frac{|k_s(|x|) - k_s(-|x|)|}{k_s(|x|) + k_s(-|x|)} \times 100\%. \quad (5.4)$$

where  $\text{PD}(|x|)$  is the percent difference at a displacement magnitude  $|x|$ . This equation also constituted a graphed representation, seen in Fig. 5.13, that easily displays the displacement at which the percent difference of  $k_s$  values at a displacement magnitude was less than 5%. This served to represent the asymmetry of the  $k_s(x)$  curve. Using the same method as previously discussed to find the acceptable displacement magnitude, the percentage of the maximum displacement that the acceptable displacement represented was calculated. Again, these results can be seen in Table 5.5 as the Asymmetric  $k_s(|x|)$  ADP. Having a higher percentage meant that the  $k_s(x)$  curve experienced less than 5% asymmetry for a larger portion of the driver's displacement.

The W1-2121S driver had the best ADP for both metrics. This would presumably result in minimal distortions caused by the driver stiffness at higher drive levels. This was followed by the W2-2243S driver and the FRS 5X-8 driver. Because both drivers had nearly the same Linear  $k_s(x)$  ADP but significantly different Asymmetric  $k_s(|x|)$  ADP, the W2-2243S would be expected to produce less distortion from the  $k_s(x)$  nonlinear behavior rather than the FRS 5X-8 driver. Finally, the TEBM36S12-8/A driver produced the most nonlinear  $k_s(x)$  behavior.

The  $Bl(x)$  nonlinear behavior, which can be seen in Fig. 5.14, was evaluated using the same metric that was used for the  $k_s(x)$  nonlinear behavior. Again, this plot showed that the  $Bl(x)$  values were nonlinear in the same two ways as the  $k_s(x)$  values. Because of this, using the same two-part metric discussed above was deemed appropriate. Following the same calculation processes to determine the Linear and Asymmetric  $Bl(x)$  ADP but using the  $Bl(x)$  values instead, the  $Bl(x)$  nonlinearities were assessed in a quantitative fashion. The percent change shown in Fig. 5.15 showed each driver only crossing over the  $\pm 5\%$  boundary twice, similar to the results seen in Fig. 5.12 with the exception of the TEBM36S12-8/A driver. The asymmetry plot showed surprising results as the W1-2121S and the W2-2243S drivers showed less than 5% asymmetry throughout their entire displacement range. The FRS 5X-8 driver crossed the 5% asymmetry metric at two displacements. The lower of the two displacements was chosen in order to ensure that the asymmetry metric was satisfied as the voice coil moved through its oscillation completely. The Linear and Asymmetric  $Bl(x)$  ADP can be seen in Table 5.5.

The W2-2243S driver and W1-2121S driver performed the best. As stated earlier and as easily seen in Fig. 5.16, both showed less than 5% asymmetry throughout their entire

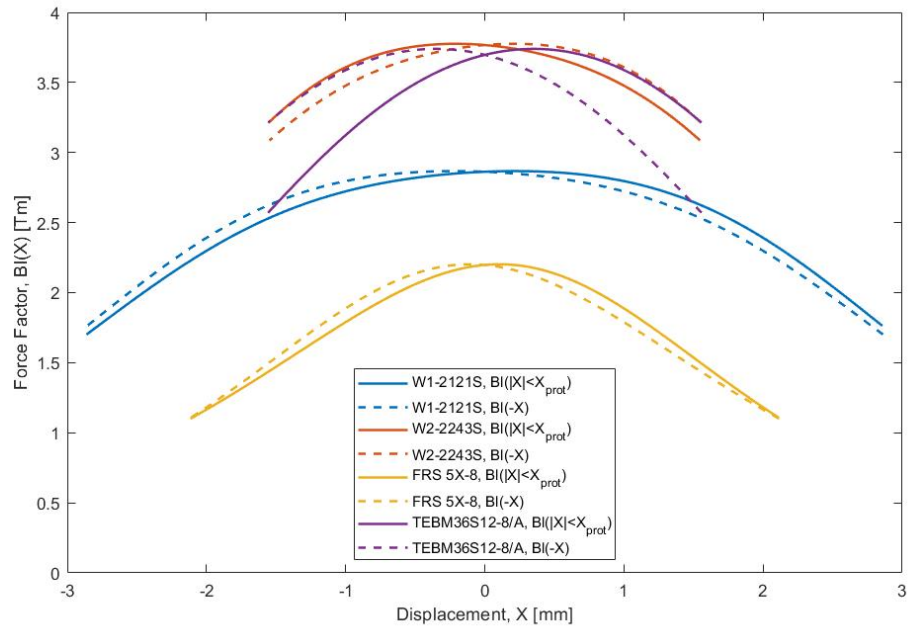


**Figure 5.14.** The force factor,  $Bl$ , characteristics for all drivers as a function of displacement. The dashed traces are each solid trace mirrored to emphasize asymmetry. Positive displacement ( $+x$ ) signifies the voice coil pushing outwards, moving away from the rear pole plate; whereas, negative displacement ( $-x$ ) refers to the voice coil moving inward towards the rear pole plate.

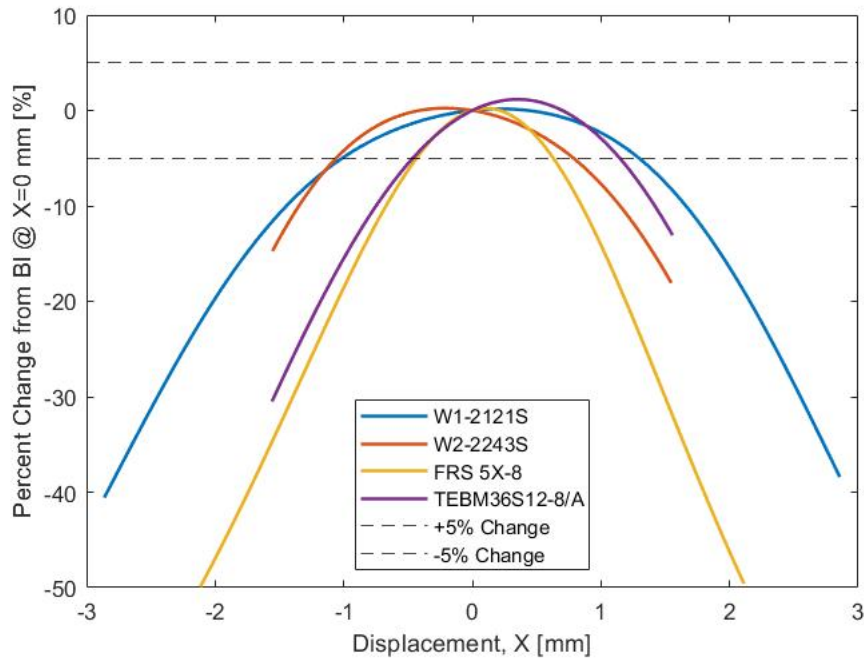


**Figure 5.15.** The percent change from  $Bl(0)$  to  $Bl(x)$  for all drivers.



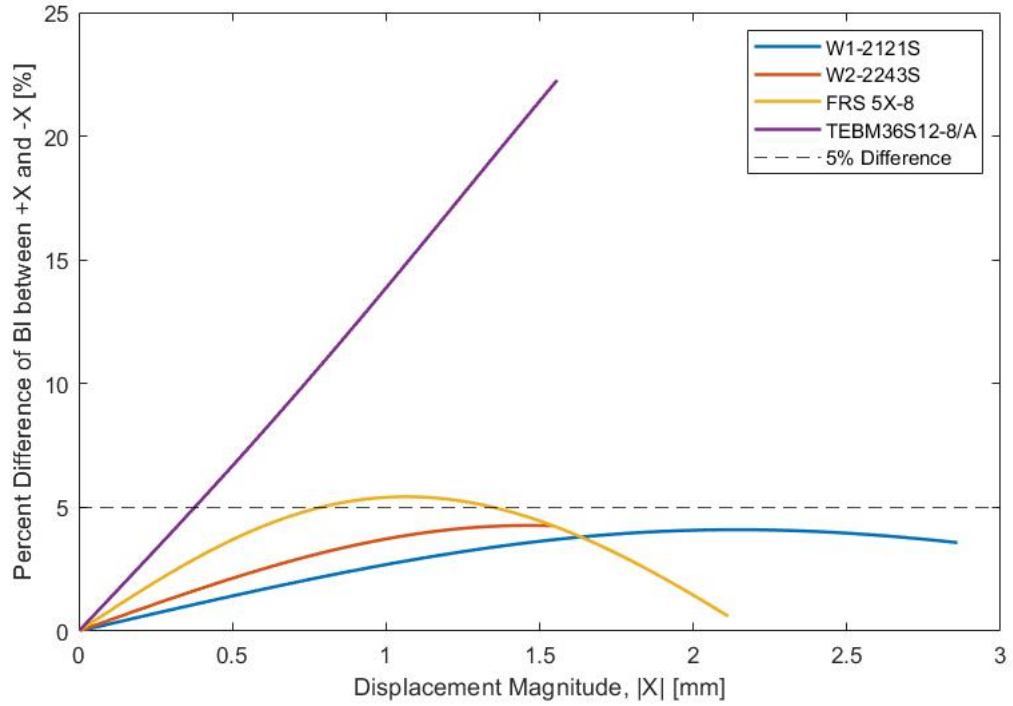


**Figure 5.16.** The percent difference between  $Bl(-|x|)$  and  $Bl(|x|)$  for all drivers. This represents the asymmetry of the  $Bl(x)$  curve in Fig. 5.14 where a larger percent difference represents more asymmetry for that displacement magnitude.

displacement. These drivers also had the highest Linear  $Bl(x)$  ADP with the W2-2243S driver having the highest and the W1-2121S having the second highest. The FRS 5X-8 driver, with a higher Asymmetric  $Bl(|x|)$  ADP than a Linear  $Bl(x)$  ADP, showed that its symmetry was compromised by its lack in constant  $Bl$ . The TEBM36S12-8/A driver performed in between the ADPs of the FRS 5X-8 driver. Determining a driver that had a more linear behavior between these two drivers would be difficult based solely on this metric.

**Table 5.5.** Acceptable Displacement Percentages

Model	Driver Model			
	<i>W1-2121S</i>	<i>W2-2243S</i>	<i>FRS 5X-8</i>	<i>TEBM36S12-8/A</i>
Linear $k_s(x)$ ADP	33.4%	27.9%	28.5%	12.4%
Asymmetric $k_s( x )$ ADP	28.3%	26.3%	17.1%	7.1%
Linear $Bl(x)$ ADP	35.2%	50.8%	20.5%	29.7%
Asymmetric $Bl( x )$ ADP	100%	100%	37.2%	24.2%



In general, the W2-2243S and W1-2121S drivers seemed to show the more acceptable nonlinear parameters. These drivers produced the best ADP values for both the  $k_s(x)$  and  $Bl(x)$  values. Following these drivers was the FRS 5X-8 driver and lastly the TEBM36S12-8/A driver. The TEBM36S12-8/A driver struggled with producing a linear and symmetric  $k_s(x)$  curve. Based on this metric, it was concluded that at higher amplitudes, the W1-2121S and W2-2243S drivers would produce the least amount of distortion due to their more acceptably linear and symmetric behavior over their displacement ranges. Due to the incredibly low performance of the  $k_s(x)$  behavior of the TEBM36S12-8/A driver, the FRS 5X-8 driver was presumed to produce less distortion at higher amplitudes, leaving the TEBM36S12-8/A driver to be the driver that would produce the most distortion.

While the mechanical stiffness of the drivers varied with voice coil displacement, the acoustical stiffness also varied with voice coil displacement. As the voice coil pulled the cone inward towards the magnet, the volume holding the trapped air would decrease increasing the stiffness provided by the enclosed air. The opposite result would happen as the voice coil pushed the cone outwards away from the magnet. Treating the enclosed air as an ideal gas with isentropic oscillations, the mechanical equivalent of the acoustical compliance can be written as

$$C_{ma} = \frac{V_{encl} A_{cone}^2}{\gamma P_{air}} \quad (5.5)$$

where  $\gamma$  is the specific heat ratio and  $P_{air}$  is the pressure of the air trapped in the enclosure. The volume of the enclosure was again taken from Table 2.3 and was modified to reflect the cone moving inwards and outwards accordingly. Again, assuming that the air is an ideal gas, the pressure of the enclosed air would change with the volume according to the Ideal Gas Law. The mechanical compliance,  $C_m$ , and the mechanical equivalent of the acoustical compliance,  $C_{ma}$ , were examined as a series combination of capacitive elements. The percent change was then found between the total compliance, represented in the mechanical domain, as the cone was at rest and when the cone was at its maximum inward and outward displacements during the LSI3 test.

While the total compliance of each driver-enclosure assembly was expected to vary less than 10%, the W1-2121S and TEBM36S12-8/A driver-enclosure assemblies' change in compliance showed that the smaller enclosure volumes would have been impacted more by the cone displacement, as these driver-enclosure assemblies had the highest expected changes in total compliance. With this more drastic change in compliance, these driver-enclosure assemblies could add more nonlinearities to the stiffness of their systems compared to the W2-2243S and FRS 5X-8 driver-enclosure assemblies.

**Table 5.6.** Expected Percent Change of Total Driver-Enclosure Compliance

<b>Model</b>	<b>Driver Model</b>			
	<i>W1-2121S</i>	<i>W2-2243S</i>	<i>FRS 5X-8</i>	<i>TEBM36S12-8/A</i>
Compliance Change with Inward Displacement	−9.59%	−2.86%	−3.77%	−7.24%
Compliance Change with Outward Displacement	9.20%	2.79%	3.71%	7.26%

# Chapter 6 |

## Conclusion

With simulation, testing, and analysis completed, the drivers were understood beyond their specifications provided by their manufacturers. The tests gave an in-depth description of how the drivers behaved while they were both inside and outside of their designed enclosures. But with analysis concluded, the results must be considered within the scope of the original application of active noise control.

As stated in Chapter 1, these drivers were considered for the application of canceling noise passing into a room through a window with using operating bandwidth of 500 Hz to 3000 Hz. Because the drivers were to be used around a window, the enclosures for the drivers were to be as small as possible for use around the window frame. The frequency response of the driver-enclosure assemblies needed to maintain a flat frequency response throughout the operating range. In order to accurately produce the noise canceling signal, the drivers needed to generate as little distortion as possible.

### 6.1 Choosing The Best Driver-Enclosure Assembly

Using the results gathered, the assemblies were compared in the light of the original application requirements. While the requirement of a smaller driver-enclosure size was necessary for the application, this was already accounted for by initially choosing drivers to test that had an appropriate diameter and creating the smallest cuboid enclosures that could fit the drivers. This left the driver and assembly behavior as the determining factor for which assembly was best suited for the ANC application.

The Tang Band W1-2121S driver was predicted to have a somewhat flat response between the operating range limits while in it's enclosure. This was not realized in the driver-enclosure assembly's frequency response measurement, potentially due to an error in the driver or the assembly construction that added stiffness to the assembly or driver.

This driver showed a moderate amount of distortion in the free-air multi-tone results but showed some of the most promising nonlinear  $k_s(x)$  and  $Bl(x)$  Acceptable Displacement Percentage results. This should help limit distortion as the excitation signal amplitude increases.

The modeled frequency response showed that the Tang Band W2-2243S driver-enclosure assembly would produce a flat frequency response within the operating frequency range. This was very nearly observed in the frequency response measured; the measured response was relatively flat except for an increase in response towards the upper limit of the operating bandwidth. The distortion measured in the free-air multi-tone signal test showed the most signal tone displacement while showing limited distortion which made this driver the least distorted driver using a low amplitude signal. The nonlinear behavior outlined by the Acceptable Displacement Percentages showed that this driver would presumably create the least amount of distortion at higher drive amplitudes.

When placed into its designed enclosure, the Visaton FRS 5X-8 driver was predicted to produce a peak in frequency response that slightly affected the lower end of the operation range. A similar peak was observed in the assembly frequency response. This measured response showed that the assembly produced a response that increased with frequency. While this increase was not drastic, it was the distortion measurements that caused concern with the viability of using this driver for the noise canceling application. The free-air multi-tone measurement showed that this driver produced more distortion than any other driver even despite the larger produced displacement. This driver produced moderate Acceptable Displacement Percentages, especially for the  $Bl(x)$  nonlinearity where the force factor showed somewhat symmetric change but showed a lack of linearity compared to the  $Bl(0)$  value. This led to the presumption that this driver may produce moderate distortion at higher amplitudes.

The Tectonic TEBM36S12-8/A assembly model also predicted a peak in response that would affect the flatness of the frequency response. This was observed in the measured frequency response where there was an increase in response that grazed the lower limit of the operating frequency range. Other than this increase, the response was one of the flattest responses measured. The free-air multi-tone measurement suggested that this driver produced little distortion; however, the displacement was the lowest of all drivers and the distortion disappeared into the measurement's noise floor fairly quickly. This driver produced the most nonlinear  $k_s(x)$  and  $Bl(x)$  behaviors according to the Acceptable Displacement Percentage metric. The driver produced a particularly nonlinear, asymmetric stiffness which was confirmed by the  $k_s(x)$  Acceptable Displacement

Percentage. Distortion would certainly be produced by these parameters' nonlinear behaviors.

Based solely on these results, the Tang Band W2-2243S assembly showed the most promising results for the noise canceling application. While the W2-2243S and TEBM36S12-8/A driver-enclosure assemblies showed somewhat flat frequency responses, the W2-2243S driver produced less multi-tone distortion relative to its broadband displacement and higher Acceptable Displacement Percentages compared to the other drivers. The W1-2121S also showed promising nonlinear trends, but the frequency response was not flat within the operating bandwidth. The FRS 5X-8 and TEBM36S12-8/A drivers showed the potential to produce more distortion than the W2-2243S driver. Of the drivers and assemblies measured, the W2-2243S assembly showed the best results for this application due to its response and its measured nonlinear behavior. This driver-enclosure assembly will help ensure that the signal generated to cancel noise passing through a building window is accurately produced.

## **6.2 The Use of Acceptable Displacement Percentages**

The nonlinear parameter behavior of the drivers was observed qualitatively by two characteristics: how constant a nonlinear parameter was and how symmetric about the resting position a nonlinear parameter values were. This qualitative observation was quantified using the Acceptable Displacement Percentage which was applied to quantify how constant and symmetric the nonlinear parameter was. Using the ADP to quantify the nonlinear parameter results proved to be a useful solution to compare the displacement-dependent nonlinear behavior of one driver to another while accounting for the different voice coil displacements from each driver. Despite the drivers will not always be driven at large amplitudes, having a larger percentage of total displacement at which the nonlinear parameters met the conditions of the ADP would ensure that more of the voice coil displacement would produce minimal distortion. While the ADP metric was not a detailed prediction of distortion production capable of describing specific harmonics produced by the nonlinear parameter behaviors, it was able to compare drivers based on the causes of nonlinear distortion regardless of the drivers' total voice coil displacements. In order to make a full prediction of the produced distortion, a nonlinear driver model should be used.

## 6.3 Future Work

While these results produced an assembly choice for this application, there are other measurements that can be done to confirm this choice. The future work suggested here could demystify some other characteristics either not explored in this research or causes for error within the research. These include an investigation into the W1-2121S assembly frequency response, driver manufacture quality control, generated distortion at large signal amplitudes, nonlinear measurements of the entire driver-enclosure assemblies, and the verification of the Klippel Analyzer 3 nonlinear parameter derivation methods.

The W1-2121S assembly showed a potential error in either the driver construction or the assembly construction. Finding the source of this potential error can be done through process of elimination. Disassembling and reassembling the driver-enclosure assembly may remove any potential error in the assembly, which can be tested by measuring the frequency response of the assembly again. If the unexpected response is no longer present, the error was in the initial driver-enclosure assembly. Measuring the frequency response of the driver alone could determine if there was a manufacturing error in the driver by showing the same oddity in response.

If there was indeed an error in the manufacturing of the W1-2121S driver, this in itself may be an oddity for the manufacturer. Regardless of the potential error source for the W1-2121S assembly, several of each driver should be tested to investigate the manufacturing quality. This is especially true for the W2-2243S driver if it is to be used in the final ANC application. If the drivers tested in this research are abnormal for the standards of the manufacturer, it would be important to know what the manufacturer usually produces. This is also important for practical use of these drivers in the ANC application as several drivers would be used in the application rather than just one. Testing several W1-2121S drivers would help determine if the one used in this research was defective or if the manufacturer does not maintain quality between the produced drivers.

The quality of each driver produced may also impact the distortion produced by each driver. These distortions could be measured using a larger signal for the multi-tone measurement. Along with this measurement, other distortion measurement methods are available to quantify the distortions produced by a driver that examine the produced distortion closer. For example, viewing the second and third harmonic distortions could give more specific insight into the distortion that a driver produces. This would create a better understanding of how the driver produces distortion and how the driver behaves

at large amplitudes, rather than presuming based purely on the parameter nonlinearities.

Along with testing the distortions of the drivers, the distortions of the assemblies should be tested as well. This comes with the idea that the stiffness added by the enclosure's trapped air may produce its own nonlinear behavior and should be examined in combination with the driver. While this was briefly examined in this work, further investigation into this nonlinearity and its potential to cause distortion should be done, especially when considering that the mechanical equivalent of the acoustical stiffness added by the enclosure is about equal to or greater than the drivers' mechanical stiffness. Testing the assemblies would further the investigation into nonlinearities.

Finally, the Klippel Analyzer 3 and dB-Lab software package are great tools for driver analysis. But just as with the MATLAB Impulse Response Measurement application, it is important to have an in-depth understanding of how the system performs its measurements and analysis. This could give a better interpretation of the results presented here.

This suggested work would require more time and resources, but it would describe more about each driver than what has been presented here. By completing other tests and gaining further understanding of the measurements performed, there would be more quantifiable evidence for choosing one driver-enclosure assembly over the others. This evidence can then help solidify the choice to use a chosen driver-enclosure assembly on a larger scale, across the whole of the ANC application.

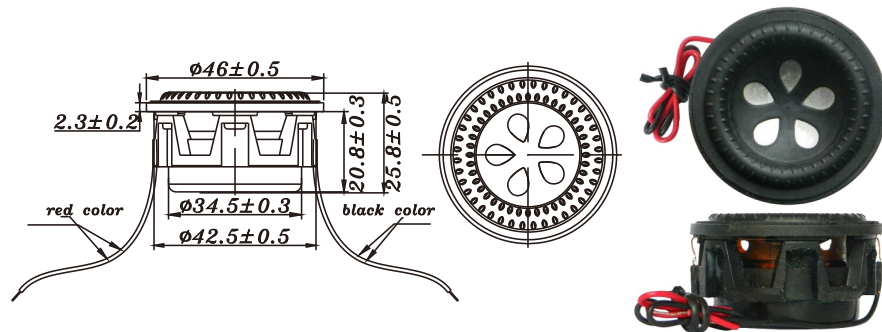
# Appendix A | Specification Sheets

The following are the specification sheets for each driver and the foam paneling in the room used for the frequency response measurements provided by the manufacturer. The driver specification sheets showed the expected resonant frequency and driver parameters in order to appropriately assess the drivers before they were chosen for this project. The foam panel specification sheet showed the sound absorption coefficient as a function of frequency.



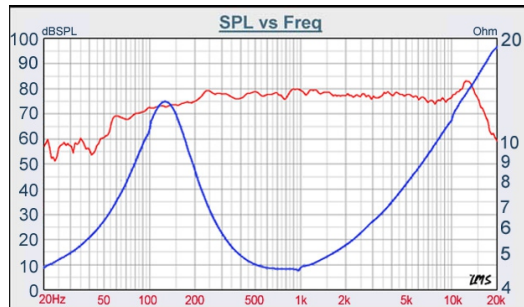
# F SERIES

# W1-2121S



- THE HIGHEST PERFORMANCE OF INNOVATIVE, TINY FULL RANGE DRIVER DESIGN
- OUTSIDE DIAMETER OF 46mm, Fo:120Hz
- ALUMINUM DIAPHRAGM WITH SANTOPRENE SURROUND
- NEODYMIUM MAGNET SYSTEM
- PATENTED PRODUCT WITH EXCELLENT CONSISTENCY
- IT'S GOOD FOR MULTIMEDIA APPLICATION

## 1" ALUM, FULL RANGE



DIAPHRAGM MTL	Aluminum
SURROUND MTL	Santoprene
NOMINAL IMPEDANCE	4 Ω
DCR IMPEDANCE	3.5 Ω
SENSITIVITY 1W/1m	79 dB
FREQUENCY RESPONSE	120 -15K Hz
FREE AIR RESONANCE	120 Hz
VOICE COIL DIAMETER	28 mm
AIR GAP HEIGHT	2.3 mm
RATED POWER INPUT	6 W
MAXIMUM POWER INPUT	12 W
FORCE FACTOR, BL	3.14 TM
TYPE OF MAGNET	Neodymium
MOVING MASS	1.68 g
FERROFLUID ENHANCED	YES
SUSPENSION COMPLIANCE	949.41uMN <sup>-1</sup>
EFFECTIVE PISTON AREA	0.0009 M <sup>2</sup>
Levc	0.070 mH
Zo	15 ohm
X-max	2.3 mm
Vas	0.11 Litr
Qts	0.35
Qms	1.33
Qes	0.47



VOICE:886.2.26570282 FAX:886.2.26580166  
E-MAIL :info@tb-speaker.com

**Figure A.1.** The specification sheet for the Tang Band W1-2121S driver [3]. The spec sheet was taken directly from <http://www.tb-speaker.com/uploads/files/e99c0126812ca22379a2179932b9e840.pdf>.

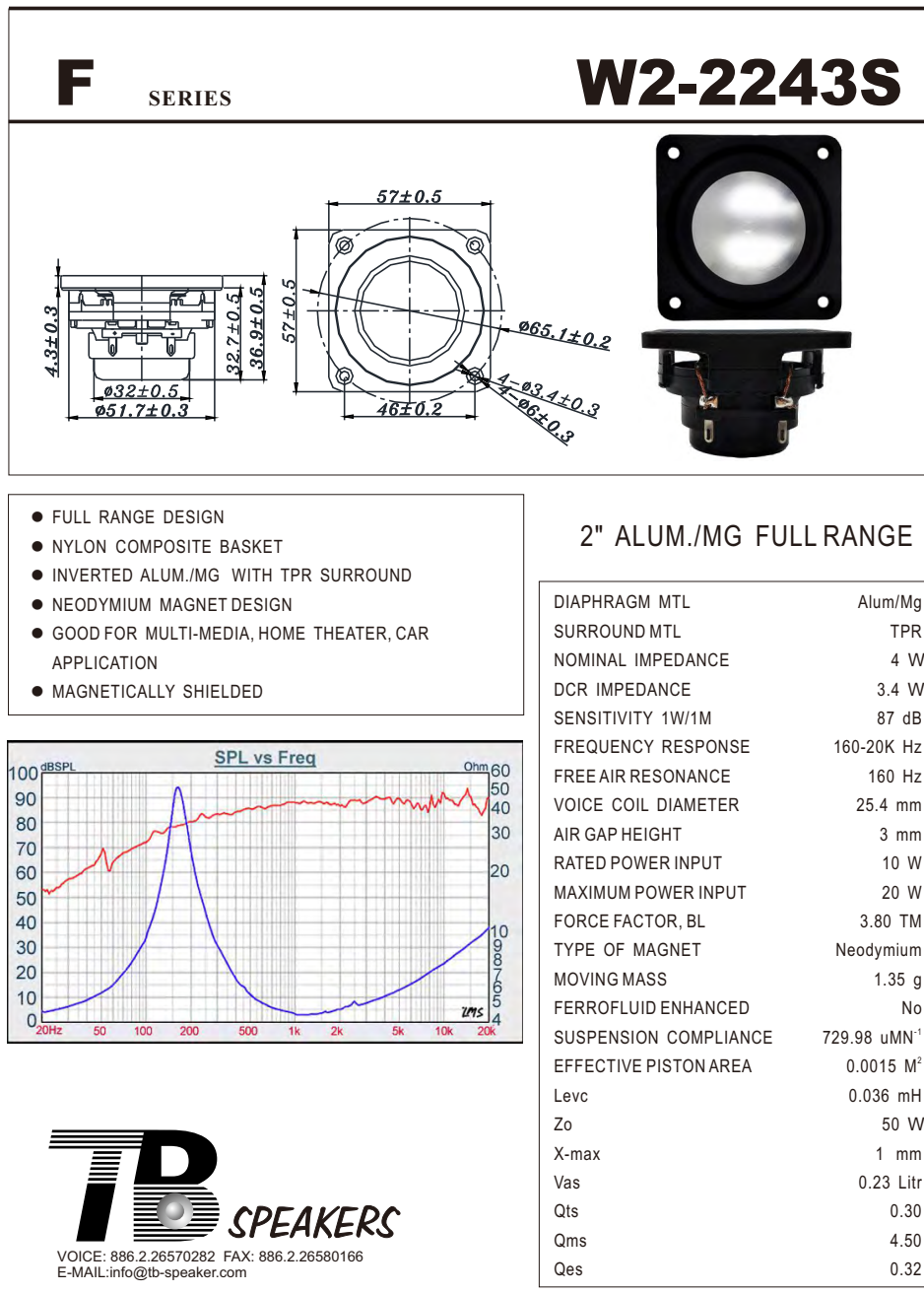
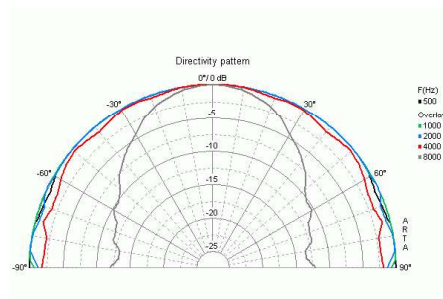
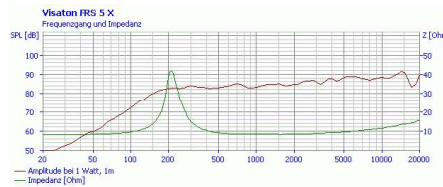
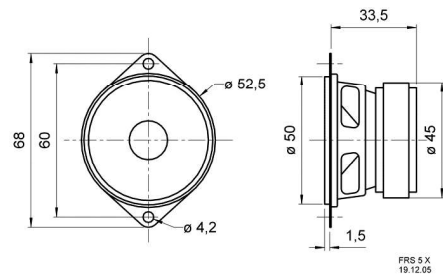


**Figure A.2.** The specification sheet for the Tang Band W2-2243S driver [4]. The spec sheet was taken directly from <http://www.tb-speaker.com/uploads/files/e4964df0494335751327c45c1160fc73.pdf>.

# FRS 5 X - 8 Ohm

Art. No. 2235



## Technische Daten / Technical data

Nennbelastbarkeit Rated power	5 W
Musikbelastbarkeit Maximum power	8 W
Nennimpedanz Z Nominal impedance Z	8 Ohm
Übertragungsbereich Frequency response	120–20000 Hz
Mittlerer Schalldruckpegel Mean sound pressure level (1 W/1 m)	86 dB
Abstrahlwinkel (-6 dB) Opening angle (-6 dB)	180°/4000 Hz
Resonanzfrequenz fs Resonance frequency fs	190 Hz
Schwingspulendurchmesser Voice coil diameter	14 mm
Schallwandöffnung Cutout diameter	46 mm
Gewicht netto Net weight	0,14 kg
Gleichstromwiderstand Rdc D.C. resistance Rdc	7,7 Ohm
Mechanischer Q-Faktor Qms Mechanical Q factor Qms	3,49
Elektrischer Q-Faktor Qes Electrical Q factor Qes	0,88
Gesamt-Q-Faktor Qts Total Q factor Qts	0,7
Äquivalentes Luftnachgiebigkeitsvolumen Vas Equivalent volume Vas	0,23 l
Effektive Membranfläche Sd Effective piston area Sd	12,5 cm²
Dynamische bewegte Masse Mms Dynamically moved mass Mms	0,7 g
Antriebsfaktor Bxl Force factor Bxl	2,87 Tm
Temperaturbereich Temperature range	-25 ... 70 °C

01.10.2015

VISATON GmbH • Ohligser Straße 29-31 • D-42781 Haan • Tel.: 02129/552-0 • Fax 02129/552-10 • E-Mail: visaton@visaton.com

**Figure A.3.** The specification sheet for the Tang Band FRS 5X-8 driver [5]. The spec sheet was taken directly from [https://www.visaton.de/sites/default/files/dd\\_product/frs5x\\_8.pdf](https://www.visaton.de/sites/default/files/dd_product/frs5x_8.pdf).

**TEBM36S12-8/A Balanced Mode Radiator**
**✓RoHS**  
**COMPLIANT**

**Features**

- Wide bandwidth and wide directivity
- Impedance: 8Ω
- Dimensions: 65mm x 65mm
- Thickness: 29.7mm
- Mass: 88.5g

**Applications**

- Docking stations
- Table radios
- Sound bars
- Computer speakers
- Wireless speakers

**Description**

The TEBM36S12-8/A Balanced-Mode Radiator (BMR) is an audio drive unit with an extended frequency response and wide directivity compared with a conventional drive unit. It combines the benefits of Tectonic bending-wave technology and pistonic modes of operation. It is ideally suited for compact audio applications that require a full-range, high performance acoustic solution.

This second generation drive unit has the same audio characteristics as its predecessor, with improved response smoothness and linearity at high excursion. A 4Ω version is also available.

**Parameters**

Parameter	Description	min	typ	max	Units
$R_e$	DC resistance	-10%	7.9	+10%	Ohms
$L_e$	Inductance	-10%	0.137	+10%	mH
$BL$	Force factor		3.87		Tm
$f_s$	Resonance frequency	-20%	148	+20%	Hz
$d_{Drv}$	Voice coil diameter		25.4		mm
$M_{ms}$	Moving mass		1.68		g
$C_{ms}$	Compliance		0.70		mmN <sup>-1</sup>
$R_{ms}$	Suspension Loss		0.49		Nsm <sup>-1</sup>
$X_{mech\ max}$	Maximum coil excursion (p-p)		8.0		mm
$S_d$	Effective piston area		17.2		cm <sup>2</sup>
$V_{AS}$	Equivalent volume		0.29		L
$Q_{ms}$	Mechanical quality factor		3.18		
$Q_{es}$	Electrical quality factor		0.83		
$Q_{ts}$	Total quality factor		0.66		

**Figure A.4.** The specification sheet for the Tectonic TEBM36S12-8/A driver [6]. The spec sheet was taken directly from [https://www.tectonicaudiolabs.com/wp-content/uploads/woocommerce\\_uploads/2018/10/T-DS-TEBM36S12-8A.pdf](https://www.tectonicaudiolabs.com/wp-content/uploads/woocommerce_uploads/2018/10/T-DS-TEBM36S12-8A.pdf).

# RIVERBANK ACOUSTICAL LABORATORIES

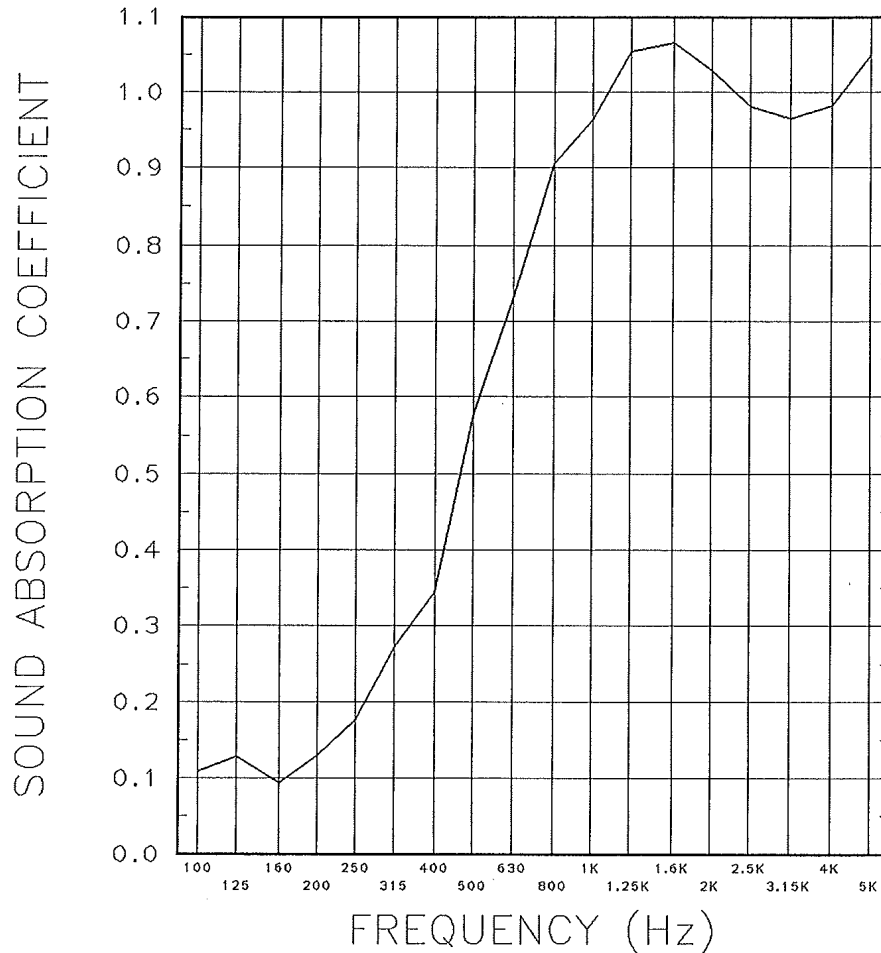
1512 BATAVIA AVENUE  
NEVA, ILLINOIS 60134

OF  
IIT RESEARCH INSTITUTE

## REPORT

630/232-0104  
FOUNDED 1918 BY  
WALLACE CLEMENT SABINE

### SOUND ABSORPTION REPORT RAL - A99-94 PAGE 4 OF 4



NRC = 0.70

THE RESULTS REPORTED ABOVE APPLY ONLY TO THE SPECIFIC SAMPLE SUBMITTED FOR MEASUREMENT. NO RESPONSIBILITY IS ASSUMED FOR PERFORMANCE OF ANY OTHER SPECIMEN.

ACCREDITED BY DEPARTMENT OF COMMERCE, NATIONAL VOLUNTARY LABORATORY  
ACCREDITATION PROGRAM FOR SELECTED TEST METHODS FOR ACOUSTICS.  
THE LABORATORY'S ACCREDITATION OR ANY OF ITS TEST REPORTS IN NO WAY CONSTITUTES  
OR IMPLIES PRODUCT CERTIFICATION, APPROVAL, OR ENDORSEMENT BY NIST.

**Figure A.5.** The sound absorption coefficient for the Auralex 2 inch Studiofoam® Pyramid™ foam paneling that lined the room in which the frequency response measurements were conducted [10]. This graph was taken directly from <https://auralex.com/content/performance/2pyramid.pdf>.

# Appendix B |

## Engineering Drawings for Enclosure Components

The enclosures were made using  $\frac{1}{2}$  inch medium-density fiberboard, or MDF. The designed parts were as follows: a 3.5 inch and 3 inch tube assembly, a 3.5 inch and 3 inch hole guide, a 3.5 inch and 3 inch back plate, a 3.5 inch and 3 inch face plate for the W1-2121S driver, a 3.5 inch face plate for the W2-2243S driver, a 3.5 inch face plate for the FRS 5X-8 driver, and a 3.5 inch face plate for the TEBM36S12-8/A driver. Figs. B.1–B.10 are the engineering drawings for part and assembly dimensions and construction. Further construction was done to create the actual enclosures. The tube assemblies in Fig. B.3 were cut to lengths according to the driver depth into the enclosure and had through holes drilled for bolt fasteners. These holes were created using the properly sized hole guide in Fig. B.9. The holes for the binding posts were drilled into both sizes of Part 008 in Fig. B.8 after the parts was made. Part numbers preceded by an 'A' signify that print as the assembly of two or more parts, e.g. in Fig. B.3 which has the part number A003. A bill of materials can be found on those assembly prints. While a 3.5 inch W1-2121S face plate was made, it was not used in this research due to the 3 inch face plate and tube assembly constituting a smaller volume.

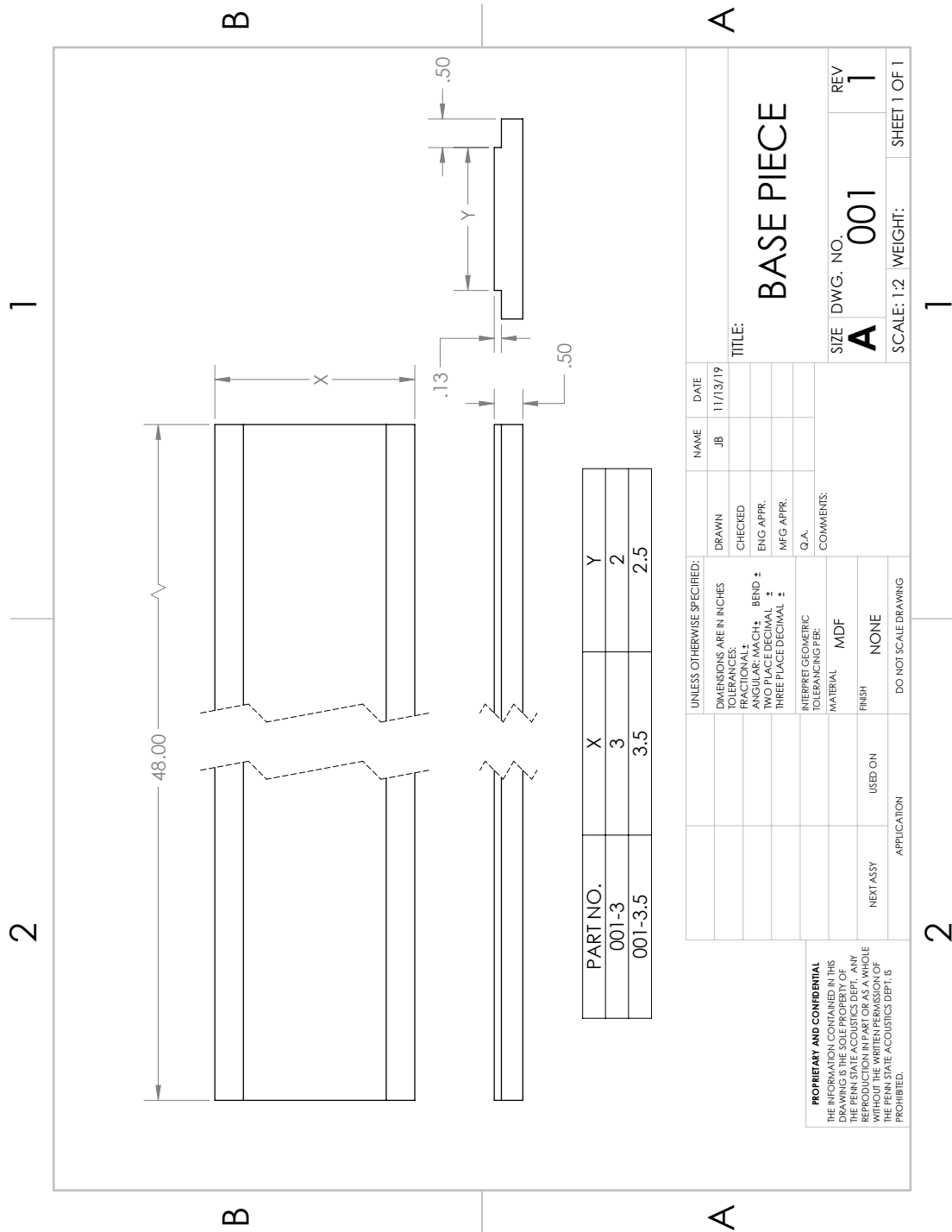


**Figure B.1.** The engineering drawing for Part 001, the base piece for the tube assembly, for 3.5 inch and 3 inch tube sizes.

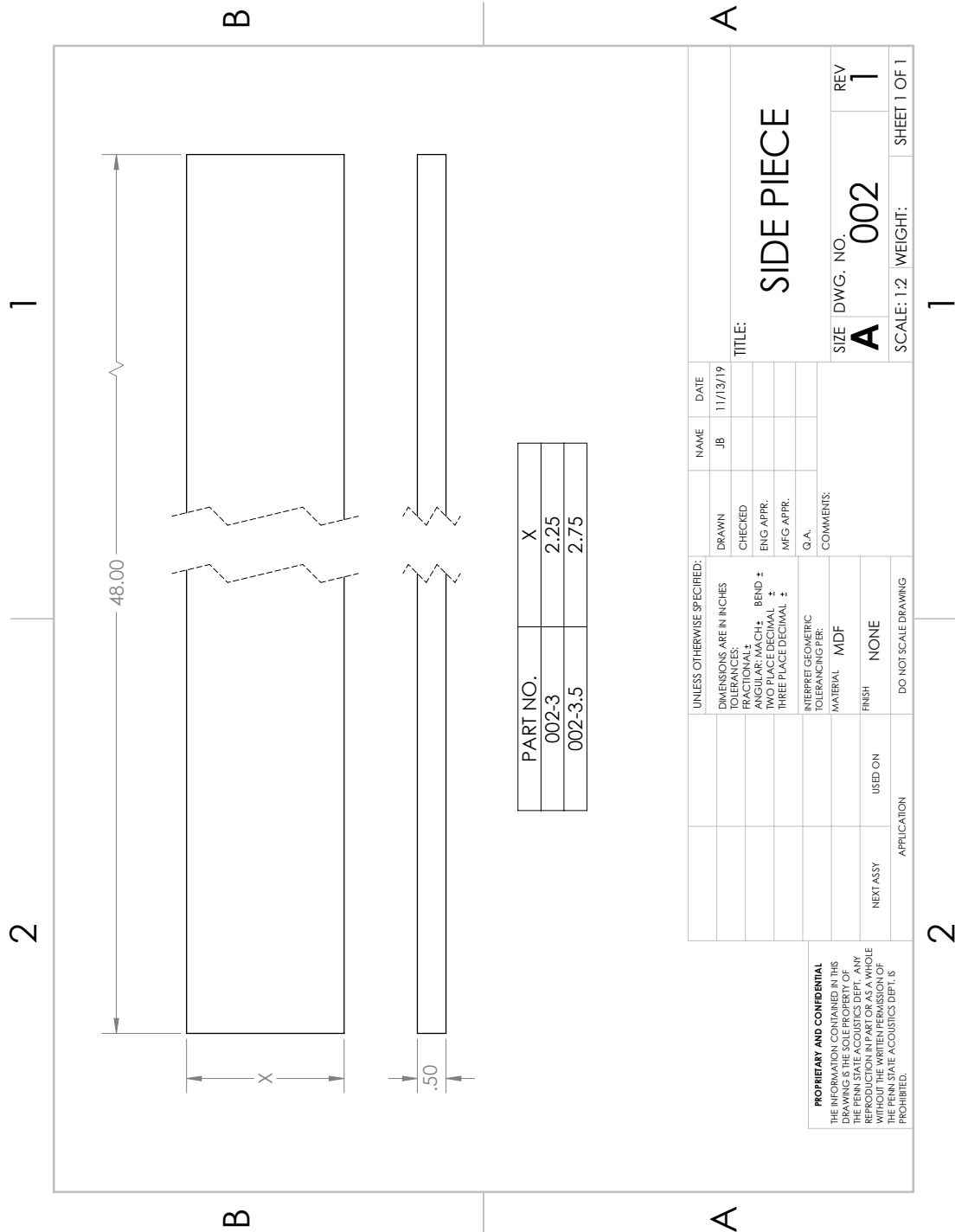


**Figure B.2.** The engineering drawing for Part 002, the side piece for the tube assembly, for 3.5 inch and 3 inch tube sizes.



**Figure B.3.** The engineering drawing for Part A003, the tube assembly, in 3.5 inch and 3 inch sizes.

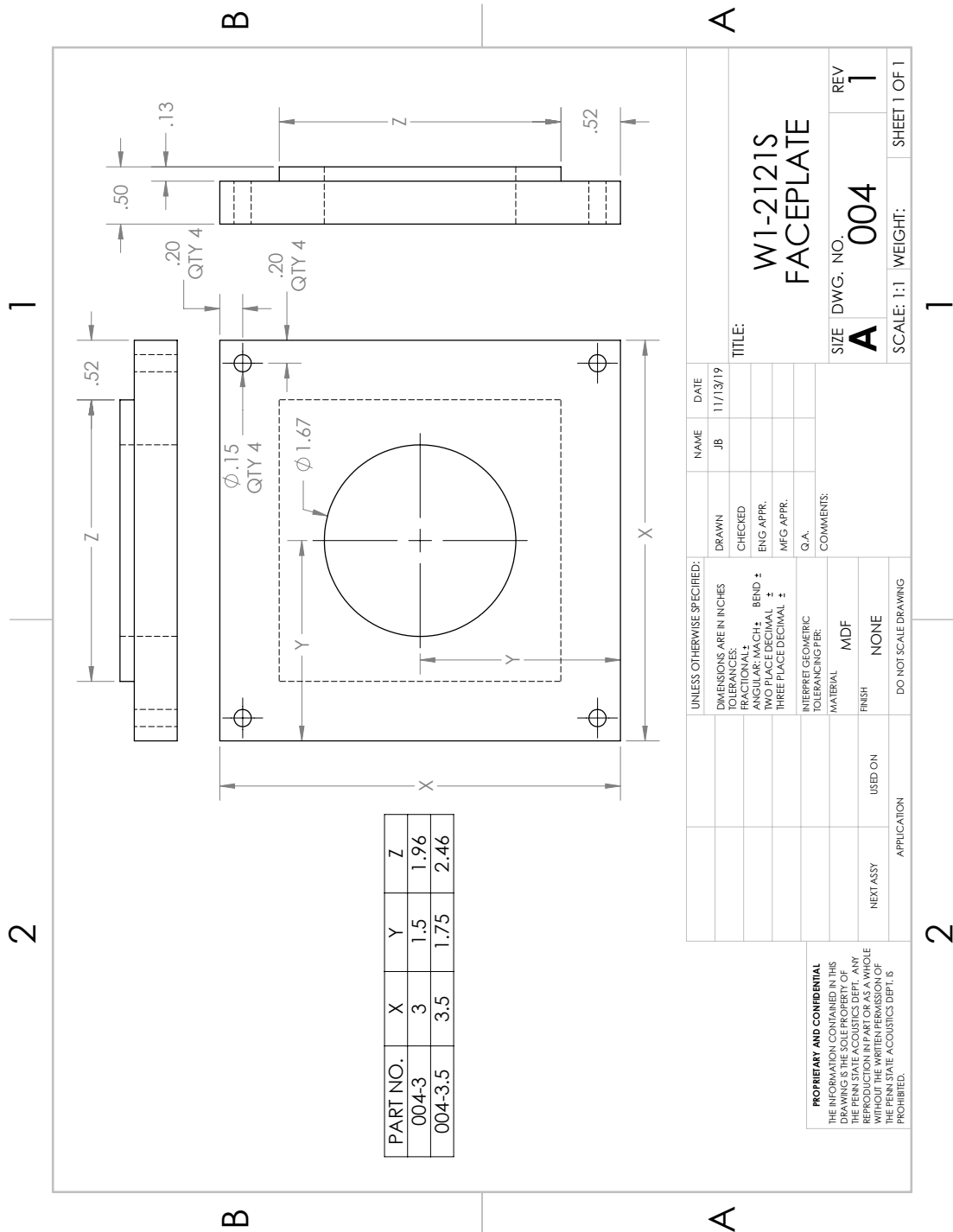


**Figure B.4.** The engineering drawing for Part 004, the W1-2121S face plate, in 3.5 inch and 3 inch sizes.

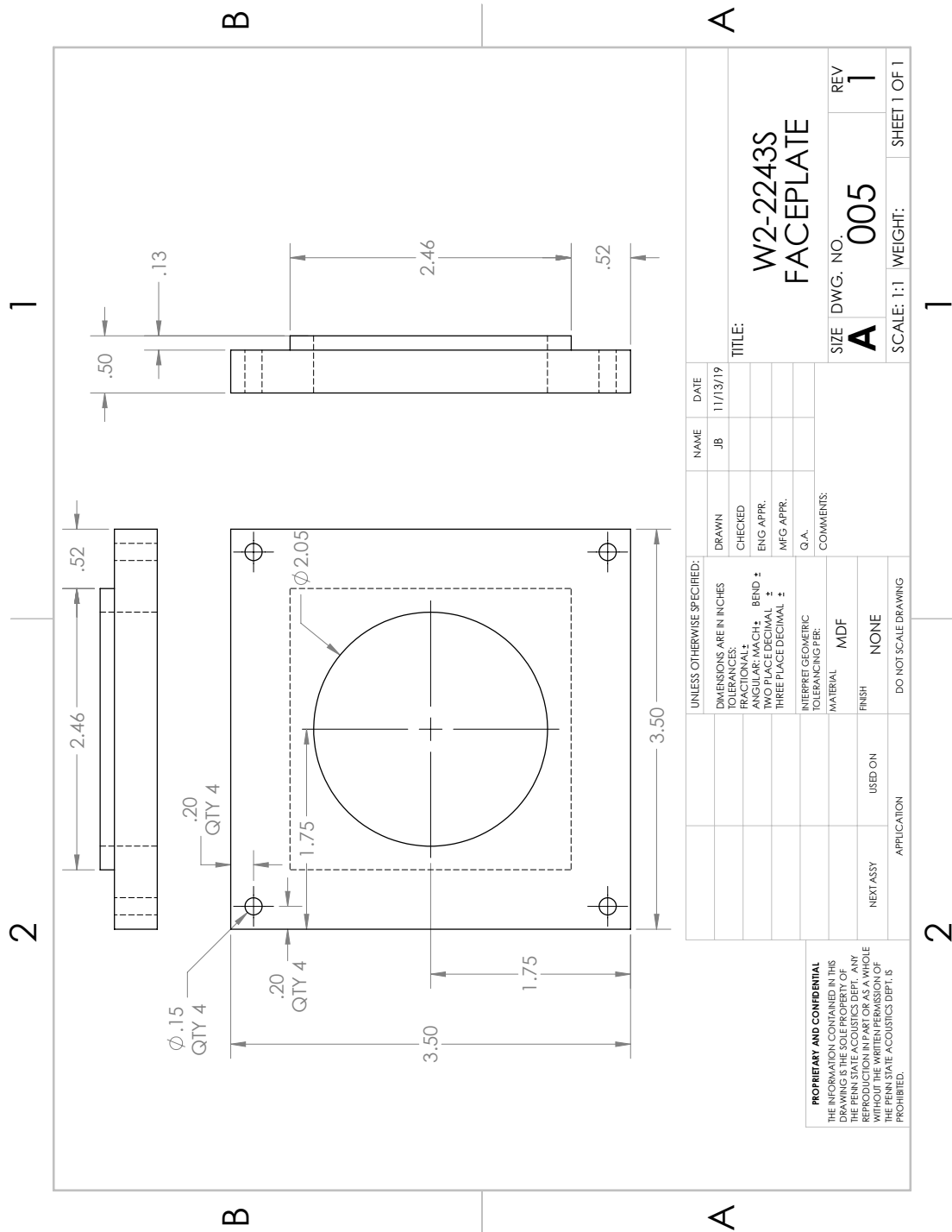
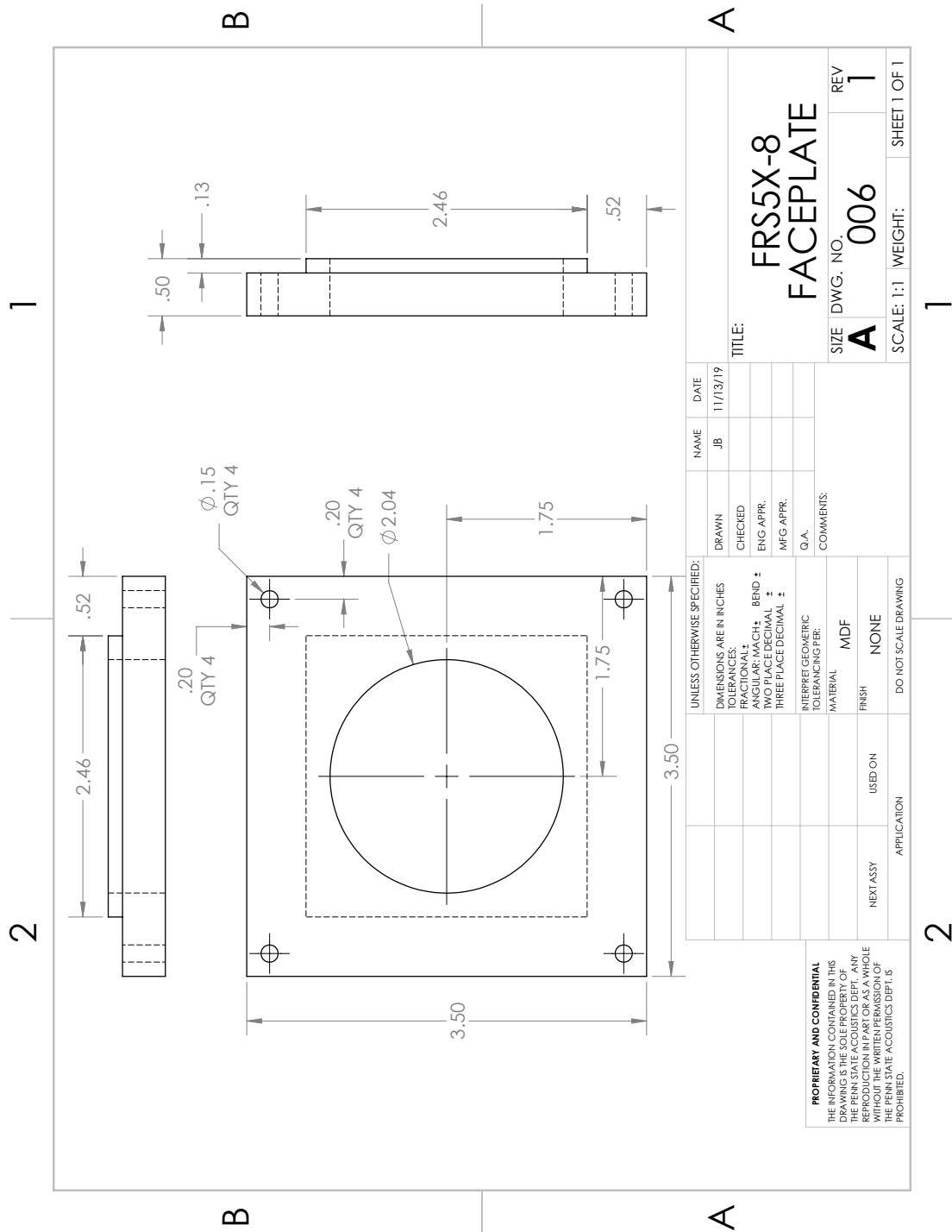
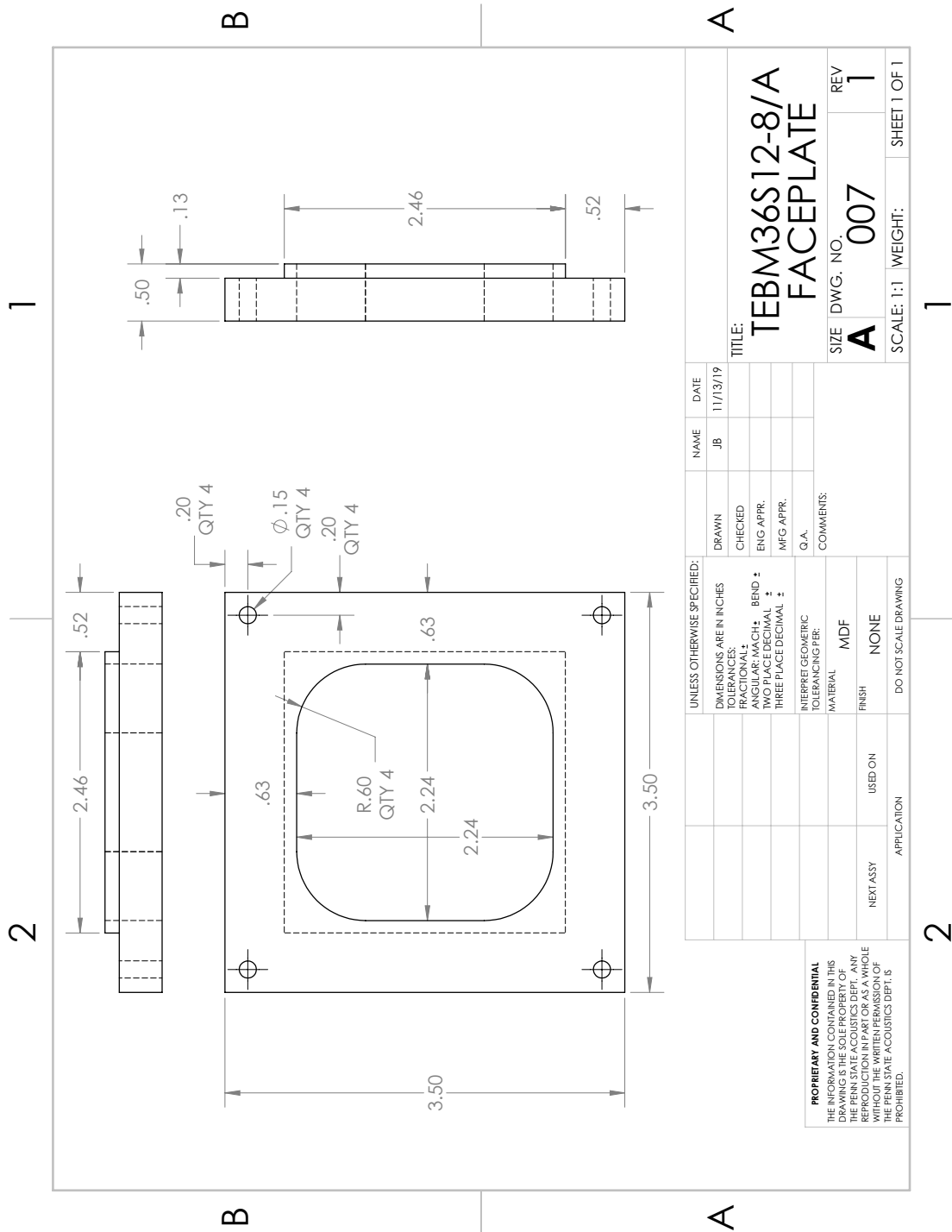


Figure B.5. The engineering drawing for Part 005, the W2-2243S face plate.



**Figure B.6.** The engineering drawing for Part 006, the FRS 5X-8 face plate.



**Figure B.7.** The engineering drawing for Part 007, the TEBM36S12-8/A face plate.

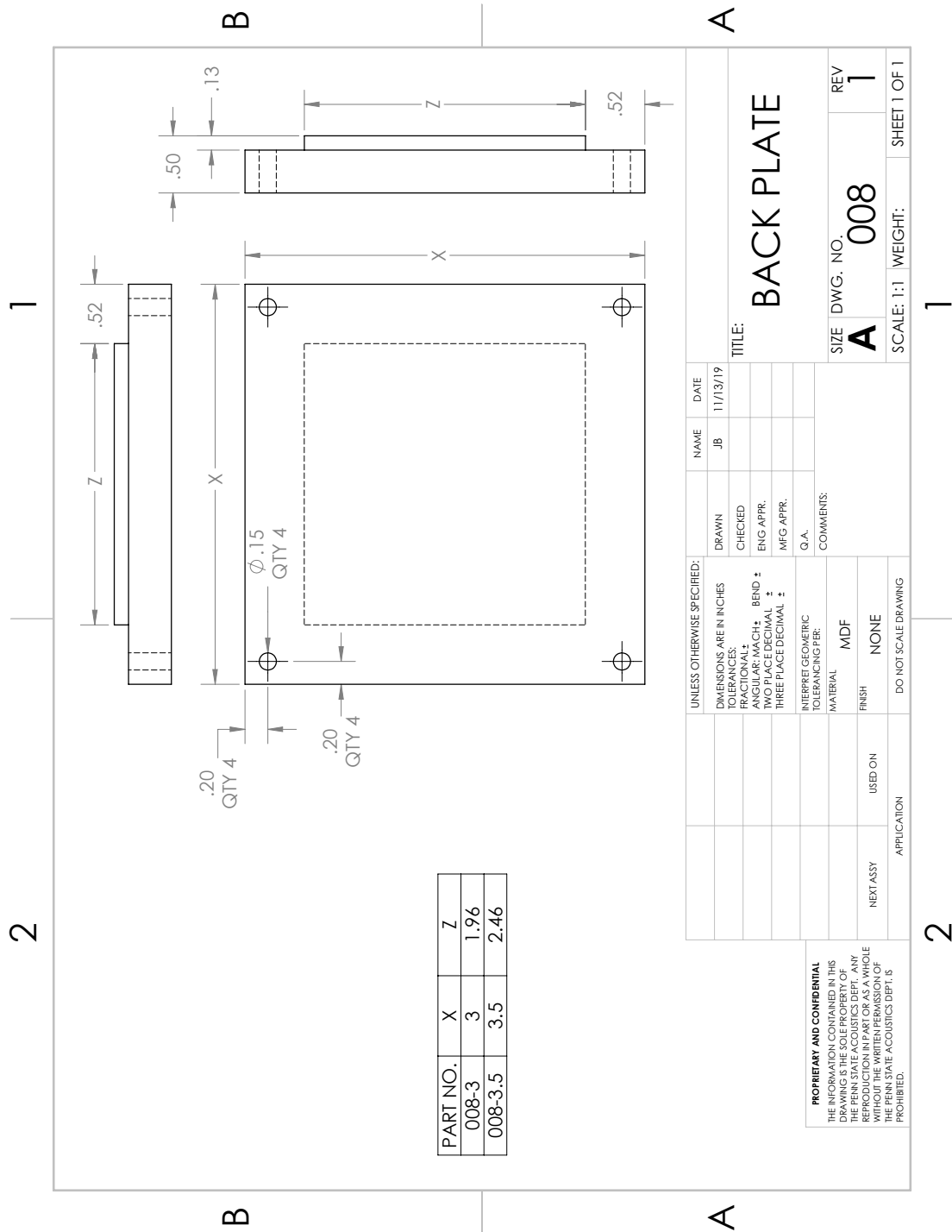
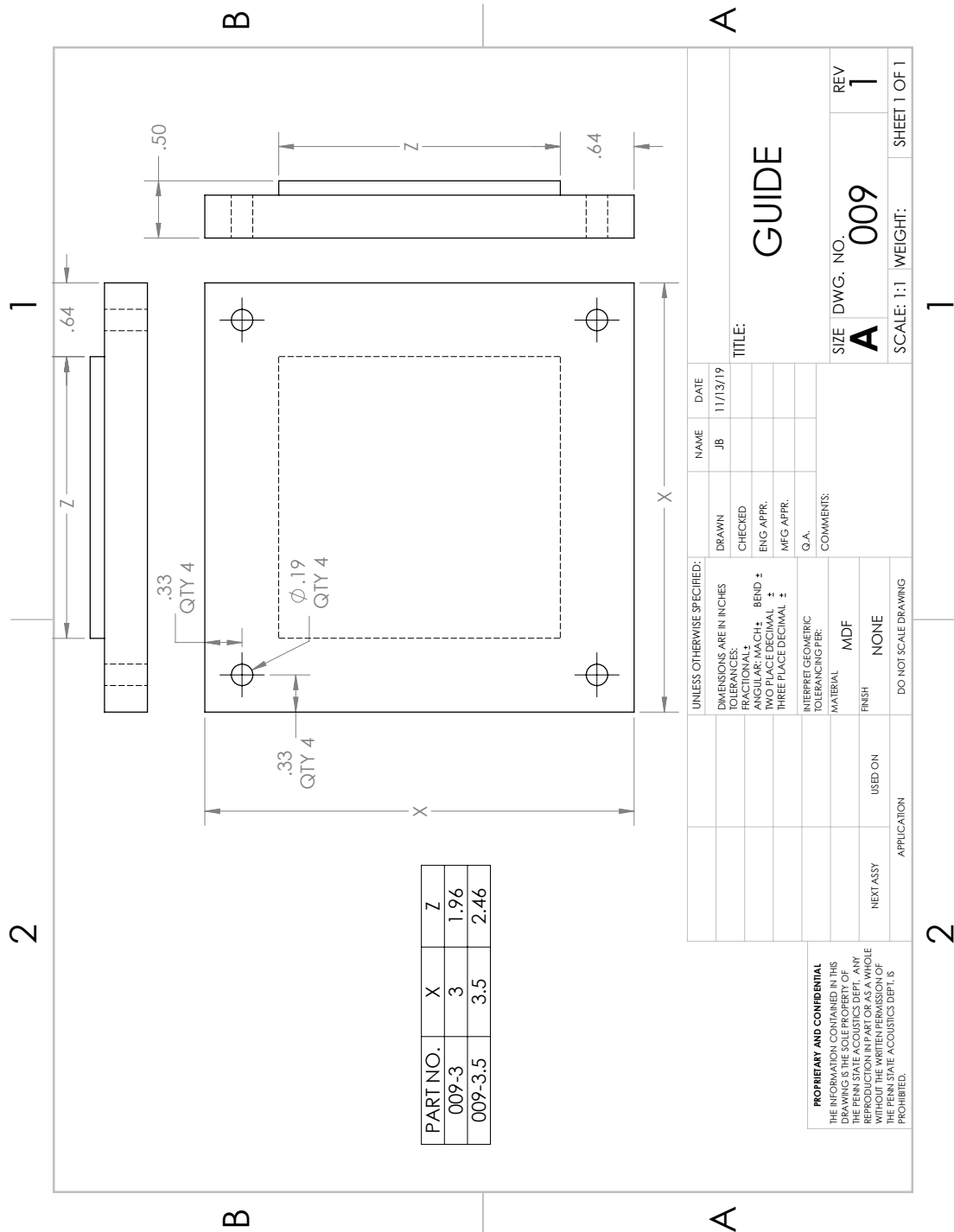


Figure B.8. The engineering drawing for Part 008, the back plate of the enclosure, in 3.5 inch and 3 inch sizes.



**Figure B.9.** The engineering drawing for Part 009, the hole guide, in 3.5 inch and 3 inch sizes.

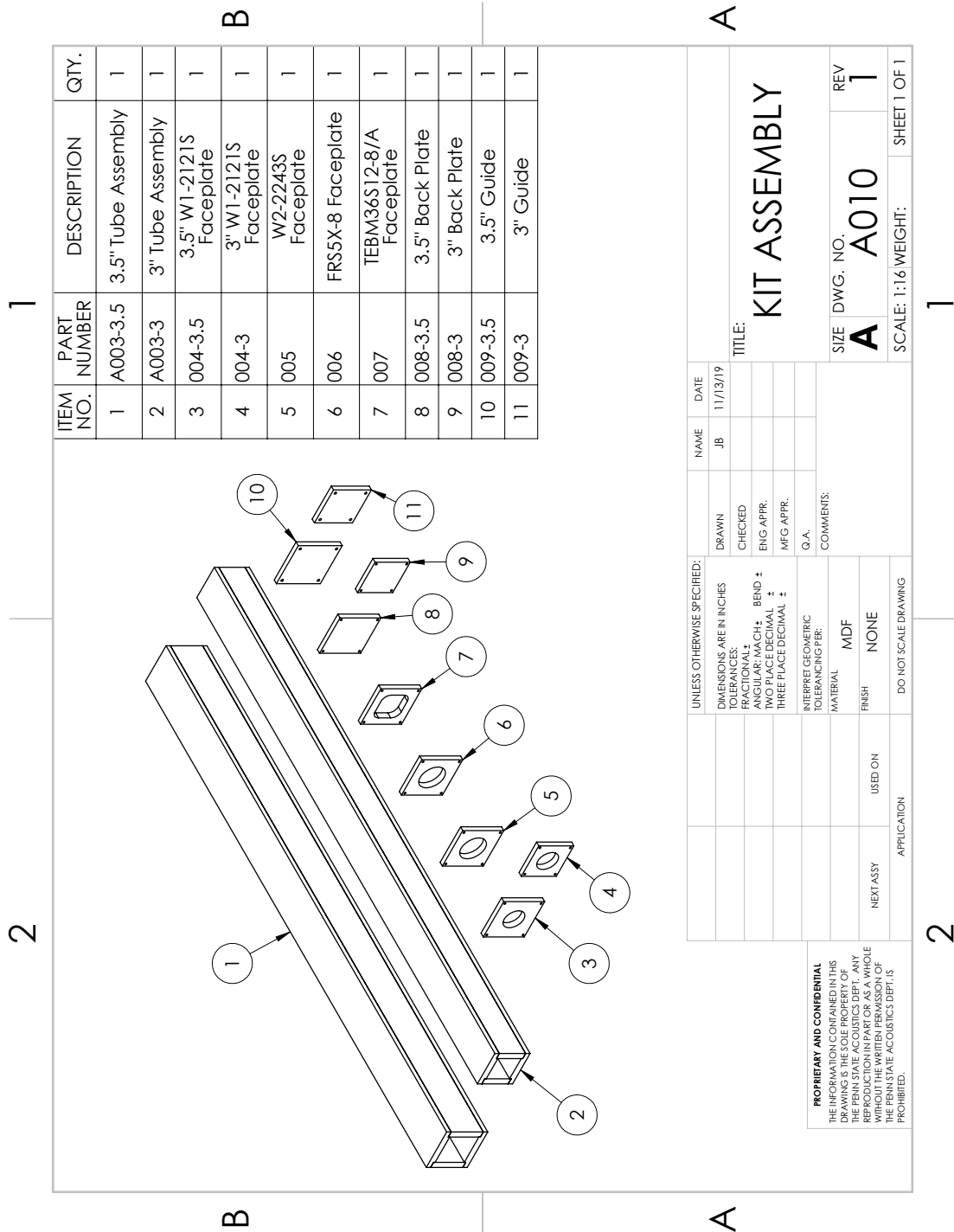


Figure B.10. The engineering drawing for Part A010, the full kit of enclosure parts made for this project.



# Appendix C |

## MATLAB Code

### C.1 Volume Finder

This code was used to calculate the air volume within an enclosure with a specific driver in the enclosure. The default configuration of this code assumes that the enclosure depth used is the smallest possible for driver being used. The code begins by asking the user which driver enclosure volume will be calculated. The following sections calculate the volume of the enclosure that is taken up by the driver and the volume taken up by the back plate and binding posts. The next section is configured to assume that the smallest enclosure depth is being used; however, there is a commented section that can request the depth from the user. The volumes are combined and a final internal enclosure volume is reported. The final section calculates the percent change in compliance as the driver cone moves inwards and outwards.

```
1 clear all
2 %% ASK WHICH DRIVER IS BEING MOUNTED IN THE ENCLOSURE
3
4 str=append('Which Driver? \n 1. FRS-5-X\n 2. W1-2121S\n ',...
5 '3. TEBM36S12-8A\n 4. W2-2243S\n\nInput: ');
6 x=input(str);
7
8 %% Catch Exception
9
10 if x~=1 && x~=2 && x~=3 && x~=4
11     str='Invalid Input. Run Program Again.';
12     disp(str);
13     return
14 end
```

```

15
16 %% CALCULATE FRONT PLATE VOLUME BASED ON THE DRIVER SPECIFIED
17 % FRS-5-X
18 if x==1
19     str='FRS-5-X Front Plate Volume Calculated';
20     RimWidth=62.64;
21     RimDepth=3.06;
22     CutDepth=10.31;      %measured to Rim
23     CutDiam=51.83;
24     Depth1=3.01;
25     Diam1=37.87;
26     Depth2=10.60;
27     Diam2=44.68;
28     Depth3=2.79;
29     Diam3=41.30;
30
31     V_cut=pi*(CutDiam/2)^2*(CutDepth-RimDepth);
32     V1=pi*(Diam1/2)^2*Depth1;
33     V2=pi*(Diam2/2)^2*Depth2;
34     V3=pi*(Diam3/2)^2*Depth3;
35     V_rim=(RimWidth^2-pi*(CutDiam/2)^2)*RimDepth;
36
37     AddedVolume_FrontPlate=V_cut-V1-V2-2*V3-V_rim;
38     disp(str);
39
40     Area_cone=1264; % mm^2
41     Depth_cone=2.113; % mm
42     AddedVolume_FrontPlate_In=AddedVolume_FrontPlate-...
43         (Area_cone*Depth_cone); % mm^3
44     AddedVolume_FrontPlate_Out=AddedVolume_FrontPlate+...
45         (Area_cone*Depth_cone); % mm^3
46
47     C_m=0.6213/1000; % m/N
48 end
49
50 % W1-2121S
51 if x==2
52     str='W1-2121S Front Plate Volume Calculated';
53     RimWidth=49.98;
54     RimDepth=3.09;
55     CutDepth=12.10;
56     CutDiam=40.45;

```

```

57 Depth1=15.50;
58 Diam1=34.48;
59 RectWidth=2.95;
60 RectLength=13.58;
61 RectDepth=14.42;
62 RectCount=6;
63
64 V_cut=pi*(CutDiam/2)^2*(CutDepth-RimDepth);
65 V1=pi*(Diam1/2)^2*Depth1;
66 V_Rect=RectWidth*RectLength*RectDepth*RectCount;
67 V_rim=(RimWidth^2-pi*(CutDiam/2)^2)*RimDepth;
68
69 AddedVolume_FrontPlate=V_cut-V1-V_Rect-V_rim;
70 disp(str);
71
72 Area_cone=886; % mm^2
73 Depth_cone=2.857; % mm
74 AddedVolume_FrontPlate_In=AddedVolume_FrontPlate-...
75     (Area_cone*Depth_cone); % mm^3
76 AddedVolume_FrontPlate_Out=AddedVolume_FrontPlate+...
77     (Area_cone*Depth_cone); % mm^3
78
79 C_m=0.4713/1000; % m/N
80 end
81
82 % TEBM36S12-8A
83 if x==3
84     str='TEBM36S12-8A Front Plate Volume Calculated';
85     RimWidth=62.7;
86     RimDepth=3.06;
87     CutWidth=57.0;
88     CutDepth=17.26; %measured to rim
89     R=15.24;
90     Depth1=9.18;
91     Diam1=48.1;
92     Depth2=15.44;
93     Diam2=36.55;
94
95     V_cut_area=(CutWidth^2-4*(R^2-(0.25*pi*R^2)));
96     V_cut=(CutWidth^2-4*(R^2-0.25*pi*R^2))*(CutDepth-RimDepth);
97     V1=pi*(Diam1/2)^2*Depth1;
98     V2=pi*(Diam2/2)^2*Depth2;

```

```

99     V_rim=(RimWidth^2-V_cut_area)*RimDepth;
100
101     AddedVolume_FrontPlate=V_cut-V1-V2-V_rim;
102     disp(str);
103
104     Area_cone=1669; % mm^2
105     Depth_cone=1.557; % mm
106     AddedVolume_FrontPlate_In=AddedVolume_FrontPlate-...
107         (Area_cone*Depth_cone); % mm^3
108     AddedVolume_FrontPlate_Out=AddedVolume_FrontPlate+...
109         (Area_cone*Depth_cone); % mm^3
110
111     C_m=0.4677/1000; % m/N
112 end
113
114 % W2-2243S
115 if x==4
116     str='W2-2243S Front Plate Volume Calculated';
117     RimWidth=62.62;
118     RimDepth=3.06;
119     CutDepth=11.25; %measured to rim
120     CutDiam=52.05;
121     RectLength=20.28;
122     RectWidth=1.60;
123     RectDepth=15.61;
124     RectCount=4;
125     Depth1=8.35;
126     Diam1=47.25;
127     Depth2=6.34;
128     Diam2=32.17;
129     Depth3=5.24;
130     Diam3=18.42;
131     Depth4=9.0;
132     Diam4=37.13;
133
134     V_cut=pi*(CutDiam/2)^2*(CutDepth-RimDepth);
135     V_rect=(RectDepth*RectLength*RectWidth)*RectCount;
136     V1=pi*(Diam1/2)^2*Depth1;
137     V2=pi*(Diam2/2)^2*Depth2;
138     V3=pi*(Diam3/2)^2*Depth3;
139     V4=pi*(Diam4/2)^2*Depth4;
140     V_rim=(RimWidth^2-pi*(CutDiam/2)^2)*RimDepth;

```

```

141
142 AddedVolume_FrontPlate=V_cut-V_rect-V1-V2+V3-V4-V_rim;
143 disp(str);
144
145 Area_cone=1521; % mm^2
146 Depth_cone=1.547; % mm
147 AddedVolume_FrontPlate_In=AddedVolume_FrontPlate-...
148     (Area_cone*Depth_cone); % mm^3
149 AddedVolume_FrontPlate_Out=AddedVolume_FrontPlate+...
150     (Area_cone*Depth_cone); % mm^3
151
152 C_m=0.2946/1000; % m/N
153 end
154
155 %% CALCULATE BACK PLATE VOLUME BASED ON DRIVER SPECIFIED
156 % Large Back Plate
157 if x==1 || x==3 || x==4
158     str='Large Back Plate Volume Calculated';
159     RimWidth=62.59;
160     RimDepth=3.06;
161     BPHoleDepth=5.53;
162     BPHoleDiam=15.875;
163     BPDepth=8.70;
164     BPDiam=7.48;
165
166     V_BPHole=pi*(BPHoleDiam/2)^2*(BPHoleDepth-RimDepth);
167     V_BP=pi*(BPDiam/2)^2*BPDepth;
168     V_rim=(RimWidth^2-2*pi*(BPHoleDiam/2)^2)*RimDepth;
169
170     AddedVolume_BackPlate=2*V_BPHole-2*V_BP-V_rim;
171     disp(str);
172 end
173
174 % Small Back Plate
175 if x==2
176     str='Small Back Plate Calculated';
177     RimWidth=49.94;
178     RimDepth=3.06;
179     BPHoleDepth=5.53;
180     BPHoleDiam=15.875;
181     BPDepth=8.70;
182     BPDiam=7.48;

```

```

183
184     V_BPHole=pi*(BPHoleDiam/2)^2*(BPHoleDepth-RimDepth);
185     V_BP=pi*(BPDiam/2)^2*BPDepth;
186     V_rim=(RimWidth^2-2*pi*(BPHoleDiam/2)^2)*RimDepth;
187
188     AddedVolume_BackPlate=2*V_BPHole-2*V_BP-V_rim;
189     disp(str);
190 end
191
192 %% CALCULATE CAVITY VOLUME
193
194 % THIS IS USED IF CAVITY DEPTHS ARE SOMETHING OTHER THAN THE SMALLEST
195 % DEPTHS FOR EACH DRIVER.
196
197 % str=append('What is the cavity depth in millimeters? \nCommon '...
198 %           'Choices are:\n14.01 for TEBM36S12-8A\n18.54 for '...
199 %           'W1-2121S\n28.08 for FRS-5-X and W2-2243S\n\nInput: ');
200 % CavityDepth=input(str);
201
202
203 % THIS IS USED IF CAVITY DEPTHS ARE THE SMALLEST POSSIBLE FOR EACH
204 % DRIVER.
205 if x==1 || x==4
206     str='Cavity Depth of 28.08mm Used in Calculation';
207     CavityDepth=28.08;
208     disp(str);
209 end
210
211 if x==2
212     str='Cavity Depth of 18.54mm Used in Calculation';
213     CavityDepth=18.54;
214     disp(str);
215 end
216
217 if x==3
218     str='Cavity Depth of 14.01mm Used in Calculation';
219     CavityDepth=14.01;
220     disp(str);
221 end
222
223 % DETERMINE THE SIZE OF TUBE USED IN ENCLOSURE ASSEMBLY
224 if x==1 || x==3 || x==4

```

```

225     str='Large Cavity Length and Width Used in Calculation';
226     CavityWidth=64.05;
227     CavityLength=64.65;
228     CavityVolume=CavityWidth*CavityLength*CavityDepth;
229     disp(str);
230 end
231
232 if x==2
233     str='Small Cavity Length and Width Used in Calculation';
234     CavityWidth=52.03;
235     CavityLength=51.18;
236
237     CavityVolume=CavityWidth*CavityLength*CavityDepth;
238     disp(str);
239 end
240
241 %% CALCULATE FINAL VOLUME
242
243 BackVolumeAssembly=CavityVolume+AddedVolume_BackPlate;
244 FinalVolume=BackVolumeAssembly+AddedVolume_FrontPlate;
245 FinalVolume_In=BackVolumeAssembly+AddedVolume_FrontPlate_In;
246 FinalVolume_Out=BackVolumeAssembly+AddedVolume_FrontPlate_Out;
247 FinalVolume=FinalVolume*(1e-9); %Converts from mm^3 to m^3
248 FinalVolume_In=FinalVolume_In*(1e-9); %Converts from mm^3 to m^3
249 FinalVolume_Out=FinalVolume_Out*(1e-9); %Converts from mm^3 to m^3
250 str=['Back Volume Assembly = ',num2str(BackVolumeAssembly),' mm^3'];
251 disp(str);
252 str=['Front Face Assembly = ',num2str(AddedVolume_FrontPlate),' mm^3'];
253 disp(str);
254 str=['Final Cavity Volume = ',num2str(FinalVolume/(1e-9)),' mm^3'];
255 disp(str);
256
257 %% Calculate Stiffness Change Due to Movement
258 str=['Mechanical Stiffness = ',num2str(C_m),' N/m'];
259 disp(str);
260
261 P1=101325;
262 V1=FinalVolume;
263 Specific_Heat_Ratio=1.401;
264
265 C_mal=(V1/(Specific_Heat_Ratio*P1))/((Area_cone*(1e-6))^2);
266 str=['Mechanical Equivalent of Acoustic Stiffness = ',...

```

```

267     num2str(1/C_ma1), ' N/m'];
268 disp(str);
269 C_tot=((C_m^(-1)+C_ma1^(-1)))^(-1);
270 str=['Mechanical Equivalent of Total Compliance = ',...
271     num2str(C_tot), ' N/m'];
272 disp(str);
273
274 V2=FinalVolume_In;
275 P2=P1*V1/V2;
276 V3=FinalVolume_Out;
277 P3=P1*V1/V3;
278
279 C_ma2=(V2/(Specific_Heat_Ratio*P2))/((Area_cone*(1e-6))^2);
280 C_tot_In=((C_m^(-1)+C_ma2^(-1)))^(-1);
281
282 C_ma3=(V3/(Specific_Heat_Ratio*P3))/((Area_cone*(1e-6))^2);
283 C_tot_Out=((C_m^(-1)+C_ma3^(-1)))^(-1);
284
285 PC_In=(C_tot_In-C_tot)/C_tot*100;
286 str=['Percent Change of Total Compliance Inward = ',...
287     num2str(PC_In), ' %'];
288 disp(str);
289 PC_Out=(C_tot_Out-C_tot)/C_tot*100;
290 str=['Percent Change of Total Compliance Outward = ',...
291     num2str(PC_Out), ' %'];
292 disp(str);

```

## C.2 Linear Parameter Characterization

The following code was used to analyze the data from the W2-2243S impedance measurement performed in section 4.1. Each driver has its own code, but the code functions the same way, just using different hardcoded values. The code begins by assigning added mass values and finding the impedance measured in each trial. The resonant frequencies are hard coded based on the measured impedance plots. The rest of the code follows the analysis process presented in section 4.2. User-created functions that are used in this data include *LabViewDataRead\_Excel.m*, which was used to read the .csv dataset file; *getAvgTimeSeries\_hann.m*, which was used to calculate the power spectral density; and *getAvgTimeSeries\_hann\_xy.m*, which was used to calculate the cross-spectral density.



```

1 close all
2 clc
3
4 names={'W2-2243S 10-31 CLEAN 1.csv',...
5       'W2-2243S 10-31 m1 2.csv',...
6       'W2-2243S 10-31 m2 1.csv',...
7       'W2-2243S 10-31 m3 1.csv',...
8       'W2-2243S 10-31 m4 1.csv',...
9       'W2-2243S 10-31 m5 1.csv'};
10
11 fs=20000;
12 BlockSize=200000;
13 N_avg=1;
14 N_ch=2;
15 dt=1/fs;
16
17 R_volt=0.3;
18 R_DC=4.0;
19 R=47.0;
20
21 %ALL MASSES ARE IN GRAMS
22 m1=2.62;
23 m2=m1+2.67;
24 m3=m2+2.61;
25 m4=m3+2.63;
26 m5=m4+2.61;
27
28 R_DC=R_DC-R_volt;
29 R=R-R_volt;
30
31 Z_e=R_DC;
32
33 % Find k and m0
34 Z_em_trans=zeros(50001,6);
35 for ii=1:length(names)
36     [xx,freq,~,~,FRF_mag,FRF_phase,~]=LabViewDataRead_Excel(names{ii},...
37         BlockSize,N_avg,N_ch,'cal');
38     [G_xy,~,~,~] = getAvgTimeSeries_hann_xy('G_xy',xx(:,1),...
39         xx(:,2),fs,100000,-.5);
40     [G_xx,freq_G,~,~] = getAvgTimeSeries_hann('G_xx',xx(:,1),fs,...
41         100000,-.5);
42     H_trans=G_xy./G_xx;

```

```

43     Z_em_trans(:,ii)=H_trans.*R-Z_e;
44 end
45
46 figure()
47 plot(freq_G,real(Z_em_trans(:,1)),'LineWidth',1.5)
48 hold on
49 xlim([10 4000])
50 ax=gca;
51 ax.FontSize=16;
52 point_x=236.4;
53 point_y=41.49;
54 dx=.8;
55 dy=1;
56 point_label={append('(' ,num2str(point_x(1)) ,',' ,...
57     num2str(point_y(1)) ,')' )};
58 scatter(point_x,point_y,'filled')
59 text(point_x(1)+dx,point_y(1)+dy,point_label(1),'FontSize',14);
60 xlabel('Frequency [Hz]','FontSize',16)
61 ylabel({'Unweighted Real'; 'DC-Shifted Impedance [Ohms]'},...
62     'FontSize',16)
63 xlim([180 300])
64 ylim([10 50])
65 hold off
66
67 figure()
68 semilogx(freq_G,real(Z_em_trans),'LineWidth',1.5)
69 hold on
70 ax=gca;
71 ax.FontSize=16;
72 xlim([10 4000])
73 ylim([-5 45])
74 xlabel('Frequency [Hz]','FontSize',16)
75 ylabel('Real DC-Shifted Impedance [Ohms]','FontSize',16)
76 legend('Unweighted','m1 Added','m2 Added','m3 Added','m4 Added',...
77     'm5 Added','FontSize',14)
78 hold off
79
80 figure()
81 semilogx(freq_G,imag(Z_em_trans(:,1)),'LineWidth',1.5)
82 hold on
83 ax=gca;
84 ax.FontSize=16;

```

```

85 xlim([10 4000])
86 ylim([-25 25])
87 point_x=[220,254.2];
88 point_y=[20.32,-21.78];
89 dx=.8;
90 dy=1;
91 point_label={append('(',num2str(point_x(1))','...',
92     num2str(point_y(1))',''),...
93     append('(',num2str(point_x(2))','...',num2str(point_y(2))',''))};
94 scatter(point_x,point_y,'filled')
95 text(point_x(1)+dx,point_y(1)+dy,point_label(1),'FontSize',14);
96 text(point_x(2)+dx,point_y(2)-dy,point_label(2),'FontSize',14);
97 xlabel('Frequency [Hz]','FontSize',16)
98 ylabel({'Unweighted Imaginary';'DC-Shifted Impedance [Ohms]'},...
99     'FontSize',16)
100 hold off
101
102 %% CHANGE p1, p2, R_square
103 mi=[0,m1,m2,m3]./1000; %m4, m5 has given bad data and has been removed
104 f0=[236.4,142,111.6,95.4];
105 linear_fit=1./((2*pi.*f0).^2);
106 [fitresult,gof]=createLinearFit(mi,linear_fit);
107 display(fitresult);
108 display(gof);
109
110 p1=0.0002946;
111 p2=4.674e-7;
112 R_square=0.9998;
113
114 mi_fit_line=(0:0.00001:mi(end));
115 fit_line=p1*mi_fit_line+p2;
116 figure()
117 plot(mi_fit_line,fit_line,'linewidth',1.5)
118 hold on
119 ax=gca;
120 ax.FontSize=16;
121 scatter(mi,linear_fit,'filled')
122 xlabel('Added Mass, m_i [kg]','FontSize',16)
123 ylabel('$ ( 2\pi f ) ^{-2} $','Interpreter','Latex','FontSize',16)
124 T=annotation('textbox','string',{sprintf(['Slope: ' num2str(p1)]),...
125     sprintf(['Y-Intercept: ' num2str(p2)]),...
126     sprintf(['R^2: ' num2str(R_square)]));

```

```

127 T.FontSize=14;
128 T.Position = [0.15 0.7 0.37 0.2];
129 T.LineStyle = '-';
130 hold off
131
132 k=1/p1;
133 m0=k*p2;
134
135 % Calculate uncertainty
136 sigma_a=sqrt((1/R_square-1)/(length(mi)-2))*(1/k);
137 sigma_b=sigma_a*sqrt(sum((mi.^2))/length(mi));
138
139 % Calculate Speaker Coeff
140
141 %% CHANGE delta_f, R_em
142 delta_f=254.2-220;
143 Q=f0(1)/delta_f;
144
145 R_em=41.51;
146
147 beta=2*pi*f0(1)/(2*Q);
148 R_m=2*(m0)*beta;
149
150 BL=sqrt(R_em*R_m);
151 C_em=(m0)/(BL^2);
152 L_em=(BL^2)/(k);
153
154 sigma_BL=0.1;
155 sigma_k=(1/p1^2)*sigma_a;
156 sigma_m0=sqrt((k^2)*(sigma_b^2)+(p2^2)*(sigma_k^2));
157 sigma_R_m=2*beta*sigma_m0;
158 sigma_C_em=sqrt((1/BL^2)^2*sigma_m0^2+(2*m0/(BL^3))^2*sigma_BL^2);
159 sigma_L_em=sqrt((BL^2/k^2)^2*sigma_k^2+(2*BL/k)^2*sigma_BL^2);
160
161 m0_grams=m0*1000;
162 Cm=1/k;
163 disp({append('m0 in grams = ',num2str(m0_grams))});
164 disp({append('Cm = ',num2str(Cm))});
165 disp({append('R_DC = ',num2str(R_DC))});
166 disp({append('BL = ',num2str(BL))});
167 disp({append('R_m = ',num2str(R_m))});
168 disp({append('Q = ',num2str(Q))});

```

```

169
170 %% Setup the Import Options and import the data
171 opts = delimitedTextImportOptions("NumVariables", 3);
172
173 % Specify range and delimiter
174 opts.DataLines = [2, Inf];
175 opts.Delimiter = ["\t", " ", ",", ";"];
176
177 % Specify column names and types
178 opts.VariableNames = ["Freq", "real", "imag"];
179 opts.VariableTypes = ["double", "double", "double"];
180
181 % Specify file level properties
182 opts.ExtraColumnsRule = "ignore";
183 opts.EmptyLineRule = "read";
184
185 % Import the data
186 model = readtable(['C:\Users\Joe Bradel\Documents\MATLAB\ACS 600\'...
187     'TB W2-2243S\Impedance Verify Model W2-2243S.txt'], opts);
188
189 %% Convert to output type
190 model = table2array(model);
191
192 %% Clear temporary variables
193 clear opts
194
195 figure('Position',[300 0 700 800])
196 subplot(3,1,1)
197 semilogx(freq_G, real(Z_em_trans(:,1)+Z_e), 'linewidth',1.5)
198 hold on
199 grid on
200 semilogx(model(:,1), -1*model(:,2), 'linewidth',1.5)
201 xlim([10 4000])
202 legend('Measured', 'Model')
203 xlabel('Frequency [Hz]')
204 ylabel('Real Impedance [Ohm]')
205 hold off
206 subplot(3,1,2)
207 semilogx(freq_G, imag(Z_em_trans(:,1)+Z_e), 'linewidth',1.5)
208 hold on
209 grid on
210 semilogx(model(:,1), -1*model(:,3), 'linewidth',1.5)

```

```

211 xlim([10 4000])
212 ylim([-32 32])
213 legend('Measured','Model')
214 xlabel('Frequency [Hz]')
215 ylabel('Imaginary Impedance [Ohm]')
216 hold off
217 subplot(3,1,3)
218 semilogx(freq_G,abs(Z_em_trans(:,1)+Z_e),'linewidth',1.5)
219 hold on
220 grid on
221 semilogx(model(:,1),abs(model(:,2)+1j*model(:,3)),'linewidth',1.5)
222 xlim([10 4000])
223 legend('Measured','Model')
224 xlabel('Frequency [Hz]')
225 ylabel('Magnitude of Impedance [Ohm]')
226 hold off

```

## C.3 Impulse and Frequency Response

This code was used to analyze and plot the impulse and frequency response data collected using the test method described in section 5.1.3. The code begins by requesting that the user choose a trial to analyze based on the excitation level. The code then plots the impulse response and calculates the transfer function, normalizing it to the sensitivity for that specific driver listed on its specification sheet. Other functions used within this code that are user-created are *getAvgTimeSeries\_hann.m*, which is used to calculate the average power spectral density; and *getAvgTimeSeries\_hann\_xy*, which was used to calculate the average cross-spectral density. Despite the naming convention of these functions, they can and were implemented using a rectangle window rather than a Hann window for the averaging.

```

1 close all
2 clc
3 set(0,'DefaultFigureWindowStyle','docked')
4
5 %% Plot Data
6 %% Get Decibel Run Input
7 str=['Which Decibel Run?\n1. 0 dB\n2. -6 dB\n3. -12 dB\n4. ' ...
8     '-24 dB\n5. -36 dB\n6. -42 dB\nInput:'];

```

```

9 Run=input(str);
10
11 % Catch input error
12 if Run<1 || Run>6
13     str='Input number must be between 1 and 6. Run Program Again.';
14     disp(str);
15     return
16 end
17
18 %% Run Post-Processing for Each Driver
19
20 DriverName={'W1','W2','FRS','TEB'};
21 dBRun={'0 dB','-6 dB','-12 dB','-24 dB','-36 dB','-42 dB'};
22 dBLabel=char(dBRun(Run));
23 MicSensitivity=-39; %dBV/Pa
24 MicCalibration=10^(MicSensitivity/20); %V/Pa
25 Voltage=[2,2,sqrt(8),sqrt(8)]; %V
26
27 Gain=20*log10(5.44/1.311);
28
29 f_ThirdOctave=zeros(32,3);
30 f_ThirdOctave(:,2)=(10.^(0.1.*(12:43))).';
31 fd=10^0.05;
32 f_ThirdOctave(:,3)=f_ThirdOctave(:,2)*fd;
33 f_ThirdOctave(:,1)=f_ThirdOctave(:,2)/fd;
34
35 for ii=1:4
36     if ii==1
37         RunRead=Run+3;
38     else
39         RunRead=Run;
40     end
41     if ii==4
42         if Run<=6 && Run>1
43             RunRead=Run-1;
44         end
45         if Run==2
46             RunRead=6;
47         end
48     end
49
50 Path=['C:\Users\Joe Bradel\Documents\MATLAB\ACS 600\Freq ' ...

```

```

51     'Resp 2-28 Mic 16132\'];
52     Mic=' 2-28 Mic 16132\';
53     VolSize='_DATA_SMALLEST_VOLUME.mat';
54     FileName=append(Path,char(DriverName(ii)),Mic,...
55         char(DriverName(ii)),VolSize);
56     load(FileName);
57
58     RunCheck=20*log10(max(...
59         measurementData.RawAudioData(RunRead,1).ExcitationSignal));
60
61     str=append('Decibel Check for ',char(DriverName(ii)),...
62         ' Run Read: ', num2str(RunCheck),' dB');
63     disp(str);
64
65     ImpResponse=measurementData.ImpulseResponse(RunRead,1).Amplitude;
66     Time=measurementData.ImpulseResponse(RunRead,1).Time;
67
68     figure('Name',[char(DriverName(ii)),' ImpResponse'])
69     plot(Time,ImpResponse,'linewidth',1.5)
70     xlabel('Time [s]')
71     ylabel('Impulse Response Amplitude')
72
73     fs=table2array(measurementData(RunRead,6));
74
75     RecSignal=measurementData.RawAudioData(RunRead,1).RecordedSignal;
76     RecSignal=RecSignal./MicCalibration;
77     RecSignal_long=[RecSignal(:, :, 1);RecSignal(:, :, 2);...
78         RecSignal(:, :, 3);RecSignal(:, :, 4);RecSignal(:, :, 5);...
79         RecSignal(:, :, 6);RecSignal(:, :, 7);RecSignal(:, :, 8);...
80         RecSignal(:, :, 9);RecSignal(:, :, 10)];
81
82     ExcSignal=measurementData.RawAudioData(RunRead,1).ExcitationSignal;
83     ExcSignalLong=[ExcSignal;ExcSignal;ExcSignal;ExcSignal;ExcSignal...
84         ;ExcSignal;ExcSignal;ExcSignal;ExcSignal;ExcSignal];
85
86     ExcSignalGain=(max(ExcSignal)*10^(Gain/20))/max(ExcSignal); % in V
87     ExcSignal=ExcSignal*ExcSignalGain;
88     ExcSignalLong=ExcSignalLong*ExcSignalGain;
89
90     ExcLevel=20*log10(abs(ExcSignal(1))); % in dBu
91
92     [G_xx,~,~,~]=getAvgTimeSeries_hann('G_xx',ExcSignalLong,fs,10000,...

```



```

93     -.5, 'Rect');
94     [G_xy, freq, ~, ~]=...
95     getAvgTimeSeries_hann_xy('G_xy', ExcSignalLong, RecSignal_long, ...
96     fs, 10000, -.5, 'Rect');
97     H=G_xy./G_xx;
98     H_norm=abs(H);
99     avgH=zeros(length(f_ThirdOctave(:,2)),1);
100    for jj=1:length(f_ThirdOctave)
101        indLower=interp1(freq,1:length(freq),f_ThirdOctave(jj,1),...
102        'nearest');
103        indUpper=interp1(freq,1:length(freq),f_ThirdOctave(jj,3),...
104        'nearest');
105        avgH(jj)=mean(H_norm(indLower:indUpper));
106    end
107
108    figure('Name',[char(DriverName(ii)),' ',dBLabel,' H=G_xy/G_xx'])
109    semilogx(freq,20*log10(H_norm./(20e-6/Voltage(ii))))
110    hold on
111    semilogx(f_ThirdOctave(:,2),20*log10(avgH./(20e-6/Voltage(ii))),...
112    'linewidth',2)
113    grid on
114    xlim([10 20000])
115    ylim([30 100])
116    xlabel('Frequency [Hz]')
117    ylabel({'Normalized Response Magnitude';...
118    '[dB re 20 \bf\mu\rmPa at 1 W]'})
119    legend('Normalized Response','1/3rd-Octave Average','location',...
120    'southeast')
121    hold off
122 end

```

## C.4 KA3 Data Plotter

This code was used to plot the data taken from the KA3 tests outlined in section 5.2.3. Furthermore, this code produces a third-octave average of the measured distortion in the multi-tone measurements discussed in subsection 5.2.5 as well as implements the Acceptable Displacement Percentage metric discussed in subsection 5.2.6. A section of the code is commented out at the beginning of the code. This should be uncommented if the user wishes to plot all measured data extracted from the Klippel Analyzer 3 system rather than just the data presented in this work. The portion of the code is a function

that reads specified .txt files and plots their data with appropriate axes and legends. The sections of code labeled 'Setup the Import Options and import the data' consist of code generated by MATLAB's Import Data feature [38] modified to work with the sections around it.

```

1  %% Clear necessary variables and set string variables
2  close all
3  clear Data
4  clear Driver1
5  clear Driver2
6  clear Driver3
7  clear Driver4
8  clc
9
10 set(0,'DefaultFigureWindowStyle','docked')
11
12 DriverName={'W1-2121S','W2-2243S','FRS 5X-8','TEBM36S12-8/A','All'};
13 Test={'0.07V','0.5V with 50ohm','Nonlinear'};
14 Result={'Magnitude of electric impedance Z(f)',...
15         'Spectrum X(f) of voice coil displacement',...
16         'Stiffness of Suspension Kms (X)',...
17         'Electrical inductance L (X,I=0)',...
18         'Electrical inductance L (X=0,I)',...
19         'Force Factor Bl (X)',...
20         'Voice Coil Displacement',...
21         'Equivalent Input Distortion Components',...
22         'Kms (X) Symmetry Range',...
23         'Bl (X) Symmetry Range'};
24
25 %% Plot All Data
26
27 % for ii=1:2
28 %     for kk=1:4
29 %         for jj=1:2
30 %             readDataFile(DriverName{kk},Test{jj},Result{ii});
31 %         end
32 %     end
33 % end
34 %
35 % readDataFile(DriverName{5},Test{3},Result{3});
36 % readDataFile(DriverName{5},Test{3},Result{4});

```

```

37 % readDataFile(DriverName{5},Test{3},Result{5});
38 % readDataFile(DriverName{5},Test{3},Result{6});
39 %
40 % for ii=7:10
41 %     for kk=1:4
42 %         readDataFile(DriverName{kk},Test{3},Result{ii});
43 %     end
44 % end
45
46 %% Plot Displacements, BL, k_s, L_e data
47
48 for kk=1:4
49     readDataFile(DriverName{kk},Test{1},Result{2});
50 end
51
52 readDataFile(DriverName{5},Test{3},Result{3});
53 readDataFile(DriverName{5},Test{3},Result{4});
54 readDataFile(DriverName{5},Test{3},Result{5});
55 readDataFile(DriverName{5},Test{3},Result{6});
56
57 for ii=9:10
58     for kk=1:4
59         readDataFile(DriverName{kk},Test{3},Result{ii});
60     end
61 end
62
63 %% Create Data Read and Plotting Function
64
65 function readDataFile(DriverName,Test,Result)
66 %Read and plot data based on the specified Driver Name, Test, and
67 %Result.
68
69 %% Set file name variables
70
71 if isequal(DriverName,'W1-2121S')
72     DriverNum=1;
73 elseif isequal(DriverName,'W2-2243S')
74     DriverNum=2;
75 elseif isequal(DriverName,'FRS 5X-8')
76     DriverNum=3;
77 elseif isequal(DriverName,'TEBM36S12-8/A')
78     DriverNum=4;

```

```

79     DriverName='TEBM36S12-8A';
80 elseif isequal(DriverName,'All')
81     DriverNum=5;
82 else
83     str='Invalid DriverName';
84     disp(str);
85     return
86 end
87
88 if isequal(Test,'Nonlinear')
89     TestNum=1;
90     if isequal(Result,'Bl (X) Symmetry Range')
91         ResultNum=1;
92         Xlabel='Amplitude [mm]';
93         Ylabel='Offset [mm]';
94         NumCol=6;
95     elseif isequal(Result,'Electrical inductance L (X,I=0)')
96         ResultNum=2;
97         Xlabel='Displacement, X [mm]';
98         Ylabel='Electrical inductance, L_e(X,I=0) [mH]';
99         NumCol=2;
100    elseif isequal(Result,'Electrical inductance L (X=0,I)')
101        ResultNum=3;
102        Xlabel='Current, I [A]';
103        Ylabel='Electrical inductance, L_e(X=0,I) [mH]';
104        NumCol=2;
105    elseif isequal(Result,'Force Factor Bl (X)')
106        ResultNum=4;
107        Xlabel='Displacement, X [mm]';
108        Ylabel='Force Factor, Bl(X) [Tm]';
109        NumCol=4;
110    elseif isequal(Result,'Kms (X) Symmetry Range')
111        ResultNum=5;
112        Xlabel='Amplitude [mm]';
113        Ylabel='Offset [mm]';
114        NumCol=6;
115    elseif isequal(Result,'Stiffness of Suspension Kms (X)')
116        ResultNum=6;
117        Xlabel='Displacement, X [mm]';
118        Ylabel='Suspension Stiffness, k_s(X) [N/mm]';
119        NumCol=4;
120    elseif isequal(Result,'Equivalent Input Distortion Components')

```

```

121     ResultNum=9;
122     Xlabel='Time [s]';
123     Ylabel='Distortion Ratio [%]';
124     NumCol=8;
125     elseif isequal(Result,'Voice Coil Displacement')
126         ResultNum=10;
127         Xlabel='Time [s]';
128         Ylabel='Voice Coil Displacement [mm]';
129         NumCol=14;
130     else
131         str='Invalid Result';
132         disp(str);
133         return
134     end
135     elseif isequal(Test,'0.07V')
136         TestNum=2;
137         if isequal(Result,'Magnitude of electric impedance Z(f)')
138             ResultNum=7;
139             Xlabel='Frequency [Hz]';
140             Ylabel='Magnitude of Impedance [Ohm]';
141             NumCol=4;
142         elseif isequal(Result,'Spectrum X(f) of voice coil displacement')
143             ResultNum=8;
144             Xlabel='Frequency [Hz]';
145             Ylabel='Displacement, X [mm]';
146             NumCol=6;
147         else
148             str='Invalid Result';
149             disp(str);
150             return
151         end
152     elseif isequal(Test,'0.5V with 50ohm')
153         TestNum=3;
154         if isequal(Result,'Magnitude of electric impedance Z(f)')
155             ResultNum=7;
156             Xlabel='Frequency [Hz]';
157             Ylabel='Magnitude of Impedance [Ohm]';
158             NumCol=4;
159         elseif isequal(Result,'Spectrum X(f) of voice coil displacement')
160             ResultNum=8;
161             Xlabel='Frequency [Hz]';
162             Ylabel='Displacement, X [mm]';

```

```

163     NumCol=6;
164 else
165     str='Invalid Result';
166     disp(str);
167     return
168 end
169 else
170     str='Invalid Test';
171     disp(str);
172     return
173 end
174
175 %% Check for Test Type/Result Type Mismatch
176 if TestNum==1
177     if ResultNum==7 || ResultNum==8
178         str='Test Type/Result Type Mismatch';
179         disp(str);
180         return
181     end
182 end
183
184 if TestNum==2 || TestNum==3
185     if ResultNum==1 || ResultNum==2 || ResultNum==3 || ResultNum==4 ...
186         || ResultNum==5 || ResultNum==6 || ResultNum==9 || ResultNum==10
187         str='Test Type/Result Type Mismatch';
188         disp(str);
189         return
190     end
191 end
192
193 %% Import data from text file
194 %% Setup the Import Options and import the data
195 if DriverNum==1 || DriverNum==2 || DriverNum==3 || DriverNum==4
196     % A portion of this code was created by MATLAB's Import Data
197     % feature, set to import .txt files extracted from the Klippel
198     % Analyzer 3 system. The code generated by MATLAB's Import Data
199     % feature was modified to be used within this code.
200     opts = delimitedTextImportOptions("NumVariables", NumCol);
201
202     % Specify range and delimiter
203     opts.DataLines = [4, Inf];
204     opts.Delimiter = "\t";

```

```

205
206 % Specify column names and types
207 if NumCol==4
208     opts.VariableNames = ["VarName1", "VarName2", "VarName3",...
209         "VarName4"];
210     opts.VariableTypes = ["double", "double", "double", "double"];
211 elseif NumCol==6
212     opts.VariableNames = ["VarName1", "VarName2", "VarName3",...
213         "VarName4", "VarName5", "VarName6"];
214     opts.VariableTypes = ["double", "double", "double", "double",...
215         "double", "double"];
216 elseif NumCol==8
217     opts.VariableNames = ["VarName1", "VarName2", "VarName3",...
218         "VarName4", "VarName5", "VarName6",...
219         "VarName7", "VarName8"];
220     opts.VariableTypes = ["double", "double", "double", "double",...
221         "double", "double", "double",...
222         "double"];
223 elseif NumCol==2
224     opts.VariableNames = ["VarName1", "VarName2"];
225     opts.VariableTypes = ["double", "double"];
226 elseif NumCol==14
227     opts.VariableNames = ["VarName1", "VarName2", "VarName3",...
228         "VarName4", "VarName5", "VarName6",...
229         "VarName7", "VarName8", "VarName9", "VarName10",...
230         "VarName11", "VarName12", "VarName13", "VarName14"];
231     opts.VariableTypes = ["double", "double", "double", "double",...
232         "double", "double", "double",...
233         "double", "double", "double", "double", "double", "double",...
234         "double"];
235 else
236     opts.VariableNames = ["VarName1", "VarName2", "VarName3",...
237         "VarName4", "VarName5", "VarName6", "VarName7", "VarName8"];
238     opts.VariableTypes = ["double", "double", "double", "double",...
239         "double", "double", "double", "double"];
240 end
241 % Specify file level properties
242 opts.ExtraColumnsRule = "ignore";
243 opts.EmptyLineRule = "read";
244
245 % Import the data
246 Path=['C:\Users\Joe Bradel\Documents\MATLAB\ACS 600\Klippel'...

```

```

247     ' Results\Data from Databases\'];
248     FileType='.txt';
249     FilePath=append(Path,DriverName,'\ ',Test,'\ ',Result,FileType);
250     Data = readtable(FilePath, opts);
251
252     %% Convert to output type
253     Data = table2array(Data);
254
255     %% Clear temporary variables
256     clear opts
257
258     % This marks the end of the code generated by MATLAB's Import
259     % Data feature.
260
261     %% Begin figure creation
262
263     figure('Name',[DriverName,' ',Result,' ',Test])
264     if ResultNum==1 || ResultNum==5                                % Symmetry Plots
265         plot(Data(:,1),Data(:,2),'linewidth',1.5)
266         hold on
267         plot(Data(:,3),Data(:,4),'linewidth',1.5)
268         plot(Data(:,5),Data(:,6),'linewidth',1.5)
269         yline(0);
270         ylim([-3 3])
271         legend('Symmetry Point','Asymmetry 5% Upper Bound',...
272             'Asymmetry 5% Lower Bound')
273     elseif ResultNum==7                                            % Impedance Plots
274         semilogx(Data(:,1),Data(:,2))
275         hold on
276         semilogx(Data(:,3),Data(:,4))
277         legend('Measured','Fitted')
278     elseif ResultNum==8                                            % Displacement Plots
279         loglog(Data(:,1),Data(:,2))
280         hold on
281         loglog(Data(:,3),Data(:,4))
282         loglog(Data(:,5),Data(:,6))
283         x=[250,315,400,500,630,800,1000,1250,1600,2000,2500,3150];
284         y=zeros(length(x),1);
285         low=[1834,2312,2909,3662,4604,5801,7299,9193,11577,13105,18341,...
286             23084];
287         high=[1840,2908,3661,4603,5800,7298,9192,11576,13104,18340,...
288             23083,29065];

```



```

289     for ii=1:length(x)
290         top=[];
291         jj=low(ii);
292         while (low(ii)<=jj) && (jj<=high(ii))
293             if isnan(Data(jj,3))
294                 inc=1;
295             else
296                 top=[top,Data(jj,4)]; %#ok<AGROW>
297                 inc=2;
298             end
299             jj=jj+inc;
300         end
301         y(ii)=mean(top);
302         clear top
303     end
304     loglog(x,y,'linewidth',1.5)
305     clear y
306     legend('Signal Lines','Noise + Distortions','Noise Floor',...
307           'Avg Distortion + Noise')
308     ylim([10e-11 10e-4])
309     xlim([500 3000])
310     elseif ResultNum==2 || ResultNum==3                % L_e Plots
311         plot(Data(:,1),Data(:,2),'linewidth',1.5)
312         ylim([0 inf])
313     elseif ResultNum==4                                % Bl Plots
314         plot(Data(:,1),Data(:,2),'linewidth',1.5)
315         hold on
316         plot(Data(:,3),Data(:,4),'linewidth',1.5,'linestyle','--',...
317               'color',[0 0.4470 0.7410])
318         legend('Bl(|X|<X_{prot})','Bl(-X)')
319         ylim([0 inf])
320     elseif ResultNum==6                                % Kms Plots
321         plot(Data(:,1),Data(:,2),'linewidth',1.5)
322         hold on
323         plot(Data(:,3),Data(:,4),'linewidth',1.5,'linestyle','--',...
324               'color',[0 0.4470 0.7410])
325         legend('k_s(|X|<X_{prot})','k_s(-X)')
326         ylim([0 inf])
327     elseif ResultNum==9
328         plot(Data(:,3),Data(:,4),'linewidth',1.5)
329         hold on
330         plot(Data(:,1),Data(:,2),'linewidth',1.5)

```

```

331     plot(Data(:,5),Data(:,6),'linewidth',1.5)
332     plot(Data(:,7),Data(:,8),'linewidth',1.5)
333     l=legend('D_{Bl}','D_{C_m}','D_{L(i)}','D_{L(x)}');
334     l.Location='NorthWest';
335     ylim([0 60])
336 elseif ResultNum==10
337     plot(Data(:,9),Data(:,10),'linewidth',1.5)
338     hold on
339     plot(Data(:,11),Data(:,12),'linewidth',1.5)
340     plot(Data(:,13),Data(:,14),'linewidth',1.5)
341     plot(Data(:,1),Data(:,2),'linewidth',1.5)
342     plot(Data(:,3),Data(:,4),'linewidth',1.5)
343     plot(Data(:,5),Data(:,6),'linewidth',1.5)
344     plot(Data(:,7),Data(:,8),'linewidth',1.5)
345     l=legend('X, measured peak','X, measured bottom',...
346             'X, measured DC','X, predicted peak',...
347             'X, predicted bottom','X, predicted DC','X, predicted DC max');
348     l.Location='NorthWest';
349     ylim([-5 5])
350 end
351 xlabel(Xlabel);
352 ylabel(Ylabel);
353 hold off
354
355 else
356     if ResultNum==2 || ResultNum==3 || ResultNum==4 || ResultNum==6
357         % A portion of this code was created by MATLAB's Import Data
358         % feature, set to import .txt files extracted from the Klippel
359         % Analyzer 3 system. The code generated by MATLAB's Import Data
360         % feature was modified to be used within this code.
361         opts = delimitedTextImportOptions("NumVariables", NumCol);
362
363         % Specify range and delimiter
364         opts.DataLines = [4, Inf];
365         opts.Delimiter = "\t";
366
367         % Specify column names and types
368         if NumCol==4
369             opts.VariableNames = ["VarName1", "VarName2", "VarName3",...
370                                   "VarName4"];
371             opts.VariableTypes = ["double", "double", "double", "double"];
372         elseif NumCol==6

```

```

373     opts.VariableNames = ["VarName1", "VarName2", "VarName3",...
374         "VarName4", "VarName5", "VarName6"];
375     opts.VariableTypes = ["double", "double", "double",...
376         "double", "double", "double"];
377 elseif NumCol==2
378     opts.VariableNames = ["VarName1", "VarName2"];
379     opts.VariableTypes = ["double", "double"];
380 else
381     opts.VariableNames = ["VarName1", "VarName2", "VarName3",...
382         "VarName4", "VarName5", "VarName6"];
383     opts.VariableTypes = ["double", "double", "double",...
384         "double", "double", "double"];
385 end
386 % Specify file level properties
387 opts.ExtraColumnsRule = "ignore";
388 opts.EmptyLineRule = "read";
389
390 % Import the data
391 Path=['C:\Users\Joe Bradel\Documents\MATLAB\ACS 600\',...
392     'Klippel Results\Data from Databases\'];
393 FileType='.txt';
394 if DriverNum==5
395     DriverNameSet={'W1-2121S';'W2-2243S';'FRS 5X-8';...
396         'TEBM36S12-8A'};
397
398     FilePath=append(Path,DriverNameSet{1},'\',Test,'\',...
399         Result,FileType);
400     Driver1 = readtable(FilePath, opts);
401     FilePath=append(Path,DriverNameSet{2},'\',Test,'\',...
402         Result,FileType);
403     Driver2 = readtable(FilePath, opts);
404     FilePath=append(Path,DriverNameSet{3},'\',Test,'\',...
405         Result,FileType);
406     Driver3 = readtable(FilePath, opts);
407     FilePath=append(Path,DriverNameSet{4},'\',Test,'\',...
408         Result,FileType);
409     Driver4 = readtable(FilePath, opts);
410     %% Convert to output type
411     Driver1 = table2array(Driver1);
412     Driver2 = table2array(Driver2);
413     Driver3 = table2array(Driver3);
414     Driver4 = table2array(Driver4);

```

```

415
416 %% Clear temporary variables
417 clear opts
418
419 % This marks the end of the code generated by MATLAB's Import
420 % Data feature.
421
422 %% Begin figure creation
423
424 if ResultNum==2 || ResultNum==3 % L_e Plots
425     figure('Name',[DriverName,' ',Result,' ',Test])
426     plot(Driver1(:,1),Driver1(:,2),'linewidth',1.5,...
427          'color',[0 0.4470 0.7410])
428     hold on
429     plot(Driver2(:,1),Driver2(:,2),'linewidth',1.5,...
430          'color',[0.8500 0.3250 0.0980])
431     plot(Driver3(:,1),Driver3(:,2),'linewidth',1.5,...
432          'color',[0.9290 0.6940 0.1250])
433     plot(Driver4(:,1),Driver4(:,2),'linewidth',1.5,...
434          'color',[0.4940 0.1840 0.5560])
435     legend('W1-2121S','W2-2243S','FRS 5X-8','TEBM36S12-8/A',...
436            'location','southwest')
437     if ResultNum==3
438         ylim([0 0.18])
439     else
440         ylim([0 0.22])
441     end
442 elseif ResultNum==4 % Bl Plots
443     figure('Name',[DriverName,' ',Result,' ',Test])
444     plot(Driver1(:,1),Driver1(:,2),'linewidth',1.5,'color',...
445          [0 0.4470 0.7410])
446     hold on
447     plot(Driver1(:,3),Driver1(:,4),'linewidth',1.5,...
448          'linestyle','--','color',[0 0.4470 0.7410])
449     plot(Driver2(:,1),Driver2(:,2),'linewidth',1.5,...
450          'color',[0.8500 0.3250 0.0980])
451     plot(Driver2(:,3),Driver2(:,4),'linewidth',1.5,...
452          'linestyle','--','color',[0.8500 0.3250 0.0980])
453     plot(Driver3(:,1),Driver3(:,2),'linewidth',1.5,...
454          'color',[0.9290 0.6940 0.1250])
455     plot(Driver3(:,3),Driver3(:,4),'linewidth',1.5,...
456          'linestyle','--','color',[0.9290 0.6940 0.1250])

```

```

457 plot(Driver4(:,1),Driver4(:,2),'linewidth',1.5,...
458       'color',[0.4940 0.1840 0.5560])
459 plot(Driver4(:,3),Driver4(:,4),'linewidth',1.5,...
460       'linestyle','--','color',[0.4940 0.1840 0.5560])
461 legend('W1-2121S, Bl(|X|<X_{prot})','W1-2121S, Bl(-X)',...
462        'W2-2243S, Bl(|X|<X_{prot})','W2-2243S, Bl(-X)',...
463        'FRS 5X-8, Bl(|X|<X_{prot})','FRS 5X-8, Bl(-X)',...
464        'TEBM36S12-8/A, Bl(|X|<X_{prot})',...
465        'TEBM36S12-8/A, Bl(-X)','location','south')
466 ylim([0 4])
467 xlabel(Xlabel);
468 ylabel(Ylabel);
469 hold off
470
471 center=[174,184.5,177.5,186.5];
472 figure('Name',[DriverName,' ',Result,' Parameter % Change'])
473 PercChange=zeros(length(Driver1(:,1)),1);
474 for ll=1:length(Driver1(:,1))
475     PercChange(ll)=100*(Driver1(ll,2)-Driver1(center(1),2))/...
476     Driver1(center(1),2);
477 end
478 plot(Driver1(:,1),PercChange,'linewidth',1.5,'color',...
479       [0 0.4470 0.7410])
480 hold on
481 PercChange=zeros(length(Driver2(:,1)),1);
482 CenterParam=(Driver2(center(2)+0.5,2)+Driver2(center(2)...
483           -0.5,2))/2;
484 for ll=1:length(Driver2(:,1))
485     PercChange(ll)=100*(Driver2(ll,2)-CenterParam)/...
486     CenterParam;
487 end
488 plot(Driver2(:,1),PercChange,'linewidth',1.5,'color',...
489       [0.8500 0.3250 0.0980])
490 PercChange=zeros(length(Driver3(:,1)),1);
491 CenterParam=(Driver3(center(3)+0.5,2)+Driver3(center(3)...
492           -0.5,2))/2;
493 for ll=1:length(Driver3(:,1))
494     PercChange(ll)=100*(Driver3(ll,2)-CenterParam)/...
495     CenterParam;
496 end
497 plot(Driver3(:,1),PercChange,'linewidth',1.5,'color',...
498       [0.9290 0.6940 0.1250])

```

```

499 PercChange=zeros(length(Driver4(:,1)),1);
500 CenterParam=(Driver4(center(4)+0.5,2)+Driver4(center(4)...
501     -0.5,2))/2;
502 for ll=1:length(Driver4(:,1))
503     PercChange(ll)=100*(Driver4(ll,2)-CenterParam)/...
504     CenterParam;
505 end
506 plot(Driver4(:,1),PercChange,'linewidth',1.5,'color',...
507     [0.4940 0.1840 0.5560])
508 yline(5,'linestyle','--','color','k');
509 yline(-5,'linestyle','--','color','k');
510 legend('W1-2121S','W2-2243S','FRS 5X-8','TEBM36S12-8/A',...
511     '+5% Change','-5% Change','location','south')
512 xlabel(Xlabel);
513 ylabel('Percent Change from B1 @ X=0 mm [%]');
514 hold off
515
516 figure('Name',[DriverName,' ',Result,' Asymmetry % Change'])
517 PercDiff=zeros(floor(length(Driver1(:,1))/2),1);
518 Amplitude=zeros(floor(length(Driver1(:,1))/2),1);
519 for ll=1:floor(length(Driver1(:,1))/2)
520     PercDiff(ll)=100*2*abs(Driver1(center(1)+ll,2)-...
521         Driver1(center(1)-ll,2))/(Driver1(center(1)+ll,2)+...
522         Driver1(center(1)-ll,2));
523     Amplitude(ll)=(Driver1(center(1)+ll,1)+abs(...
524         Driver1(center(1)-ll,1)))/2;
525 end
526 plot(Amplitude,PercDiff,'linewidth',1.5,'color',...
527     [0 0.4470 0.7410])
528 hold on
529 PercDiff=zeros(floor(length(Driver2(:,1))/2),1);
530 Amplitude=zeros(floor(length(Driver2(:,1))/2),1);
531 for ll=0:floor(length(Driver2(:,1))/2)-1
532     PercDiff(ll+1)=100*2*abs(Driver2(center(2)+0.5+ll,2)-...
533         Driver2(center(2)-0.5-ll,2))/...
534         (Driver2(center(2)+0.5+ll,2)+Driver2(center(2)-0.5-ll,2));
535     Amplitude(ll+1)=(Driver2(center(2)+0.5+ll,1)+abs(...
536         Driver2(center(2)-0.5-ll,1)))/2;
537 end
538 plot(Amplitude,PercDiff,'linewidth',1.5,'color',...
539     [0.8500 0.3250 0.0980])
540 PercDiff=zeros(floor(length(Driver3(:,1))/2),1);

```

```

541 Amplitude=zeros(floor(length(Driver3(:,1))/2),1);
542 for ll=0:floor(length(Driver3(:,1))/2)-1
543     PercDiff(ll+1)=100*2*abs(Driver3(center(3)+0.5+ll,2)-...
544         Driver3(center(3)-0.5-ll,2))/...
545         (Driver3(center(3)+0.5+ll,2)+Driver3(center(3)-0.5-ll,2));
546     Amplitude(ll+1)=(Driver3(center(3)+0.5+ll,1)+abs(...
547         Driver3(center(3)-0.5-ll,1)))/2;
548 end
549 plot(Amplitude,PercDiff,'linewidth',1.5,'color',...
550     [0.9290 0.6940 0.1250])
551 PercDiff=zeros(floor(length(Driver4(:,1))/2),1);
552 Amplitude=zeros(floor(length(Driver4(:,1))/2),1);
553 for ll=0:floor(length(Driver4(:,1))/2)-1
554     PercDiff(ll+1)=100*2*abs(Driver4(center(4)+0.5+ll,2)-...
555         Driver4(center(4)-0.5-ll,2))/...
556         (Driver4(center(4)+0.5+ll,2)+Driver4(center(4)-0.5-ll,2));
557     Amplitude(ll+1)=(Driver4(center(4)+0.5+ll,1)+abs(...
558         Driver4(center(4)-0.5-ll,1)))/2;
559 end
560 plot(Amplitude,PercDiff,'linewidth',1.5,'color',...
561     [0.4940 0.1840 0.5560])
562 yline(5,'linestyle','--','color','k');
563 legend('W1-2121S','W2-2243S','FRS 5X-8','TEBM36S12-8/A',...
564     '% Difference','location','northeast')
565 xlabel('Displacement Magnitude, |X| [mm]');
566 ylabel('Percent Difference of B1 between +X and -X [%]');
567 hold off
568
569 elseif ResultNum==6 % Kms Plots
570     figure('Name',[DriverName,' ',Result,' ',Test])
571     plot(Driver1(:,1),Driver1(:,2),'linewidth',1.5,'color',...
572         [0 0.4470 0.7410])
573     hold on
574     plot(Driver1(:,3),Driver1(:,4),'linewidth',1.5,...
575         'linestyle','--','color',[0 0.4470 0.7410])
576     plot(Driver2(:,1),Driver2(:,2),'linewidth',1.5,...
577         'color',[0.8500 0.3250 0.0980])
578     plot(Driver2(:,3),Driver2(:,4),'linewidth',1.5,...
579         'linestyle','--','color',[0.8500 0.3250 0.0980])
580     plot(Driver3(:,1),Driver3(:,2),'linewidth',1.5,...
581         'color',[0.9290 0.6940 0.1250])
582     plot(Driver3(:,3),Driver3(:,4),'linewidth',1.5,...

```

```

583     'linestyle','--','color',[0.9290 0.6940 0.1250])
584 plot(Driver4(:,1),Driver4(:,2),'linewidth',1.5,...
585     'color',[0.4940 0.1840 0.5560])
586 plot(Driver4(:,3),Driver4(:,4),'linewidth',1.5,...
587     'linestyle','--','color',[0.4940 0.1840 0.5560])
588 legend('W1-2121S, k_s(|X|<X_{prot})',...
589     'W1-2121S, k_s(-X)', 'W2-2243S, k_s(|X|<X_{prot})',...
590     'W2-2243S, k_s(-X)', 'FRS 5X-8, k_s(|X|<X_{prot})',...
591     'FRS 5X-8, k_s(-X)',...
592     'TEBM36S12-8/A, k_s(|X|<X_{prot})',...
593     'TEBM36S12-8/A, k_s(-X)', 'location','north')
594 ylim([0 4])
595 xlabel(Xlabel);
596 ylabel(Ylabel);
597 hold off
598
599 center=[174,184.5,177.5,186.5];
600 figure('Name',[DriverName,' ',Result,' Parameter % Change'])
601 PercChange=zeros(length(Driver1(:,1)),1);
602 for ll=1:length(Driver1(:,1))
603     PercChange(ll)=100*(Driver1(ll,2)-Driver1(center(1),2))/...
604     Driver1(center(1),2);
605 end
606 plot(Driver1(:,1),PercChange,'linewidth',1.5,'color',...
607     [0 0.4470 0.7410])
608 hold on
609 PercChange=zeros(length(Driver2(:,1)),1);
610 CenterParam=(Driver2(center(2)+0.5,2)+Driver2(center(2)...
611     -0.5,2))/2;
612 for ll=1:length(Driver2(:,1))
613     PercChange(ll)=100*(Driver2(ll,2)-CenterParam)/...
614     CenterParam;
615 end
616 plot(Driver2(:,1),PercChange,'linewidth',1.5,'color',...
617     [0.8500 0.3250 0.0980])
618 PercChange=zeros(length(Driver3(:,1)),1);
619 CenterParam=(Driver3(center(3)+0.5,2)+Driver3(center(3)...
620     -0.5,2))/2;
621 for ll=1:length(Driver3(:,1))
622     PercChange(ll)=100*(Driver3(ll,2)-CenterParam)/...
623     CenterParam;
624 end

```



```

625 plot(Driver3(:,1),PercChange,'linewidth',1.5,'color',...
626       [0.9290 0.6940 0.1250])
627 PercChange=zeros(length(Driver4(:,1)),1);
628 CenterParam=(Driver4(center(4)+0.5,2)+Driver4(center(4)...
629           -0.5,2))/2;
630 for ll=1:length(Driver4(:,1))
631     PercChange(ll)=100*(Driver4(ll,2)-CenterParam)/...
632         CenterParam;
633 end
634 plot(Driver4(:,1),PercChange,'linewidth',1.5,'color',...
635       [0.4940 0.1840 0.5560])
636 yline(5,'linestyle','--','color','k');
637 yline(-5,'linestyle','--','color','k');
638 legend('W1-2121S','W2-2243S','FRS 5X-8','TEBM36S12-8/A',...
639        '+5% Change','-5% Change','location','north')
640 xlabel(Xlabel);
641 ylabel('Percent Change from k_s @ X=0 mm [%]');
642 hold off
643
644 figure('Name',[DriverName,' ',Result,' Asymmetry % Change'])
645 PercDiff=zeros(floor(length(Driver1(:,1))/2),1);
646 Amplitude=zeros(floor(length(Driver1(:,1))/2),1);
647 for ll=1:floor(length(Driver1(:,1))/2)
648     PercDiff(ll)=100*2*abs(Driver1(center(1)+ll,2)-...
649         Driver1(center(1)-ll,2))/(Driver1(center(1)+ll,2)+...
650         Driver1(center(1)-ll,2));
651     Amplitude(ll)=(Driver1(center(1)+ll,1)+abs(...
652         Driver1(center(1)-ll,1)))/2;
653 end
654 plot(Amplitude,PercDiff,'linewidth',1.5,'color',...
655       [0 0.4470 0.7410])
656 hold on
657 PercDiff=zeros(floor(length(Driver2(:,1))/2),1);
658 Amplitude=zeros(floor(length(Driver2(:,1))/2),1);
659 for ll=0:floor(length(Driver2(:,1))/2)-1
660     PercDiff(ll+1)=100*2*abs(Driver2(center(2)+0.5+ll,2)-...
661         Driver2(center(2)-0.5-ll,2))/...
662         (Driver2(center(2)+0.5+ll,2)+Driver2(center(2)-0.5-ll,2));
663     Amplitude(ll+1)=(Driver2(center(2)+0.5+ll,1)+abs(...
664         Driver2(center(2)-0.5-ll,1)))/2;
665 end
666 plot(Amplitude,PercDiff,'linewidth',1.5,'color',...

```

```

667         [0.8500 0.3250 0.0980])
668     PercDiff=zeros(floor(length(Driver3(:,1))/2),1);
669     Amplitude=zeros(floor(length(Driver3(:,1))/2),1);
670     for ll=0:floor(length(Driver3(:,1))/2)-1
671         PercDiff(ll+1)=100*2*abs(Driver3(center(3)+0.5+ll,2)-...
672             Driver3(center(3)-0.5-ll,2))/...
673             (Driver3(center(3)+0.5+ll,2)+Driver3(center(3)-0.5-ll,2));
674         Amplitude(ll+1)=(Driver3(center(3)+0.5+ll,1)+abs(...
675             Driver3(center(3)-0.5-ll,1)))/2;
676     end
677     plot(Amplitude,PercDiff,'linewidth',1.5,'color',...
678         [0.9290 0.6940 0.1250])
679     PercDiff=zeros(floor(length(Driver4(:,1))/2),1);
680     Amplitude=zeros(floor(length(Driver4(:,1))/2),1);
681     for ll=0:floor(length(Driver4(:,1))/2)-1
682         PercDiff(ll+1)=100*2*abs(Driver4(center(4)+0.5+ll,2)-...
683             Driver4(center(4)-0.5-ll,2))/...
684             (Driver4(center(4)+0.5+ll,2)+Driver4(center(4)-0.5-ll,2));
685         Amplitude(ll+1)=(Driver4(center(4)+0.5+ll,1)+abs(...
686             Driver4(center(4)-0.5-ll,1)))/2;
687     end
688     plot(Amplitude,PercDiff,'linewidth',1.5,'color',...
689         [0.4940 0.1840 0.5560])
690     yline(5,'linestyle','--','color','k');
691     legend('W1-2121S','W2-2243S','FRS 5X-8','TEBM36S12-8/A',...
692         '5% Difference','location','northwest')
693     xlabel('Displacement Magnitude, |X| [mm]');
694     ylabel('Percent Difference of k_s between +X and -X [%]');
695     hold off
696 end
697 else
698     str='Cannot Graph All Results on Single Plot';
699     disp(str)
700     return
701 end
702 end
703 end
704 end

```

# Appendix D |

## Impulse Response Measurement Results

The impulse responses measured using the method described in subsection 5.1.3 helped to determine the optimal excitation level for determining the assemblies frequency responses. There were several excitation levels tested so that the optimal excitation level could be found. The excitation signal generated by the *ImpulseResponseAppModel.m* application in MATLAB [28] was affected by an amplifier before arriving at the speaker terminals. These impulse response calculations were completed without the *ImpulseResponseAppModel.m* application knowing the true excitation level at the speaker terminals; however, the 'spikes' that often signify the addition of distortion in the system [26] were still observable to help create an informed choice for the optimal excitation level. As the excitation level was lowered, the measurements came closer to the noise floor, which may have caused 'lumps' in the impulse response. The 6.36 dBV excitation level was ultimately chosen because the resulting measurement proved to be loud enough to be above the noise floor but quiet enough to limit added distortion. Figs. D.1–D.6 show the impulse responses for the W1-2121S assembly, Figs. D.7–D.12 show the impulse responses for the W2-2243S assembly, Figs. D.13–D.18 show the impulse responses for the FRS 5X-8 assembly, and Figs. D.19–D.24 show the impulse responses for the TEBM36S12-8/A assembly all in the following excitation level order: 12.36 dBV, 6.36 dBV, 0.36 dBV, –11.36 dBV, –23.64 dBV, and –29.64 dBV.

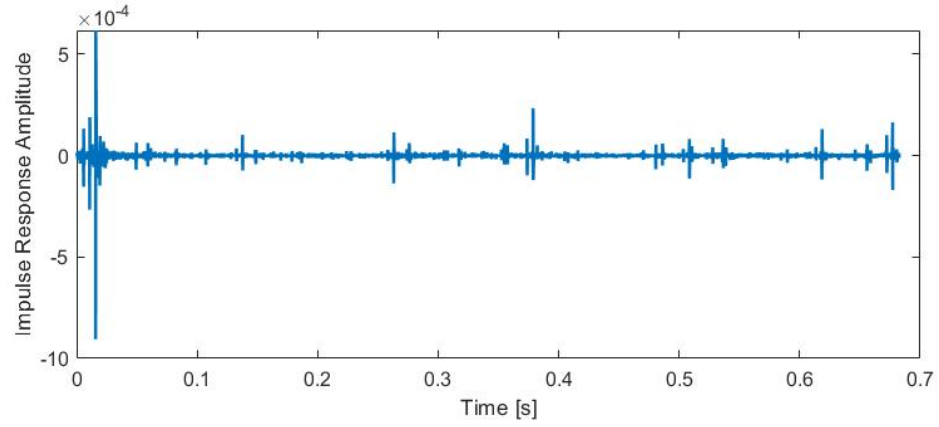


**Figure D.1.** The impulse response for the W1-2121S driver with an excitation signal level of 12.36 dBV.

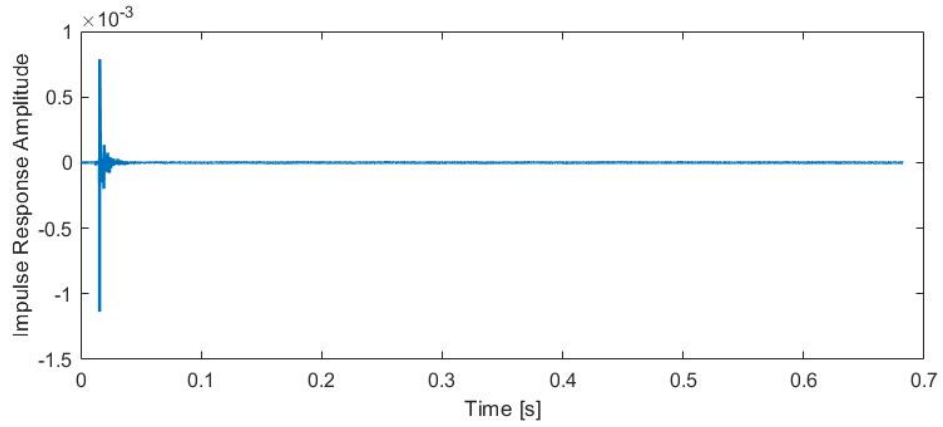


**Figure D.2.** The impulse response for the W1-2121S driver with an excitation signal level of 6.36 dBV.

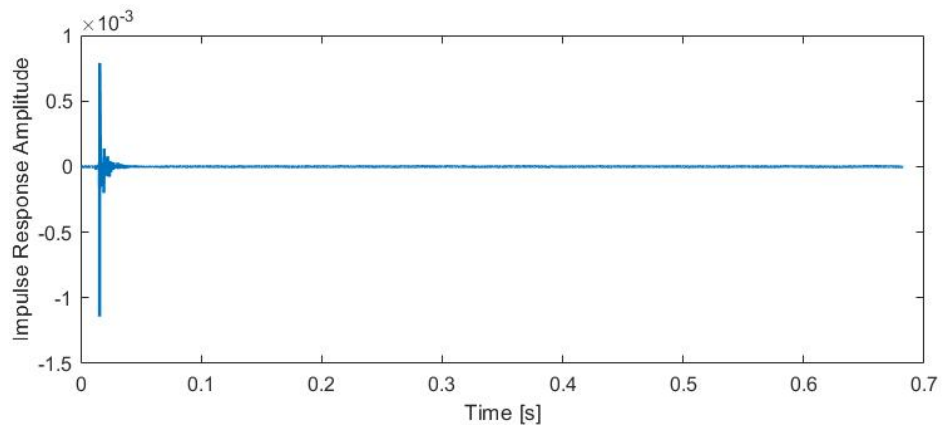


**Figure D.3.** The impulse response for the W1-2121S driver with an excitation signal level of 0.36 dBV.

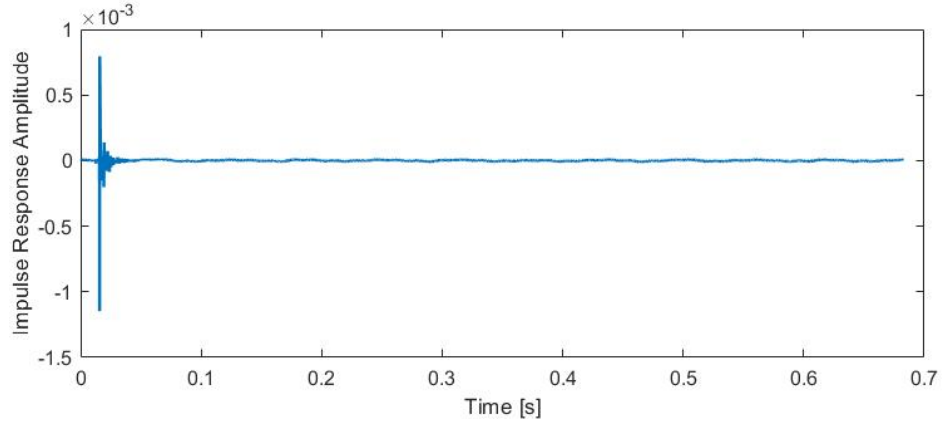


**Figure D.4.** The impulse response for the W1-2121S driver with an excitation signal level of  $-11.36$  dBV.

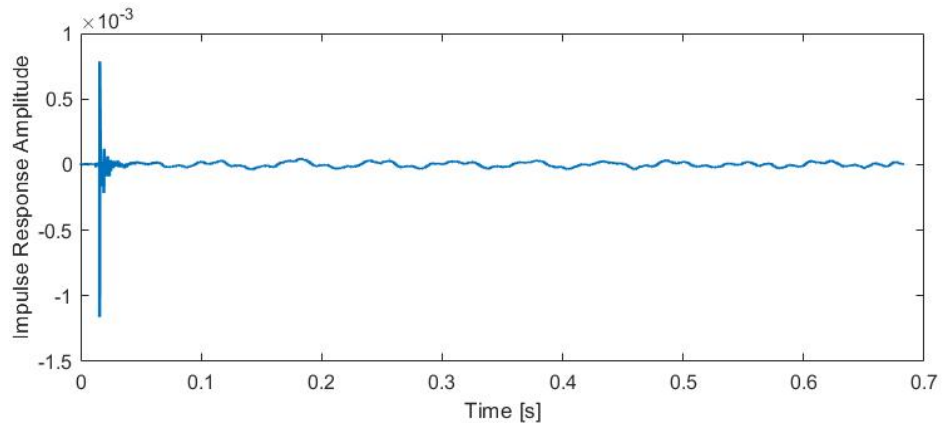


**Figure D.5.** The impulse response for the W1-2121S driver with an excitation signal level of  $-23.64$  dBV.

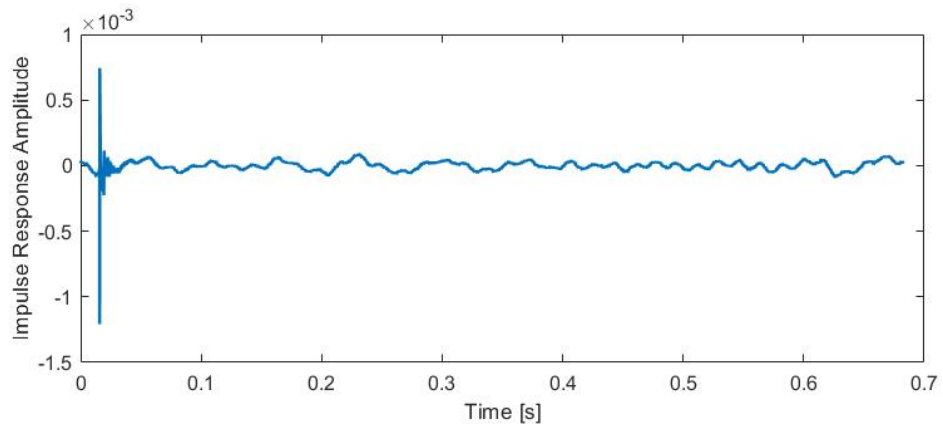


**Figure D.6.** The impulse response for the W1-2121S driver with an excitation signal level of  $-29.64$  dBV.

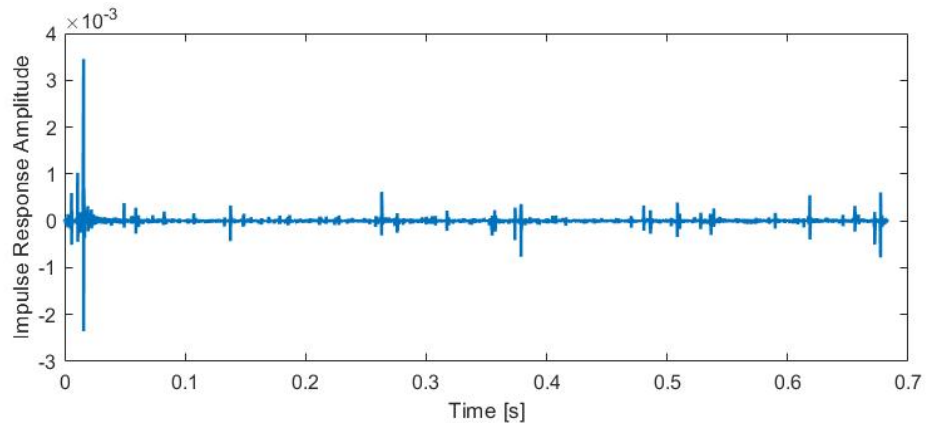


**Figure D.7.** The impulse response for the W2-2243S driver with an excitation signal level of 12.36 dBV.

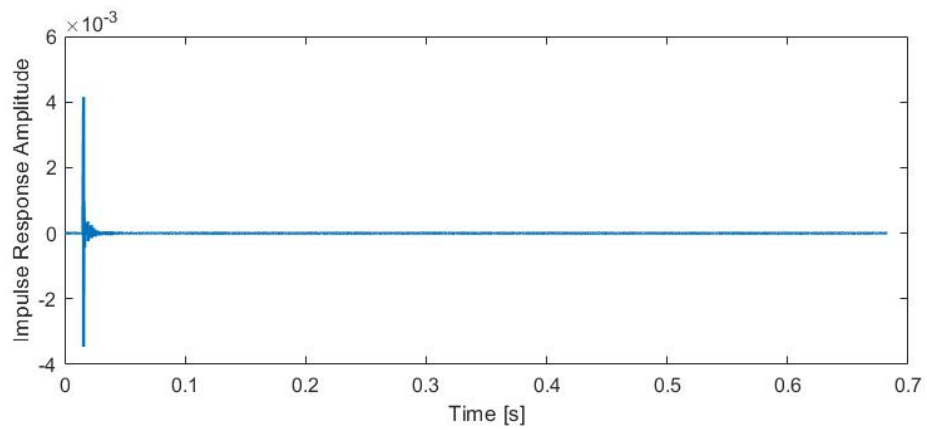


**Figure D.8.** The impulse response for the W2-2243S driver with an excitation signal level of 6.36 dBV.

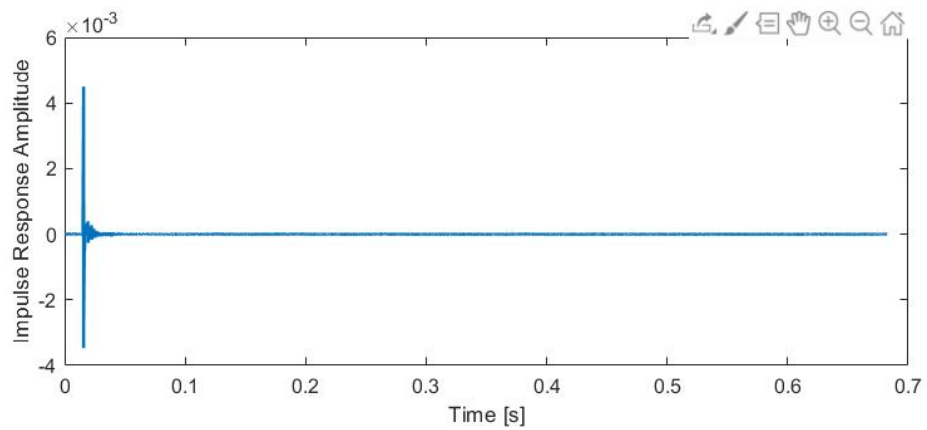


**Figure D.9.** The impulse response for the W2-2243S driver with an excitation signal level of 0.36 dBV.

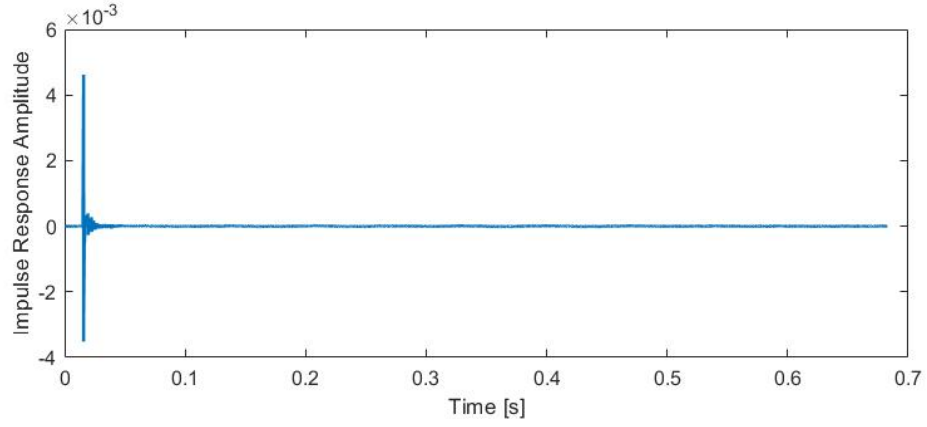


**Figure D.10.** The impulse response for the W2-2243S driver with an excitation signal level of  $-11.36$  dBV.

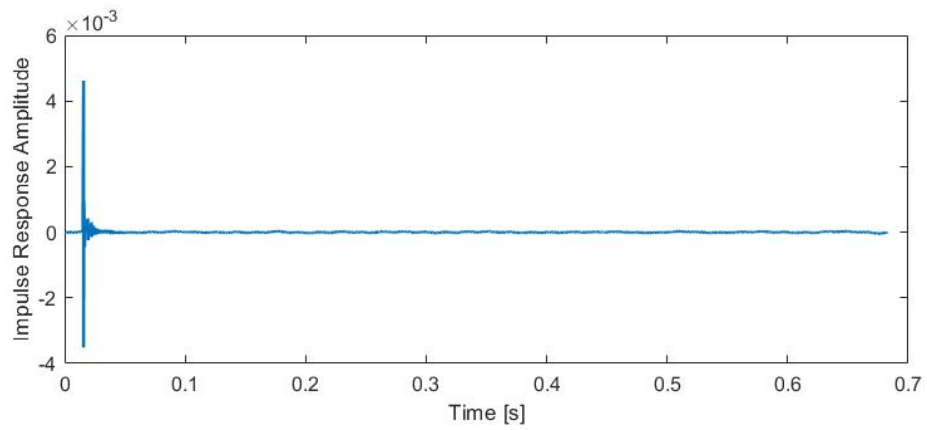


**Figure D.11.** The impulse response for the W2-2243S driver with an excitation signal level of  $-23.64$  dBV.

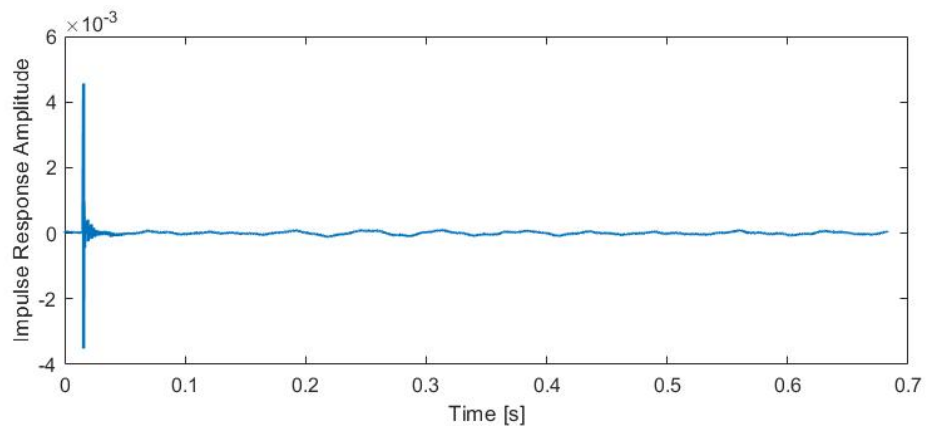


**Figure D.12.** The impulse response for the W2-2243S driver with an excitation signal level of  $-29.64$  dBV.

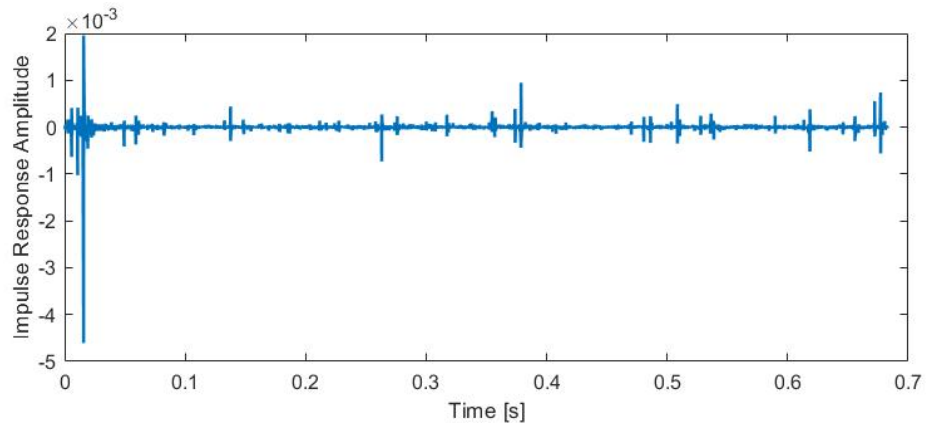


**Figure D.13.** The impulse response for the FRS 5X-8 driver with an excitation signal level of 12.36 dBV.

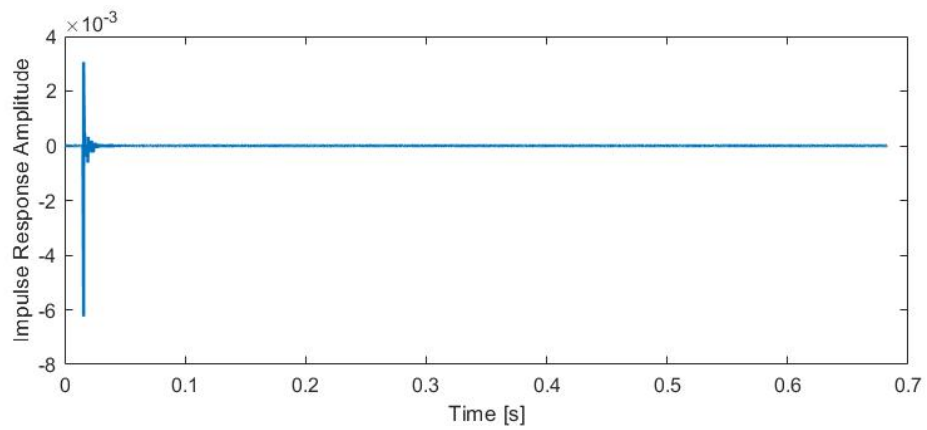


**Figure D.14.** The impulse response for the FRS 5X-8 driver with an excitation signal level of 6.36 dBV.

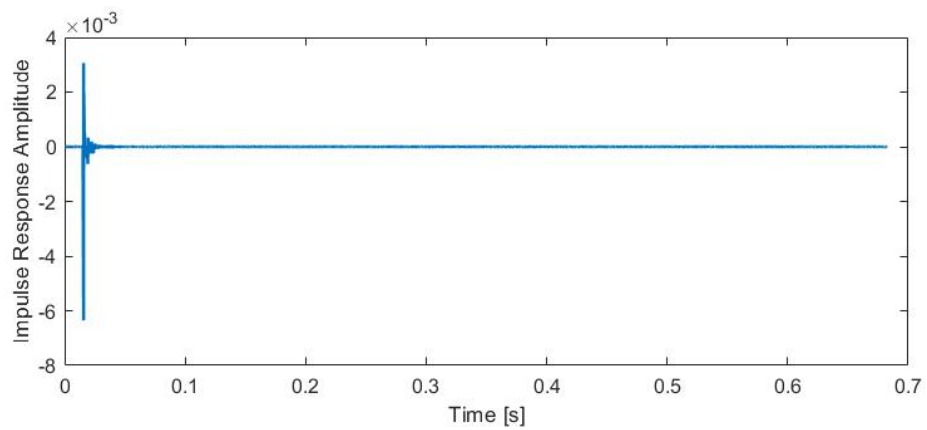


**Figure D.15.** The impulse response for the FRS 5X-8 driver with an excitation signal level of 0.36 dBV.



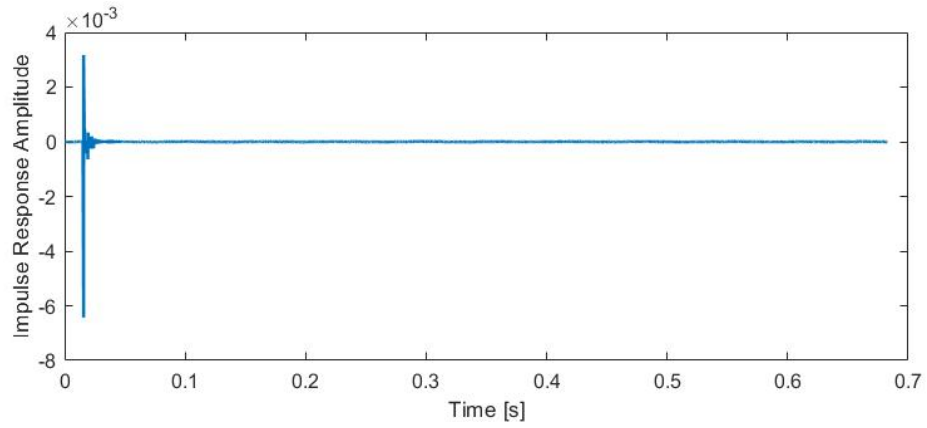


**Figure D.16.** The impulse response for the FRS 5X-8 driver with an excitation signal level of  $-11.36$  dBV.

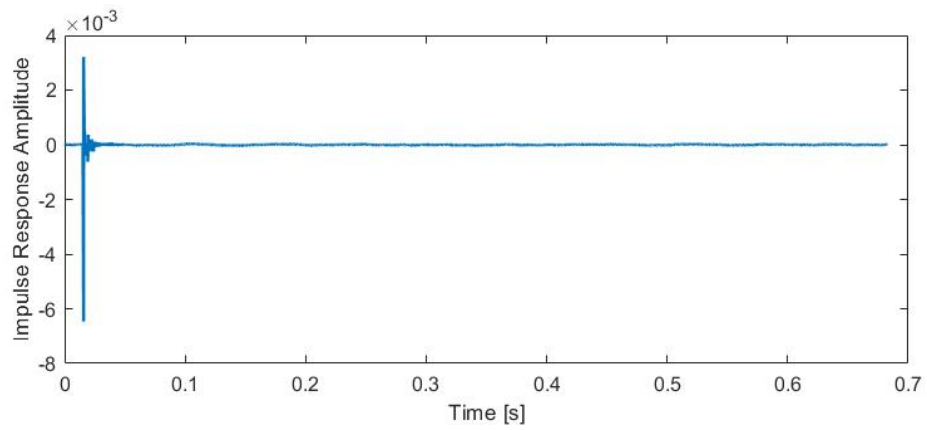


**Figure D.17.** The impulse response for the FRS 5X-8 driver with an excitation signal level of  $-23.64$  dBV.

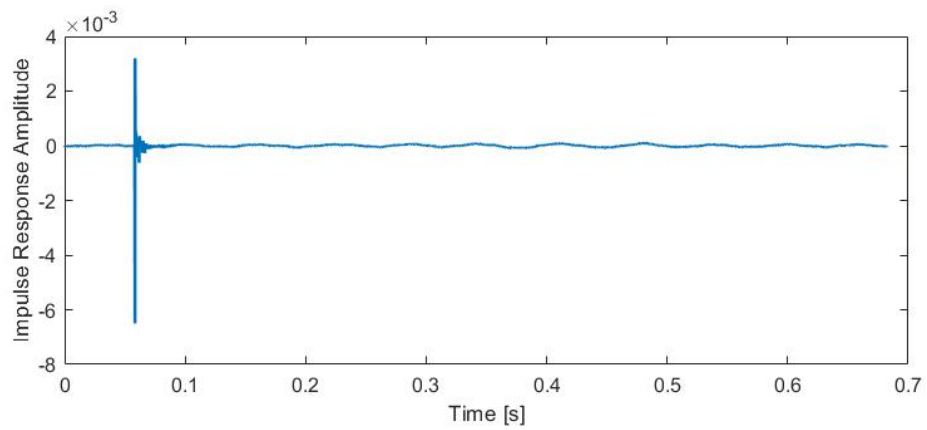


**Figure D.18.** The impulse response for the FRS 5X-8 driver with an excitation signal level of  $-29.64$  dBV.

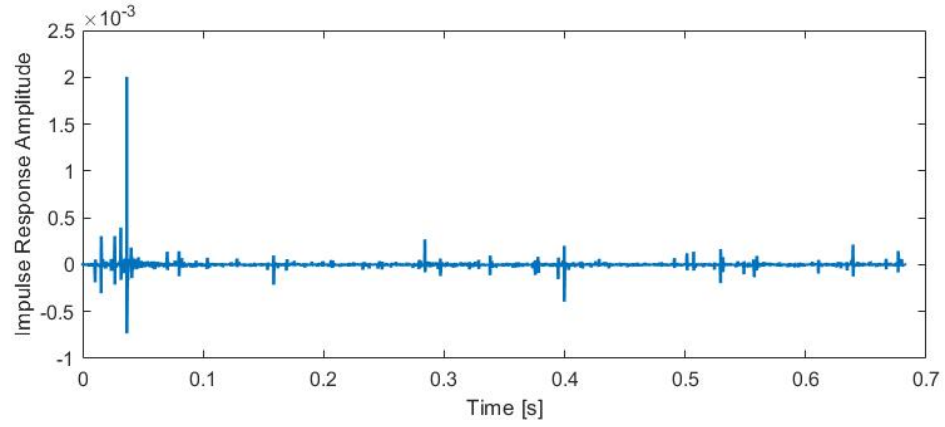


**Figure D.19.** The impulse response for the TEBM36S12-8/A driver with an excitation signal level of 12.36 dBV.

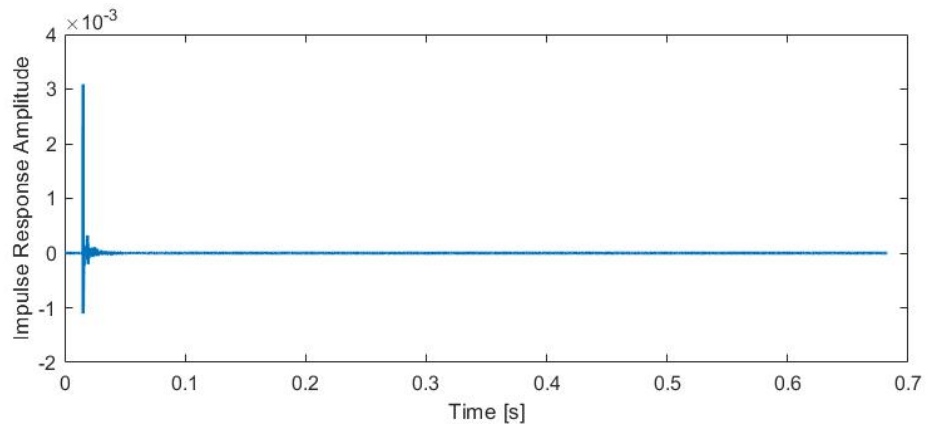


**Figure D.20.** The impulse response for the TEBM36S12-8/A driver with an excitation signal level of 6.36 dBV.

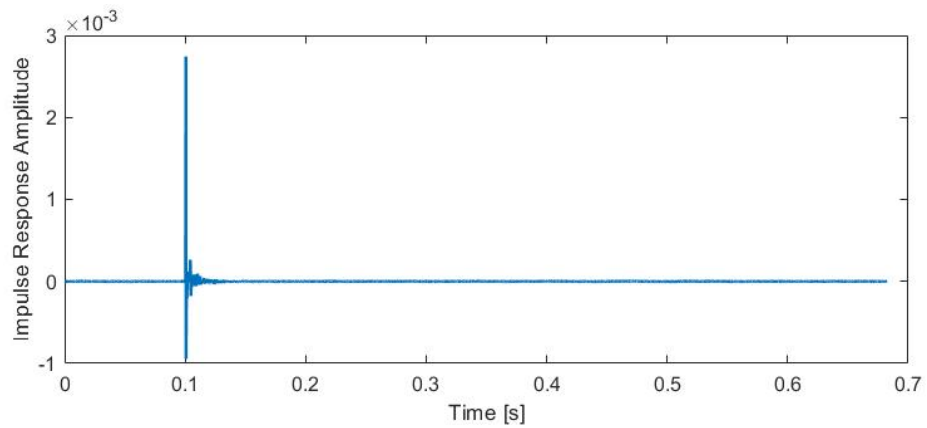


**Figure D.21.** The impulse response for the TEBM36S12-8/A driver with an excitation signal level of 0.36 dBV.

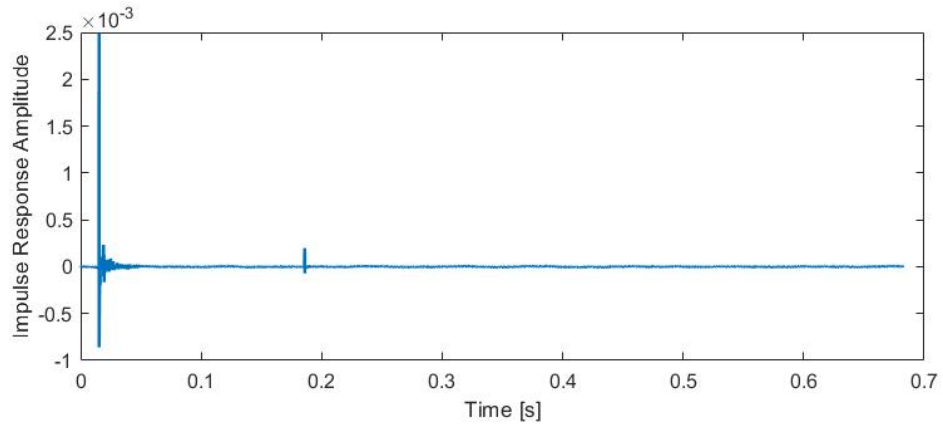


**Figure D.22.** The impulse response for the TEBM36S12-8/A driver with an excitation signal level of  $-11.36$  dBV.

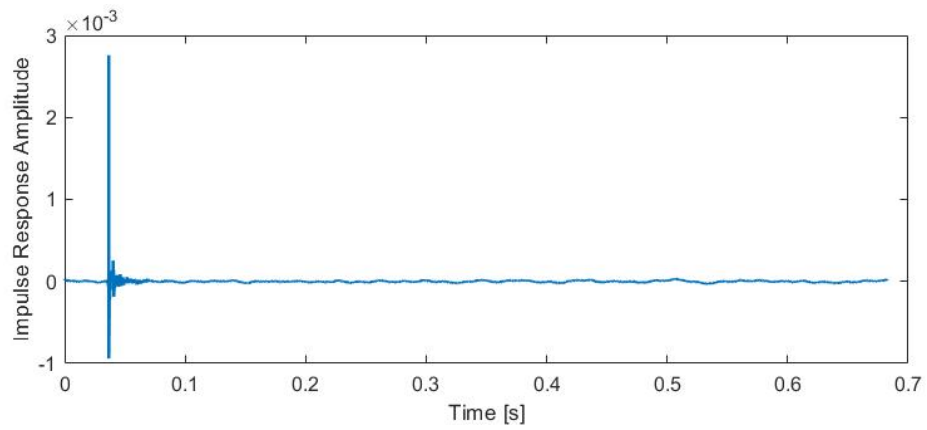


**Figure D.23.** The impulse response for the TEBM36S12-8/A driver with an excitation signal level of  $-23.64$  dBV.

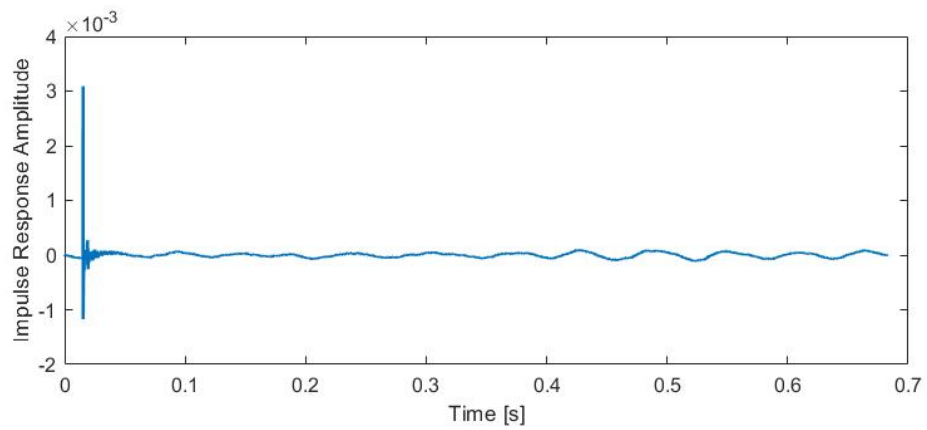


**Figure D.24.** The impulse response for the TEBM36S12-8/A driver with an excitation signal level of  $-29.64$  dBV.

# Bibliography

- [1] MÜLLER, G. and M. MÖSER (2013) *Handbook of Engineering Acoustics*, Springer-Verlag, Berlin Heidelberg.
- [2] BLACKSTOCK, D. T. (2000) *Fundamentals of Physical Acoustics*, Wiley, New York.
- [3] TB SPEAKER (2014), “W1-2121S 1" Alum. Full Range Driver,” .  
URL <http://www.tb-speaker.com/uploads/files/e99c0126812ca22379a2179932b9e840.pdf>
- [4] ——— (2014), “W2-2243S 2" Alum/Mg Neodymium Full Range,” .  
URL <http://www.tb-speaker.com/uploads/files/e4964df0494335751327c45c1160fc73.pdf>
- [5] VISATON (2017), “FRS 5 X - 8 Ohm,” .  
URL [https://www.visaton.de/sites/default/files/dd\\_product/frs5x\\_8.pdf](https://www.visaton.de/sites/default/files/dd_product/frs5x_8.pdf)
- [6] TECTONIC, “TEBM36S12-8/A,” .  
URL [https://www.tectonicaudiolabs.com/wp-content/uploads/woocommerce\\_uploads/2018/10/T-DS-TEBM36S12-8A.pdf](https://www.tectonicaudiolabs.com/wp-content/uploads/woocommerce_uploads/2018/10/T-DS-TEBM36S12-8A.pdf)
- [7] BERANEK, L. L. and T. J. MELLOW (2019) *Acoustics: Sound Fields, Transducers and Vibration*, 2 ed., Academic Press.
- [8] BERANEK, L. L. (1954) *Acoustics*, 1 ed., The American Institute of Physics for the Acoustical Society of America, New York.
- [9] KLIPPEL, “Multi-Tone Distortion,” .  
URL <https://www.klippel.de/know-how/measurements/nonlinear-distortion/multi-tone-distortion.html>
- [10] AURALEX (1999), “Riverbank Acoustical Laboratories of IIT Research Institute Report,” .  
URL <https://auralex.com/content/performance/2pyramid.pdf>
- [11] GUICKING, D. (1990) “On the invention of active noise control by Paul Lueg,” *The Journal of the Acoustical Society of America*, **87**(5), pp. 2251–2254.  
URL <https://doi.org/10.1121/1.399195>

- [12] RUMSEY, F. (2003) “Automotive Audio,” *J. Audio Eng. Soc.*, **51**(6), pp. 570–574.
- [13] HASHIMOTO, H., I. KAKUHARI, K. TERAJ, and Y. NAKAMURA (2001) “Active Control System for Low Frequency Road Noise Combined with an Audio System,” *J. Audio Eng. Soc.*
- [14] GEORGE, N. V. and G. PANDA (2012) “A robust filtered-s LMS algorithm for nonlinear active noise control,” *Applied Acoustics*, **73**, pp. 836–841.
- [15] COSTALUNGA, A., C. TRIPODI, L. EBRI, M. VIZZACCARO, L. CATTANI, E. UGOLOTTI, and T. NILI (2018) “Experimental results on active road noise cancellation in car interior,” *J. Audio Eng. Soc.*
- [16] KLIPPEL, W. (1991) “The nonlinear large-signal transfer characteristics of electro-dynamical loudspeakers at low frequencies,” *J. Audio Eng. Soc.*  
URL <https://www.aes.org/e-lib/browse.cfm?elib=5644>
- [17] ——— (2005) “Loudspeaker Nonlinearities - Causes, Parameters, Symptoms,” *J. Audio Eng. Soc.*  
URL <https://www.aes.org/e-lib/browse.cfm?elib=13346>
- [18] ——— (2001) “Prediction of Loudspeaker Performance at High Amplitudes,” *J. Audio Eng. Soc.*  
URL <https://www.aes.org/e-lib/browse.cfm?elib=9834>
- [19] HUNT, F. V. (1954) *Electroacoustics: The Analysis of Transduction, and Its Historical Background*, Wiley, New York.
- [20] VANDERKOOY, J. (1994) “Aspects of MLS Measuring Systems,” *J. Audio Eng. Soc.*, **42**(4), pp. 219–231.  
URL <http://www.aes.org/e-lib/browse.cfm?elib=6951>
- [21] AUDIO ENGINEERING SOCIETY (2012) *AES standard for acoustics - Methods of measuring and specifying the performance of loudspeakers for professional applications - Drive units*, Audio Engineering Society, Inc., New York.
- [22] ANALOG DEVICES (2020), “LTspice,” .  
URL <https://www.analog.com/en/design-center/design-tools-and-calculators/ltspice-simulator.html>
- [23] VANDERKOOY, J. (1989) “A Model of Loudspeaker Driver Impedance Incorporating Eddy Currents in the Pole Structure,” *J. Audio Eng. Soc.*, **37**(3), pp. 119–128.  
URL <https://www.aes.org/tmpFiles/elib/20201002/6100.pdf>
- [24] MACWILLIAMS, F. J. and N. J. A. SLOANE (1976) “Pseudo-Random Sequences and Arrays,” in *Proceedings of the IEEE*, vol. 64, pp. 1715–1729.

- [25] RIFE, D. D. and J. VANDERKOOY (1989) “Transfer-Function Measurement using Maximum-Length Sequences,” *J. Audio Eng. Soc.*, **37**.  
URL <https://www.aes.org/e-lib/browse.cfm?elib=4900>
- [26] DUNN, C. and M. J. HAWKSFORD (1993) “Distortion Immunity of MLS-Derived Impulse Response Measurements,” *J. Audio Eng. Soc.*, **41**(5), pp. 314–335.  
URL <http://www.aes.org/e-lib/browse.cfm?elib=7004>
- [27] STAN, G.-B., J.-J. EMBRECHTS, and D. ARCHAMBEAU (2002) “Comparison of Different Impulse Response Measurement Techniques,” *J. Audio Eng. Soc.*, **50**(4), pp. 249–262.  
URL <http://www.aes.org/e-lib/browse.cfm?elib=11083>
- [28] MATHWORKS (2018), “Impulse Response Measurer,” .  
URL <https://www.mathworks.com/help/audio/ref/impulseresponsemeasurer-app.html>
- [29] ——— (2006), “freqz,” .  
URL <https://www.mathworks.com/help/signal/ref/freqz.html>
- [30] AURALEX (2020), “Studiofoam Pyramids,” .  
URL <https://auralex.com/studiofoam-pyramid/>
- [31] KEYENCE, “Sensor Head Spot Type, Laser Class 2 - LK-H052,” .  
URL [https://www.keyence.com/products/measure/laser-1d/lk-g5000/models/lk-h052/?search\\_{\\_}dl=1](https://www.keyence.com/products/measure/laser-1d/lk-g5000/models/lk-h052/?search_{_}dl=1)
- [32] KLIPPEL, “KA3 - Klippel Analyzer System 3,” .  
URL <https://www.klippel.de/products/rd-system/analyzer-hardware/ka3-klippel-analyzer-3.html{#}content>
- [33] ———, “DB-LAB SOFTWARE,” .  
URL <https://www.klippel.de/products/rd-system/software/db-lab-software.html>
- [34] ———, “Linear Parameter Measurement (LPM),” .  
URL <https://www.klippel.de/products/rd-system/modules/lpm-linear-parameter-measurement.html>
- [35] ———, “Large Signal Identification (LSI),” .  
URL <https://www.klippel.de/products/rd-system/modules/lsi3-large-signal-identification.html>
- [36] LEACH, W. M. (2002) “Loudspeaker voice-coil inductance losses: Circuit models, parameter estimation, and effect on frequency response,” *J. Audio Eng. Soc.*, **50**(6), pp. 442–450.  
URL <https://www.aes.org/tmpFiles/elib/20201003/11074.pdf>

- [37] WRIGHT, J. R. (1990) “Empirical model for loudspeaker motor impedance,” *J. Audio Eng. Soc.*, **38**(10), pp. 749–754.  
URL <https://www.aes.org/tmpFiles/elib/20201003/5918.pdf>
- [38] MATHWORKS (2020), “Import Text Files,” .  
URL [https://www.mathworks.com/help/matlab/import\\_export/ways-to-import-text-files.html](https://www.mathworks.com/help/matlab/import_export/ways-to-import-text-files.html)